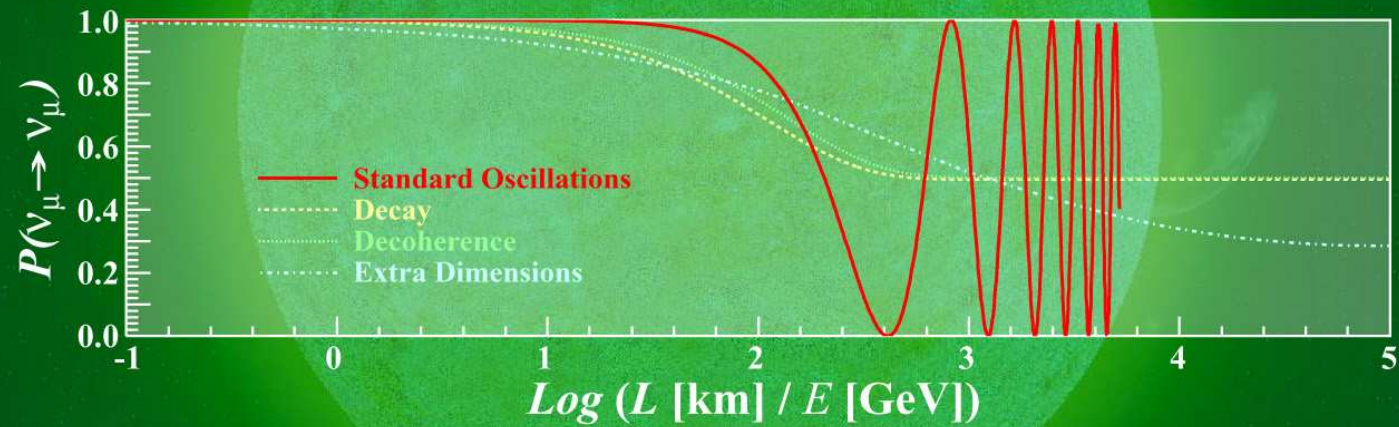


V.Naumov

From Cosmic Rays to Neutrino Oscillations

Part II



JINR, Dubna April 2006

Contents

I	INTRODUCTION TO NEUTRINO OSCILLATIONS	7
1	Bruno Pontecorvo	8
2	Neutrino masses and mixing in the Standard Model	10
2.1	Interaction Lagrangians and currents	10
2.2	Dirac neutrinos	12
2.2.1	Parametrization of mixing matrix for Dirac neutrinos	14
2.2.2	Neutrinoless muon decay	18
2.2.3	Nuclear beta decay	19
2.3	Majorana neutrinos	28
2.3.1	Parametrization of mixing matrix for Majorana neutrinos	31
2.3.2	Neutrinoless double beta decay	33
2.4	See-saw mechanism	39
2.4.1	Dirac-Majorana mass term for one generation	39
2.4.2	The See-saw	42
2.4.3	More neutral fermions	44
3	Neutrino oscillations in vacuum	46
3.1	Macroscopic Feynman diagrams	46
3.2	Quantum mechanical approach	53
3.2.1	Simplest case: two flavor vacuum oscillations	57

4	Neutrino oscillations in matter	58
4.1	Neutrino refraction in matter	58
4.1.1	Matter of constant density	59
4.2	Propagation of high-energy mixed neutrinos through matter	63
4.2.1	Generalized MSW equation	63
4.2.2	Master equation	65
4.2.3	Total cross sections	71
4.2.4	Indices of refraction	75
4.2.5	Eigenproblem and mixing matrix in matter	77
4.2.6	Adiabatic solution	85
4.2.7	Matter of constant density and composition	91
4.2.8	Conclusions	102

II SOLAR NEUTRINOS 103

5	The pp fusion step by step	104
5.1	The pp I branch	109
5.2	The pep fusion	111
5.3	The pp II branch	112
5.4	The pp III branch	113
5.5	The pp IV branch (hep reaction)	114
5.6	The full pp chain	115
6	An excursus: the elemental abundance in the Sun	116

7 The CNO cycle 118

8 Solar neutrino spectrum 121

III SOLAR NEUTRINO EXPERIMENTS 125

9 Current status 126

10 **Cl-Ar detector at Homestake 128**

10.1 Solar Neutrino Puzzle, Number I' 135

10.2 Solar Neutrino Puzzle, Number II' 136

10.3 Solutions 140

10.3.1 Astrophysics and/or Nuclear Physics 140

10.3.2 Nonstandard Neutrino Properties 142

10.3.3 Exotics and Science Fiction 143

11 **Ga-Ge detectors (SAGE, GALLEX, GNO) 144**

12 **H₂O detectors (Kamiokande and Super- Kamiokande) 154**

13 **D₂O detector SNO 162**

IV REACTOR NEUTRINO EXPERIMENTS 164

14 Terrestrial neutrinos 165

15	Past and current (Bugey, Gösgen, Krasnoyarsk, Palo Verde, Savannah River Site, Braidwood, ...)	167
16	CHOOZ, Double-CHOOZ, Triple-CHOOZ	168
17	KamLAND	169
18	What next? (Angra, DaYa-Bay, KASKA, TEXONO,...)	170

V NEUTRINO TELESCOPES 171

19	Detectors for high-energy neutrino astronomy	172
20	DUMAND	176
21	Baikal neutrino telescope	179
22	AMANDA	193
23	KM3 projects (IceCube, NEMO, NESTOR,...)	206

VI FUTURE UNDERGROUND 207

24	List of relevant experimental projects	208
25	Hyper-Kamiokande	209
26	MEMPHYS	210

27	MONOLITH	215
28	216
29	217
30	218

Part I

INTRODUCTION TO NEUTRINO OSCILLATIONS

1 Bruno Pontecorvo

Bruno M. Pontecorvo (*Pisa, August 22, 1913 – Dubna, September 24, 1993*) was a great physicist who had enormous impact on the development of neutrino physics. In particular he was the pioneer of neutrino oscillations. He came to this idea in 1957, soon after the two-component neutrino theory was proposed by Landau, Lee and Yang and Salam and confirmed by Goldhaber *et al.* It was very nontrivial to propose neutrino oscillations in 1957, at the time when only one type of neutrino was known. Oscillations which B. Pontecorvo considered were $\nu_L \rightleftharpoons \bar{\nu}_L$ i.e. oscillations between active and sterile neutrinos.^a

^aB. Pontecorvo proposed the existence of sterile neutrinos as well as the term “sterile neutrino” itself (1967) so popular nowadays.



Бруно Понтекорво

[From the JINR's official site about Bruno Pontecorvo,
URL: <<http://pontecorvo.jinr.ru/>>.]



Chlorine-Argon idea (Canada).



Swinging neutrinos.

Both cartoons were drawn by Mikhail Bilenky for the celebration of Bruno Pontecorvo's 75th Anniversary held at Dubna (August 1988).

[Borrowed from S. M. Bilenky, "Bruno Pontecorvo: Mister Neutrino," a report at the 3rd International Workshop "Neutrino Oscillations in Venice," Venice, February 7-10, 2006 (physics/0603039).]

2 Neutrino masses and mixing in the Standard Model

2.1 Interaction Lagrangians and currents

The Standard Model (SM) Lagrangians for charged and neutral current neutrino interactions are assumed to be

$$\mathcal{L}_I^{\text{CC}}(x) = -\frac{g}{2\sqrt{2}}j_\alpha^{\text{CC}}(x)W^\alpha(x) + \text{H.c.} \quad \text{and} \quad \mathcal{L}_I^{\text{NC}}(x) = -\frac{g}{2\cos\theta_W}j_\alpha^{\text{NC}}(x)Z^\alpha(x).$$

Here g is the SU(2) (electro-weak) gauge coupling constant

$$g^2 = 4\sqrt{2}M_W^2G_F, \quad g\sin\theta_W = |e|$$

and θ_W is the weak mixing (Weinberg) angle ($\sin^2\theta_W(M_Z) = 0.23120$).

The leptonic charged current and neutrino neutral current are given by the expressions:

$$j_\alpha^{\text{CC}}(x) = 2 \sum_{\ell=e,\mu,\tau,\dots} \bar{\nu}_{\ell,L}(x)\gamma_\alpha\ell_L(x) \quad \text{and} \quad j_\alpha^{\text{NC}}(x) = \sum_{\ell=e,\mu,\tau,\dots} \bar{\nu}_{\ell,L}(x)\gamma_\alpha\nu_{\ell,L}(x).$$

The currents may include (yet unknown) heavy neutrinos and corresponding charged leptons. The left- and right-handed fermion fields are defined as usually:

$$\nu_{\ell,L/R}(x) = \left(\frac{1 \pm \gamma_5}{2}\right)\nu_\ell(x) \quad \text{and} \quad \ell_{L/R}(x) = \left(\frac{1 \pm \gamma_5}{2}\right)\ell(x).$$

Note that the kinetic term of the Lagrangian includes both L and R handed neutrinos and moreover, it can include other sterile neutrinos:

$$\begin{aligned}\mathcal{L}_0 &= \frac{i}{2} [\bar{\nu}(x)\gamma^\alpha\partial_\alpha\nu(x) - \partial_\alpha\bar{\nu}(x)\gamma^\alpha\nu(x)] \equiv \frac{i}{2}\bar{\nu}(x)\overleftrightarrow{\partial}\nu(x) \\ &= \frac{i}{2} \left[\bar{\nu}_L(x)\overleftrightarrow{\partial}\nu_L(x) + \bar{\nu}_R(x)\overleftrightarrow{\partial}\nu_R(x) \right],\end{aligned}$$

$$\boldsymbol{\nu}(x) = \boldsymbol{\nu}_L(x) + \boldsymbol{\nu}_R(x) = \begin{pmatrix} \nu_e(x) \\ \nu_\mu(x) \\ \nu_\tau(x) \\ \vdots \\ \vdots \\ \vdots \end{pmatrix}, \quad \boldsymbol{\nu}_{L/R}(x) = \begin{pmatrix} \nu_{e,L/R}(x) \\ \nu_{\mu,L/R}(x) \\ \nu_{\tau,L/R}(x) \\ \vdots \\ \vdots \\ \vdots \end{pmatrix} = \frac{1 \pm \gamma_5}{2} \begin{pmatrix} \nu_e(x) \\ \nu_\mu(x) \\ \nu_\tau(x) \\ \vdots \\ \vdots \\ \vdots \end{pmatrix}.$$

Neutrino chirality:

$$\gamma_5\nu_L = -\nu_L, \quad \gamma_5\nu_R = +\nu_R,$$

There are two types of possible neutrino mass terms: Dirac and Majorana.

2.2 Dirac neutrinos

The Dirac mass term has the form

$$\mathcal{L}_D(x) = -\bar{\nu}_R(x)\mathbf{M}_D\nu_L(x) + \text{H.c.},$$

where \mathbf{M}_D is a $N \times N$ complex *nondiagonal* matrix. In general, $N \geq 3$ that is the column ν_L may include the heavy *active* neutrino fields as well as *sterile* neutrino fields which do not enter into the standard charged and neutral currents.

An arbitrary complex matrix can be diagonalized by means of an appropriate *biunitary* transformation. One has

$$\mathbf{M}_D = \tilde{\mathbf{V}}\mathbf{m}\mathbf{V}^\dagger, \quad \mathbf{m} = ||m_{kl}|| = ||m_k\delta_{kl}||,$$

where \mathbf{V} and $\tilde{\mathbf{V}}$ are unitary matrices and $m_k \geq 0$. Therefore

$$\mathcal{L}_D(x) = -\bar{\nu}'_R(x)\mathbf{m}\nu'_L(x) + \text{H.c.} = -\bar{\nu}'(x)\mathbf{m}\nu'(x) = -\sum_{k=1}^N m_k \bar{\nu}_k(x)\nu_k(x),$$

$$\nu'_L(x) = \mathbf{V}^\dagger\nu_L(x), \quad \nu'_R(x) = \tilde{\mathbf{V}}^\dagger\nu_R(x), \quad \nu'(x) = (\nu_1, \nu_2, \dots, \nu_N)^T.$$

It is easy to prove that the kinetic term in the neutrino Lagrangian is transformed to

$$\mathcal{L}_0 = \frac{i}{2} \bar{\nu}'(x) \overleftrightarrow{\partial} \nu'(x) = \frac{i}{2} \sum_k \bar{\nu}_k(x) \overleftrightarrow{\partial} \nu_k(x).$$

Hence, one can conclude that $\nu_k(x)$ is the field of a Dirac neutrino with the mass m_k and the flavor LH neutrino fields $\nu_{\ell,L}(x)$ present in the standard weak lepton currents are linear combinations of the LH components of the fields of neutrinos with definite masses:

$$\nu_L = \mathbf{V}\nu'_L \quad \text{or} \quad \nu_{\ell,L} = \sum_k V_{\ell k} \nu_{k,L}.$$

The matrix \mathbf{V} is sometimes referred to as the Pontecorvo-Maki-Nakagawa-Sakata (PMNS) neutrino (vacuum) mixing matrix.^a

It can be proved that the Lagrangian of the theory with the Dirac mass term is invariant with respect to the global gauge transformation

$$\nu_k(x) \rightarrow e^{i\Lambda} \nu_k(x), \quad \ell(x) \rightarrow e^{i\Lambda} \ell(x), \quad \Lambda = \text{const.}$$

This means that the lepton charge

$$L = \sum_{\ell=e,\mu,\tau,\dots} L_\ell$$

common to all charged leptons and all neutrinos ν_k is conserved. However **the individual lepton flavor numbers L_ℓ numbers (electron, muon, tauon,...) are no longer conserved.**

^aOf course it is not the same as the Cabibbo-Kobayashi-Maskawa (CKM) quark mixing matrix. It seems however that the PMNS and CKM matrices are, in a sense, *complementary* (see below).

2.2.1 Parametrization of mixing matrix for Dirac neutrinos

It is well known that a complex $n \times n$ unitary matrix depends on n^2 real parameters. The classical result by Murnaghan^a states that the matrices from the unitary group $U(n)$ are products of a diagonal phase matrix

$$\Gamma = \text{diag} (e^{i\alpha_1}, e^{i\alpha_2}, \dots, e^{i\alpha_n}),$$

containing n phases α_k , and $n(n - 1)/2$ matrices whose main building blocks have the form

$$\begin{pmatrix} \cos \theta & \sin \theta e^{-i\phi} \\ -\sin \theta e^{+i\phi} & \cos \theta \end{pmatrix} = \begin{pmatrix} 1 & 0 \\ 0 & e^{+i\phi} \end{pmatrix} \underbrace{\begin{pmatrix} \cos \theta & \sin \theta \\ -\sin \theta & \cos \theta \end{pmatrix}}_{\text{Euler rotation}} \begin{pmatrix} 1 & 0 \\ 0 & e^{-i\phi} \end{pmatrix}.$$

Therefore any $n \times n$ unitary matrix can be parametrized in terms of

$n(n - 1)/2$ “angles” (taking values within $[0, \pi/2]$)

and

$n(n + 1)/2$ “phases” (taking values within $[0, 2\pi)$).

The usual parametrization of both the (CKM) and (PMNS) matrices is of this type.

^aF. D. Murnaghan, “The unitary and rotation groups,” Washington, DC: Sparta Books (1962).

One can reduce the number of the phases further by taking into account that the Lagrangian with the Dirac mass term is invariant with respect to the transformation

$$\ell \mapsto e^{ia_\ell} \ell, \quad \nu_k \mapsto e^{ib_\ell} \nu_k, \quad V_{\ell k} \mapsto e^{i(b_k - a_\ell)} V_{\ell k},$$

and to the global gauge transformation

$$\ell \mapsto e^{i\Lambda} \ell, \quad \nu_k \mapsto e^{i\Lambda} \nu_k.$$

Therefore $2N - 1$ phases are unphysical and the number of physical (*Dirac*) phases is

$$n_D = \frac{N(N+1)}{2} - (2N-1) = \frac{N^2 - 3N + 2}{2} = \frac{(N-1)(N-2)}{2} \quad (N \geq 2);$$

$$n_D(2) = 0, \quad n_D(3) = 1, \quad n_D(4) = 3, \dots$$

The nonzero phases lead to the CP and T violation in the neutrino sector.

Three-neutrino case

In the most interesting (today!) case of three lepton generations one defines the orthogonal rotation matrices in the ij -planes which depend upon the mixing angles θ_{ij} :

$$\mathbf{O}_{12} = \underbrace{\begin{pmatrix} c_{12} & s_{12} & 0 \\ -s_{12} & c_{12} & 0 \\ 0 & 0 & 1 \end{pmatrix}}_{\text{Solar matrix}}, \quad \mathbf{O}_{13} = \underbrace{\begin{pmatrix} c_{13} & 0 & s_{13} \\ 0 & 1 & 0 \\ -s_{13} & 0 & c_{13} \end{pmatrix}}_{\text{Bona vacantia (as yet)}}, \quad \mathbf{O}_{23} = \underbrace{\begin{pmatrix} 1 & 0 & 0 \\ 0 & c_{23} & s_{23} \\ 0 & -s_{23} & c_{23} \end{pmatrix}}_{\text{Atmospheric matrix}},$$

(where $c_{ij} \equiv \cos \theta_{ij}$, $s_{ij} \equiv \sin \theta_{ij}$) and the diagonal matrix with the Dirac phase factor:

$$\Gamma_D = \text{diag}(1, 1, e^{i\delta}).$$

The parameter δ is commonly referred to as the Dirac CP-violation phase.

Finally, by taking into account the Murnaghan theorem, the PMNS mixing matrix for the Dirac neutrinos can be parametrized as^a

$$\begin{aligned} \mathbf{V}_{(D)} &= \mathbf{O}_{23} \Gamma_D \mathbf{O}_{13} \Gamma_D^\dagger \mathbf{O}_{12} \\ &= \begin{pmatrix} c_{12}c_{13} & s_{12}c_{13} & s_{13}e^{-i\delta} \\ -s_{12}c_{23} - c_{12}s_{23}s_{13}e^{i\delta} & c_{12}c_{23} - s_{12}s_{23}s_{13}e^{i\delta} & s_{23}c_{13} \\ s_{12}s_{23} - c_{12}c_{23}s_{13}e^{i\delta} & -c_{12}s_{23} - s_{12}c_{23}s_{13}e^{i\delta} & c_{23}c_{13} \end{pmatrix}. \end{aligned}$$

^aThis is the *Chau–Keung presentation* advocated by the PDG for both CKM and PMNS matrices.

Since the Dirac mass term violates conservation of the individual lepton numbers L_e, L_μ and L_τ , it allows many lepton family number violating processes, like

$$\begin{aligned} \mu^\pm &\rightarrow e^\pm + \gamma, \quad \mu^\pm \rightarrow e^\pm + e^+ + e^-, \\ K^+ &\rightarrow \pi^+ + \mu^\pm + e^\mp, \quad K^- \rightarrow \pi^- + \mu^\pm + e^\mp, \\ \mu^- + (A, Z) &\rightarrow e^- + (A, Z), \quad \tau^- + (A, Z) \rightarrow \mu^- + (A, Z), \dots \end{aligned}$$

Table 1: Current limits on the simplest lepton family number violating μ and τ decays. [From S. Eidelman *et al.* (Particle Data Group), "Review of particle physics," *Phys. Lett. B* **592** (2004) 1–1109.].

Decay Modes	Fraction	C.L.	Decay Modes	Fraction	C.L.
$\mu^- \rightarrow \nu_e \bar{\nu}_\mu$	$< 1.2\%$	90%	$\tau^- \rightarrow e^- \gamma$	$< 2.7 \times 10^{-6}$	90%
$\mu^- \rightarrow e^- \gamma$	$< 1.2 \times 10^{-11}$	90%	$\tau^- \rightarrow \mu^- \gamma$	$< 1.1 \times 10^{-6}$	90%
$\mu^- \rightarrow e^- e^+ e^-$	$< 1.0 \times 10^{-12}$	90%	$\tau^- \rightarrow e^- \pi^0$	$< 3.7 \times 10^{-6}$	90%
$\mu^- \rightarrow 2\gamma$	$< 7.2 \times 10^{-11}$	90%	$\tau^- \rightarrow \mu^- \pi^0$	$< 4.0 \times 10^{-6}$	90%

However the neutrinoless double beta decay^a $(A, Z) \rightarrow (A, Z + 2) + 2e^-$ and the processes like $K^+ \rightarrow \pi^- + \mu^+ + e^+$, $K^- \rightarrow \pi^+ + \mu^- + e^-$, etc. are forbidden as a consequence of the total lepton charge conservation.

^aHereafter abbreviated as $(\beta\beta)_{0\nu}$.

2.2.2 Neutrinoless muon decay

The L_μ and L_e muon decay $\mu^- \rightarrow e^- \gamma$ is allowed if $V_{\mu k}^* V_{ek} \neq 0$ for $k = 1, 2$ or 3 . The corresponding Feynman diagrams include W loops and thus the decay width is strongly suppressed by the neutrino to W boson mass ratios:

$$R = \frac{\Gamma(\mu^- \rightarrow e^- \gamma)}{\Gamma(\mu^- \rightarrow e^- \nu_\mu \bar{\nu}_e)} = \frac{3\alpha}{32\pi} \left| \sum_k V_{\mu k}^* V_{ek} \frac{m_k}{m_W} \right|^2.$$

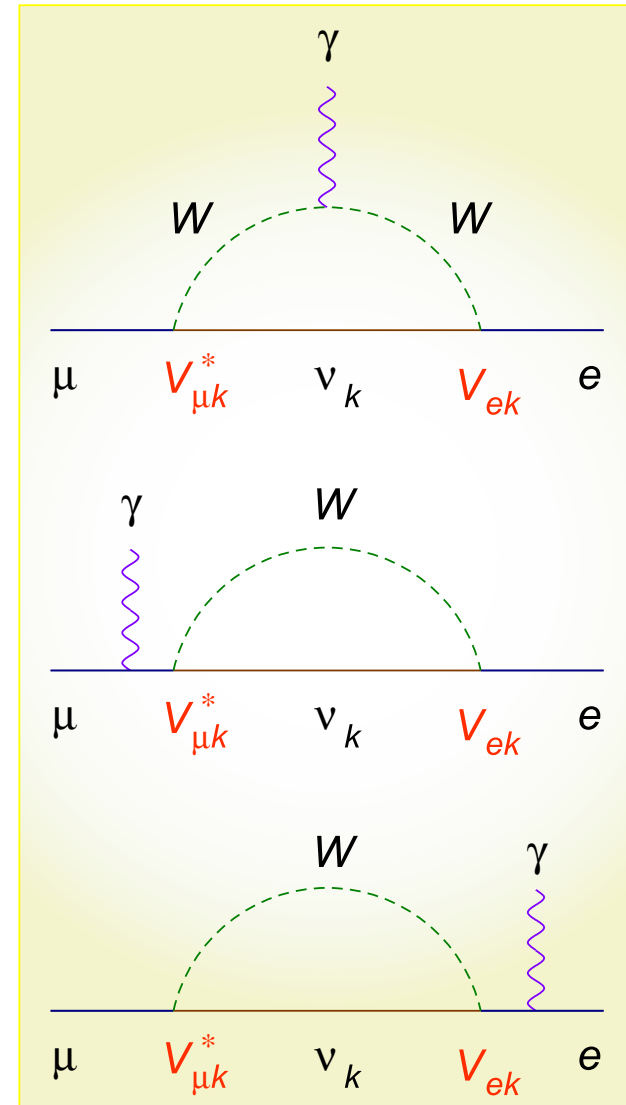
Since $m_k/m_W = 1.24 \times 10^{-11}$ ($m_k/1$ eV), the ratio can be estimated as

$$R \approx 3.37 \times 10^{-26} \left| \sum_k V_{\mu k}^* V_{ek} \left(\frac{m_k}{1 \text{ eV}} \right) \right|^2,$$

while the current experimental upper limit is (at least!) 15 orders of magnitude larger:

$$R_{(\text{exp})} < 1.2 \times 10^{-11} \text{ at } 90\% \text{ C.L.}$$

(see Table 1) \implies **NO GO...**



2.2.3 Nuclear beta decay

The method of measurement of the (anti)neutrino mass through the investigation of the high-energy part of the β -spectrum was proposed by Perrin (1933) and Fermi (1934).

The first experiments on the measurement of the neutrino mass with this method have been done by Curran, Angus and Cockcroft (1948) and Hanna and Pontecorvo (1949).

The energy spectrum of electrons in the decay $(A, Z) \rightarrow (A, Z + 1) + e^- + \bar{\nu}_e$ is^a

$$\frac{d\Gamma}{dT} = \sum_k |V_{ek}|^2 \frac{d\Gamma_k}{dT}, \quad (1)$$

$$\frac{d\Gamma_k}{dT} = \frac{(G_F \cos \theta_C)^2}{2\pi^3} p p_k (T + m_e) (Q - T) |\mathcal{M}|^2 F(T) \theta(Q - T - m_k). \quad (2)$$

Here G_F is the Fermi constant, θ_C is the Cabibbo angle, m_e , p and T are the mass, magnitude of the momentum and kinetic energy of the electron, respectively,

$$p_k = \sqrt{E_k^2 - m_k^2} = \sqrt{(Q - T)^2 - m_k^2}$$

is the magnitude of the neutrino momentum, Q is the energy released in the decay (the endpoint of the β spectrum in case of zero neutrino mass), \mathcal{M} is the nuclear matrix element, and $F(T)$ is the Fermi function, which describes the Coulomb interaction of the final particles. The step function in Eq. (2) ensures that a neutrino

^aThe recoil of the final nucleus and radiative corrections (luckily small) are neglected.

state ν_k is only produced if its total energy is larger than its mass: $E_k = Q - T \geq m_k$. As it is seen from Eq. (1), the largest distortion of the β -spectrum due to neutrino masses can be observed in the region

$$Q - T \sim m_k. \quad (3)$$

However, for $\max(m_k) \simeq 1 \text{ eV}$ only a very small part (about 10^{-13}) of the decays give contribution to the region (3). This is the reason why in the analysis of the results of the measurement of the β -spectrum a relatively large part of the spectrum is used.^b Taking this into account and applying unitarity of the mixing matrix, we can write

$$\begin{aligned} \sum_k |V_{ek}|^2 p_k &\approx \sum_k |V_{ek}|^2 (Q - T) \left[1 - \frac{m_k^2}{2(Q - T)^2} \right] \\ &= (Q - T) \left[1 - \frac{1}{2(Q - T)^2} \sum_k |V_{ek}|^2 m_k^2 \right] \approx \sqrt{(Q - T)^2 - m_\beta^2}, \end{aligned}$$

where the effective neutrino mass m_β is defined by

$$m_\beta^2 = \sum_k |V_{ek}|^2 m_k^2$$

and it was assumed that $\max(m_k^2) \ll 4(Q - T)^2$.

^bFor example, in the Mainz tritium experiment (see below) the last 70 eV of the spectrum is used.

Finally, the β -spectrum that is used for fitting the data can be presented as

$$\frac{d\Gamma}{dT} \propto p(T + m_e) |\mathcal{M}|^2 F(T) K^2(T),$$

where

$$K(T) \propto \sqrt{\frac{d\Gamma/dT}{p(T + m_e) |\mathcal{M}|^2 F(T)}} \\ \approx (Q - T) \left[1 - \frac{m_\beta^2}{(Q - T)^2} \right]^{1/4}$$

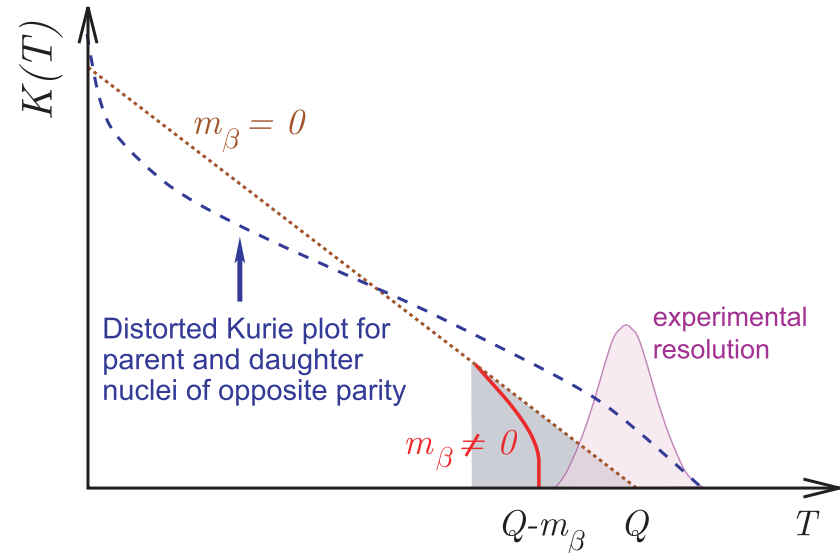
is the so-called *Kurie plot*.

Unfortunately, the real situation is much more complicated.

In an actual experiment, the measurable quantity is a sum of β spectra, leading each with probability $P_n = P_n(E_0 - V_n - E)$ to a final state n of excitation energy V_n :

$$\frac{d\Gamma(T, Q)}{dT} \mapsto \sum_n P_n (E_0 - V_n - E) \frac{d\Gamma(T, E_0 - V_n)}{dT}.$$

Here $E_0 = Q - \mathcal{E}$ and \mathcal{E} is the recoil energy of the daughter nucleus.



Kurie plot for allowed processes is a sensitive test of the effective neutrino mass m_β while the first order forbidden processes should have a distorted Kurie plot.

Example: Tritium beta decay. ^a

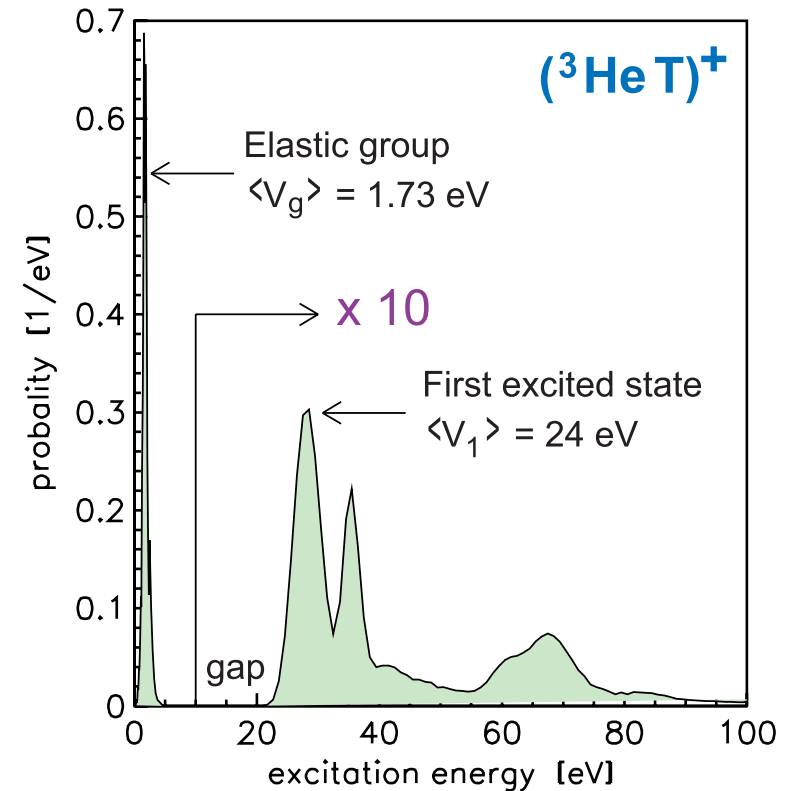
An important issue is the decay of molecular tritium $T_2 \rightarrow ({}^3\text{HeT})^+ + e^- + \bar{\nu}_e$. Considering the most precise direct determination of the mass difference

$$m(T) - m({}^3\text{He}) = (18590.1 \pm 1.7) \text{ eV}/c^2$$

and taking into account the recoil and apparatus effects (these are taken for the Mainz experiment) one derives an endpoint energy of the molecular ion $({}^3\text{HeT})^+$ ground state:

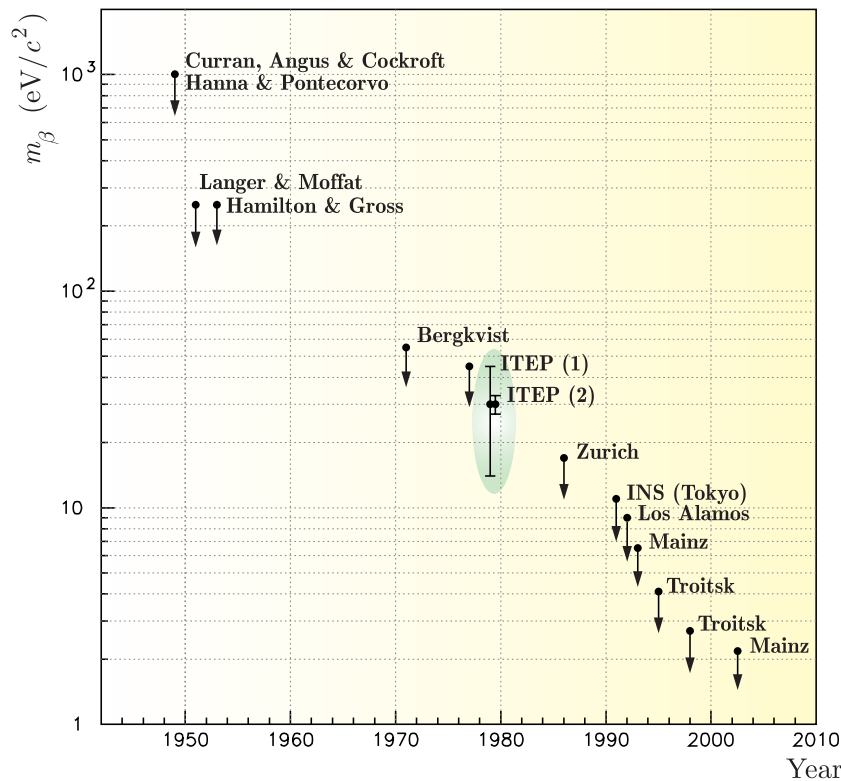
$$E_0 = (18574.3 \pm 1.7) \text{ eV}.$$

The excitation spectrum is shown in the figure. The first group concerns rotational and vibrational excitation of the molecule in its electronic ground state; it comprises a fraction of $P_g = 57.4\%$ of the total rate.



Excitation spectrum of the daughter molecular ion $({}^3\text{HeT})^+$ in β decay of molecular tritium.

^aFor more details, see C. Kraus *et al.*, "Final results from phase II of the Mainz neutrino mass search in tritium β decay," *Eur. Phys. J. C* **40** (2005) 447–468 (hep-ex/0412056).



Progress of the neutrino mass measurements in tritium β decay, including the final Mainz phase II upper limit (see below).

[The compilation is taken from V. M. Lobashev, "Direct search for mass of neutrino," in Proceedings of the 18th International Conference on Physics in Collision ("PIC 98"), Frascati, June 17–19, 1998, pp. 179–194.]

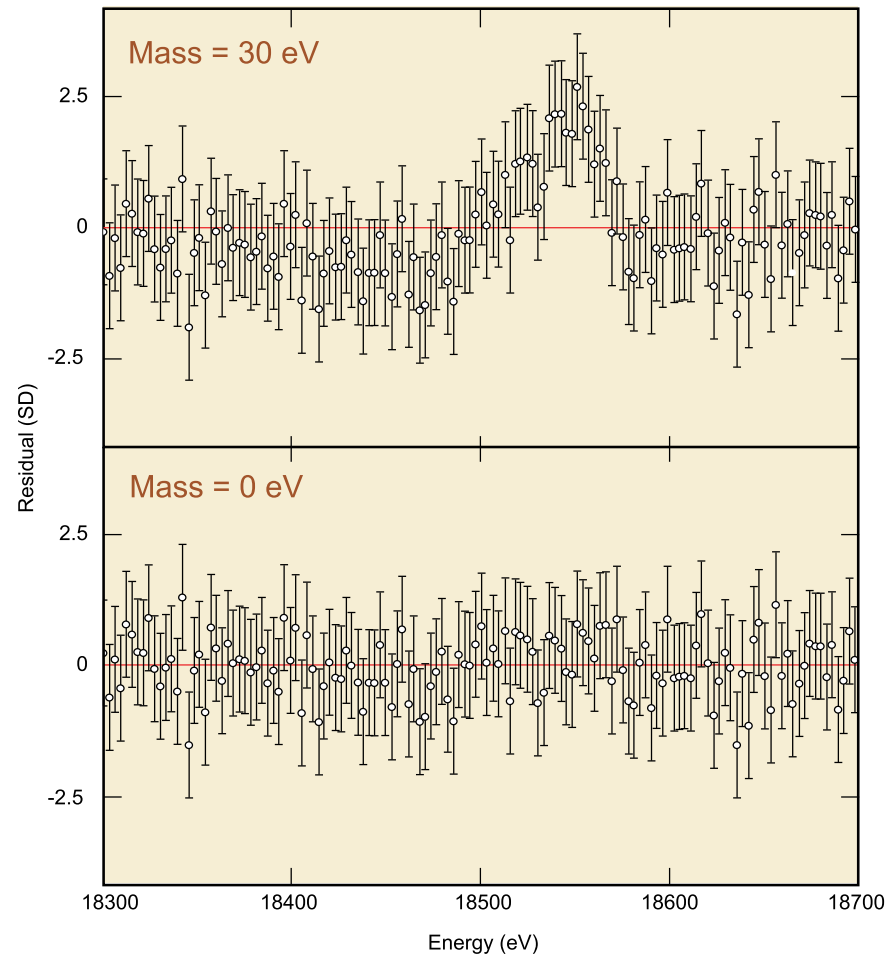
The history of the search for the neutrino mass in the tritium β decay counts almost 55 years (see figure). In 1980, the steady improvement of the upper limit was suddenly speeded up by a report of the ITEP group (Moscow) on the observation of the nonzero neutrino mass effect in the β -spectrum in the valine molecule ($C_5H_{11}NO_2$). The reported result was^a

$$14 \leq m_\beta \leq 46 \text{ eV}/c^2 \quad (99\% \text{ C.L.})$$

This research stimulated more than 20 experimental proposals with an intention to check this claim. Alas!... in several years the experimental groups from Zurich, Tokyo, Los Alamos, and then Livermore refuted the ITEP result.

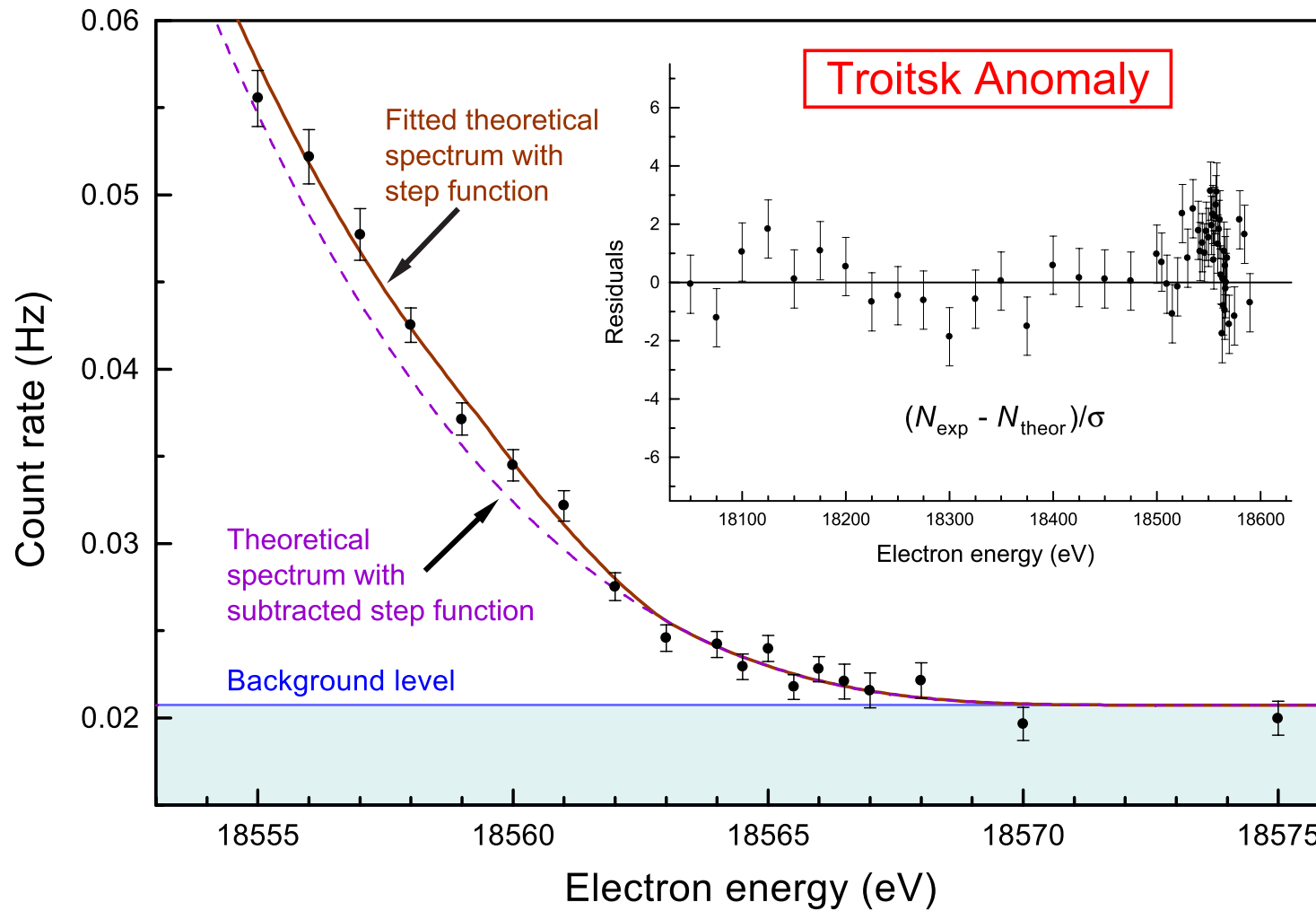
^aV. A. Lyubimov *et al.*, "An estimate of the ν_e mass from the β -spectrum of tritium in the valine molecule," Phys. Lett. B **94** (1980) 266–268 (327 citations in SPIRES!)

The top figure shows the data points from the tail of the β -spectrum measured in the Los Alamos tritium experiment compared with the expected values (the straight line) for $m_\beta = 30$ eV. The data wander from the line, ruling out the possibility of a 30-eV neutrino. The bottom figure shows the same data points compared with the expectation for $m_\beta = 0$. While the data clearly favor a neutrino mass of zero, the best fit is actually for a **slightly negative** m_β . (Note that in the bottom plot, the data points lie, on average, slightly above the line, so this is not a perfect fit.) Both plots display “residuals,” which indicate how many standard deviations each data point is from a particular hypothesis.



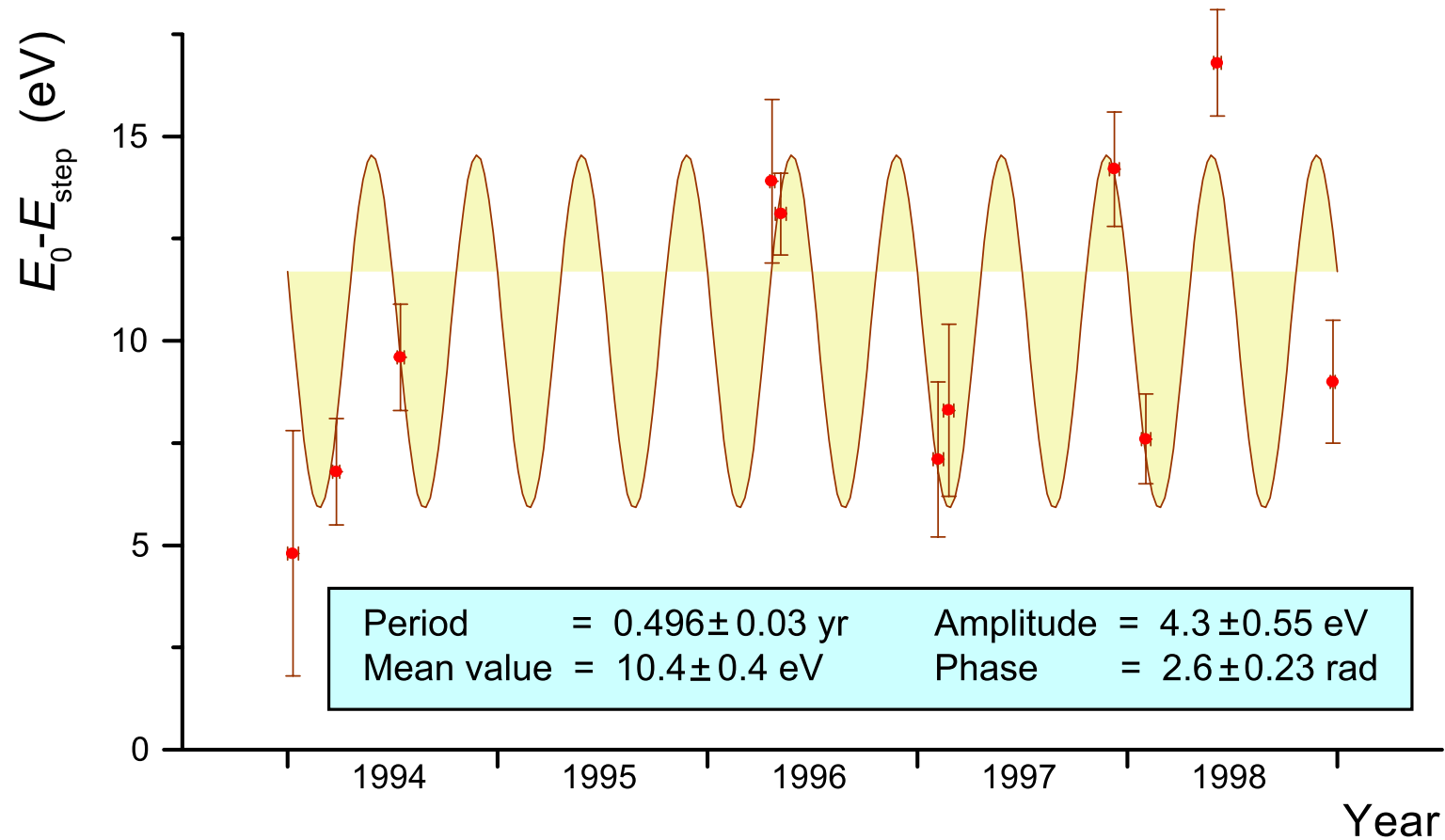
Did the neutrino weigh 30 electron volts?

[Borrowed from T. J. Bowles and R. G. H. Robertson (as told to D. Kestenbaum), “Tritium beta decay and the search for neutrino mass,” *Los Alamos Science*, Nu. 25 (1997) 6-11.]



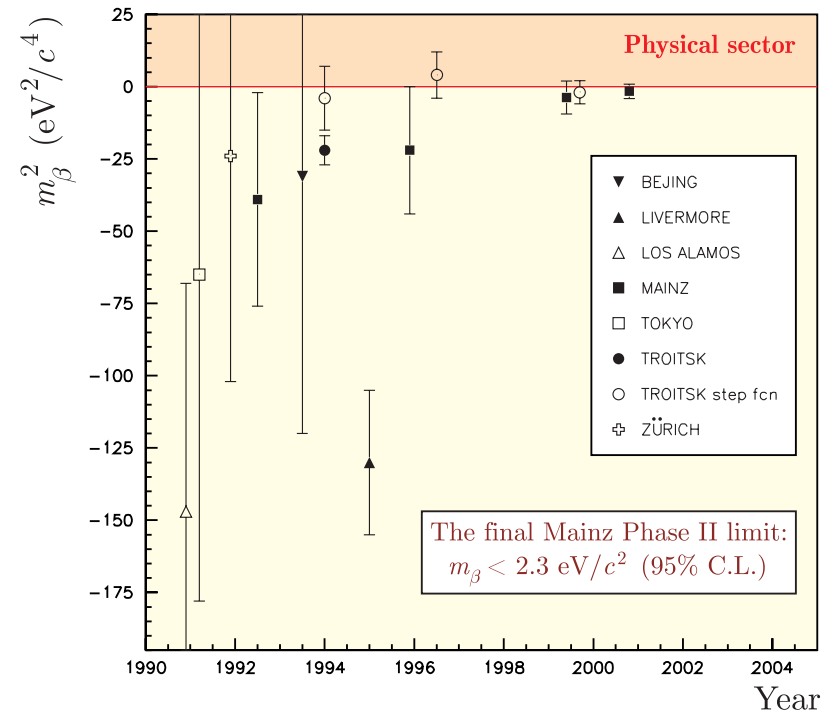
Part of experimental β -spectrum in the Troitsk ν -mass experiment near the end-point.
[V. M. Lobashev *et al.*, "Direct search for mass of neutrino and anomaly in the tritium beta-spectrum," *Phys. Lett. B* **460** (1999) 227–235.]

The Troitsk group reported on a step like anomaly which appeared in their integral spectra with an amplitude of about 6×10^{-11} of the total decay rate and at variable positions in the range from 5 to 15 eV below the endpoint.



The change in time of the positions of these steps seemed to be compatible with a half year period. The phenomenology and origin of the Troitsk anomaly are barely known.

Published results of the squared neutrino mass values m_β^2 obtained from tritium decay since 1990 are shown in figure. The already finished experiments at Los Alamos, Zürich, Tokyo, Beijing and Livermore used magnetic spectrometers, the experiments at Troitsk and Mainz are using electrostatic filters with magnetic adiabatic collimation. The progress in the observable m_β of the final Mainz result as compared to the most sensitive earlier experiments using momentum analysing spectrometers approaches **2 orders of magnitude**.



The Mainz experiment does not confirm the Troitsk anomaly being however compatible with the main Troitsk result $m_\beta^2 = (-2.3 \pm 2.5_{\text{stat}} \pm 2.0_{\text{syst}}) \text{ eV}^2/c^4$.

[From C. Kraus *et al.*, “Final results from phase II of the Mainz neutrino mass search in tritium β decay,” *Eur. Phys. J. C* **40** (2005) 447–468 (hep-ex/0412056).]

The negative m_β^2 sector is not necessarily unphysical and might also be fitted by a model with **tachyonic neutrinos**. But this point would come up only in case of an unambiguous experimental negative m_β^2 result.

2.3 Majorana neutrinos

The charge conjugated bispinor field ψ^c is defined by the transformation

$$\psi \longmapsto \psi^c = C\bar{\psi}^T, \quad \bar{\psi} \longmapsto \bar{\psi}^c = -\psi^T C,$$

where C is the charge-conjugation matrix which satisfies the conditions

$$C\gamma_\alpha^T C^\dagger = -\gamma_\alpha, \quad C\gamma_5^T C^\dagger = \gamma_5, \quad C^\dagger = C^{-1} = C, \quad C^T = -C,$$

and thus coincides (up to a phase factor) with the inversion of the axes x^0 and x^2 :

$$C = \gamma_0\gamma_2 = \begin{pmatrix} 0 & \sigma_2 \\ \sigma_2 & 0 \end{pmatrix}$$

Reminder:

The Pauli matrices:

$$\sigma_0 \equiv 1 = \begin{pmatrix} 1 & 0 \\ 0 & 1 \end{pmatrix}, \quad \sigma_1 = \begin{pmatrix} 0 & 1 \\ 1 & 0 \end{pmatrix}, \quad \sigma_2 = \begin{pmatrix} 0 & -i \\ i & 0 \end{pmatrix}, \quad \sigma_3 = \begin{pmatrix} 1 & 0 \\ 0 & -1 \end{pmatrix}.$$

The Dirac matrices:

$$\gamma^0 = \gamma_0 = \begin{pmatrix} \sigma_0 & 0 \\ 0 & -\sigma_0 \end{pmatrix}, \quad \gamma^k = -\gamma_k = \begin{pmatrix} 0 & \sigma_k \\ -\sigma_k & 0 \end{pmatrix}, \quad k = 1, 2, 3, \quad \gamma^5 = \gamma_5 = -\begin{pmatrix} 0 & \sigma_0 \\ \sigma_0 & 0 \end{pmatrix}.$$

Clearly a charged fermion field $\psi(x)$ is different from the charge conjugated field $\psi^c(x)$.

But for a *neutral* fermion field $\nu(x)$ the equality $\nu^c(x) = \nu(x)$ is not forbidden.

This is the *Majorana condition*^a (**Majorana neutrino and antineutrino coincide**).

In the chiral representation

$$\nu = \begin{pmatrix} \phi \\ \chi \end{pmatrix}, \quad \nu^c = C\bar{\nu}^T = \begin{pmatrix} -\sigma_2\chi^* \\ +\sigma_2\phi^* \end{pmatrix}.$$

According to the Majorana condition

$$\phi = -\sigma_2\chi^* \quad \text{and} \quad \chi = \sigma_2\phi^* \quad \implies \quad \phi + \chi = \sigma_2(\phi - \chi)^*.$$

(The Majorana neutrino is two-component, i.e. needs only one chiral projection). Then

$$\nu_L = \left(\frac{1 + \gamma_5}{2} \right) \nu = \begin{pmatrix} \phi - \chi \\ \chi - \phi \end{pmatrix} \quad \text{and} \quad \nu_R = \left(\frac{1 - \gamma_5}{2} \right) \nu = \begin{pmatrix} \phi + \chi \\ \phi + \chi \end{pmatrix} = \nu_L^c.$$

Therefore

$$\nu = \nu_L + \nu_R = \nu_L + \nu_L^c.$$

Now we can construct the Majorana mass term in the general N -neutrino case. It is

$$\mathcal{L}_M(x) = -\frac{1}{2}\bar{\nu}_L^c(x)\mathbf{M}_M\nu_L(x) + \text{H.c.},$$

^aMore generally, $\nu^c(x) = e^{i\phi}\nu(x)$ ($\phi = \text{const}$).

where \mathbf{M}_M is a $N \times N$ complex *nondiagonal* matrix and, in general, $N \geq 3$.

It can be proved that the \mathbf{M}_M should be symmetric,

$$\mathbf{M}_M^T = \mathbf{M}_M.$$

If one assume for a simplification that its spectrum is nondegenerate, the mass matrix can be diagonalized by means of the following transformation

$$\mathbf{M}_M = \mathbf{V}^* \mathbf{m} \mathbf{V}^\dagger, \quad \mathbf{m} = ||m_{kl}|| = ||m_k \delta_{kl}||,$$

where \mathbf{V} is a unitary matrix and $m_k \geq 0$. Therefore

$$\mathcal{L}_M(x) = -\frac{1}{2} [(\bar{\nu}'_L)^c \mathbf{m} \nu'_L + \bar{\nu}'_L \mathbf{m} (\nu'_L)^c] = -\frac{1}{2} \bar{\nu}' \mathbf{m} \nu' = -\frac{1}{2} \sum_{k=1}^N m_k \bar{\nu}_k \nu_k,$$

$$\nu'_L = \mathbf{V}^\dagger \nu_L, \quad (\nu'_L)^c = C \left(\overline{\nu'_L} \right)^T, \quad \nu' = \nu'_L + (\nu'_L)^c.$$

The last equality means that the fields $\nu_k(x)$ are Majorana neutrino fields.

Considering that the kinetic term in the neutrino Lagrangian is transformed to

$$\mathcal{L}_0 = \frac{i}{4} \bar{\nu}'(x) \overleftrightarrow{\partial} \nu'(x) = \frac{i}{4} \sum_k \bar{\nu}_k(x) \overleftrightarrow{\partial} \nu_k(x),$$

one can conclude that $\nu_k(x)$ is the field with the definite mass m_k .

The flavor LH neutrino fields $\nu_{\ell,L}(x)$ present in the standard weak lepton currents are linear combinations of the LH components of the fields of neutrinos with definite masses:

$$\nu_L = \mathbf{V}\nu'_L \quad \text{or} \quad \nu_{\ell,L} = \sum_k V_{\ell k} \nu_{k,L}.$$

Of course **neutrino mixing matrix** \mathbf{V} is not the same as in the case of Dirac neutrinos. There is no global gauge transformations under which the Majorana mass term (in its most general form) could be invariant. This implies that there are no conserved lepton charges that could allow us to distinguish Majorana ν s and $\bar{\nu}$ s. In other words,

the Majorana neutrinos are truly neutral fermions.

2.3.1 Parametrization of mixing matrix for Majorana neutrinos

Since the Majorana neutrinos are not rephasable, there may be a lot of extra phase factors in the mixing matrix. The Lagrangian with the Majorana mass term is invariant with respect to the transformation

$$\ell \mapsto e^{ia_\ell} \ell, \quad V_{\ell k} \mapsto e^{-ia_\ell} V_{\ell k}$$

Therefore N phases are unphysical and the number of the physical phases now is

$$\frac{N(N+1)}{2} - N = \frac{N(N-1)}{2} = \underbrace{\frac{(N-1)(N-2)}{2}}_{\text{Dirac phases}} + \underbrace{(N-1)}_{\text{Majorana phases}} = n_D + n_M;$$

$$n_M(2) = 1, \quad n_M(3) = 2, \quad n_M(4) = 3, \dots$$

In the case of three lepton generations one defines the diagonal matrix with the extra phase factors: $\mathbf{\Gamma}_M = \text{diag}(e^{i\alpha_1/2}, e^{i\alpha_2/2}, 1)$, where $\alpha_{1,2}$ are commonly referred to as the Majorana CP-violation phases. Then the PMNS matrix can be parametrized as

$$\mathbf{V}_{(M)} = \mathbf{O}_{23}\mathbf{\Gamma}_D\mathbf{O}_{13}\mathbf{\Gamma}_D^\dagger\mathbf{O}_{12}\mathbf{\Gamma}_M = \mathbf{V}_{(D)}\mathbf{\Gamma}_M$$

$$= \begin{pmatrix} c_{12}c_{13} & s_{12}c_{13} & s_{13}e^{-i\delta} \\ -s_{12}c_{23} - c_{12}s_{23}s_{13}e^{i\delta} & c_{12}c_{23} - s_{12}s_{23}s_{13}e^{i\delta} & s_{23}c_{13} \\ s_{12}s_{23} - c_{12}c_{23}s_{13}e^{i\delta} & -c_{12}s_{23} - s_{12}c_{23}s_{13}e^{i\delta} & c_{23}c_{13} \end{pmatrix} \begin{pmatrix} e^{i\alpha_1/2} & 0 & 0 \\ 0 & e^{i\alpha_2/2} & 0 \\ 0 & 0 & 1 \end{pmatrix},$$

Neither L_ℓ nor $L = \sum_\ell L_\ell$ is conserved allowing a lot of new processes, for example, $\tau^- \rightarrow e^+(\mu^+)\pi^-\pi^-$, $\tau^- \rightarrow e^+(\mu^+)\pi^-K^-$, $\pi^- \rightarrow \mu^+\bar{\nu}_e$, $K^+ \rightarrow \pi^-\mu^+e^+$, $K^+ \rightarrow \pi^0e^+\bar{\nu}_e$, $D^+ \rightarrow K^-\mu^+\mu^+$, $B^+ \rightarrow K^-e^+\mu^+$, $\Xi^- \rightarrow p\mu^-\mu^-$, $\Lambda_c^+ \rightarrow \Sigma^-\mu^+\mu^+$, etc.

No one was discovered yet but (may be!?) the $(\beta\beta)_{0\nu}$ decay. Thus we have to discuss this issue with some details.

2.3.2 Neutrinoless double beta decay

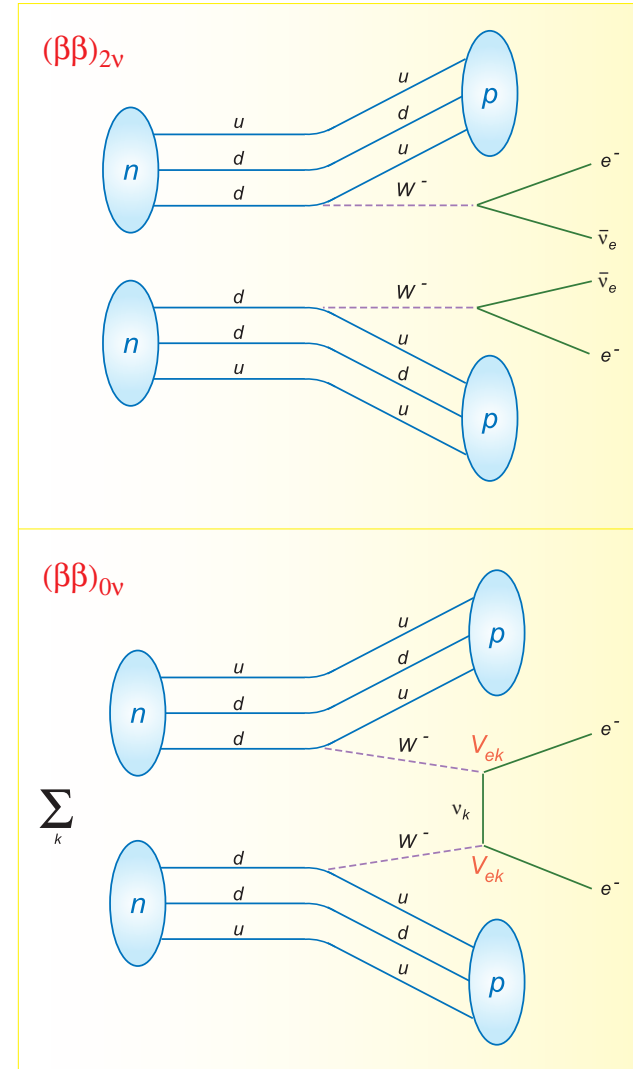
The theory with Majorana neutrinos allows the decay $(A, Z) \rightarrow (A, Z + 2) + 2e^-$ with $\Delta L = 2$. The decay rate for this process is expressed as follows:

$$\left[T_{1/2}^{0\nu} \right]^{-1} = G_Z^{0\nu} |m_{\beta\beta}|^2 \left| \mathcal{M}_F^{0\nu} - (g_A/g_V)^2 \mathcal{M}_{GT}^{0\nu} \right|^2,$$

where $G_Z^{0\nu}$ is the two-body phase-space factor including coupling constant, $\mathcal{M}_{F/GT}^{0\nu}$ are the Fermi/Gamow-Teller nuclear matrix elements. The constants g_V and g_A are the vector and axial-vector relative weak coupling constants, respectively. The complex parameter $m_{\beta\beta}$ is the *effective Majorana electron neutrino mass* given by

$$\begin{aligned} m_{\beta\beta} &= \sum_k V_{ek}^2 m_k \\ &= |V_{e1}|^2 m_1 + |V_{e2}|^2 m_2 e^{i\phi_2} + |V_{e3}|^2 m_3 e^{i\phi_3}, \end{aligned}$$

Here $\phi_2 = \alpha_2 - \alpha_1$ (pure Majorana phase) and $\phi_3 = -(\alpha_2 + 2\delta)$ (mixture of Dirac and Majorana CP-violation phases).

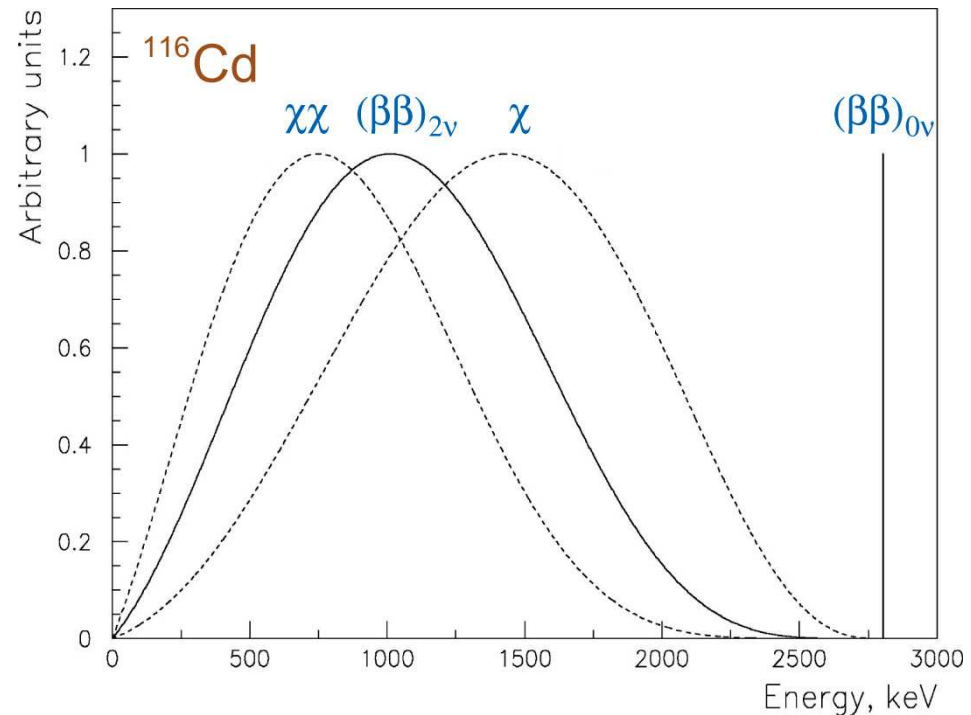


The electron sum energy spectrum of the $(\beta\beta)_{2\nu}$ mode as well as of the exotic modes with one or two majorons in final state,

$$(A, Z) \rightarrow (A, Z + 2) + 2e^{-} + \chi,$$

$$(A, Z) \rightarrow (A, Z + 2) + 2e^{-} + 2\chi,$$

is *continuous* because the available energy release ($Q_{\beta\beta}$) is shared between the electrons and other final state particles. In contrast, the two electrons from the $(\beta\beta)_{0\nu}$ decay carry the full available energy, and hence the electron sum energy spectrum has a sharp peak at the $Q_{\beta\beta}$ value. This feature allows one to distinguish the $(\beta\beta)_{0\nu}$ decay signal from the background.



The electron sum energy spectra calculated for the different β decay modes of cadmium-116.

[From Y. Zdesenko, "Colloquium: The future of double beta decay research," *Rev. Mod. Phys.* **74** (2003) 663–684.]

Majoron is a Nambu-Goldstone boson, – a hypothetical neutral pseudoscalar zero-mass particle which couples to Majorana neutrinos and may be emitted in the neutrinoless β decay. It is a consequence of the spontaneous breaking of the global $B - L$ symmetry.

Table 2: Summary of the most recent $\beta\beta_{2\nu}$ experiments and calculations.

[From E. Fiorini, "Experimental prospects of neutrinoless double beta decay," Phys. Scripta T121 (2005) 86–93].

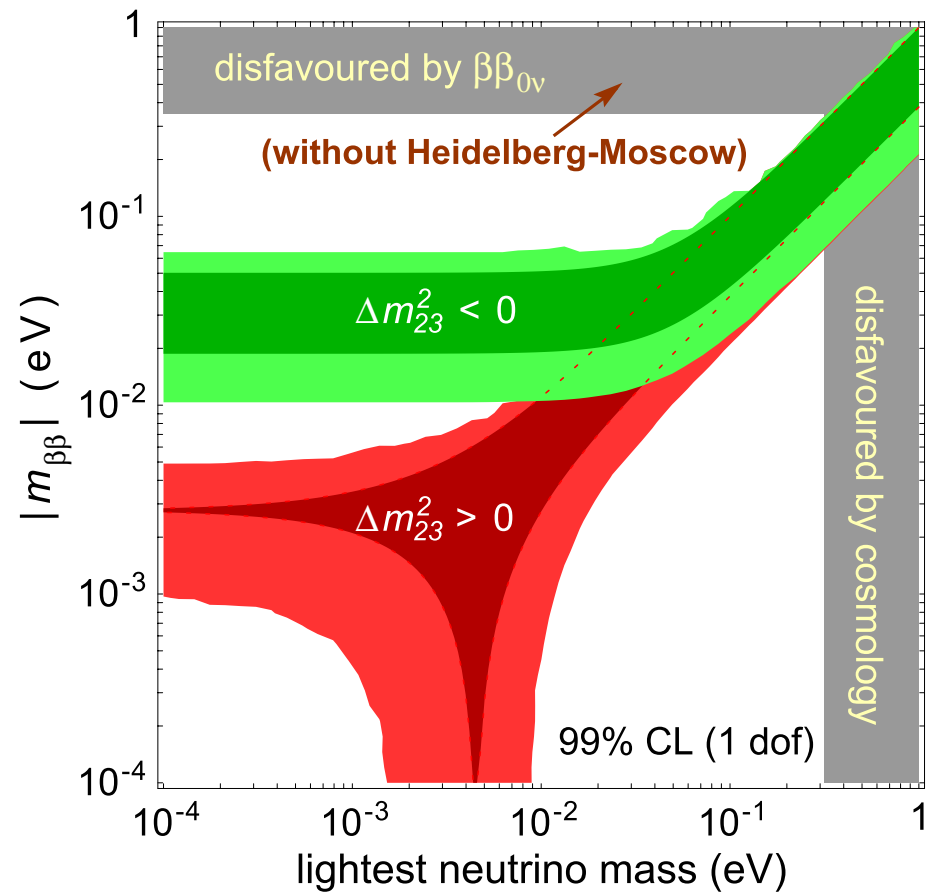
Element	Isotope	$T_{1/2}^{2\nu}$ (years)	
		Measured	Calculated
Calcium	${}^{48}_{20}\text{Ca}$	$4.2^{+2.1}_{-1.0} \times 10^{19}$	$6 \times 10^{18} - 5 \times 10^{20}$
Germanium	${}^{76}_{32}\text{Ge}$	$1.42^{+0.09}_{-0.07} \times 10^{21}$	$7 \times 10^{19} - 6 \times 10^{22}$
Selenium	${}^{82}_{34}\text{Se}$	$(0.9 \pm 0.1) \times 10^{20}$	$3 \times 10^{18} - 6 \times 10^{21}$
Zirconium	${}^{96}_{40}\text{Zr}$	$2.1^{+0.8}_{-0.4} \times 10^{19}$	$3 \times 10^{17} - 6 \times 10^{20}$
Molybdenum	${}^{100}_{42}\text{Mo}$	$(8.0 \pm 0.7) \times 10^{18}$	$1 \times 10^{17} - 2 \times 10^{22}$
Molybdenum	${}^{100}_{42}\text{Mo} (0^{+*})$	$(6.8 \pm 1.2) \times 10^{20}$	$5 \times 10^{19} - 2 \times 10^{21}$
Cadmium	${}^{116}_{48}\text{Cd}$	$3.3^{+0.4}_{-0.3} \times 10^{19}$	$3 \times 10^{18} - 2 \times 10^{21}$
Tellurium	${}^{128}_{52}\text{Te}$	$(2.5 \pm 0.4) \times 10^{24}$	$9 \times 10^{22} - 3 \times 10^{25}$
Tellurium	${}^{130}_{52}\text{Te}$	$(9.0 \pm 1.5) \times 10^{20}$	$2 \times 10^{19} - 7 \times 10^{20}$
Neodymium	${}^{150}_{60}\text{Nd}$	$(7.0 \pm 1.7) \times 10^{18}$	$6 \times 10^{16} - 4 \times 10^{20}$
Uranium	${}^{238}_{92}\text{U}$	$(2.0 \pm 0.6) \times 10^{21}$	$1.2 \times 10^{19} - ? \times 10^{21}$

The standard $(\beta\beta)_{2\nu}$ is observed for 10 isotopes with $T_{1/2}^{2\nu} \sim 10^{19-25}$ years (see table).

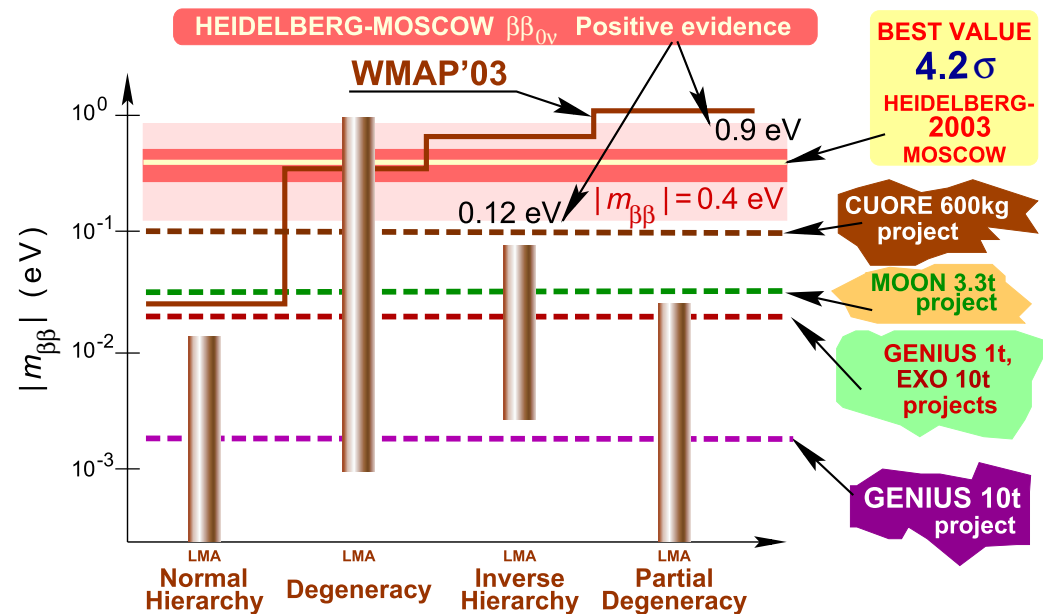
The figure summarizes the present knowledge of the absolute Majorana mass scale. Shown are the 99% CL regions allowed by the neutrino oscillation data in the plane of $m_{\beta\beta}$ and m_L – the mass of lightest neutrino. The two bands marked with $\Delta m_{23}^2 > 0$ and $\Delta m_{23}^2 < 0$ correspond to the *normal mass hierarchy* (i.e. $m_1 \ll m_2 \ll m_3$) and *inverted mass hierarchy* (i.e. $m_3 \ll m_1 \approx m_2$), respectively. For a given m_L the range of $m_{\beta\beta}$ is determined by variations of the Majorana phase and uncertainties in the neutrino oscillation parameters.

The darker regions show how the $m_{\beta\beta}$ range would shrink if the present best-fit values of the oscillation parameters were confirmed with negligible error.

[From A. Strumia and F. Vissani, “Implications of neutrino data circa 2005,” Nucl. Phys. B **726** (2005) 294–316 (hep-ph/0503246).]



The only evidence for the $(\beta\beta)_{0\nu}$ decay has been obtained by the Heidelberg-Moscow (HM) (**sub**)collaboration in the Gran Sasso lab. The HM best value of the effective neutrino mass is $|m_{\beta\beta}| = 0.4 \text{ eV}$. Allowing conservatively for an uncertainty of the nuclear matrix element of $\pm 50\%$ the 3σ confidence range may widen to $(0.1 - 0.9) \text{ eV}$. The bars in the figure denote allowed ranges of $|m_{\beta\beta}|$ in different neutrino mass scenarios, still allowed by neutrino oscillation experiments. All models except the *degenerate* one are excluded by the new $(\beta\beta)_{0\nu}$ decay result. Also shown is the exclusion line from WMAP, plotted for $\sum_k m_k < 1.0 \text{ eV}$ (which is perhaps too strict). WMAP does not rule out any of the neutrino mass schemes.



Further shown are the expected sensitivities for the future potential $(\beta\beta)_{0\nu}$ decay experiments CUORE, MOON, EXO and GENIUS.

[From H. V. Klapdor-Kleingrothaus, "First evidence for neutrinoless double beta decay and world status of double beta experiments," hep-ph/0512263.]

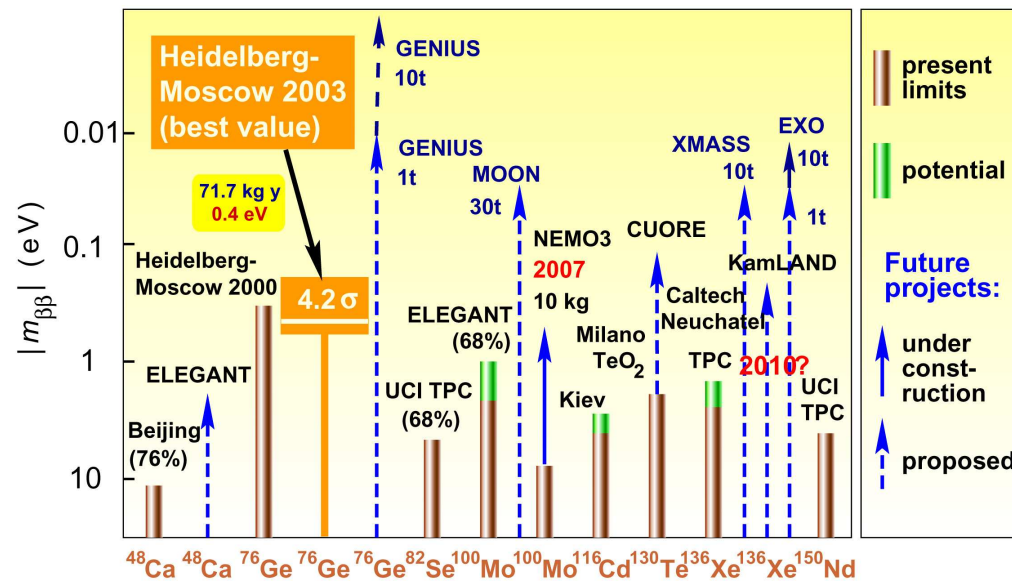


Figure shows the HM-2000 and HM-2003 results in comparison with the potential of the most promising other $(\beta\beta)_{0\nu}$ experiments as well as the expected potential of several future projects. Given are limits for $|m_{\beta\beta}|$, except for the HM-2003 experiment where the measured *value* is given (confidence range and best value).

[The histogram is built by combining the data from papers H. V. Klapdor-Kleingrothaus *et al.*, "Latest results from the Heidelberg-Moscow double beta decay experiment," *Eur. Phys. J. A* **12** (2001) 147–154 (hep-ph/0103062) and H. V. Klapdor-Kleingrothaus, "First evidence for neutrinoless double beta decay and world status of double beta experiments," in *Proceedings of the 11th International Workshop on Neutrino Telescopes, Venice, Feb. 22–25, 2005*, edited by M. Baldo-Ceolin, pp. 215–237 (hep-ph/0512263).]

New approaches and considerably enlarged experiments are required to fix the $(\beta\beta)_{0\nu}$ half life with higher accuracy. This will, however, only marginally improve the precision of the deduced effective neutrino mass $|m_{\beta\beta}|$ (or its upper limit), because of the uncertainties in the nuclear matrix elements, which probably hardly can be reduced to less than 50%.

2.4 See-saw mechanism

2.4.1 Dirac-Majorana mass term for one generation

It is possible to consider mixed models in which both Majorana and Dirac mass terms are present. For simplicity sake we'll start with a toy model for one lepton generation.

Let us consider a theory containing two independent neutrino fields ν_L and ν_R :

$$\left\{ \begin{array}{l} \nu_L \text{ would generally represent any active neutrino (e.g., } \nu_L = \nu_{eL}), \\ \nu_R \text{ can represents a right handed field unrelated to any of these or} \\ \text{it can be charge conjugate of any of the active neutrinos (e.g., } \nu_R = (\nu_{\mu L})^c). \end{array} \right.$$

We can write the following generic mass term between ν_L and ν_R :

$$\mathcal{L}_m = - \underbrace{m_D \bar{\nu}_L \nu_R}_{\text{Dirac mass term}} - \underbrace{(1/2) [m_L \bar{\nu}_L \nu_L^c + m_R \bar{\nu}_R^c \nu_R]}_{\text{Majorana mass term}} + \text{H.c.} \quad (4)$$

- ★ As we know, the Dirac mass term respects L while the Majorana mass term violates it.
- ★ The parameter m_D in Eq. (4) is in general complex but we'll assume it to be real (but **not necessarily positive**).
- ★ The parameters m_L , and m_R in Eq. (4) can be chosen **real** and (by an appropriate rephasing the fields ν_L and ν_R) **non-negative**, but the latter is not assumed.
- ★ Obviously, neither ν_L nor ν_R is a mass eigenstate.

In order to obtain the *mass basis* we can apply the useful identity^a

$$\bar{\nu}_L \nu_R = (\bar{\nu}_R)^c (\nu_L)^c$$

which allows us to rewrite Eq. (4) as follows

$$\mathcal{L}_m = -\frac{1}{2} (\bar{\nu}_L, (\bar{\nu}_R)^c) \begin{pmatrix} m_L & m_D \\ m_D & m_R \end{pmatrix} \begin{pmatrix} (\nu_L)^c \\ \nu_R \end{pmatrix} + \text{H.c.} \equiv -\frac{1}{2} \bar{\nu}_L \mathbf{M} (\nu_L)^c + \text{H.c.}$$

If (for simplicity) *CP* conservation is assumed the matrix \mathbf{M} can be diagonalized through the standard orthogonal transformation

$$\mathbf{V} = \begin{pmatrix} \cos \theta & \sin \theta \\ -\sin \theta & \cos \theta \end{pmatrix} \quad \text{with} \quad \theta = \frac{1}{2} \arctan \left(\frac{2m_D}{m_R - m_L} \right).$$

and we have

$$\mathbf{V}^T \mathbf{M} \mathbf{V} = \text{diag}(m_1, m_2),$$

where $m_{1,2}$ are eigenvalues of \mathbf{M} given by

$$m_{1,2} = \frac{1}{2} \left(m_L + m_R \pm \sqrt{(m_L - m_R)^2 + 4m_D^2} \right).$$

^aA particular case of a more general relation $\bar{\psi}_1 \Gamma \psi_2 = \bar{\psi}_2^c C \Gamma^T C^{-1} \psi_1^c$, where $\psi_{1,2}$ are Dirac spinors and Γ represents a product of the Dirac γ matrices.

The eigenvalues are real if (as we assume) $m_{D,L,R}$ are real, but **not necessarily positive**. Let us define $\zeta_k = \text{sign } m_k$ and rewrite the mass term in the new basis:

$$\mathcal{L}_m = -\frac{1}{2} [\zeta_1 |m_1| \bar{\nu}_{1L} (\nu_{1L})^c + \zeta_2 |m_2| (\bar{\nu}_{2R})^c \nu_{2R}] + \text{H.c.}, \quad (5)$$

The new fields ν_{1L} and ν_{2R} represent chiral components of two different neutrino states with “masses” m_1 and m_2 , respectively:

$$\begin{pmatrix} \nu_L \\ \nu_R^c \end{pmatrix} = \mathbf{V} \begin{pmatrix} \nu_{1L} \\ \nu_{2R}^c \end{pmatrix} \implies \begin{cases} \nu_{1L} = \cos \theta \nu_L - \sin \theta \nu_R^c, \\ \nu_{2R} = \sin \theta \nu_L^c + \cos \theta \nu_R. \end{cases}$$

Now we define two 4-component fields

$$\nu_1 = \nu_{1L} + \zeta_1 (\nu_{1L})^c \quad \text{and} \quad \nu_2 = \nu_{2R} + \zeta_2 (\nu_{2R})^c.$$

Certainly, these fields are self-conjugate,

$$\nu_k^c = \zeta_k \nu_k \quad (k = 1, 2)$$

and therefore they describe Majorana neutrinos. In terms of these fields Eq. (6) is

$$\mathcal{L}_m = -\frac{1}{2} (|m_1| \bar{\nu}_1 \nu_1 + |m_2| \bar{\nu}_2 \nu_2). \quad (6)$$

We can conclude therefore that $\nu_k(x)$ is the Majorana neutrino field with the definite (physical) mass $|m_k|$.

There are several special cases of the Dirac-Majorana mass matrix \mathbf{M} which are of considerable phenomenological importance, in particular,

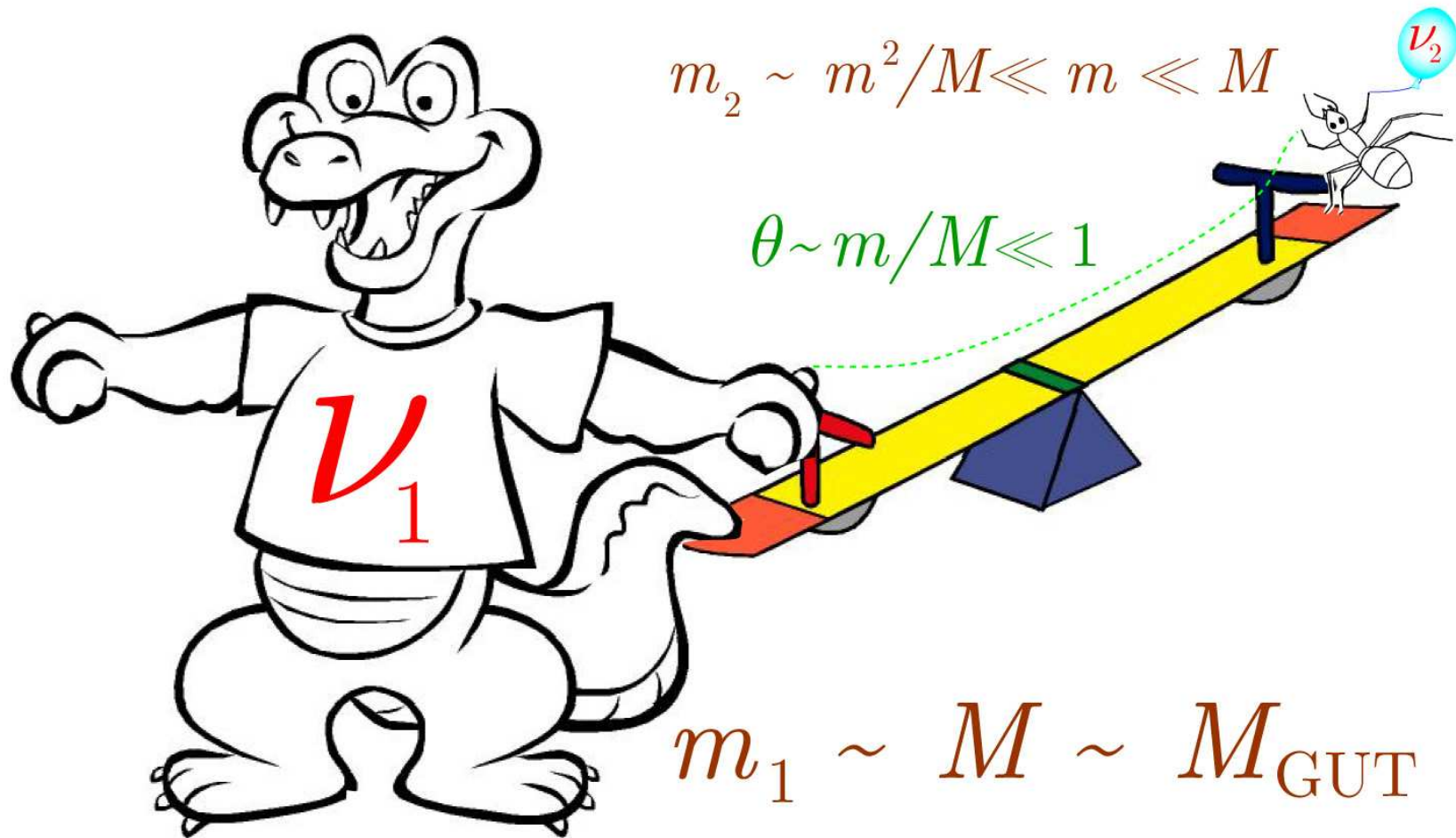
$$\begin{aligned}
 \text{(A): } \mathbf{M} &= \begin{pmatrix} 0 & m \\ m & 0 \end{pmatrix} \implies |m_{1,2}| = m, \quad \theta = \frac{\pi}{4} \quad (\text{maximal mixing}) \\
 &\qquad\qquad\qquad \text{two Majorana fields are equivalent to one Dirac field;} \\
 \text{(B): } \mathbf{M} &= \begin{pmatrix} m_L & m \\ m & m_L \end{pmatrix} \implies m_{1,2} = m_L \pm m_D, \quad \theta = \frac{\pi}{4} \quad (\text{maximal mixing}); \\
 \text{(C): } \mathbf{M} &= \begin{pmatrix} 0 & m \\ m & M \end{pmatrix} \quad \text{or, more generally, } |m_L| \ll |m_R|, \quad m_D > 0.
 \end{aligned}$$

A generalization of case (A), $|m_{L,R}| \ll |m_D|$, leads to the so-called “Pseudo-Dirac neutrinos” and to the ν_L (active) $\leftrightarrow \nu_R$ (sterile) oscillations with almost maximal mixing ($\tan 2\theta \gg 1$).

2.4.2 The See-saw

The case (C) with $m \ll M$ is the simplest example of the seesaw mechanism. It leads to two masses, one very large $m_1 \approx M$ other $m_2 \approx m^2/M \ll m$, suppressed compared to entries in \mathbf{M} . In particular, one can assume

$$m \sim m_\ell \text{ or } m_q \quad (0.5 \text{ MeV to } 200 \text{ GeV}) \quad \text{and} \quad M \sim M_{\text{GUT}} \sim 10^{15-16} \text{ GeV}.$$



Then, m_2 can range from $\sim 10^{-14}$ eV to ~ 0.04 eV. The mixing between the heavy and light neutrinos is extremely small: $\theta \approx m/M \sim 10^{-20} - 10^{-13} \lll 1$.

2.4.3 More neutral fermions

A generalization of the above scheme to N generations is almost straightforward but technically cumbersome. Let's consider it schematically for $N = 3$.

- If neutral fermions are added to the SM fields, then the flavour neutrinos can acquire mass by mixing with them.
- The additional neutrinos can be
 - $SU(2) \times U(1)$ singlets (e.g., right-handed neutrinos), or
 - $SU(2) \times U(1)$ doublets (e.g., Higgsino in SUSY), or
 - $SU(2) \times U(1)$ triplets (e.g., Wino in SUSY).
- Addition of three right-handed neutrinos \mathcal{N}_{iR} leads to the see-saw mechanism with the following mass terms:

$$\mathcal{L}_m = - \sum_{ij} \left[\bar{\nu}_{iL} M_{ij}^D \mathcal{N}_{jR} - \frac{1}{2} (\mathcal{N}_{iR})^c M_{ij}^R \mathcal{N}_{jR} + \text{H.c.} \right].$$

- The above equation gives the see-saw 6×6 mass matrix

$$\mathbf{M} = \begin{pmatrix} \mathbf{0} & \mathbf{m}_D \\ \mathbf{m}_D^T & \mathbf{M}_R \end{pmatrix}.$$

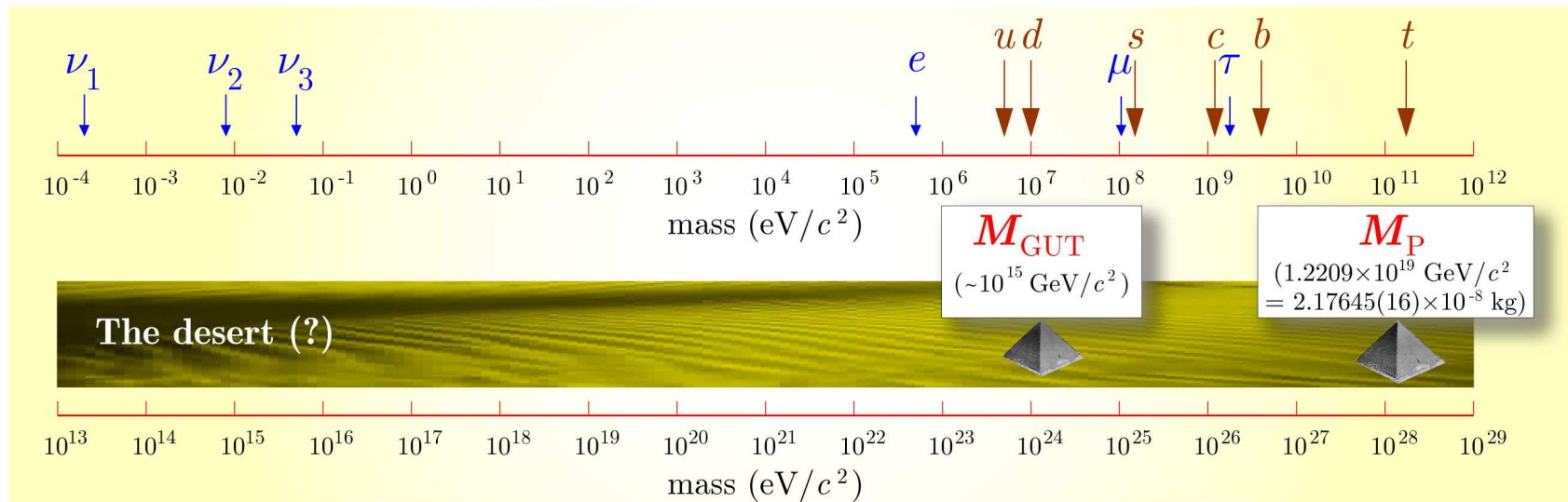
Both \mathbf{m}_D and \mathbf{m}_R are 3×3 matrices in the generation space.

When \mathbf{M}_R is nonsingular and its scale M is much larger than that in \mathbf{m}_R ,^a one get

$$\mathbf{m}_\nu \sim -\mathbf{m}_D \mathbf{M}_R^{-1} \mathbf{m}_D^T.$$

All the neutrino masses are automatically suppressed due to the large scale $M \sim M_{\text{GUT}}$ in \mathbf{M}_R . One gets the following mass hierarchy for a diagonal \mathbf{M}_R

$$m_1 : m_2 : m_3 \propto m_{D1}^2 : m_{D2}^2 : m_{D3}^2$$



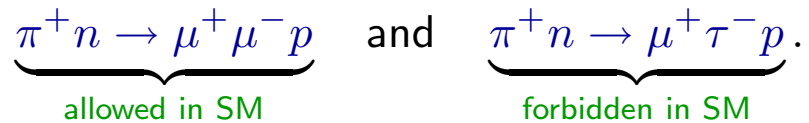
Here m_{Dk} are eigenvalues of \mathbf{m}_D . As long as these eigenvalues are hierarchical, the Majorana neutrino masses also display the hierarchy.

^aA large M is natural in, e.g., grand unified $SO(10)$ theories which therefore provide a nice framework to understand small neutrino masses.

3 Neutrino oscillations in vacuum

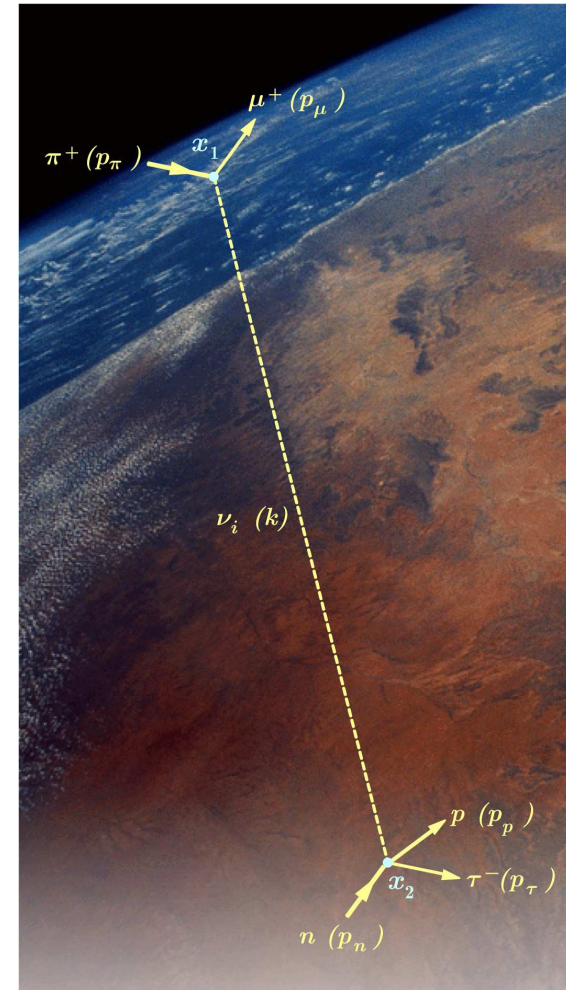
3.1 Macroscopic Feynman diagrams

Let us consider two reactions



The first one is allowed in the SM while the second reaction is forbidden by conservation of the individual lepton numbers $L_{\mu, \tau}$. However, our previous consideration suggests that in a model extended by inclusion of a Dirac or Majorana mass term these numbers are no longer conserved and the second process becomes also possible through the Feynman diagrams like one shown in the figure. The diagram describes the process of a pion decay with subsequent quasielastic neutrino scattering off a neutron with production of a τ lepton. The 4-momenta of the particles are shown in parentheses.

The mass eigenstate neutrino ν_k is in a virtual state between the space-time points of its production ($x_1 = (t_1, \mathbf{x}_1)$) and absorption ($x_2 = (t_2, \mathbf{x}_2)$).



The amplitude of the process under consideration,

$$\mathcal{M}(x_1, x_2) = \langle \text{out} | \text{in} \rangle = \langle \mu^+, \tau^-, p | \pi^+, n \rangle,$$

is given by the sum of N diagrams with $i = 1, 2, \dots, N$ ($N = 3$ from here on).

The diagrams are quite unusual considering that the points x_1 and x_2 are separated by a **macroscopic** spatial interval $|\mathbf{x}_1 - \mathbf{x}_2|$. However, there are solid evidences that just the processes of this kind were already detected in the underground experiments **Kamiokande**, **IMB**, **SOUDAN 2**, **Super-Kamiokande**, and **MACRO** exploring atmospheric neutrinos crossing the Earth (see Part I of these lectures). Moreover, these results are confirmed by two accelerator experiments – **K2K** and (very recently) **MINOS** (FNAL, NuMI Beam).^a

A careful consideration demonstrates that the situation is even more nontrivial. Neglecting the matter effects, the general structure of the amplitude can be written as

$$\mathcal{M}(x_1, x_2) = \sum_j \int d^4 y_1 d^4 y_2 A_2(x_2 - y_2) V_{\tau j}^* G_j(y_2 - y_1) V_{\mu j} A_1(y_1 - x_1),$$

where $A_1(y_1 - x_1)$ and $A_2(x_2 - y_2)$ are the matrices describing the vertices x_1 and x_2 (decay and interaction) and

^aD. A. Petyt (for the MINOS Collaboration), “First MINOS results from the NuMI Beam,” report in the University of Minnesota Joint Experimental/Theoretical Physics Seminar, Fermilab March 30, 2006.

$$G_j(y_2 - y_1) = \langle 0|T[\nu_j(y_1)\bar{\nu}_j(y_2)]|0\rangle = i \int \frac{d^4q}{(2\pi)^4} \frac{\hat{q} - m_j}{q^2 - m_j^2 + i0} e^{iq(y_2 - y_1)}$$

is the Green function describing the propagation of the virtual neutrino ν_j between the space-time points y_1 and y_2 ($T[\dots]$ denotes the standard T -ordering operator).

The following simple but important statements can be proved:

- ★ $\mathcal{M}(x_1, x_2) \equiv 0$ if the neutrino mass spectrum is degenerate ($m_1 = m_2 = m_3$). This is an obvious consequence of the unitarity of the mixing matrix which in particular provides $\sum_j V_{\mu j} V_{\tau j}^* = 0$.
- ★ If the wave functions of any of the “colliding” particles (pion or neutron) are plane waves that is

$$\Phi_\pi(x) = e^{-ip_\pi x} = e^{-i(E_\pi t - \mathbf{p}_\pi \mathbf{x})} \quad \text{or} \quad \Psi_n(x) = e^{-ip_n x} = e^{-i(E_n t - \mathbf{p}_n \mathbf{x})},$$

the amplitude is suppressed by the factor

$$\sum_j V_{\mu j} V_{\tau j}^* \left(\frac{m_j}{E_\nu} \right)^2 = 10^{-20} \sum_j V_{\mu j} V_{\tau j}^* \left(\frac{m_j}{1 \text{ eV}/c^2} \right)^2 \left(\frac{10 \text{ GeV}}{E_\nu} \right)^2,$$

where $E_\nu \equiv k_0 = E_\pi - E_\mu$ is the virtual neutrino energy (independent of m_j). This is a consequence of the energy-momentum conservation in each vertex.

A nontrivial (but not the most general) situation occurs when both wave functions $\Phi_\pi(x)$ and $\Psi_n(x)$ are localized within neighborhoods of the points \mathbf{x}_1 and \mathbf{x}_2 :

$$\Phi_\pi(x) = e^{-iE_\pi t} \varphi_\pi(\mathbf{x} - \mathbf{x}_1) \quad \text{and} \quad \Psi_n(x) = e^{-iE_n t} \psi_n(\mathbf{x} - \mathbf{x}_2).$$

According to the uncertainty principle this means that there is a spread in the momenta of these particles. In this case, by applying the crucial **Grimus-Stockinger theorem**^a one can prove that in the asymptotic limit $L = |\mathbf{x}_1 - \mathbf{x}_2| \rightarrow \infty$, $\mathcal{M}(x_1, x_2) \rightarrow \mathcal{M}_\infty(L)$ and

$$\mathcal{M}_\infty(L) = \frac{\mathcal{M}_1 \mathcal{M}_2}{L} \sum_j V_{\mu j} V_{\tau j}^* e^{i q_j L}, \quad \text{where} \quad q_j = \sqrt{E_\nu^2 - m_j^2}, \quad E_\nu = E_\pi - E_\mu.$$

^aSee W. Grimus and P. Stockinger, "Real oscillations of virtual neutrinos," Phys. Rev. D **54** (1996) 3414–3419 (hep-ph/9603430).

The theorem states: Let $\Phi = \Phi(\mathbf{q})$ be a 3 times continuously differentiable function such that Φ itself and all its first and second derivatives decrease at least like $|\mathbf{q}|^{-2}$ for $|\mathbf{q}| \rightarrow \infty$, a a real number, and

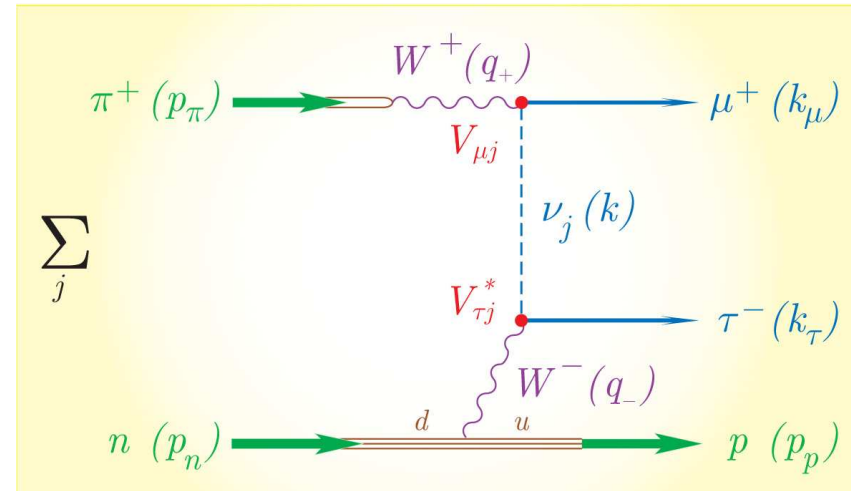
$$J(\mathbf{L}) \equiv \int d^3 q \frac{\Phi(\mathbf{q})}{a - |\mathbf{q}|^2 + i0} \exp(-i\mathbf{q}\mathbf{L}).$$

Then in the asymptotic limit $L = |\mathbf{L}| \rightarrow \infty$ one obtains, for $a > 0$,

$$J(\mathbf{L}) \rightarrow -\frac{2\pi^2}{L} \Phi(-\sqrt{a}\mathbf{l}) \exp(i\sqrt{a}L) + \mathcal{O}(L^{-3/2}), \quad \mathbf{l} \equiv \frac{\mathbf{L}}{L},$$

whereas for $a < 0$ the integral $J(\mathbf{L})$ decreases like L^{-2} .

To calculate the factors \mathcal{M}_1 and \mathcal{M}_2 as functions of the momenta of the initial and final particles, respectively, one have to “decipher” the vertices of our macro-diagram by applying an interaction model (like that shown in the figure on right). *It is by no means a simple or straightforward task.* One can prove however that after quadrating the amplitude we will arrive at something like



$$L^{-2} d\Gamma(\pi^+ \rightarrow \mu^+ \nu_\mu) \times P(\nu_\mu \rightarrow \nu_\tau) \times d\sigma(\nu_\tau + n \rightarrow p + \tau),$$

where $d\Gamma$ is the differential width of standard pion decay, $d\sigma$ is the differential cross section for the quasielastic $\nu_\tau n$ interaction and

$$P(\nu_\mu \rightarrow \nu_\tau) \equiv \left| \sum_j V_{\mu j} V_{\tau j}^* e^{iq_j L} \right|^2$$

The latter can be *interpreted* as the probability of the transition of **real** muon neutrino to **real** tauon neutrino (both having energy $E_\nu = E_\pi - E_\mu$) on the path L between the neutrino source (decay) and the detector.

The factor L^2 accounts for the geometrical decrease of the neutrino flux.

This obtained result is almost independent of the specific process. This allows us to generalize it quite straightforwardly and write out the formula for the transition probability between any neutrino pair:

$$P(\nu_\alpha \rightarrow \nu_\beta) = \left| \sum_j V_{\alpha j} V_{\beta j}^* e^{iq_j L} \right|^2 = \sum_{jk} V_{\alpha j} V_{\beta k} (V_{\alpha k} V_{\beta j})^* \exp [i(q_j - q_k)L]. \quad (7)$$

Important notes

- ★ In order to obtain \mathcal{M}_∞ we have performed the asymptotic limit $L \rightarrow \infty$. From the proof of the Grimus-Stockinger theorem it follows that “ L large” means

$$L \gg 2 \times 10^{-16} \text{ m} \times (1 \text{ GeV}/\overline{E}_\nu),$$

where \overline{E}_ν is an average neutrino energy. For every thinkable neutrino experiment this is very well fulfilled and corrections to \mathcal{M}_∞ are suppressed by $1/\sqrt{\overline{E}_\nu}$.

- ★ The factor $1/L$ in the asymptotic amplitude corresponds to the geometrical decrease of the neutrino “flux” by $1/L^2$ in the “cross section”.
- ★ From the derivation one can conclude that neutrino oscillations between the neutrino with masses m_j and m_k can only take place if

$$|q_j - q_k| \lesssim \sigma,$$

where σ is the minimum of the widths of the Fourier transformations of the involved wave functions. In coordinate space this simply means that corresponding widths must be smaller than the oscillation lengths defined by

$$L_{jk} = \frac{4\pi E_\nu}{m_j^2 - m_k^2} \equiv \frac{4\pi E_\nu}{\Delta m_{jk}^2} \approx 2.48 \text{ m} \times \frac{E_\nu (\text{MeV})}{\Delta m_{jk}^2 (\text{eV}^2)}.$$

- ★ The nature of neutrinos (Dirac or Majorana) was not specified in our schematic consideration. It can be shown however that the difference between $\mathcal{M}_\infty^{\text{Dirac}}$ and $\mathcal{M}_\infty^{\text{Majorana}}$ is of the order of m_j/E_ν .

3.2 Quantum mechanical approach

The **flavor** neutrino eigenstates which can be written as a vector

$$|\nu\rangle_f = (|\nu_e\rangle, |\nu_\mu\rangle, |\nu_\tau\rangle, \dots)^T \equiv (|\nu_\alpha\rangle)^T$$

are defined as the states which correspond to the charge leptons $\alpha = e, \mu, \tau$. The correspondence is established through the charged current interactions of active neutrinos and charged leptons. In general, the flavor states have no definite masses.

The neutrino **mass** eigenstates

$$|\nu\rangle_m = (|\nu_1\rangle, |\nu_2\rangle, |\nu_3\rangle, \dots)^T \equiv (|\nu_k\rangle)^T$$

are, by definition, the states with the definite masses m_k , $k = 1, 2, 3, \dots$

Since $|\nu_\alpha\rangle$ and $|\nu_k\rangle$ are not identical, they are related to each other through a unitary transformation

$$|\nu_\alpha\rangle = \sum_k \hat{V}_{\alpha k} |\nu_k\rangle \quad \text{or} \quad |\nu\rangle_f = \hat{\mathbf{V}} |\nu\rangle_m,$$

where $\hat{\mathbf{V}} = \|\hat{V}_{\alpha k}\|$ is a unitary (in general, $N \times N$) matrix. In order to find out the correspondence between $\hat{\mathbf{V}}$ and the PMNS mixing matrix \mathbf{V} we can normalize the “ f ” and “ m ” states by the following conditions

$$\langle 0 | \nu_{\alpha L}(x) | \nu_{\alpha'} \rangle = \delta_{\alpha\alpha'} \quad \text{and} \quad \langle 0 | \nu_{k L}(x) | \nu_{k'} \rangle = \delta_{kk'}.$$

From these conditions we obtain

$$\sum_k V_{\alpha k} \hat{V}_{\alpha' k} = \delta_{\alpha\alpha'} \quad \text{and} \quad \sum_{\alpha} V_{\alpha k} \hat{V}_{\alpha k'} = \delta_{kk'}.$$

Therefore

$$\hat{\mathbf{V}} \equiv \mathbf{V}^\dagger$$

and

$$|\nu\rangle_f = \mathbf{V}^\dagger |\nu\rangle_m \quad \Longleftrightarrow \quad |\nu\rangle_m = \mathbf{V} |\nu\rangle_f.$$

The time evolution of a single mass eigenstate $|\nu_k\rangle$ with momentum p_ν is trivial,

$$i \frac{d}{dt} |\nu_k(t)\rangle = E_k |\nu_k(t)\rangle \quad \Longrightarrow \quad |\nu_k(t)\rangle = e^{-iE_k(t-t_0)} |\nu_k(t_0)\rangle,$$

where $E_k = \sqrt{p_\nu^2 + m_k^2}$ is the total energy in the state $|\nu_k\rangle$. Therefore, assuming that all the components of the neutrino wave packet have the same momenta, one can write

$$i \frac{d}{dt} |\nu(t)\rangle_m = \mathbf{H}_0 |\nu(t)\rangle_m, \quad \text{where} \quad \mathbf{H}_0 = \text{diag}(E_1, E_2, E_3, \dots). \quad (8)$$

(\mathbf{H}_0 is the vacuum Hamiltonian.) From Eqs. (53) and (8) we have

$$i \frac{d}{dt} |\nu(t)\rangle_f = \mathbf{V}^\dagger \mathbf{H}_0 \mathbf{V} |\nu(t)\rangle_f. \quad (9)$$

Solution to this equation is obvious:

$$\begin{aligned}
|\nu(t)\rangle_f &= \mathbf{V}^\dagger e^{-i\mathbf{H}_0(t-t_0)} \mathbf{V} |\nu(t_0)\rangle_f \\
&= \mathbf{V}^\dagger \text{diag} \left(e^{-iE_1(t-t_0)}, e^{-iE_2(t-t_0)}, \dots \right) \mathbf{V} |\nu(t_0)\rangle_f.
\end{aligned} \tag{10}$$

In the ultrarelativistic limit $p_\nu^2 \gg m_k^2$, which is valid for almost all interesting circumstances (except for the relic neutrinos),

$$E_k = \sqrt{p_\nu^2 + m_k^2} \approx p_\nu + \frac{m_k^2}{2p_\nu} \approx E_\nu + \frac{m_k^2}{2E_\nu}.$$

By applying this approximation and Eq. (10) one can derive the survival and transition probabilities

$$\begin{aligned}
P[\nu_\alpha(t_0) \rightarrow \nu_\beta(t)] &\equiv P_{\alpha\beta}(t-t_0) = |\langle \nu_\beta(t) | \nu_\alpha(t_0) \rangle|^2 \\
&= \left| \sum_k V_{\alpha k} V_{\beta k}^* \exp[iE_k(t-t_0)] \right|^2 \\
&= \sum_{jk} V_{\alpha j} V_{\beta k} (V_{\alpha k} V_{\beta j})^* \exp[i(E_j - E_k)(t-t_0)] \\
&\approx \sum_{jk} V_{\alpha j} V_{\beta k} (V_{\alpha k} V_{\beta j})^* \exp[i\Delta m_{jk}^2(t-t_0)/2E_\nu].
\end{aligned}$$

The next standard approximation is

$$v_k = p_\nu / E_k \approx c = 1$$

from which it follows that

$$t - t_0 \approx L = \text{source-detector distance.}$$

This approximation is in fact contradictory since the corresponding corrections are also of the order of $m_k' E_\nu$. However, only with this approximation we arrive at the formula^a

$$\begin{aligned} P_{\alpha\beta}(L) &\approx \sum_{jk} V_{\alpha j} V_{\beta k} (V_{\alpha k} V_{\beta j})^* \exp(i\Delta m_{jk}^2 L / 2E_\nu) \\ &= \sum_{jk} V_{\alpha j} V_{\beta k} (V_{\alpha k} V_{\beta j})^* \exp[2i\pi L / L_{jk}], \end{aligned} \quad (11)$$

which marvellously and enigmatically fits the field-theoretical (“diagrammatic”) result (7) (written in the ultrarelativistic limit).

The range of applicability of the standard quantum-mechanical approach is very limited.

^aAs above, $L_{jk} = 4\pi E_\nu / \Delta m_{jk}^2$ are the oscillation lengths.

3.2.1 Simplest case: two flavor vacuum oscillations

Let us now consider the simplest 2-flavor case with $i = 2, 3$ and $\alpha = \mu, \tau$ (the most favorable due to the SK and other underground experiments). The 2×2 vacuum mixing matrix can be parametrized (due to the unitarity) with a single parameter, $\theta = \theta_{23}$, the vacuum mixing angle,

$$\mathbf{V} = \begin{pmatrix} \cos \theta & \sin \theta \\ -\sin \theta & \cos \theta \end{pmatrix}, \quad 0 \leq \theta \leq \pi/2.$$

Equation (11) then becomes very simple:

$$P_{\alpha\alpha'}(L) = \frac{1}{2} \sin^2 2\theta \left[1 - \cos \left(\frac{2\pi L}{L_\nu} \right) \right],$$
$$L_\nu \equiv L_{23} = \frac{4\pi E_\nu}{\Delta m_{23}^2} \approx 2R_\oplus \left(\frac{E_\nu}{10 \text{ GeV}} \right) \left(\frac{0.002 \text{ eV}^2}{\Delta m_{23}^2} \right)$$

where R_\oplus is the mean radius of the Earth. Since 10 GeV is a typical energy for the atmospheric neutrinos, the Earth is surprisingly very suitable for studying the atmospheric neutrino oscillations in rather wide range of the parameter Δm_{23}^2 .

4 Neutrino oscillations in matter

4.1 Neutrino refraction in matter

It has been noted by Wolfenstein^a that neutrino oscillations in a medium are affected by interactions even if the thickness of the medium is negligible in comparison with the neutrino mean free path.

Let us forget for the moment about the inelastic collisions and consider the simplest case of a ultrarelativistic neutrino which moves in an external (effective) potential W formed by the matter background. If the neutrino momentum in vacuum was \mathbf{p} then its energy was $\simeq p = |\mathbf{p}|$. When the neutrino enters into the medium, its energy becomes $E = p + W$. Let us now introduce the index of refraction $n = p/E$ which is a positive value in the absence of inelastic collisions. Therefore

$$W = (1 - n)E \simeq (1 - n)p. \quad (12)$$

In the last step, we took into account that neutrino interaction with matter is very weak, $|W| \ll E$, and thus $E \simeq p$ is a good approximation.

The natural generalization of Eq. (9) for the time evolution of neutrino flavor states in matter then follows from this simple consideration and the quantum-mechanical correspondence principle.

^aL. Wolfenstein, Phys. Rev. D **17** (1978) 2369.

This is the famous **Wolfenstein equation**:

$$i \frac{d}{dt} |\nu(t)\rangle_f = [\mathbf{VH}_0\mathbf{V}^\dagger + \mathbf{W}(t)] |\nu(t)\rangle_f, \quad (13)$$

where

$$\mathbf{W}(t) = \text{diag} (1 - n_{\nu_e}, 1 - n_{\nu_\mu}, 1 - n_{\nu_\tau}, \dots) \quad (14)$$

is the interaction Hamiltonian.

It will be useful for the following to introduce the *time-evolution operator* for the flavor states defined by

$$|\nu(t)\rangle_f = \mathbf{S}(t) |\nu(0)\rangle_f.$$

Taking into account that $|\nu(t)\rangle_f$ must satisfy Eq. (13) for any initial condition $|\nu(t=0)\rangle_f = |\nu(0)\rangle_f$, the Wolfenstein equation can be immediately rewritten in terms of the evolution operator:

$$i\dot{\mathbf{S}}(t) = [\mathbf{VH}_0\mathbf{V}^\dagger + \mathbf{W}(t)] \mathbf{S}(t), \quad \mathbf{S}(0) = \mathbf{1}. \quad (15)$$

This equation (or its equivalent (13)) cannot be solved analytically in the general case of a medium with a varying (along the neutrino pass) density. But for a medium with a slowly (adiabatically) varying density distribution the approximate solution can be obtained by a diagonalization of the effective Hamiltonian. Below we will consider this method for a rather general 2-flavor case but now let us illustrate (without derivation) the simplest situation with a matter of constant density.

4.1.1 Matter of constant density

In the 2-flavor case, the transition probability is given by the formula very similar to that for vacuum:

$$P_{\alpha\alpha'}(L) = \frac{1}{2} \sin^2 2\theta_m \left[1 - \cos \left(\frac{2\pi L}{L_m} \right) \right],$$
$$L_m = L_v \left[1 - 2\kappa (L_v/L_0) \cos \theta + (L_v/L_0)^2 \right]^{-1/2}.$$

The L_m is called the **oscillation length in matter** and is defined through the following quantities:

$$L_v \equiv L_{23} = \frac{4\pi E}{\Delta m^2}, \quad L_0 = \frac{\sqrt{2}\pi A}{G_F N_A Z \rho} \approx 2R_\oplus \left(\frac{A}{2Z} \right) \left(\frac{2.5 \text{ g/cm}^3}{\rho} \right),$$
$$\kappa = \text{sign} (m_3^2 - m_2^2), \quad \Delta m^2 = |m_3^2 - m_2^2|.$$

The parameter θ_m is called the **mixing angle in matter** and is given by

$$\sin 2\theta_m = \sin 2\theta \left(\frac{L_m}{L_v} \right), \quad \cos 2\theta_m = \left(\cos 2\theta - \kappa \frac{L_v}{L_0} \right) \left(\frac{L_m}{L_v} \right).$$

The solution for antineutrinos is the same but with the replacement $\kappa \mapsto -\kappa$. The closeness of the value of L_0 to the Earth's diameter is even more surprising than that for L_v . The matter effects are important for atmospheric neutrinos.

“The matter doesn’t matter”

Lincoln Wolfenstein, lecture given at 28th SLAC Summer Institute on Particle Physics “Neutrinos from the Lab, the Sun, and the Cosmos”, Stanford, CA, Aug. 14-25, 2000.

When neutrinos propagate through vacuum there is a phase change

$$\exp(-im_i^2 t/2p_\nu).$$

For two **mixed** flavors there is a resulting oscillation with length

$$L_{\text{vac}} = \frac{4\pi E_\nu}{\Delta m^2} \approx D_\oplus \left(\frac{E_\nu}{10 \text{ GeV}} \right) \left(\frac{0.002 \text{ eV}^2}{\Delta m^2} \right).$$

In matter there is an additional phase change due to **refraction** associated with forward scattering

$$\exp[ip_\nu(\text{Re } n - 1)t]$$

and the characteristic length (for a normal medium) is

$$L_{\text{ref}} = \frac{\sqrt{2}A}{G_F N_A Z \rho} \approx D_\oplus \left(\frac{A}{2Z} \right) \left(\frac{2.5 \text{ g/cm}^2}{\rho} \right).$$

It is generally believed that the imaginary part of the index of refraction n which describes the neutrino **absorption** due to inelastic interactions *does not affect the*

oscillation probabilities or at the least inelastic interactions can be somewhat *decoupled* from oscillations.

The conventional arguments are

❖ $\text{Re } n - 1 \propto G_F$ while $\text{Im } n \propto G_F^2$

❖ Only Δn may affect the oscillations and $\Delta \text{Im } n$ is all the more negligible.

It will be shown that these arguments do not work for sufficiently high neutrino energies and/or for thick media \implies in general absorption cannot be decoupled from refraction and mixing.

By using another cant phrase of Wolfenstein, one can say that

“In some circumstances the matter could matter.”

4.2 Propagation of high-energy mixed neutrinos through matter

4.2.1 Generalized MSW equation

Let $f_{\nu_\alpha A}(0)$ be the amplitude for the ν_α zero-angle scattering from particle A of the matter background ($A = e, p, n, \dots$),

$\rho(t)$ – the matter density (in g/cm^3),

$Y_A(t)$ – the number of particles A per amu in the point t of the medium,

$N_0 = 6.02214199 \times 10^{23} \text{ cm}^{-3}$ – the reference particle number density (numerically equal to the Avogadro's number).

Then the index of refraction of ν_α for small $|n - 1|$ is given by

$$n_\alpha(t) = 1 + \frac{2\pi N_0 \rho(t)}{p_\nu^2} \sum_A Y_A(t) f_{\nu_\alpha A}(0),$$

where p_ν is the neutrino momentum. Since the amplitude $f_{\nu_\alpha A}(0)$ is in general a **complex number**, the index of refraction is also **complex**. Its real part is responsible for neutrino refraction while the imaginary part – for absorption. From the optical theorem of quantum mechanics we have

$$\text{Im} [f_{\nu_\alpha A}(0)] = \frac{p_\nu}{4\pi} \sigma_{\nu_\alpha A}^{\text{tot}}(p_\nu).$$

This implies that

$$p_\nu \text{Im} [n_\alpha(t)] = \frac{1}{2} N_0 \rho(t) \sum_A Y_A(t) \sigma_{\nu_\alpha A}^{\text{tot}}(p_\nu) = \frac{1}{2\Lambda_\alpha(p_\nu, t)},$$

where $\Lambda_\alpha(p_\nu, t)$ is the mean free path of ν_α in the point t of the medium.

Note:

The dimension of Λ_α is **cm**,

$$\Lambda_\alpha(p_\nu, t) = \frac{1}{\Sigma_\alpha^{\text{tot}}(p_\nu, t)} = \frac{\lambda_a^{\text{tot}}(p_\nu, t)}{\rho(t)}.$$

Since the neutrino momentum, p_ν , is an extrinsic variable in Eq. (16), we will sometimes omit this argument to simplify formulas.

The generalized MSW equation for the time-evolution operator

$$\mathbf{S}(t) = \begin{pmatrix} S_{\alpha\alpha}(t) & S_{\alpha\beta}(t) \\ S_{\beta\alpha}(t) & S_{\beta\beta}(t) \end{pmatrix}$$

of two mixed stable neutrino flavors ν_α and ν_β propagating through an absorbing medium can be written as

$$i \frac{d}{dt} \mathbf{S}(t) = [\mathbf{V} \mathbf{H}_0 \mathbf{V}^T + \mathbf{W}(t)] \mathbf{S}(t), \quad (\mathbf{S}(0) = \mathbf{1}). \quad (16)$$

Here

$$\mathbf{V} = \begin{pmatrix} \cos \theta & \sin \theta \\ -\sin \theta & \cos \theta \end{pmatrix} \quad \text{is the vacuum mixing matrix } (0 \leq \theta \leq \pi/2),$$

$$\mathbf{H}_0 = \begin{pmatrix} E_1 & 0 \\ 0 & E_2 \end{pmatrix} \quad \text{is the vacuum Hamiltonian for } \nu \text{ mass eigenstates,}$$

$$E_i = \sqrt{p_\nu^2 + m_i^2} \simeq p_\nu + m_i^2/2p_\nu \quad \text{is the energy of the } \nu_i \text{ eigenstate,}$$

$$\mathbf{W}(t) = -p_\nu \begin{pmatrix} n_\alpha(t) - 1 & 0 \\ 0 & n_\beta(t) - 1 \end{pmatrix} \quad \text{is the interaction Hamiltonian.}$$

4.2.2 Master equation

It is useful to transform MSW equation into the one with a traceless Hamiltonian. For this purpose we define the matrix

$$\tilde{\mathbf{S}}(t) = \exp \left\{ \frac{i}{2} \int_0^t \text{Tr} [\mathbf{H}_0 + \mathbf{W}(t')] dt' \right\} \mathbf{S}(t).$$

The master equation (ME) for this matrix then is

$$i \frac{d}{dt} \tilde{\mathbf{S}}(t) = \mathbf{H}(t) \tilde{\mathbf{S}}(t), \quad \tilde{\mathbf{S}}(0) = \mathbf{1} \quad (17)$$

Here

$$\mathbf{H}(t) = \begin{pmatrix} q(t) - \Delta_c & \Delta_s \\ \Delta_s & -q(t) + \Delta_c \end{pmatrix},$$

$$\Delta_c = \Delta \cos 2\theta, \quad \Delta_s = \Delta \sin 2\theta, \quad \Delta = \frac{m_2^2 - m_1^2}{4p_\nu},$$

$$q(t) = q_R(t) + iq_I(t) = \frac{1}{2}p_\nu [n_\beta(t) - n_\alpha(t)].$$

The Hamiltonian for **antineutrinos** is of the same form as $\mathbf{H}(t)$ but

$$\text{Re}[f_{\bar{\nu}_\alpha A}(0)] = -\text{Re}[f_{\nu_\alpha A}(0)] \quad \text{and} \quad \text{Im}[f_{\bar{\nu}_\alpha A}(0)] \neq \text{Im}[f_{\nu_\alpha A}(0)].$$

The neutrino oscillation probabilities are

$$P[\nu_\alpha(0) \rightarrow \nu_{\alpha'}(t)] \equiv P_{\alpha\alpha'}(t) = |S_{\alpha'\alpha}(t)|^2 = A(t) \left| \tilde{S}_{\alpha'\alpha}(t) \right|^2, \quad (18)$$

where

$$A(t) = \exp \left[- \int_0^t \frac{dt'}{\Lambda(t')} \right], \quad \frac{1}{\Lambda(t)} = \frac{1}{2} \left[\frac{1}{\Lambda_\alpha(t)} + \frac{1}{\Lambda_\beta(t)} \right].$$

Owing to the complex potential q , the Hamiltonian $\mathbf{H}(t)$ is **non-Hermitian** and the new evolution operator $\tilde{\mathbf{S}}(t)$ is **nonunitary**. As a result, there are no conventional relations between $P_{\alpha\alpha'}(t)$.

Since

$$q_I(t) = \frac{1}{4} \left[\frac{1}{\Lambda_\beta(t)} - \frac{1}{\Lambda_\alpha(t)} \right],$$

the matrix $\mathbf{H}(t)$ becomes Hermitian when $\Lambda_\alpha = \Lambda_\beta$. If this is the case **at any t** , the ME reduces to the standard MSW equation and inelastic scattering results in the common exponential attenuation of the probabilities. From here, we shall consider the more general and more interesting case, when $\Lambda_\alpha \neq \Lambda_\beta$.

Examples

$\nu_\alpha - \nu_s$ This is the extreme example. Since $\Lambda_s = \infty$, we have $\Lambda = 2\Lambda_\alpha$ and $q_I = -1/4\Lambda_\alpha$. So $q_I \neq 0$ **at any energy**. Even without solving the evolution equation, one can expect the penetrability of active neutrinos to be essentially modified in this case because, roughly speaking, they spend a certain part of life in the sterile state. In other words, sterile neutrinos “tow” their active companions through the medium as a tugboat. On the other hand, the active neutrinos “retard” the sterile ones, like a bulky barge retards its tugboat. As a result, the sterile neutrinos undergo some absorption.

$\nu_{e,\mu} - \nu_\tau$ Essentially at all energies, $\sigma_{\nu_{e,\mu}N}^{\text{CC}} > \sigma_{\nu_\tau N}^{\text{CC}}$. This is because of large value of the τ lepton mass, m_τ , which leads to several consequences:

- ❖ high neutrino energy threshold for τ production;
- ❖ sharp shrinkage of the phase spaces for CC $\nu_\tau N$ reactions;

- ❖ kinematic correction factors ($\propto m_\tau^2$) to the nucleon structure functions (the corresponding structures are negligible for e production and small for μ production).

The neutral current contributions are canceled out from q_I . Thus, in the context of the master equation, ν_τ can be treated as (almost) sterile within the energy range for which $\sigma_{\nu_{e,\mu}N}^{\text{CC}} \gg \sigma_{\nu_\tau N}^{\text{CC}}$ (see Figs. 2–4 below).

$\bar{\nu}_e - \bar{\nu}_\alpha$ A similar situation, while in quite a different and narrow energy range, holds in the case of mixing of $\bar{\nu}_e$ with some other flavor. This is a particular case for a normal C asymmetric medium, because of the W boson resonance formed in the neighborhood of $E_\nu^{\text{res}} = m_W^2/2m_e \approx 6.33$ PeV through the reactions

$$\bar{\nu}_e e^- \rightarrow W^- \rightarrow \text{hadrons} \quad \text{and} \quad \bar{\nu}_e e^- \rightarrow W^- \rightarrow \bar{\nu}_\ell \ell^- \quad (\ell = e, \mu, \tau).$$

Let's remind that $\sigma_{\bar{\nu}_e e}^{\text{tot}} \approx 250 \sigma_{\bar{\nu}_e N}^{\text{tot}}$ just at the resonance peak (see Fig. 1 and Table 3 below).

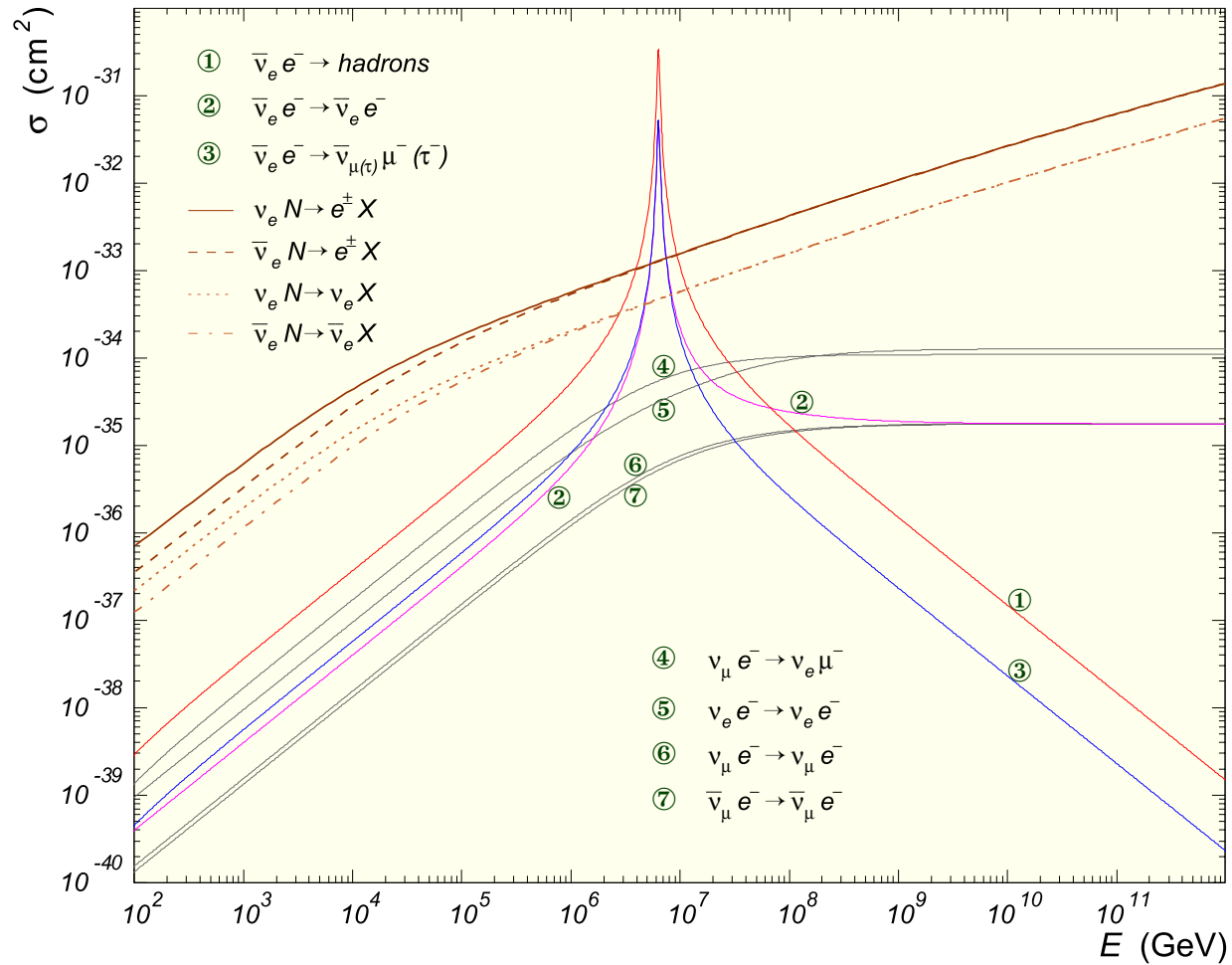


Figure 1: Total cross sections for (anti)neutrino interactions on electron targets. The cross sections for (anti)neutrino CC and NC interactions on isoscalar nucleon are also shown for a comparison.

Table 3: Integrated cross sections for neutrino-electron and neutrino-nucleon scattering at $E_\nu = m_W^2/2m_e \approx 6.331$ PeV.

Reaction	σ (cm ²)	Reaction	σ (cm ²)
$\nu_\mu e \rightarrow \nu_\mu e$	5.86×10^{-36}	$\nu_\mu N \rightarrow \mu^- + \text{anything}$	1.43×10^{-33}
$\bar{\nu}_\mu e \rightarrow \bar{\nu}_\mu e$	5.16×10^{-36}	$\nu_\mu N \rightarrow \nu_\mu + \text{anything}$	6.04×10^{-34}
$\nu_\mu e \rightarrow \mu \nu_e$	5.42×10^{-35}	$\bar{\nu}_\mu N \rightarrow \mu^+ + \text{anything}$	1.41×10^{-33}
$\nu_e e \rightarrow \nu_e e$	3.10×10^{-35}	$\bar{\nu}_\mu N \rightarrow \bar{\nu}_\mu + \text{anything}$	5.98×10^{-34}
$\bar{\nu}_e e \rightarrow \bar{\nu}_e e$	5.215×10^{-32}		
$\bar{\nu}_e e \rightarrow \bar{\nu}_\mu \mu$	5.214×10^{-32}		
$\bar{\nu}_e e \rightarrow \bar{\nu}_\tau \tau$	5.208×10^{-32}		
$\bar{\nu}_e e \rightarrow \text{hadrons}$	3.352×10^{-31}		
$\bar{\nu}_e e \rightarrow \text{anything}$	4.917×10^{-31}		

Just at the resonance peak, $\sigma_{\bar{\nu}_e e}^{\text{tot}} \approx 250 \sigma_{\bar{\nu}_e N}^{\text{tot}}$.

Note:

The cross sections for electron targets listed in Table 3 were calculated using the formulas given by Gandhi *et al.*,^a but some numerical values are different since the input parameters were updated.

^aR. Gandhi, C. Quigg, M. H. Reno, and I. Sarcevic, "Ultra-high-energy neutrino interactions," *Astropart. Phys.* **5** (1996) 81–110 (hep-ph/9512364).

4.2.3 Total cross sections

According to Albright and Jarlskog^a

$$\frac{d\sigma_{\nu, \bar{\nu}}^{\text{CC}}}{dxdy} = \frac{G_F^2 m_N E_\nu}{\pi} (A_1 F_1 + A_2 F_2 \pm A_3 F_3 + A_4 F_4 + A_5 F_5),$$

where $F_i = F_i(x, Q^2)$ are the nucleon structure functions and A_i are the kinematic factors $i = 1, \dots, 5$). These factors were calculated by many authors^b and the most accurate formulas were given by Paschos and Yu:

$$A_1 = xy^2 + \frac{m_l^2 y}{2m_N E_\nu}, \quad A_2 = 1 - y - \frac{m_N}{2E_\nu} xy - \frac{m_l^2}{4E_\nu^2}, \quad A_3 = xy \left(1 - \frac{y}{2}\right) - \frac{m_l^2 y}{4m_N E_\nu},$$
$$A_4 = \frac{m_l^2}{2m_N E_\nu} \left(xy + \frac{m_l^2}{2m_N E_\nu}\right), \quad A_5 = -\frac{m_l^2}{2m_N E_\nu}.$$

The contributions proportional to m_l^2 must vanish as $E_\nu \gg m_l$. However they remain surprisingly important even at very high energies.

^aC. H. Albright and C. Jarlskog, Nucl. Phys. **B84** (1975) 467. See also I. Ju, Phys. Rev. **D8** (1973) 3103 and V. D. Barger *et al.*, Phys. Rev. **D16** (1977) 2141.

^bSee previous footnote and also the more recent papers: S. Dutta, R. Gandhi, and B. Mukhopadhyaya, Eur. Phys. J. C **18** (2000) 405 (hep-ph/9905475); N. I. Starkov, J. Phys. G: Nucl. Part. Phys. **27** (2001) L81; E. A. Paschos and J. Y. Yu, Phys. Rev. **D65** (2002) 033002 (hep-ph/0107261).

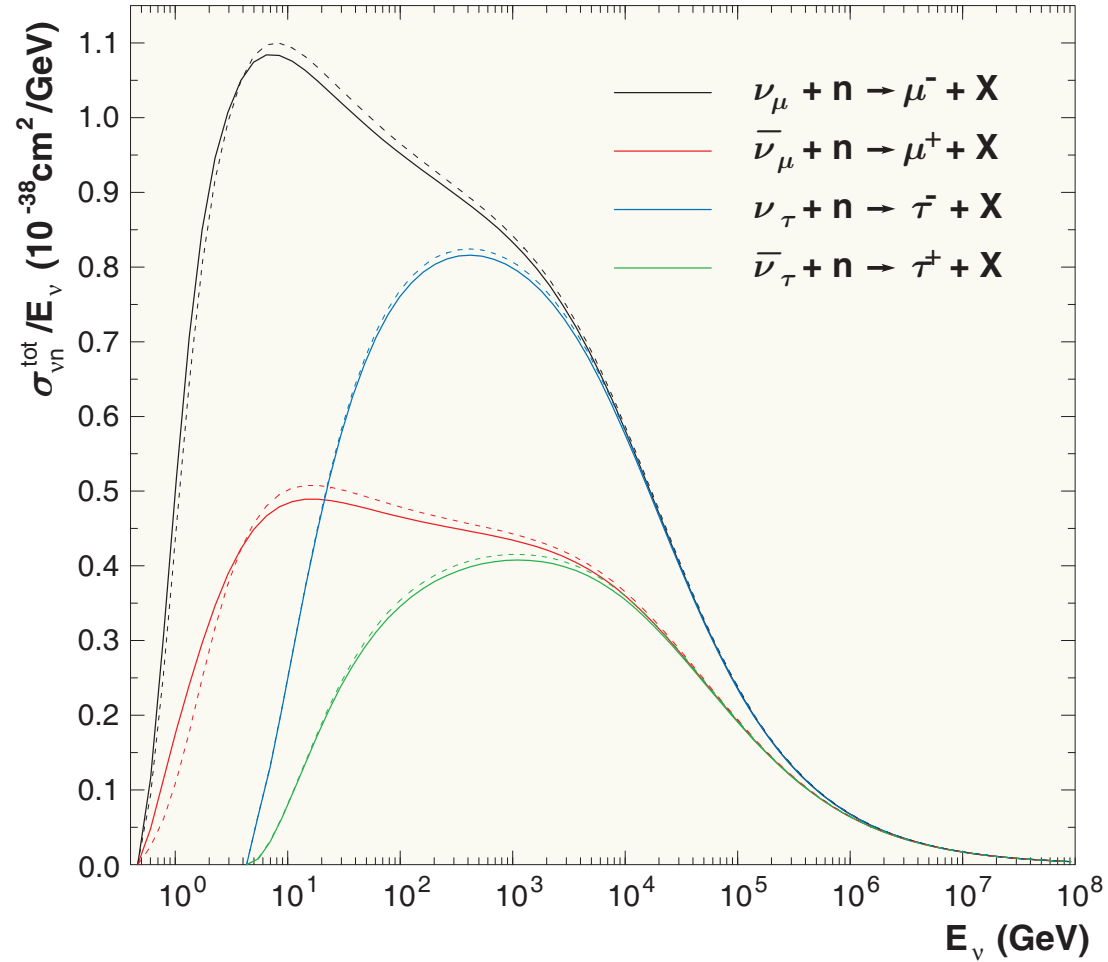


Figure 2: Total inelastic νn cross sections evaluated with the MRST 2002 NNLO PDF model modified according to Bodek–Yang prescription (solid lines) and unmodified (dashed lines).

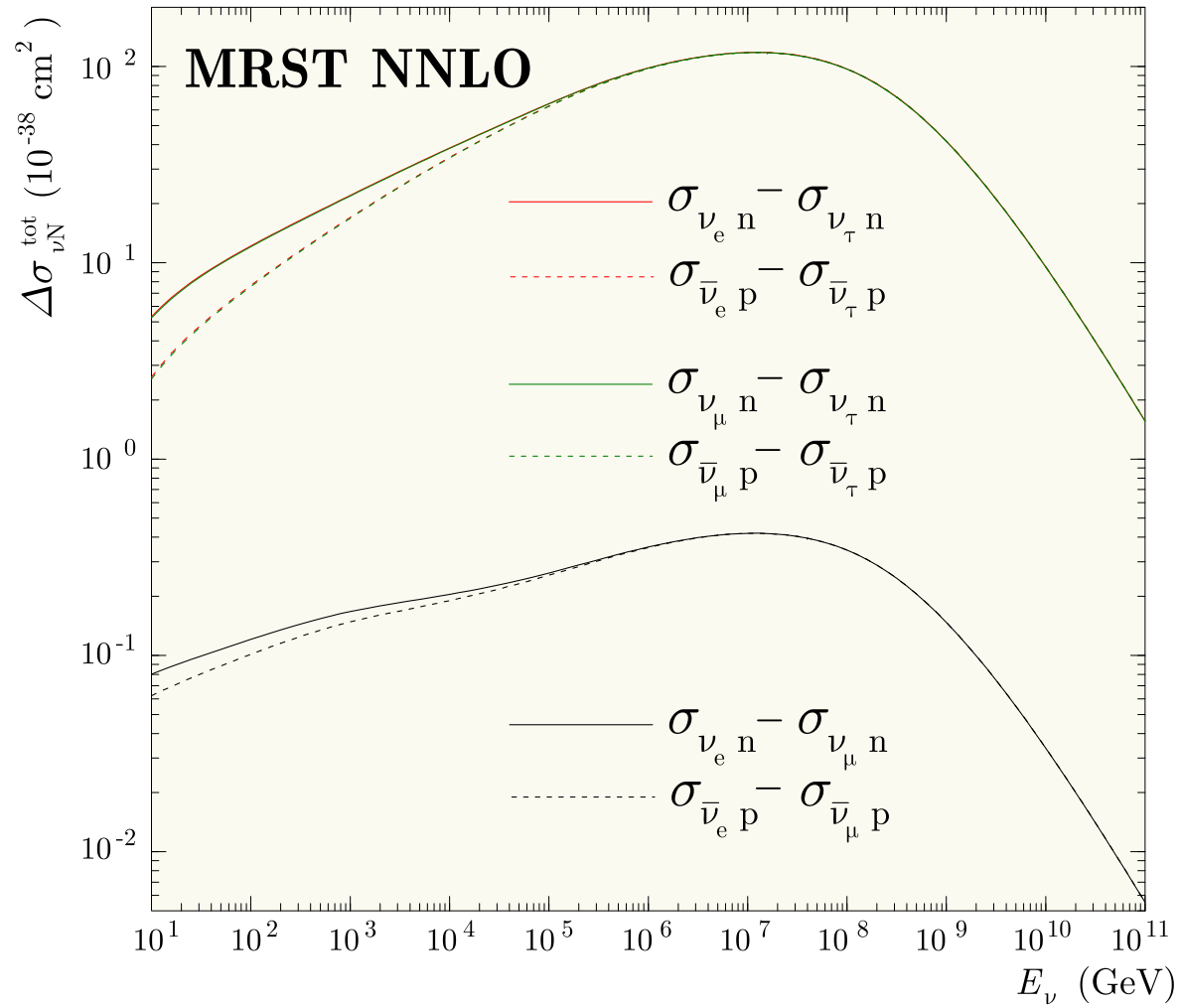


Figure 3: Differences between the total neutrino cross sections for proton and neutron targets evaluated with the MRST 2002 NNLO PDF model.

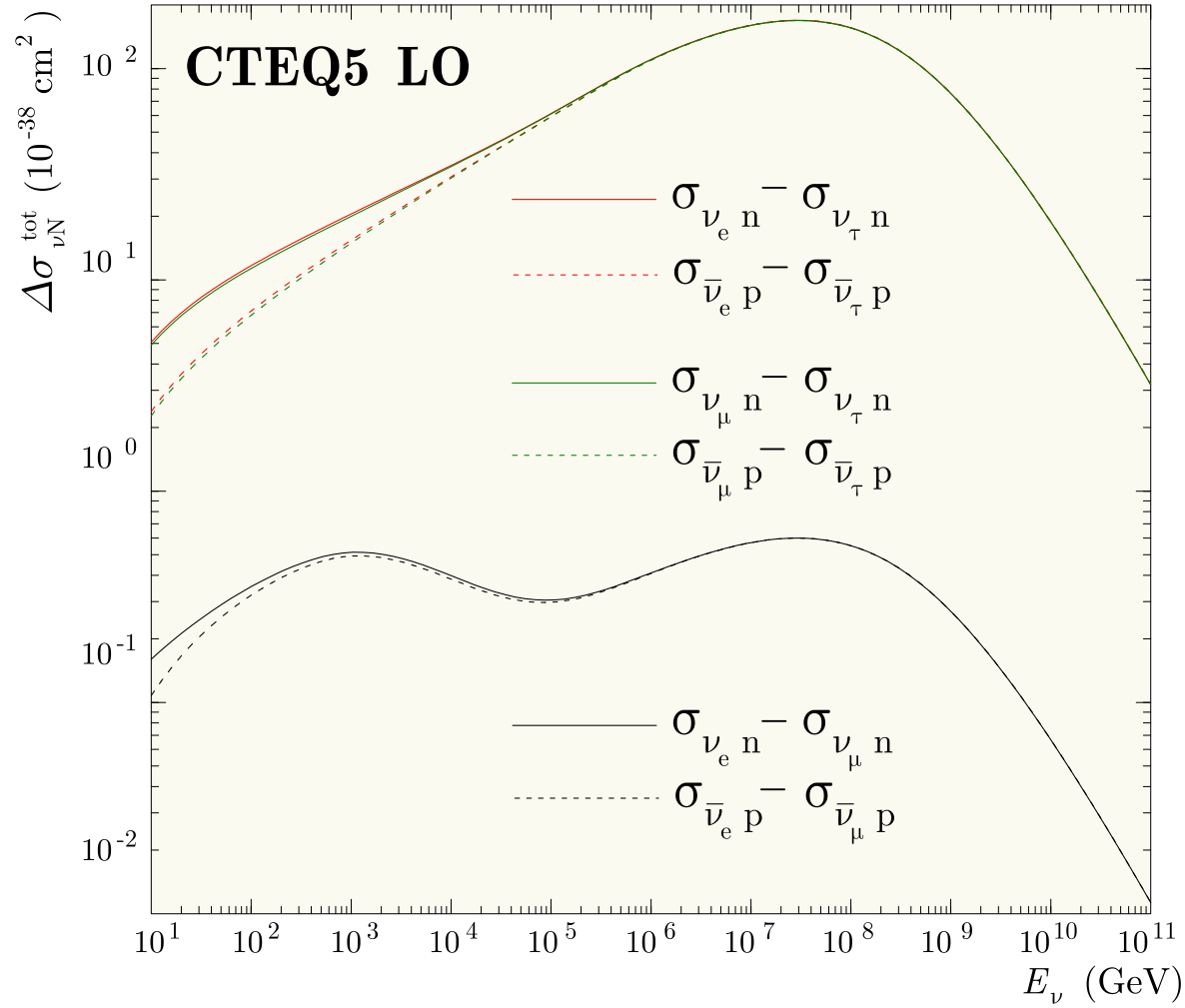


Figure 4: Differences between the total neutrino cross sections for proton and neutron targets evaluated with the CTEQ5-DIS LO PDF model.

4.2.4 Indices of refraction

For $E_\nu \ll \min(m_{W,Z}^2/2m_A)$ and for an electroneutral nonpolarized cold medium, the q_R is **energy independent**. In the leading orders of the standard electroweak theory it is

$$q_R = \begin{cases} \frac{1}{2}V_0 Y_p \rho & \text{for } \alpha = e \text{ and } \beta = \mu \text{ or } \tau, \\ -\frac{1}{2}a_\tau V_0 (Y_p + b_\tau Y_n) \rho & \text{for } \alpha = \mu \text{ and } \beta = \tau, \\ \frac{1}{2}V_0 (Y_p - \frac{1}{2}Y_n) \rho & \text{for } \alpha = e \text{ and } \beta = s, \\ \frac{1}{4}V_0 Y_n \rho & \text{for } \alpha = \mu \text{ or } \tau \text{ and } \beta = s, \end{cases}$$

where

$$V_0 = \sqrt{2}G_F N_0 \simeq 7.63 \times 10^{-14} \text{ eV} \quad \left(L_0 = \frac{2\pi}{V_0} \simeq 1.62 \times 10^4 \text{ km} \sim D_\oplus \right),$$

$$a_\tau = \frac{3\alpha r_\tau [\ln(1/r_\tau) - 1]}{4\pi \sin^2 \theta_W} \simeq 2.44 \times 10^{-5}, \quad b_\tau = \frac{\ln(1/r_\tau) - 2/3}{\ln(1/r_\tau) - 1} \simeq 1.05,$$

α is the fine-structure constant, θ_W is the weak-mixing angle and $r_\tau = (m_\tau/m_W)^2$.

Notes:

- ❖ For an isoscalar medium the $|q_R|$ is of the same order of magnitude for any pair of flavors but $\nu_\mu - \nu_\tau$.
- ❖ For an isoscalar medium $q_R^{(\nu_\mu - \nu_\tau)} / q_R^{(\nu_e - \nu_\mu)} \approx -5 \times 10^{-5}$.

- ❖ For certain regions of a neutron-rich medium the value of $q_R^{(\nu_e-\nu_s)}$ may become vanishingly small. In this case, the one-loop radiative corrections must be taken into account.
- ❖ For very high energies the q_R have to be corrected for the gauge boson propagators and strong-interaction effects.

One can expect $|q_R|$ to be either an energy-independent or decreasing function for any pair of mixed neutrino flavors. On the other hand, there are several cases of much current interest when $|q_I|$ either increases with energy without bound (mixing between active and sterile neutrino states) or has a broad or sharp maximum (as for $\nu_\mu - \nu_\tau$ or $\bar{\nu}_e - \bar{\nu}_\mu$ mixings, respectively).

Numerical estimations suggest that for every of these cases there is an energy range in which q_R and q_I are **comparable in magnitude**. Since $q_R \propto \rho$ and $q_I \propto$ and are dependent upon the composition of the medium (Y_A) there may exist some more specific situations, when

$$|q_R| \sim |q_I| \sim |\Delta|$$

or even

$$|q_R| \sim |\Delta_c| \quad \text{and} \quad |q_I| \sim |\Delta_s|.$$

If this is the case, the refraction, absorption and mixing become interestingly superimposed.

4.2.5 Eigenproblem and mixing matrix in matter

Eigenvalues

The matrix $\mathbf{H}(t)$ has two complex instantaneous eigenvalues, $\varepsilon(t)$ and $-\varepsilon(t)$, with $\varepsilon = \varepsilon_R + i\varepsilon_I$ satisfying the characteristic equation

$$\varepsilon^2 = (q - q_+)(q - q_-),$$

where $q_{\pm} = \Delta_c \pm i\Delta_s = \Delta e^{\pm 2i\theta}$. The solution is

$$\begin{aligned}\varepsilon_R^2 &= \frac{1}{2} (\varepsilon_0^2 - q_I^2) + \frac{1}{2} \sqrt{(\varepsilon_0^2 - q_I^2)^2 + 4q_I^2 (\varepsilon_0^2 - \Delta_s^2)}, \\ \varepsilon_I &= \frac{q_I (q_R - \Delta_c)}{\varepsilon_R} \quad (\text{provided } q_R \neq \Delta_c),\end{aligned}$$

with

$$\varepsilon_0 = \sqrt{\Delta^2 - 2\Delta_c q_R + q_R^2} \geq |\Delta_s|, \quad \text{sign}(\varepsilon_R) \stackrel{\text{def}}{=} \text{sign}(\Delta) \equiv \zeta.$$

(At that choice $\varepsilon = \Delta$ for vacuum and $\varepsilon = \zeta\varepsilon_0$ if $q_I = 0$.)

In the vicinity of the MSW resonance, $q_R = q_R(t_*) = \Delta_c$

$$\begin{aligned}\lim_{q_R \rightarrow \Delta_c \pm 0} \varepsilon_R &= \Delta_s \sqrt{\max(1 - \Delta_I^2/\Delta_s^2, 0)}, \\ \lim_{q_R \rightarrow \Delta_c \pm 0} \varepsilon_I &= \pm \zeta \Delta_I \sqrt{\max(1 - \Delta_s^2/\Delta_I^2, 0)},\end{aligned}$$

where $\Delta_I = q_I(t_*)$. Therefore the resonance value of $|\varepsilon_R|$ (which is inversely proportional to the neutrino oscillation length in matter) is always **smaller** than the conventional MSW value $|\Delta_s|$ and *vanishes* if $\Delta_I^2 < \Delta_s^2$ (ε_I remains finite in this case). In neutrino transition through the region of resonance density $\rho = \rho(t_*)$, ε_I undergoes discontinuous jump while ε_R remains continuous. The corresponding cuts in the q plane are placed outside the circle $|q| \leq |\Delta|$. If $\Delta_I^2 > \Delta_s^2$, the imaginary part of ε vanishes while the real part remains finite.

A distinctive feature of the characteristic equation is the existence of two mutually conjugate “**super-resonance**” points q_{\pm} in which ε vanishes giving rise to the **total degeneracy** of the levels of the system (impossible in the “standard MSW” solution). Certainly, the behavior of the system in the vicinity of these points must be dramatically different from the conventional pattern.

The “**super-resonance**” conditions are physically realizable for various meaningful mixing scenarios.

Some useful relations

$$\varepsilon_R^2 = \frac{2q_I^2 (\varepsilon_0^2 - \Delta_s^2)}{\sqrt{(\varepsilon_0^2 - q_I^2)^2 + 4q_I^2 (\varepsilon_0^2 - \Delta_s^2)} - \varepsilon_0^2 + q_I^2},$$

$$\varepsilon_I = \frac{\sqrt{(\varepsilon_0^2 - q_I^2)^2 + 4q_I^2 (\varepsilon_0^2 - \Delta_s^2)} - \varepsilon_0^2 + q_I^2}{2q_I (q_R - \Delta_c)},$$

$$\frac{\partial \varepsilon_R}{\partial q_R} = \frac{\partial \varepsilon_I}{\partial q_I} = \frac{q_I \varepsilon_I + (q_R - \Delta_c) \varepsilon_R}{\varepsilon_R^2 + \varepsilon_I^2},$$

$$\frac{\partial \varepsilon_I}{\partial q_R} = -\frac{\partial \varepsilon_R}{\partial q_I} = \frac{q_I \varepsilon_R - (q_R - \Delta_c) \varepsilon_I}{\varepsilon_R^2 + \varepsilon_I^2},$$

$$\operatorname{Re} \left[\frac{q(t) - \Delta_c}{\varepsilon} \right] = \left(\frac{q_R - \Delta_c}{\varepsilon_R} \right) \left(\frac{\varepsilon_R^2 + q_I^2}{\varepsilon_R^2 + \varepsilon_I^2} \right),$$

$$\operatorname{Im} \left[\frac{q(t) - \Delta_c}{\varepsilon} \right] = \left(\frac{q_I}{\varepsilon_R} \right) \left(\frac{\varepsilon_R^2 - \varepsilon_0^2 + \Delta_s^2}{\varepsilon_R^2 + \varepsilon_I^2} \right),$$

$$(q_R - \Delta_c)^2 = \varepsilon_0^2 - \Delta_s^2.$$

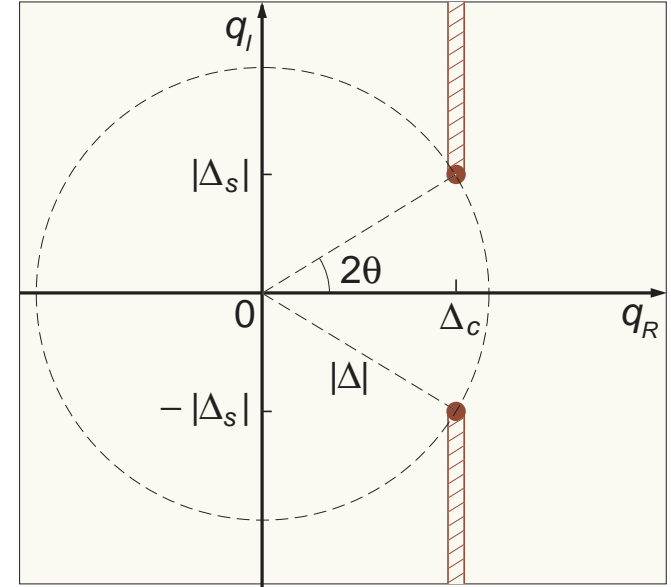


Figure 5: Zeros and cuts of ε in the q plane for $\Delta_c > 0$. The cuts are placed outside the circle $|q| \leq |\Delta|$ parallel to axis $q_R = 0$. The MSW resonance point is $(\Delta_c, 0)$ and the two “super-resonance” points are $(\Delta_c, \pm\Delta_s)$.

Eigenstates

In order to simplify the solution to the eigenstate problem we'll assume that the phase trajectory $q = q(t)$ does not cross the points q_{\pm} at any t . In non-Hermitian quantum dynamics one has to consider the two pairs of instantaneous eigenvectors $|\Psi_{\pm}\rangle$ and $|\bar{\Psi}_{\pm}\rangle$ which obey the relations

$$\mathbf{H}|\Psi_{\pm}\rangle = \pm \varepsilon |\Psi_{\pm}\rangle \quad \text{and} \quad \mathbf{H}^{\dagger}|\bar{\Psi}_{\pm}\rangle = \pm \varepsilon^* |\bar{\Psi}_{\pm}\rangle. \quad (19)$$

and (for $q \neq q_{\pm}$) form a complete biorthogonal and biorthonormal set,

$$\langle \bar{\Psi}_{\pm} | \Psi_{\pm} \rangle = 1, \quad \langle \bar{\Psi}_{\pm} | \Psi_{\mp} \rangle = 0, \quad |\Psi_{+}\rangle \langle \bar{\Psi}_{+}| + |\Psi_{-}\rangle \langle \bar{\Psi}_{-}| = \mathbf{1}.$$

Therefore, the eigenvectors are defined up to a gauge transformation

$$|\Psi_{\pm}\rangle \mapsto e^{if_{\pm}} |\Psi_{\pm}\rangle, \quad |\bar{\Psi}_{\pm}\rangle \mapsto e^{-if_{\pm}^*} |\bar{\Psi}_{\pm}\rangle,$$

with **arbitrary complex functions** $f_{\pm}(t)$ such that $\text{Im}(f_{\pm})$ vanish as $q = 0$.^a Thus it is sufficient to find any particular solution of Eqs. (19). Taking into account that $\mathbf{H}^{\dagger} = \mathbf{H}^*$, we may set $|\bar{\Psi}_{\pm}\rangle = |\Psi_{\pm}^*\rangle$ and hence the eigenvectors can be found from the identity

$$\mathbf{H} = \varepsilon |\Psi_{+}\rangle \langle \Psi_{+}^*| - \varepsilon |\Psi_{-}\rangle \langle \Psi_{-}^*|.$$

^aFor our aims, the class of the gauge functions may be restricted without loss of generality by the condition $f_{\pm}|_{q=0} = 0$.

Setting $|\Psi_{\pm}\rangle = (v_{\pm}, \pm v_{\mp})^T$ we arrive at the equations

$$v_{\pm}^2 = \frac{\varepsilon \pm (q - \Delta_c)}{2\varepsilon}, \quad v_+ v_- = \frac{\Delta_s}{2\varepsilon},$$

a particular solution of which can be written as

$$v_+ = \sqrt{\left| \frac{\varepsilon + q - \Delta_c}{2\varepsilon} \right|} e^{i(\varphi - \psi)/2},$$

$$v_- = \zeta \sqrt{\left| \frac{\varepsilon - q + \Delta_c}{2\varepsilon} \right|} e^{i(-\varphi - \psi)/2}.$$

where

$$\varphi = \arg(\varepsilon + q - \Delta_c) = -\arg(\varepsilon - q + \Delta_c) = \arctan\left(\frac{q_I}{\varepsilon_R}\right),$$

$$\psi = \arg(\varepsilon) = \arctan\left(\frac{\varepsilon_I}{\varepsilon_R}\right),$$

and we have fixed the remaining gauge ambiguity by a comparison with the vacuum case.

Mixing angle in matter

It may be sometimes useful to define the complex mixing angle in matter $\Theta = \Theta_R + i\Theta_I$ by the relations

$$\sin \Theta = v_+ \quad \text{and} \quad \cos \Theta = v_-$$

or, equivalently,

$$\sin 2\Theta = \frac{\Delta_s}{\varepsilon}, \quad \cos 2\Theta = \frac{\Delta_c - q}{\varepsilon},$$

The real and imaginary parts of Θ are found to be

$$\begin{aligned} \text{Re}(\Theta) \equiv \Theta_R &= \frac{1}{2} \arctan \left[\frac{(q_I - \Delta_s) \varepsilon_R - (q_R - \Delta_c) \varepsilon_I}{(q_R - \Delta_c) \varepsilon_R + (q_I - \Delta_s) \varepsilon_I} \right], \\ \text{Im}(\Theta) \equiv \Theta_I &= \frac{1}{4} \ln \left[\frac{\varepsilon_R^2 + \varepsilon_I^2}{(q_R - \Delta_c)^2 + (q_I - \Delta_s)^2} \right]. \end{aligned}$$

$$\begin{aligned} \cos \Theta &= \cos \Theta_R \cosh \Theta_I - i \sin \Theta_R \sinh \Theta_I, \\ \sin \Theta &= \sin \Theta_R \cosh \Theta_I + i \cos \Theta_R \sinh \Theta_I. \end{aligned}$$

Having regard to the prescription for the sign of ε_R , one can verify that $\Theta = \theta$ if $q = 0$ (vacuum case) and $\Theta = 0$ if $\Delta_s = 0$ (no mixing or $m_1^2 = m_2^2$). It is also clear that Θ becomes the standard MSW mixing angle with $\text{Im}(\Theta) = 0$ when $q_I = 0$ ($\Lambda_\alpha = \Lambda_\beta$).

Mixing matrix in matter

In order to build up the solution to ME for the nondegenerated case one has to diagonalize the Hamiltonian. Generally a non-Hermitian matrix cannot be diagonalized by a single unitary transformation. But in our simple case this can be done by a complex orthogonal matrix (extended mixing matrix in matter)

$$\mathbf{U}_f = \mathbf{U} \exp(i\mathbf{f}),$$

where $\mathbf{f} = \text{diag}(f_-, f_+)$ and

$$\mathbf{U} = (|\Psi_-\rangle, |\Psi_+\rangle) = \begin{pmatrix} v_- & v_+ \\ -v_+ & v_- \end{pmatrix} = \begin{pmatrix} \cos \Theta & \sin \Theta \\ -\sin \Theta & \cos \Theta \end{pmatrix}.$$

Properties of \mathbf{U} :

$$\mathbf{U}^T \mathbf{H} \mathbf{U} = \text{diag}(-\varepsilon, \varepsilon), \quad \mathbf{U}^T \mathbf{U} = \mathbf{1}, \quad \mathbf{U}|_{q=0} = \mathbf{V}.$$

From CE it follows that

$$\partial\varepsilon/\partial q = (q - \Delta_c)/\varepsilon$$

and thus

$$\frac{\partial v_{\pm}}{\partial q} = \pm \frac{\Delta_s^2 v_{\mp}}{2\varepsilon^2}.$$

We therefore have

$$i\mathbf{U}^T \dot{\mathbf{U}} = -\Omega \begin{pmatrix} 0 & -i \\ i & 0 \end{pmatrix} = -\Omega \boldsymbol{\sigma}_2,$$

where

$$\Omega = \frac{\dot{q}\Delta_s}{2\varepsilon^2} = \frac{i}{4} \frac{d}{dt} \ln \left(\frac{q - q_+}{q - q_-} \right).$$

Properties of \mathbf{U}_f :

$$\begin{aligned} \mathbf{U}_f^T \mathbf{H} \mathbf{U}_f &= \text{diag}(-\varepsilon, \varepsilon), \quad \mathbf{U}_f^T \mathbf{U}_f = \mathbf{1}, \quad \mathbf{U}_f|_{q=0} = \mathbf{V}, \\ i\mathbf{U}_f^T \dot{\mathbf{U}}_f &= -\Omega e^{-if} \boldsymbol{\sigma}_2 e^{if} - \dot{\mathbf{f}}. \end{aligned}$$

4.2.6 Adiabatic solution

Formal solution to ME in the most general form:

$$\tilde{\mathbf{S}}(t) = \mathbf{U}_f(t) \exp[-i\Phi(t)] \mathbf{X}_f(t) \mathbf{U}_f^T(0). \quad (20)$$

Here $\Phi(t) = \text{diag}(-\Phi(t), \Phi(t))$ and $\Phi(t) = \Phi_R(t) + i\Phi_I(t)$ is the complex dynamical phase, defined by

$$\Phi_R(t) = \int_0^t \varepsilon_R(t') dt', \quad \Phi_I(t) = \int_0^t \varepsilon_I(t') dt',$$

and $\mathbf{X}_f(t)$ must satisfy the equation

$$i\dot{\mathbf{X}}_f(t) = \left[\Omega(t)e^{-i\mathbf{f}(t)} \mathbf{F}(t)e^{i\mathbf{f}(t)} + \dot{\mathbf{f}}(t) \right] \mathbf{X}_f(t), \quad \mathbf{X}_f(0) = \mathbf{1},$$

where

$$\mathbf{F}(t) = e^{i\Phi(t)} \boldsymbol{\sigma}_2 e^{-i\Phi(t)} = \begin{pmatrix} 0 & -ie^{-2i\Phi(t)} \\ ie^{2i\Phi(t)} & 0 \end{pmatrix}.$$

It can be proved now that the right side of Eq. (20) is gauge-invariant i.e. it **does not depend** on the unphysical complex phases $f_{\pm}(t)$. This crucial fact is closely related to the absence of the Abelian topological phases in the system under consideration.

Finally, we can put $f_{\pm} = 0$ in Eq. (20) and the result is

$$\tilde{\mathbf{S}}(t) = \mathbf{U}(t) \exp[-i\Phi(t)] \mathbf{X}(t) \mathbf{U}^T(0), \quad (21a)$$

$$i\dot{\mathbf{X}}(t) = \Omega(t)\mathbf{F}(t)\mathbf{X}(t), \quad \mathbf{X}(0) = \mathbf{1}. \quad (21b)$$

These equations, being equivalent to the ME, have nevertheless a restricted range of practical usage on account of poles and cuts as well as decaying and increasing exponents in the “Hamiltonian” $\Omega\mathbf{F}$.

Adiabatic theorem

The adiabatic theorem of Hermitian quantum mechanics can almost straightforwardly be extended to ME under the requirements:

- (a) the potential q is a sufficiently smooth and slow function of t ;
- (b) the imaginary part of the dynamical phase is a bounded function i.e.
 $\lim_{t \rightarrow \infty} |\Phi_I(t)|$ is finite;

- (c) the phase trajectory $q = q(t)$ is placed far from the singularities for any t .

The first requirement breaks down for a condensed medium with a sharp boundary or layered structure (like the Earth). If however the requirement (a) is valid inside each layer (t_i, t_{i+1}) , the problem reduces to Eqs. (21) by applying the rule

$$\tilde{\mathbf{S}}(t) \equiv \tilde{\mathbf{S}}(t, 0) = \tilde{\mathbf{S}}(t, t_n) \dots \tilde{\mathbf{S}}(t_2, t_1) \tilde{\mathbf{S}}(t_1, 0),$$

where $\tilde{\mathbf{S}}(t_{i+1}, t_i)$ is the time-evolution operator for the i -th layer.

The requirement (b) alone is not too restrictive considering that for many astrophysical objects (like stars, galactic nuclei, jets and so on) the density ρ exponentially disappears to the periphery and, on the other hand, $\varepsilon_I \rightarrow 0$ as $\rho \rightarrow 0$. In this instance, the function $\Phi_I(t)$ must be t independent for sufficiently large t . But, in the case of a steep density profile, the requirements (a) and (b) may be inconsistent.

The important case of violation of the requirement (c) is the subject of a special study which is beyond the scope of this study.

It is interesting to note in this connection that, in the Hermitian case, a general adiabatic theorem has been proved without the traditional gap condition [J. E. Avron and A. Elgart, Commun. Math. Phys. **203** (1999) 445].

The solution

Presume that all necessary conditions do hold for $0 \leq t \leq T$. Then, in the adiabatic limit, we can put $\Omega = 0$ in Eq. (21b). Therefore $\mathbf{X} = \mathbf{1}$ and Eq. (21a) yields

$$\begin{aligned}\tilde{S}_{\alpha\alpha}(t) &= v_+(0)v_+(t)e^{-i\Phi(t)} + v_-(0)v_-(t)e^{i\Phi(t)}, \\ \tilde{S}_{\alpha\beta}(t) &= v_-(0)v_+(t)e^{-i\Phi(t)} - v_+(0)v_-(t)e^{i\Phi(t)}, \\ \tilde{S}_{\beta\alpha}(t) &= v_+(0)v_-(t)e^{-i\Phi(t)} - v_-(0)v_+(t)e^{i\Phi(t)}, \\ \tilde{S}_{\beta\beta}(t) &= v_-(0)v_-(t)e^{-i\Phi(t)} + v_+(0)v_+(t)e^{i\Phi(t)},\end{aligned}$$

Taking into account Eq. (18) we obtain the survival and transition probabilities:

$$\begin{aligned}
P_{\alpha\alpha}(t) &= A(t) \left\{ \left[I_+^+(t)e^{\Phi_I(t)} + I_-^-(t)e^{-\Phi_I(t)} \right]^2 - I^2(t) \sin^2 [\Phi_R(t) - \varphi_+(t)] \right\}, \\
P_{\alpha\beta}(t) &= A(t) \left\{ \left[I_+^-(t)e^{\Phi_I(t)} - I_-^+(t)e^{-\Phi_I(t)} \right]^2 + I^2(t) \sin^2 [\Phi_R(t) - \varphi_-(t)] \right\}, \\
P_{\beta\alpha}(t) &= A(t) \left\{ \left[I_-^+(t)e^{\Phi_I(t)} - I_+^-(t)e^{-\Phi_I(t)} \right]^2 + I^2(t) \sin^2 [\Phi_R(t) + \varphi_-(t)] \right\}, \\
P_{\beta\beta}(t) &= A(t) \left\{ \left[I_-^-(t)e^{\Phi_I(t)} + I_+^+(t)e^{-\Phi_I(t)} \right]^2 - I^2(t) \sin^2 [\Phi_R(t) + \varphi_+(t)] \right\},
\end{aligned} \tag{22}$$

where we have denoted for compactness

$$\begin{aligned}
I_\zeta^{\zeta'}(t) &= |v_\zeta(0)v_{\zeta'}(t)| \quad (\zeta, \zeta' = \pm), \\
\varphi_\pm(t) &= \frac{\varphi(0) \pm \varphi(t)}{2}, \\
I^2(t) &= 4I_+^+(t)I_-^-(t) = 4I_+^-(t)I_-^+(t) = \frac{\Delta_s^2}{|\varepsilon(0)\varepsilon(t)|}.
\end{aligned}$$

Limiting cases

In the event that the conditions

$$\left| \frac{1}{\Lambda_\beta(t)} - \frac{1}{\Lambda_\alpha(t)} \right| \ll 4\varepsilon_0(t) \quad \text{and} \quad t \ll \min [\Lambda_\alpha(t), \Lambda_\beta(t)]$$

are satisfied for any $t \in [0, T]$, the formulas (22) reduce to the standard MSW adiabatic solution

$$\left. \begin{aligned} P_{\alpha\alpha}(t) = P_{\beta\beta}(t) &= \frac{1}{2} [1 + J(t)] - I_0^2(t) \sin^2 [\Phi_0(t)], \\ P_{\alpha\beta}(t) = P_{\beta\alpha}(t) &= \frac{1}{2} [1 - J(t)] + I_0^2(t) \sin^2 [\Phi_0(t)], \end{aligned} \right\} \quad (\text{MSW})$$

where

$$J(t) = \frac{\Delta^2 - \Delta_c [q_R(0) + q_R(t)] + q_R(0)q_R(t)}{\varepsilon_0(0)\varepsilon_0(t)},$$

$$I_0^2(t) = \frac{\Delta_s^2}{\varepsilon_0(0)\varepsilon_0(t)}, \quad \Phi_0(t) = \int_0^t \varepsilon_0(t') dt'.$$

Needless to say either of the above conditions or both may be violated for sufficiently high neutrino energies and/or for thick media, resulting in radical differences between the two solutions. These differences are of obvious interest to high-energy neutrino astrophysics.

It is perhaps even more instructive to examine the distinctions between the general adiabatic solution (22) and its “classical limit”

$$\left. \begin{aligned} P_{\alpha\alpha}(t) &= \exp \left[- \int_0^t \frac{dt'}{\Lambda_\alpha(t')} \right], & P_{\alpha\beta}(t) &= 0, \\ P_{\beta\beta}(t) &= \exp \left[- \int_0^t \frac{dt'}{\Lambda_\beta(t')} \right], & P_{\beta\alpha}(t) &= 0, \end{aligned} \right\} \quad (\Delta_s = 0)$$

which takes place either in the absence of mixing or for $m_1^2 = m_2^2$.

Note:

Considering that $\Omega \propto \Delta_s$, the classical limit is the exact solution to the master equation (for $\Delta_s = 0$). Therefore it can be derived directly from Eq. (17). To make certain that the adiabatic solution has correct classical limit, the following relations are useful:

$$\lim_{\Delta_s \rightarrow 0} \varepsilon(t) = \zeta \zeta_R [q(t) - \Delta_c] \quad \text{and} \quad \lim_{\Delta_s \rightarrow 0} |v_\pm(t)|^2 = \frac{1}{2} (\zeta \zeta_R \pm 1),$$

where $\zeta_R = \text{sign} [q_R(t) - \Delta_c]$.

4.2.7 Matter of constant density and composition

In this simple case, the adiabatic approximation becomes **exact** and thus free from the above-mentioned conceptual difficulties. For definiteness sake we assume $\Lambda_\alpha < \Lambda_\beta$ (and thus $q_I < 0$) from here. The opposite case can be considered in a similar way. Let's denote

$$\frac{1}{\Lambda_\pm} = \frac{1}{2} \left(\frac{1}{\Lambda_\alpha} + \frac{1}{\Lambda_\beta} \right) \pm \frac{\xi}{2} \left(\frac{1}{\Lambda_\alpha} - \frac{1}{\Lambda_\beta} \right),$$

$$I_\pm^2 = \frac{1}{4} \left(1 + \frac{\varepsilon_0^2 + q_I^2 - \Delta_s^2}{\varepsilon_R^2 + \varepsilon_I^2} \right) \pm \frac{\xi}{2} \left(\frac{\varepsilon_R^2 + q_I^2}{\varepsilon_R^2 + \varepsilon_I^2} \right),$$

$$L = \frac{\pi}{|\varepsilon_R|} \quad \text{and} \quad \xi = \left| \frac{q_R - \Delta_c}{\varepsilon_R} \right|.$$

As is easy to see,

$$I_\pm^\pm = \begin{cases} I_\pm & \text{if } \text{sign}(q_R - \Delta_c) = +\zeta, \\ I_\mp & \text{if } \text{sign}(q_R - \Delta_c) = -\zeta, \end{cases}$$

$$I_+^- = I_-^+ = \sqrt{I_+ I_-} = \frac{I}{2} = \left| \frac{\Delta_s}{2\varepsilon} \right| \quad \text{and} \quad \text{sign}(\varphi) = -\zeta.$$

By applying these identities the neutrino oscillation probabilities can be written as

$$\begin{aligned}
 P_{\alpha\alpha}(t) &= \left(I_+ e^{-t/2\Lambda_+} + I_- e^{-t/2\Lambda_-} \right)^2 - I^2 e^{-t/\Lambda} \sin^2 \left(\frac{\pi t}{L} + |\varphi| \right), \\
 P_{\beta\beta}(t) &= \left(I_- e^{-t/2\Lambda_+} + I_+ e^{-t/2\Lambda_-} \right)^2 - I^2 e^{-t/\Lambda} \sin^2 \left(\frac{\pi t}{L} - |\varphi| \right), \\
 P_{\alpha\beta}(t) &= P_{\beta\alpha}(t) = \frac{1}{4} I^2 \left(e^{-t/2\Lambda_-} - e^{-t/2\Lambda_+} \right)^2 + I^2 e^{-t/\Lambda} \sin^2 \left(\frac{\pi t}{L} \right).
 \end{aligned}$$

The difference between the survival probabilities for ν_α and ν_β is

$$\begin{aligned}
 P_{\alpha\alpha}(t) - P_{\beta\beta}(t) &= -\zeta \operatorname{Re} \left(\frac{q - \Delta_c}{\varepsilon} \right) \left(e^{-t/2\Lambda_-} - e^{-t/2\Lambda_+} \right) \\
 &\quad + I^2 e^{-t/\Lambda} \sin \varphi \sin \left(\frac{2\pi t}{L} \right).
 \end{aligned}$$

Case $|q| \gtrsim |\Delta_s|$

Let's examine the case when Λ_+ and Λ_- are vastly different in magnitude. This will be true when $\Lambda_\beta \gg \Lambda_\alpha$ and the factor ξ is not too small. The second condition holds if q_R is away from the MSW resonance value Δ_c and the following dimensionless parameter

$$\varkappa = \frac{\Delta_s}{|q|} \approx 0.033 \times \sin 2\theta \left(\frac{\Delta m^2}{10^{-3} \text{ eV}^2} \right) \left(\frac{100 \text{ GeV}}{E_\nu} \right) \left(\frac{V_0}{|q|} \right)$$

is **sufficiently small**. In fact we assume $|\varkappa| \lesssim 1$ and impose no specific restriction for the ratio q_R/q_I . This spans several possibilities:

- ★ small Δm^2 ,
- ★ small mixing angle,
- ★ high energy,
- ★ high matter density.

The last two possibilities are of special interest because the inequality $|\varkappa| \lesssim 1$ may be fulfilled for a wide range of the mixing parameters Δm^2 and θ by changing E_ν and/or ρ . In other words, this condition is by no means artificial or too restrictive.

After elementary while a bit tedious calculations we obtain

$$\xi = 1 - \frac{1}{2}\varkappa^2 + \mathcal{O}(\varkappa^3), \quad I^2 = \varkappa^2 + \mathcal{O}(\varkappa^3),$$
$$I_+ = 1 + \mathcal{O}(\varkappa^2), \quad I_- = \frac{1}{4}\varkappa^2 + \mathcal{O}(\varkappa^3);$$

$$\Lambda \approx 2\Lambda_\alpha,$$

$$\Lambda_+ \approx \left(1 + \frac{\varkappa^2}{4}\right) \Lambda_\alpha \approx \Lambda_\alpha,$$

$$\Lambda_- \approx \left(\frac{4}{\varkappa^2}\right) \Lambda_\alpha \gg \Lambda_\alpha.$$

Due to the wide spread among the length/time scales Λ_\pm , Λ and L as well as among the amplitudes I_\pm and I , the regimes of neutrino oscillations are quite diverse for different ranges of variable t .

With reference to Figs. 6–9, one can see a regular gradation from slow (at $t \lesssim \Lambda_\mu$) to very fast (at $t \gtrsim \Lambda_\mu$) neutrino oscillations followed by the asymptotic nonoscillatory behavior:

$$P_{\mu\mu}(t) \simeq \frac{\varkappa^4}{16} e^{-t/\Lambda_-},$$

$$P_{ss}(t) \simeq e^{-t/\Lambda_-},$$

$$P_{\mu s}(t) = P_{s\mu}(t) \simeq \frac{\varkappa^2}{4} e^{-t/\Lambda_-}.$$

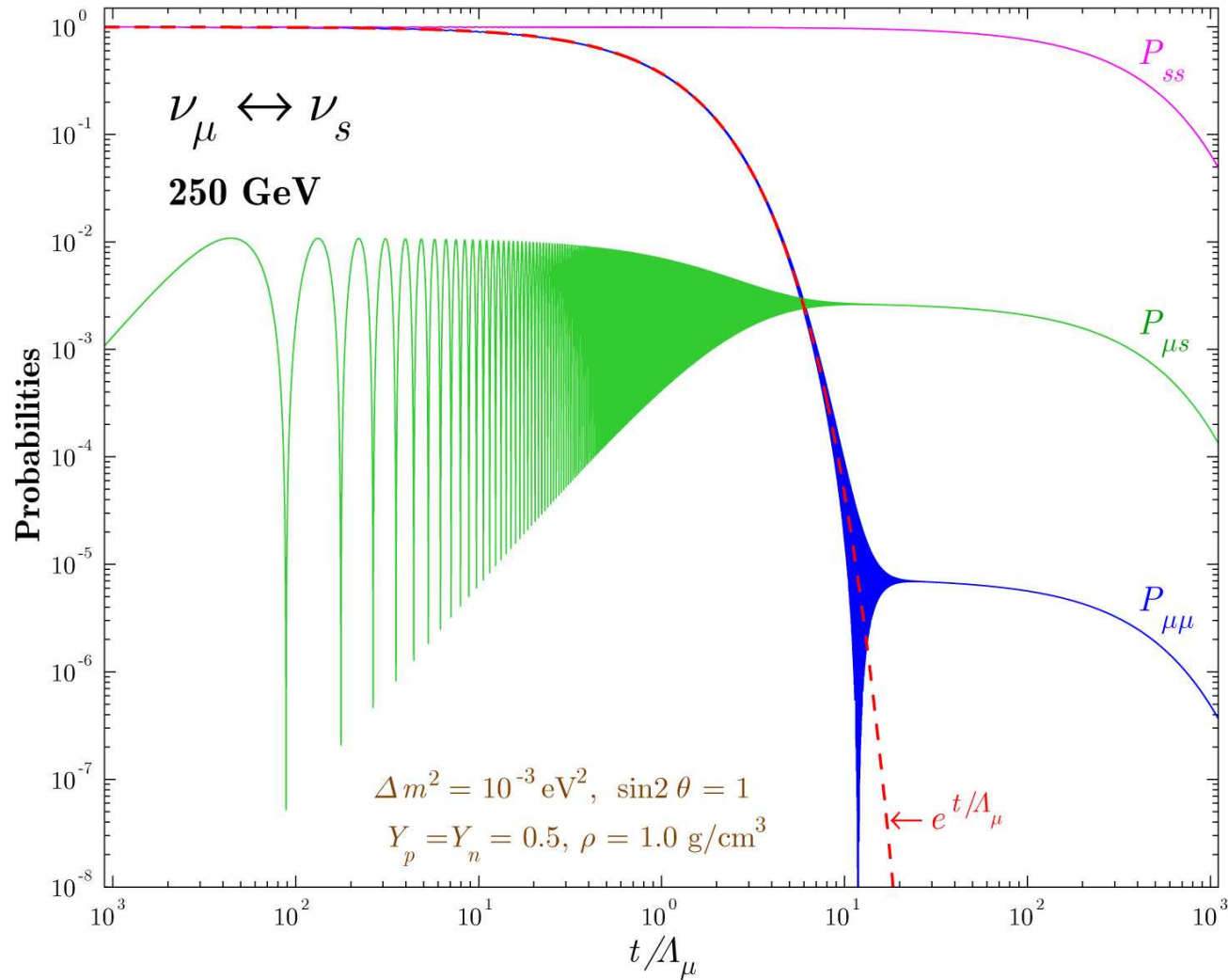


Figure 6: Survival and transition probabilities for $\nu_\mu \leftrightarrow \nu_s$ oscillations ($E_\nu = 250 \text{ GeV}$, $\rho = 1 \text{ g/cm}^3$).

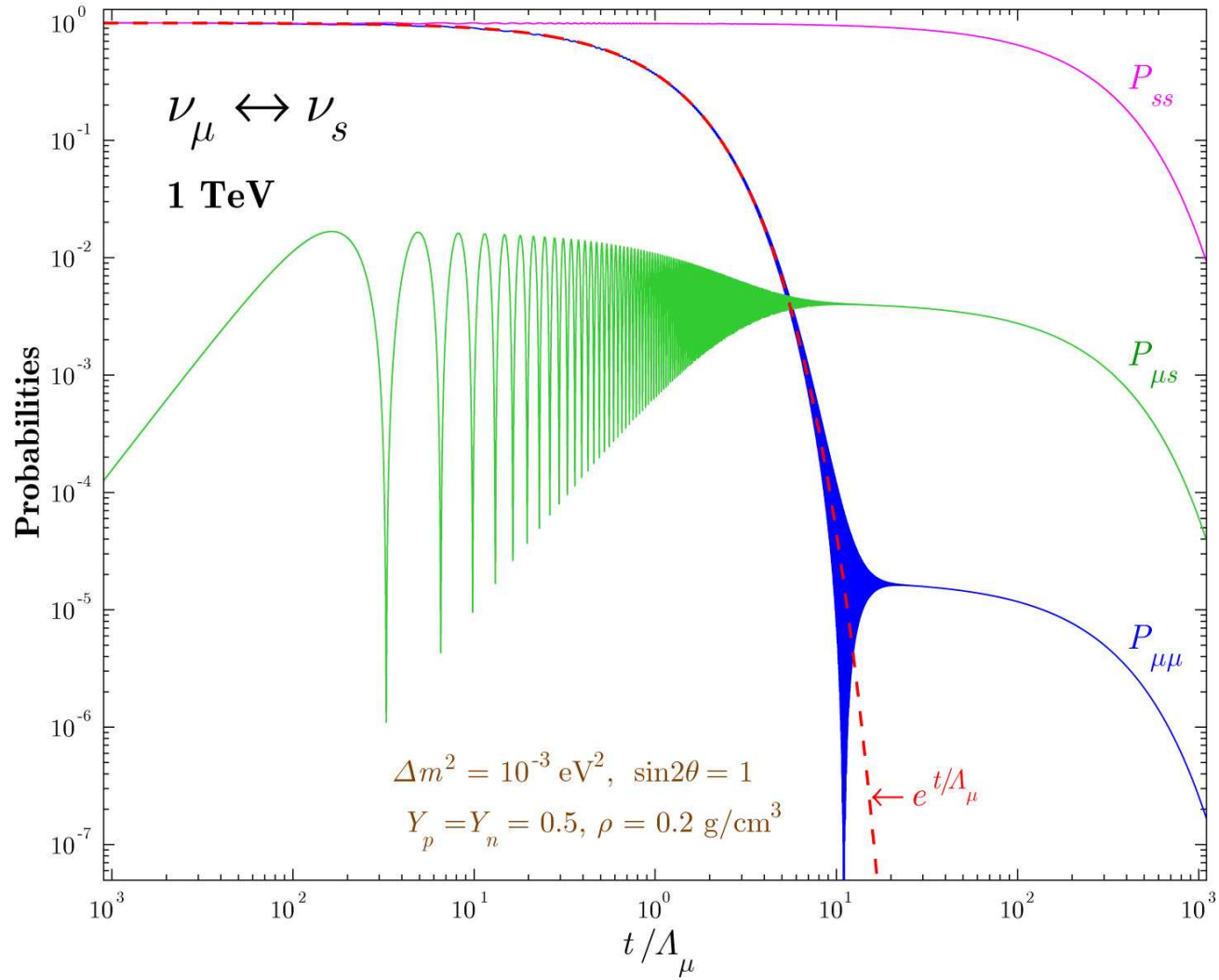


Figure 7: Survival and transition probabilities for $\nu_\mu \leftrightarrow \nu_s$ oscillations ($E_\nu = 1000 \text{ GeV}$, $\rho = 0.2 \text{ g/cm}^3$).

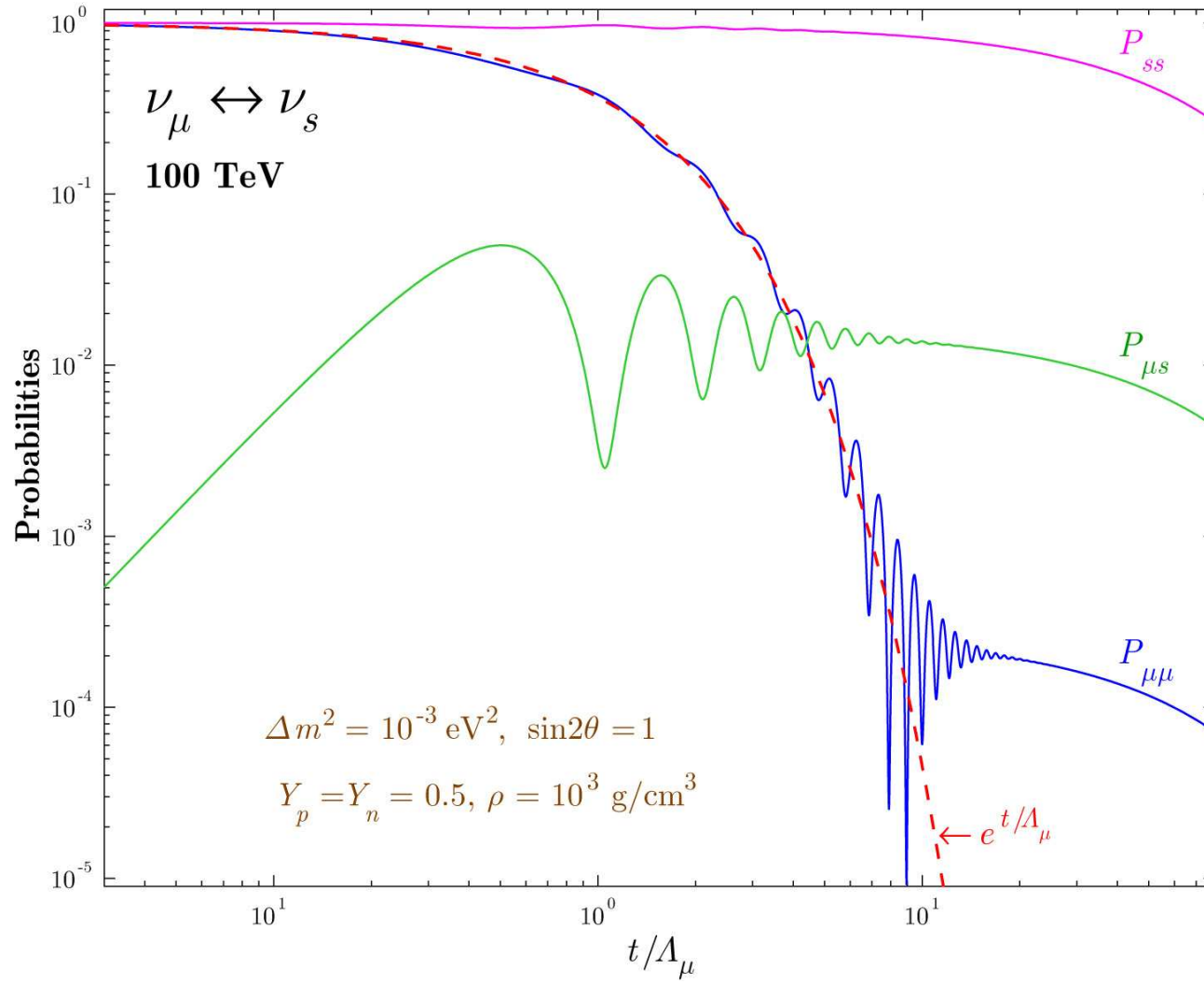


Figure 8: Survival and transition probabilities for $\nu_\mu \leftrightarrow \nu_s$ oscillations ($E_\nu = 100 \text{ TeV}$, $\rho = 10^{-3} \text{ g/cm}^3$).

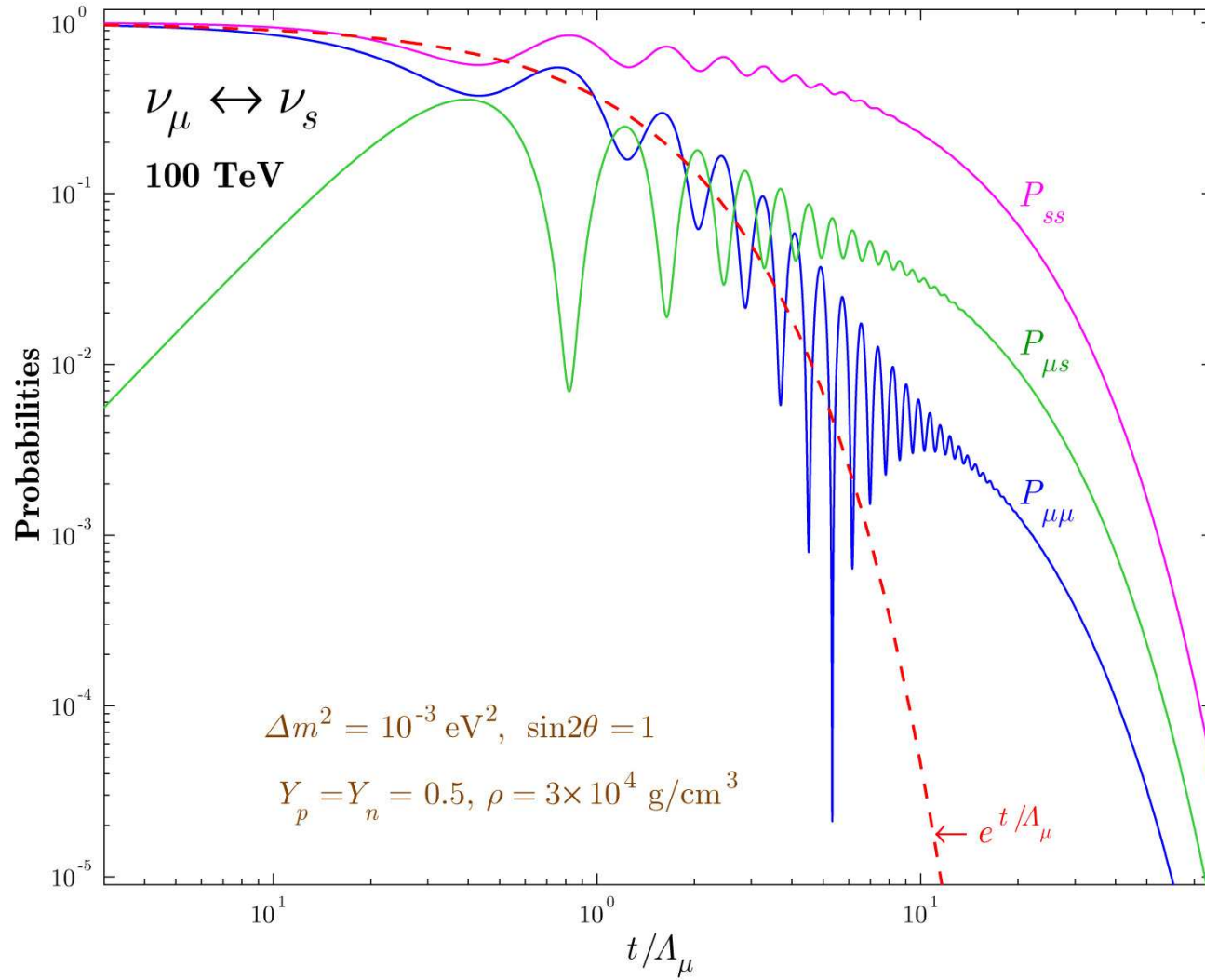


Figure 9: Survival and transition probabilities for $\nu_\mu \leftrightarrow \nu_s$ oscillations ($E_\nu = 100 \text{ TeV}$, $\rho = 3 \times 10^{-4} \text{ g/cm}^3$).

Degenerate case

The consideration must be completed for the case of degeneracy. Due to the condition $q_I < 0$, the density and composition of the “degenerate environment” are fine-tuned in such a way that $q = q_{-\zeta} = \Delta_c - i|\Delta_s|$. The simplest way is in coming back to the master equation. Indeed, in the limit of $q = q_{-\zeta}$, the Hamiltonian reduces to

$$\mathbf{H} = |\Delta_s| \begin{pmatrix} -i & \zeta \\ \zeta & i \end{pmatrix} \equiv |\Delta_s| \mathbf{h}_\zeta.$$

Considering that $\mathbf{h}_\zeta^2 = \mathbf{0}$, we promptly arrive at the solution of ME:

$$\tilde{\mathbf{S}}(t) = \mathbf{1} - it |\Delta_s| \mathbf{h}_\zeta$$

and thus

$$\begin{aligned} P_{\alpha\alpha}(t) &= (1 - |\Delta_s|t)^2 e^{-t/\Lambda}, \\ P_{\beta\beta}(t) &= (1 + |\Delta_s|t)^2 e^{-t/\Lambda}, \\ P_{\alpha\beta}(t) &= P_{\beta\alpha}(t) = (\Delta_s t)^2 e^{-t/\Lambda}. \end{aligned}$$

Since $1/\Lambda_\beta = 1/\Lambda_\alpha - 4|\Delta_s|$, the necessary condition for the total degeneration is $4\Lambda_\alpha |\Delta_s| \leq 1$ and thus $1/\Lambda = 1/\Lambda_\alpha - 2|\Delta_s| \geq 2|\Delta_s|$. The equality only occurs when ν_β is sterile.

The degenerate solution must be compared with the standard MSW solution

$$\left. \begin{aligned} P_{\alpha\alpha}(t) = P_{ss}(t) &= \frac{1}{2} [1 + \cos(2\Delta_s t)], \\ P_{\alpha s}(t) = P_{s\alpha}(t) &= \frac{1}{2} [1 - \cos(2\Delta_s t)], \end{aligned} \right\} \quad (\text{MSW})$$

and with the classical penetration coefficient

$$\exp(-t/\Lambda_\alpha)$$

(with $1/\Lambda_\alpha$ numerically equal to $4|\Delta_s|$) relevant to the transport of unmixed active neutrinos through the same environment.

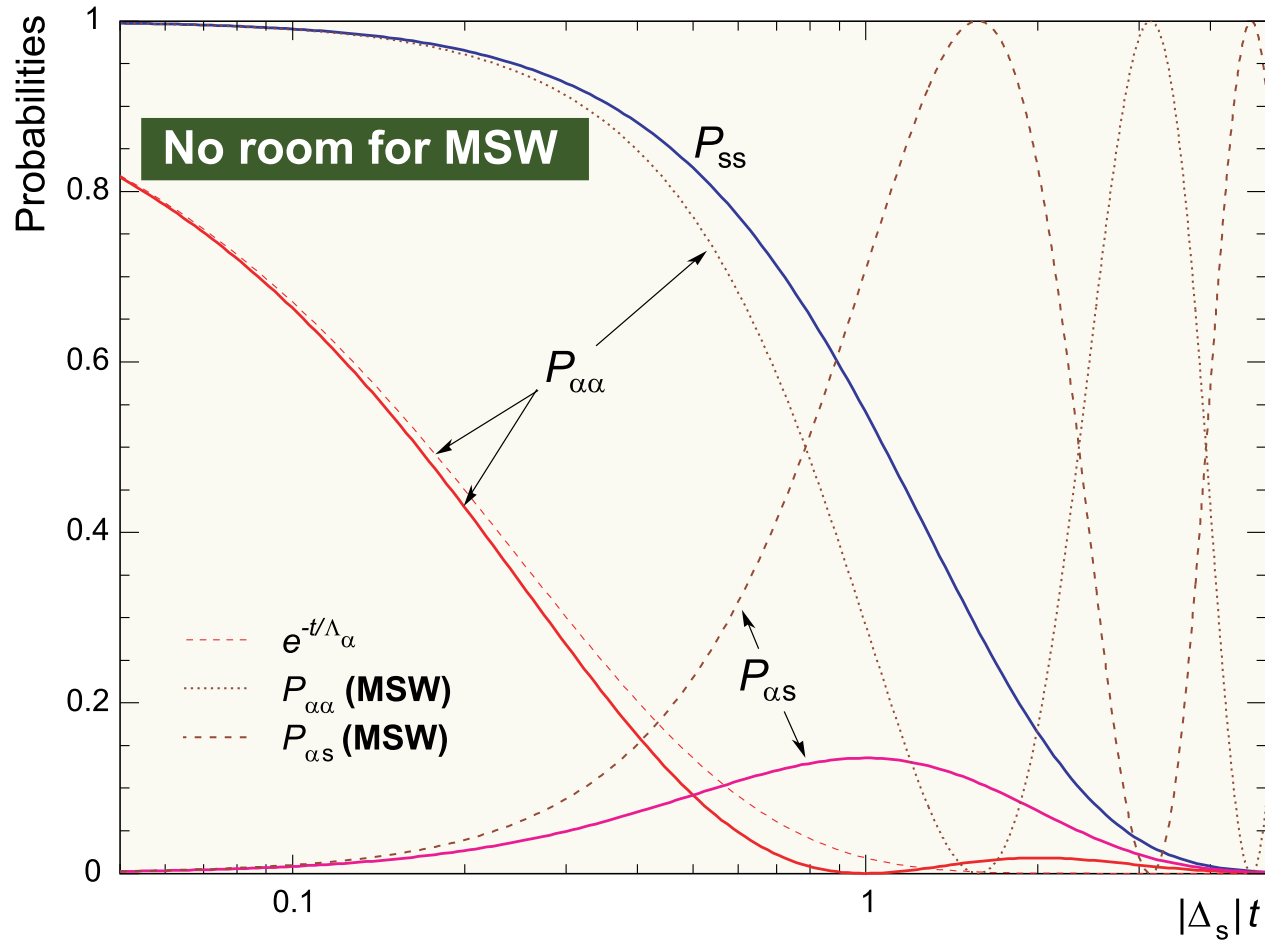


Figure 10: Survival and transition probabilities for $\nu_\alpha \leftrightarrow \nu_s$ oscillations in the case of degeneracy ($q = q_{-\zeta}$). The standard MSW probabilities (dotted and dash-dotted curves) together with the penetration coefficient for unmixed ν_α (dashed curve) are also shown.

4.2.8 Conclusions

We have considered, on the basis of the MSW evolution equation with complex indices of refraction, the conjoint effects of neutrino mixing, refraction and absorption on high-energy neutrino propagation through matter. The adiabatic solution with correct asymptotics in the standard MSW and classical limits has been derived. In the general case the adiabatic behavior is very different from the conventional limiting cases.

A noteworthy example is given by the active-to-sterile neutrino mixing. It has been demonstrated that, under proper conditions, the survival probability of active neutrinos propagating through a very thick medium of constant density may become many orders of magnitude larger than it would be in the absence of mixing. The quantitative characteristics of this phenomenon are highly responsive to changes in density and composition of the medium as well as to neutrino energy and mixing parameters.

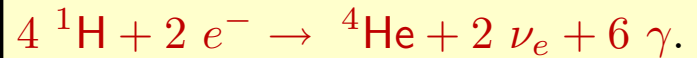
Considering a great variety of latent astrophysical sources of high-energy neutrinos, the effect may open a new window for observational neutrino astrophysics.

Part II

SOLAR NEUTRINOS

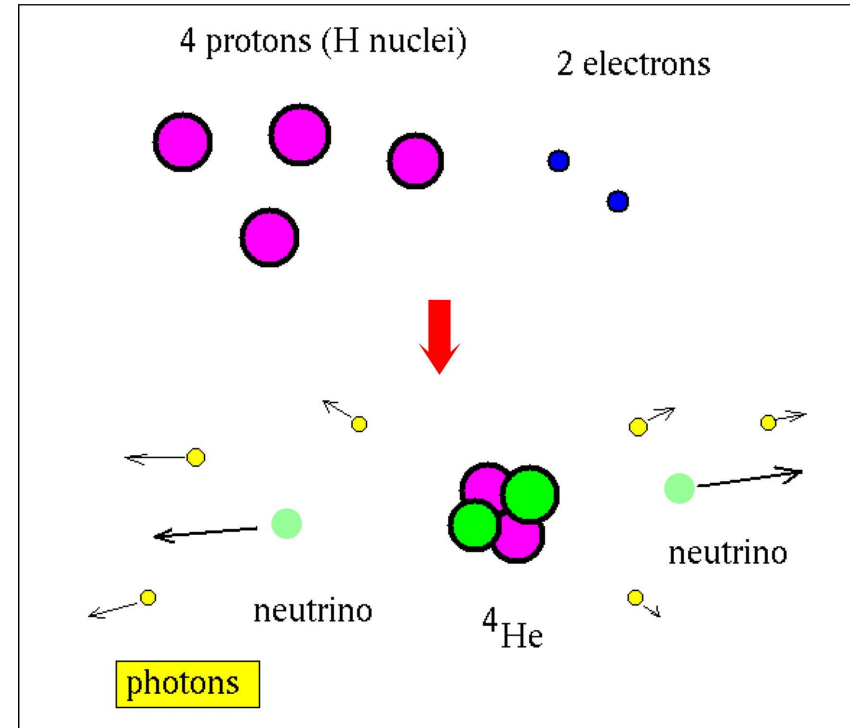
5 The pp fusion step by step

The evidence is strong that the overall fusion reaction is “burning” hydrogen to make helium:



In this reaction, the final particles have less internal energy than the starting particles. Since energy is conserved, the extra energy is released as

- ★ energy of motion of the nuclei and electrons in the solar gas,
- ★ the production of lots of low energy photons and, finally,
- ★ the energy of the neutrinos, which easily shoot out of the Sun.



That is the gas gets hotter and has lots of photons (and neutrinos). The energy release in this reaction is $\Delta E = (4 \times 1.007825u - 4.002603u) \times 931\text{ MeV}/u = 26.7\text{ MeV}$ each time the reaction happens.

The fusion reaction as given above is a summary. Really it may only occur in several steps since the temperature in the Sun is too low and, as a result,

an inelastic collision of two nuclei in the Sun is nearly impossible.

The two nuclei have to get within $r_p \sim 10^{-13}$ cm for the strong interactions to hold them together but they repel each other. For example, the potential energy for Coulomb interaction of two protons is

$$U_{\text{Coulomb}} = \frac{e^2}{r_p} \approx 2 \times 10^{-6} \text{ erg} \approx 1.2 \text{ MeV.}$$

Since $T_{\odot} \lesssim 1.5 \times 10^7$ K (the helioseismology confirms this!)

$$\langle E_p^{\text{kin}} \rangle = \frac{3}{2} kT_{\odot} \lesssim 2 \text{ keV.}$$

Assuming Maxwellian distribution, the fraction of protons with $E_p^{\text{kin}} > U_{\text{Coulomb}}$ is

$$\exp(-E_p^{\text{kin}} / \langle E_p^{\text{kin}} \rangle) < e^{-600} \sim 10^{-260}.$$

Considering that the number of protons in the Sun is about 10^{57} we can conclude that

the classical probability of the fusion is ZERO.

Let's estimate the quantum probability. The nucleus wave function can be written

$$\psi \propto \exp \left(i \int p dx \right).$$

$$E_p^{\text{kin}} = \frac{p^2}{2m} = E_0 - U; \quad \Rightarrow \quad p = \sqrt{2m(E_0 - U)}$$

The repulsion energy of two nuclei with charges Z_1e and Z_2e is $U = Z_1Z_2e^2/r$ and the classical turning point ($p = 0$) is given by

$$r_1 = Z_1Z_2e^2/E_0.$$

In quantum theory

$$p = i\sqrt{2m(U - E_0)} \quad \text{for } r < r_1$$

and thus the probability of the barrier penetration (tunnel effect) can be estimated as

$$\psi^2(r) \propto \exp \left[-2 \int_r^{r_1} \sqrt{2m[U(r') - E_0]} dr' \right].$$

where $r \sim r_p$ is the radius of nuclear interaction. It is assumed here that one of the nuclei is in rest ($m_2 = \infty$). To take into account its finite mass one have to replace m with the effective dynamic mass of the colliding particles:

$$m \longmapsto M = \frac{m_1m_2}{m_1 + m_2} = \frac{A_1A_2}{A_1 + A_2}m_p = Am_p.$$

Considering that usually $r_p \ll r_1$, for rough estimation we can put $r = 0$. Then the barrier penetration probability is given by

$$\psi^2(r) \approx \psi^2(0) = e^{-\phi},$$

where ($\hbar = c = 1 \implies e^2/\hbar c = \alpha$)

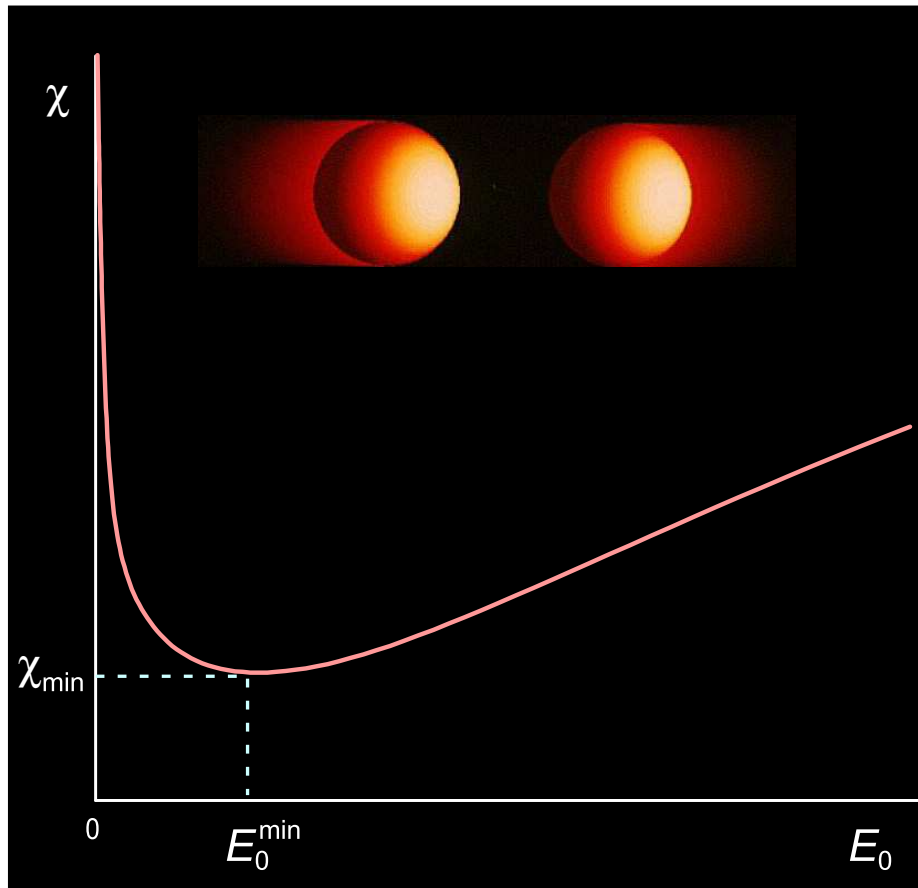
$$\phi = 2r_1 \sqrt{2ME_0} \int_0^1 \sqrt{1/x - 1} dx = \pi r_1 \sqrt{2ME_0} = \pi Z_1 Z_2 \alpha \sqrt{2M/E_0}.$$

In thermal equilibrium with the temperature T the number of particles with energy E_0 is proportional to $\exp(-E_0/kT)$. Therefore the full probability is proportional to

$$\int e^{-\chi(E_0)} dE_0, \quad \text{where} \quad \chi = \sqrt{\frac{E_1}{E_0}} + \frac{E_0}{kT} \quad \text{and} \quad E_1 = 2\pi^2 Z_1^2 Z_2^2 \alpha^2 M.$$

The integral can be evaluated by using the saddle-point technique considering that the function χ has a sharp minimum (and thus $e^{-\chi}$ has a sharp maximum, – *Gamov's peak*). The minimum is given by

$$\frac{d\chi}{dE_0} = -\frac{1}{2E_0} \sqrt{\frac{E_1}{E_0}} + \frac{1}{kT} = 0.$$



The Gamov's peak is given by

$$E_0^{\min} = E_1^{1/3} (kT/2)^{2/3} \\ \simeq 0.122 (AZ_1^2 Z_2^2 T_9^2)^{1/3} \text{ MeV},$$

$$\chi_{\min} = 3 \left(\frac{E_1}{4kT} \right)^{1/3} \\ \simeq 4.25 \left(\frac{AZ_1^2 Z_2^2}{T_9} \right)^{1/3},$$

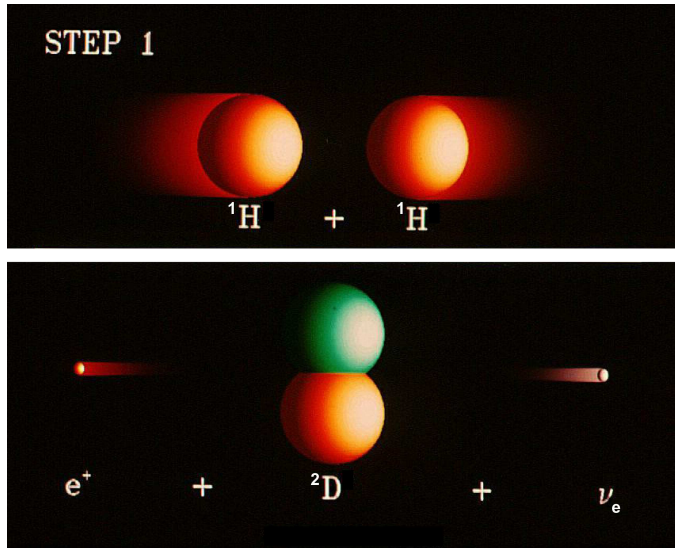
where $T_9 = T/(10^9 \text{ K})$. Now one can approximate $\chi(E_0)$ by

$$\chi(E_0) \simeq \chi_{\min} + \kappa (1 - E_0/E_0^{\min})^2, \\ \kappa = (3/8) (2E_1/kT)^{1/3}.$$

Finally, the full probability is estimated by $C(T) \exp[-\chi_{\min}(T)]$. In particular, for the pp fusion in the center of the Sun ($T_9 \simeq 0.015$)

$$E_0^{\min} \simeq 5.9 \text{ keV}, \quad \chi_{\min} \simeq 13.7, \quad \exp(-\chi_{\min}) \simeq 1.15 \times 10^{-6}.$$

5.1 The pp I branch



Note: the secondary positron very quickly encounters a free electron in the Sun and both particles annihilate, their mass energy appearing as two 511 KeV γ s: $e^+e^- \rightarrow \gamma\gamma$.

The energy liberation in this reaction is $Q = 1.442$ MeV, including ~ 250 keV taking away by neutrinos ($E_\nu \leq 420$ keV). The number of deuterium nuclei generated in 1 cm^3 per 1 sec is

$$\frac{d[\text{D}]}{dt} = C_D \frac{n_p^2}{N_A T_9^{2/3}} \exp\left(-\frac{3.38}{T_9^{1/3}}\right),$$

$$C_D \approx 2.1 \times 10^{-15} \text{ cm}^{-3} \text{ s}^{-1}.$$

By introducing the weight concentrations for the chemical elements

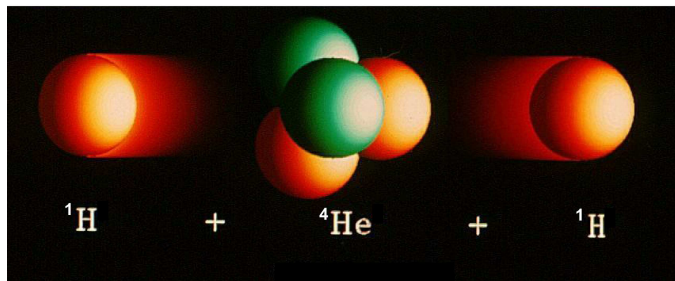
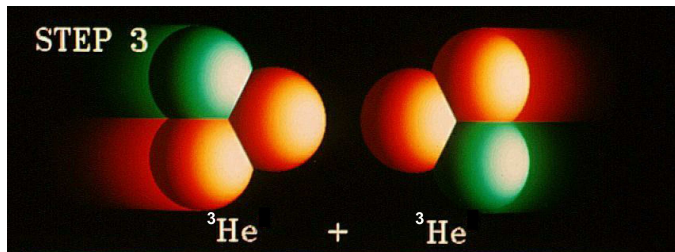
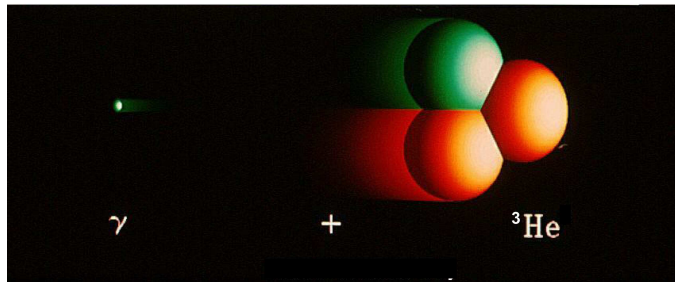
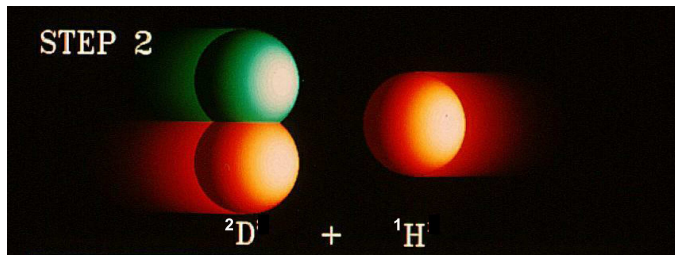
$$X(i) = \frac{m_{\text{H}} n_i A_i}{\rho} = \frac{n_i A_i}{N_A \rho},$$

we can write the reaction rate:

$$\dot{X}(\text{D}) = C_1 \rho [X(\text{H})]^2 T_9^{-2/3} e^{-3.38/T_9^{1/3}}$$

$$(C_1 \approx 2.1 \times 10^{-15} \text{ s}^{-1}).$$

The characteristic time is $\tau_1 \approx 1.3 \times 10^{10}$ yr at $\rho = 100 \text{ g/cm}^3$ and $T = 1.3 \times 10^7$ K. The reaction is very rare. That's why the Sun is still burning after $\sim 4.6 \times 10^9$ years!



The energy liberation: $Q = 5.493 \text{ MeV}$;
the reaction rate:

$$\dot{X}({}^3\text{He}) = C_2 \rho X({}^1\text{H}) X({}^2\text{D}) T_9^{-2/3} e^{-3.72/T_9^{1/3}},$$

$$C_2 \approx 3.98 \times 10^3 \text{ s}^{-1} \approx 2 \times 10^{18} C_1,$$

$$\text{and } \tau_2 \approx 6 \text{ s}.$$

The energy liberation: $Q = 12.859 \text{ MeV}$;
the reaction rate:

$$\dot{X}({}^4\text{He}) = C_3 \rho [X({}^3\text{He})]^2 T_9^{-2/3} e^{-12.28/T_9^{1/3}},$$

$$C_3 \approx 1.3 \times 10^{10} \text{ s}^{-1} \approx 6 \times 10^6 C_2,$$

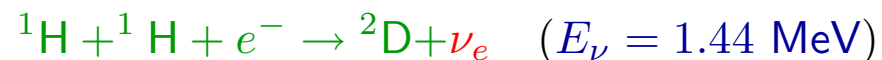
$$\text{and } \tau_3 \approx 10^6 \text{ yr}.$$

Even at temperatures in the Sun's core, 1.5×10^7 K, the average lifetime of a proton against *pp* fusion is about $\sim 10^{10}$ yr. It is an extremely slow reaction, and it is this time scale that sets the stellar clock, so to speak, by determining how long the star will remain a stable main sequence object.

In contrast, the deuteron created will only last about a few seconds before it hits into another proton and fusion creates a ${}^3\text{He}$ nucleus. Therefore it cannot accrue and its stationary concentration is given by $X(\text{D}) = (\tau_2/\tau_1)X(\text{H}) \approx 10^{-17}X(\text{H})$. The ${}^3\text{He}$ nucleus will last about 250,000 years before it hits another ${}^3\text{He}$ nucleus hard enough for the two to stick together.

5.2 The pep fusion

The deuterium can also be produced in the reaction

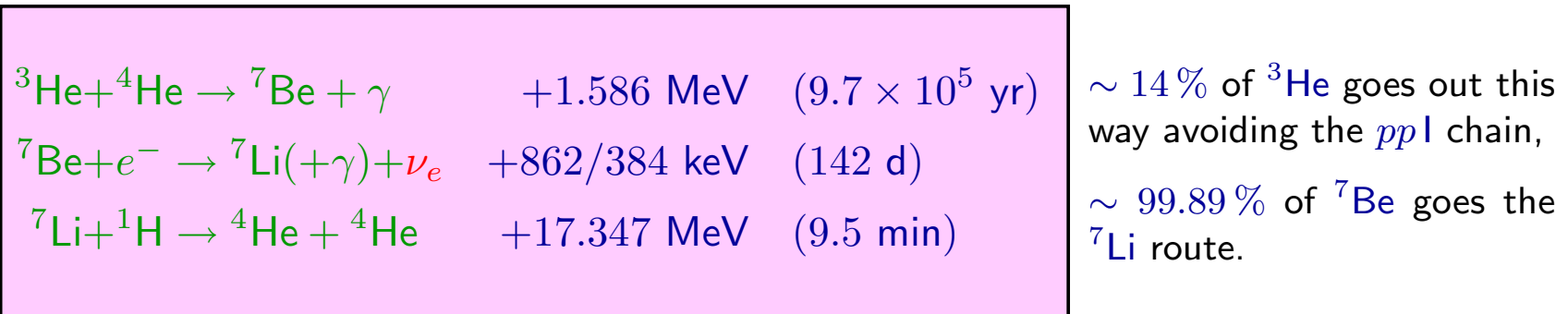


which has a characteristic time scale $\sim 10^{12}$ yr that is rather larger than the age of the Universe at this time. So it is *insignificant* in the Sun as far as energy generation is concerned. Nevertheless, the *pep* fusion accounts for about 0.25% of the deuterons created in the *pp* chain.

Enough *pep* fusions happen to produce a detectable number of neutrinos, so the reaction must be accounted for by those interested in the *solar neutrino problem*.

5.3 The pp II branch

The ${}^3\text{He}$ does not always have to hit another ${}^3\text{He}$ nucleus. It could hit a ${}^4\text{He}$ forming stable ${}^7\text{Be}$. But ${}^7\text{Be}$ has an affinity for electron capture, and can absorb free electrons. The electron turns one of the Be protons into a neutron, changing the ${}^7\text{Be}$ into ${}^7\text{Li}$, while tossing out a neutrino. The ${}^7\text{Li}$ will then quickly fuse with a free proton, resulting in unstable ${}^8\text{Be}$ which immediately falls apart into two stable ${}^4\text{He}$ nuclei.

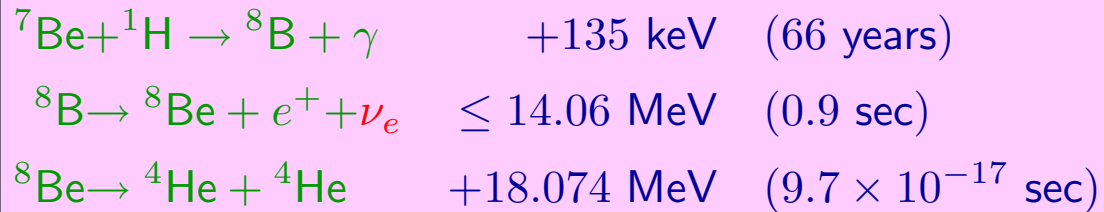


$\sim 90\%$ of ${}^7\text{Li}$ nuclei are in the ground state and thus $E_\nu = 862$ keV; the rest lithium is created in an excited state and $E_\nu = 384$ keV.

Note: Fusion with ${}^4\text{He}$ is less likely, because there is more ${}^3\text{He}$ around deep inside the stellar core. But in heavier stars, where the temperatures exceed about 2.4×10^7 K, the *ppII* chain can rival the *ppI* chain for energy production inside the star. This is because at higher temperatures the ${}^3\text{He}$ gets used up faster, driving down its abundance compared to ${}^4\text{He}$.

5.4 The pp III branch

The ${}^7\text{Be}$ has two ways to go – it can either absorb an electron, as in *pp II* (99.89%), or absorb a proton, as in *pp III* (0.11%). Absorbing a proton raises the nucleus from beryllium to boron, and the ${}^7\text{Be}$ becomes ${}^8\text{B}$. But ${}^8\text{B}$ is unstable and takes < 1 second, fairly independent of temperature, to spit out a positron and a neutrino to become beryllium again, only this time it's ${}^8\text{Be}$. But ${}^8\text{Be}$ falls apart in a hurry into two ${}^4\text{He}$ nuclei, and once again we have turned hydrogen into helium.



$\sim 0.11\%$ of ${}^7\text{Be}$ goes this route.

Of course, $e^+e^- \rightarrow \gamma\gamma$.

Note: In low mass stars the internal temperature is not high enough to finish the *pp* cycle. They produce the first stage of *pp* fusion up to ${}^3\text{He}$, but are unable to force the last stage of ${}^3\text{He}$ fusion, either with another ${}^3\text{He}$ or an ${}^4\text{He}$. So they fuse hydrogen into ${}^3\text{He}$ instead of ${}^4\text{He}$. This fact is confirmed by the observation that low mass stars are often anomalously rich in ${}^3\text{He}$ compared to ${}^4\text{He}$.

5.5 The pp IV branch (hep reaction)

The low-energy cross section for the “hep reaction”

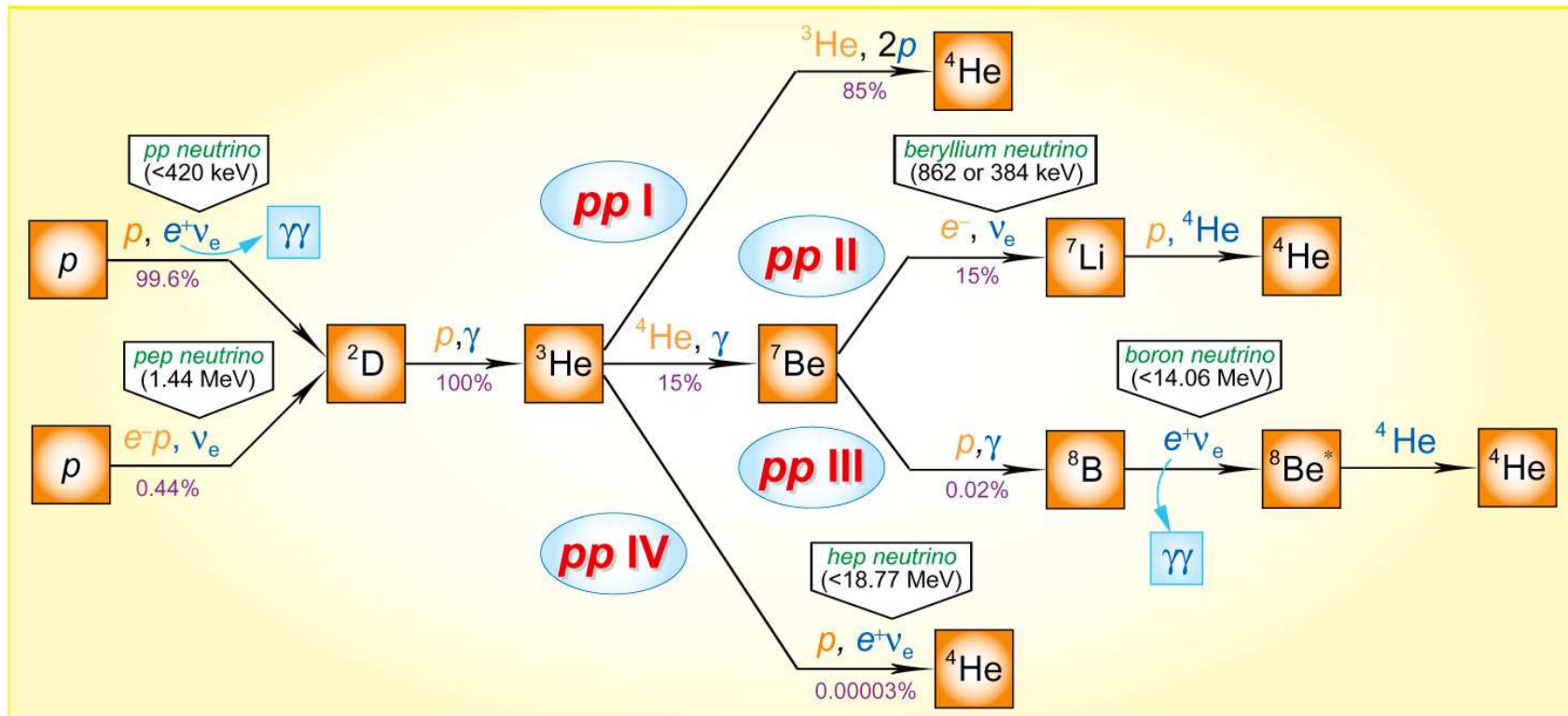


is uncertain. While the probability of the *pp IV* branch is estimated to be about $3 \times 10^{-5}\%$, the hep produces highest-energy solar neutrinos,

$$E_\nu \leq 18.77 \text{ MeV},$$

which can at some level influence the electron energy spectrum produced by solar neutrino interactions and measured in the high-threshold detectors like Super-Kamiokande and SNO.

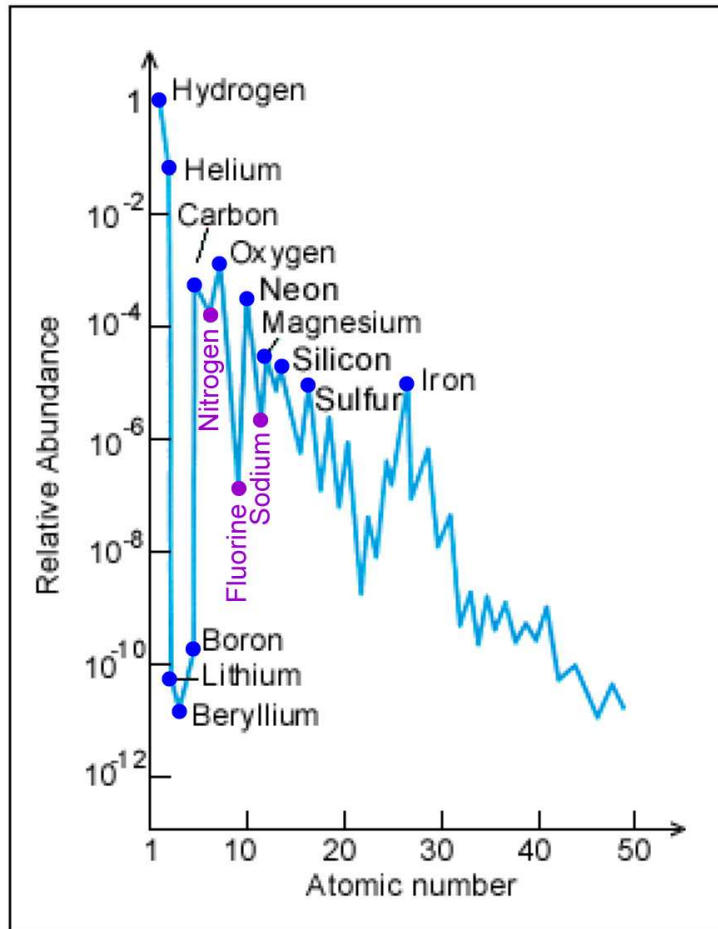
5.6 The full pp chain



The diagram shows the full *pp* chain responsible for production of about 98.4% of the solar energy. The neutrinos export 3%, 4%, and 28% of the energy in *pp I*, *pp II*, *pp III*, respectively. All four *pp* chains are active simultaneously in a H-burning star containing significant ${}^4\text{He}$. The details depend on density, temperature and composition but in the SUN the *pp I* dominates.

6 An excursus: the elemental abundance in the Sun

The matter that formed the Sun had already been cycled through one or more generations of stars. We can see elements up to and beyond ^{56}Fe in the heliosphere.



ELEMENTAL ABUNDANCE IN THE SUN

Element	% by mass	% by number
Hydrogen	73.4	92.0
Helium	25.0	7.8
Oxygen	0.80	0.06
Carbon	0.20	0.02
Neon	0.16	0.01
Iron	0.14	0.003
Nitrogen	0.09	0.008
Silicon	0.09	0.004
Magnesium	0.06	0.003
Sulfur	0.05	0.002

The current solar abundance curve is shown in the figure (the ordinate compares all elements to **Hydrogen**) and the relative abundances of the elements (by mass and by number) are shown in the table.

Comments:

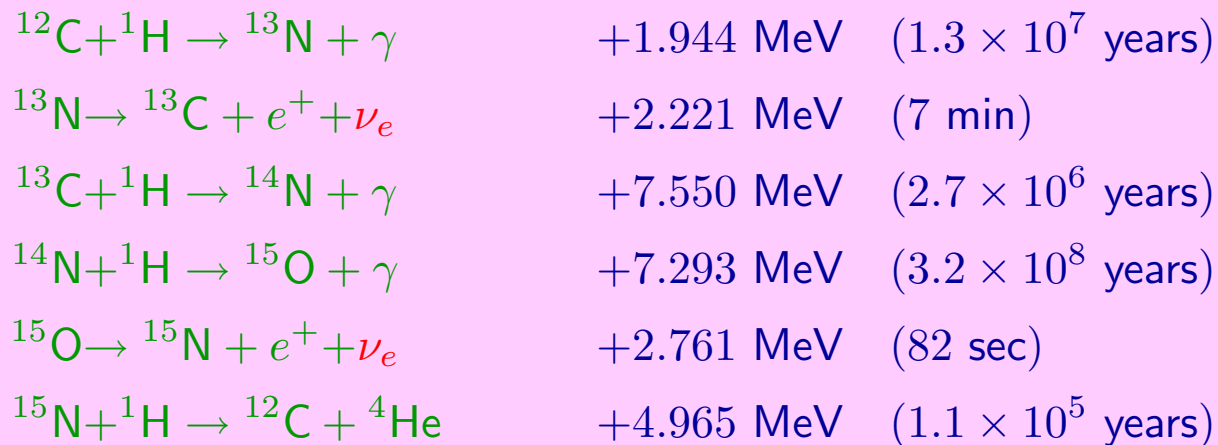
1. The general trend is towards ever decreasing abundances as the atomic number increases.
2. There is a distinct zig-zag (up-down) pattern to the whole curve. For example,
 - between **Carbon** and **Oxygen** there is a decrease (the element is **Nitrogen**);
 - between **Neon** and **Magnesium** the decrease element is **Sodium**;
 - the largest drop is between **Oxygen** and **Neon**, the element that thus decreases notably is **Fluorine**.

The reason for this fluctuating pattern is just this: elements with *odd* numbers of nucleons are less stable, resulting in one unpaired (odd) proton or neutron – those that pair these particles result in offsetting spins in opposite directions that enhance stability.

3. There is a huge drop in abundance for the **Lithium-Beryllium-Boron** triplet. This results from two factors:
 - at the Big Bang, nuclear processes that could fuse the proper **H** or **He** isotopes into **Li** and/or the other two were statistically very rare and hence inefficient, and
 - some of the **Li-Be-B** that formed and survived may be destroyed in processes with stars.

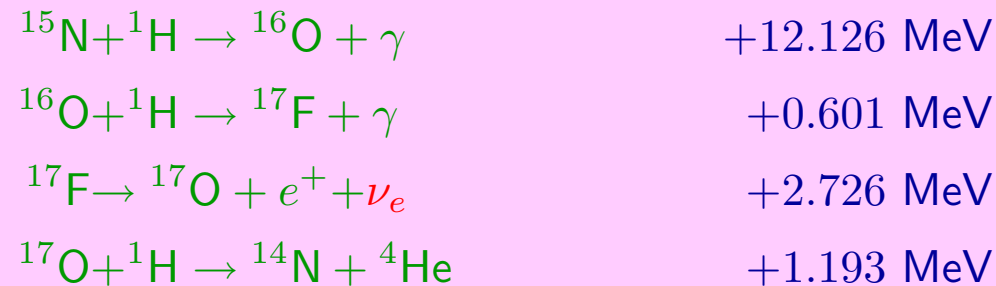
7 The CNO cycle

The presence of the “impurities” in the solar core opens the door to another fusion reaction. The most important (after the *pp*) is the **CNO bi-cycle**, which is responsible for as much as **1.6%** of the Sun’s total output. The main CNO reactions (“**cycle I**”) are



- The cycle uses **carbon**, **nitrogen**, and **oxygen** as catalysts to suck up four protons and build a ^4He nucleus out of them. The relative abundances of **C**, **N**, and **O** do not change.
- The cycle does not start until the *pp* fusion has begun, and provides the energy necessary to allow a low level of proton fusions onto the heavier nuclei.
- The cycle timescale is determined by the slowest reaction ($^{14}\text{N} + ^1\text{H}$) while the approach to equilibrium is determined by the second slowest reaction ($^{12}\text{C} + ^1\text{H}$).

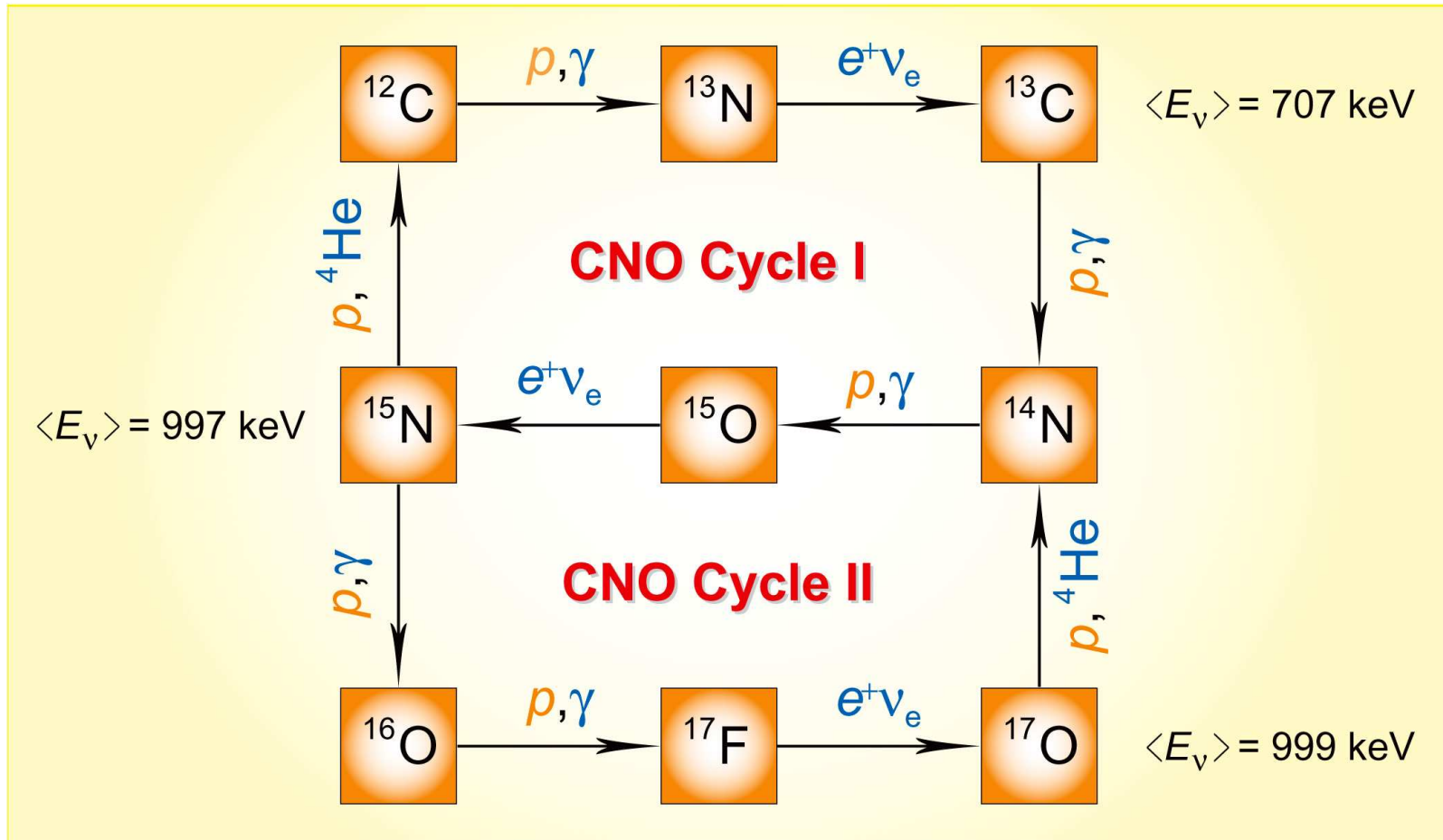
The second minor branch (“[cycle II](#)”) is a similar type of cycle, and it joins onto the first. Starting with ^{14}N , the process steps through two of the last-three reactions given above until ^{15}N is produced. It then proceeds as follows to convert ^{15}N back into ^{14}N , with the production of ^{17}F (fluorine-17) occurring in one of the steps:



The latter cycle is much less frequent, with the first reaction having a probability of about 4×10^{-4} relative to the last reaction of the [cycle I](#).

The fractions of the nuclear energy loss from the core through neutrino emission in the first and second branches of the CNO process are [6%](#) and [4%](#), respectively.

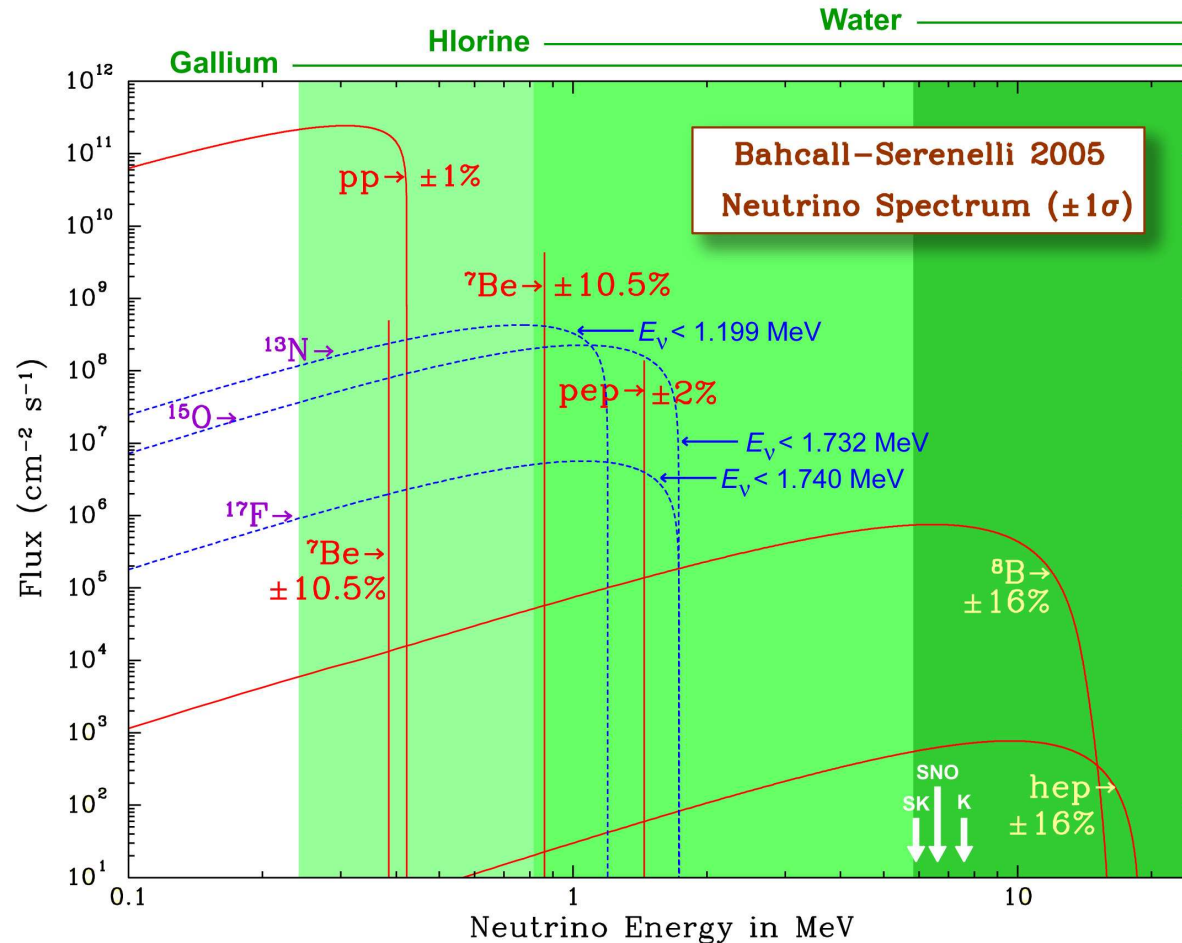
Note: The CNO cycle lacks significance at the low temperatures in the Sun. For abundances characteristic of the Sun, the CNO process becomes important for core temperatures of roughly 1.5×10^7 K ([1.3 keV](#)), and it provides virtually all of the conversion of hydrogen into helium in the later stages of the solar lifetime when the temperature exceed 2.5×10^7 K ([2.2 keV](#)).



The diagram of the full CNO bi-cycle responsible for production of about 1.5-1.6% of the solar energy. The cycle I dominates.

Note: The CNO cycles III and IV are essential for the hydrogen burning in massive stars. The full net includes ^{18}F , ^{18}O , and ^{19}F .

8 Solar neutrino spectrum



Solar neutrino energy spectrum at Earth calculated in the Bahcall-Serenelli solar model “BS05(OP)”.

Also shown the uncertainties of the neutrino flux calculation (on the 1σ level) and the threshold neutrino energies for the gallium, chlorine and water detectors.

[From J. N. Bahcall, A. M. Serenelli, and S. Basu, “New solar opacities, abundances, helioseismology, and neutrino fluxes,” *Astrophys. J.* **621** (2005) L85-L88 (astro-ph/0412440).]

Comparison between the “Standard Solar Models” of Bahcall & Pinsonneult (1995) [BP95] and of Dar & Shaviv (1996) [DS96].^a

Parameter/Effect	BSP98	DS96
M_{\odot}	1.9899×10^{33} g	1.9899×10^{33} g
L_{\odot}	3.844×10^{33} erg s ⁻¹	3.844×10^{33} erg s ⁻¹
R_{\odot}	6.9599×10^{10} cm	6.9599×10^{10} cm
t_{\odot}	4.566×10^9 yr	4.57×10^9 yr
Rotation	Not Included	Not Included
Magnetic Field	Not Included	Not Included
Mass Loss	Not Included	Not Included
Angular Momentum Loss	Not Included	Not Included
Pre-main Sequence Evolution	Not Included	Included
Initial Abundances :		
⁴ He	Adjusted	Adjusted
C, N, O, Ne	Adjusted	Adjusted
All Other Elements	Adjusted	Meteoritic

^aFrom A. Dar and G. Shaviv, “The solar neutrino problem: An update,” Phys. Rept. **311** (1999) 115–141 (astro-ph/9808098).

Continued

Parameter/Effect	BSP98	DS96
Photospheric Abundances :		
⁴ He	Predicted	Predicted
C, N, O, Ne	Photospheric	Photospheric
All Other Elements	Meteoritic	Predicted
Radiative Opacities	OPAL 1996	OPAL 1996
Equation of State	Straniero 1996?	Dar – Shaviv 1996
Partial Ionization Effects	Not Included	Included
Diffusion of Elements :		
H, ⁴ He	Included	Included
Heavier Elements	Approximated by Fe	All Included
Partial Ionization Effects	Not Included	Included
Nuclear Reaction Rates :		
S ₁₁ (0) eV · b	4.00×10^{-19}	4.07×10^{-19}
S ₃₃ (0) MeV · b	5.3	5.6
S ₃₄ (0) keV · b	0.53	0.45
S ₁₇ (0) eV · b	19	17
Screening Effects	Included	Included
Nuclear Equilibrium	Imposed	Not Assumed

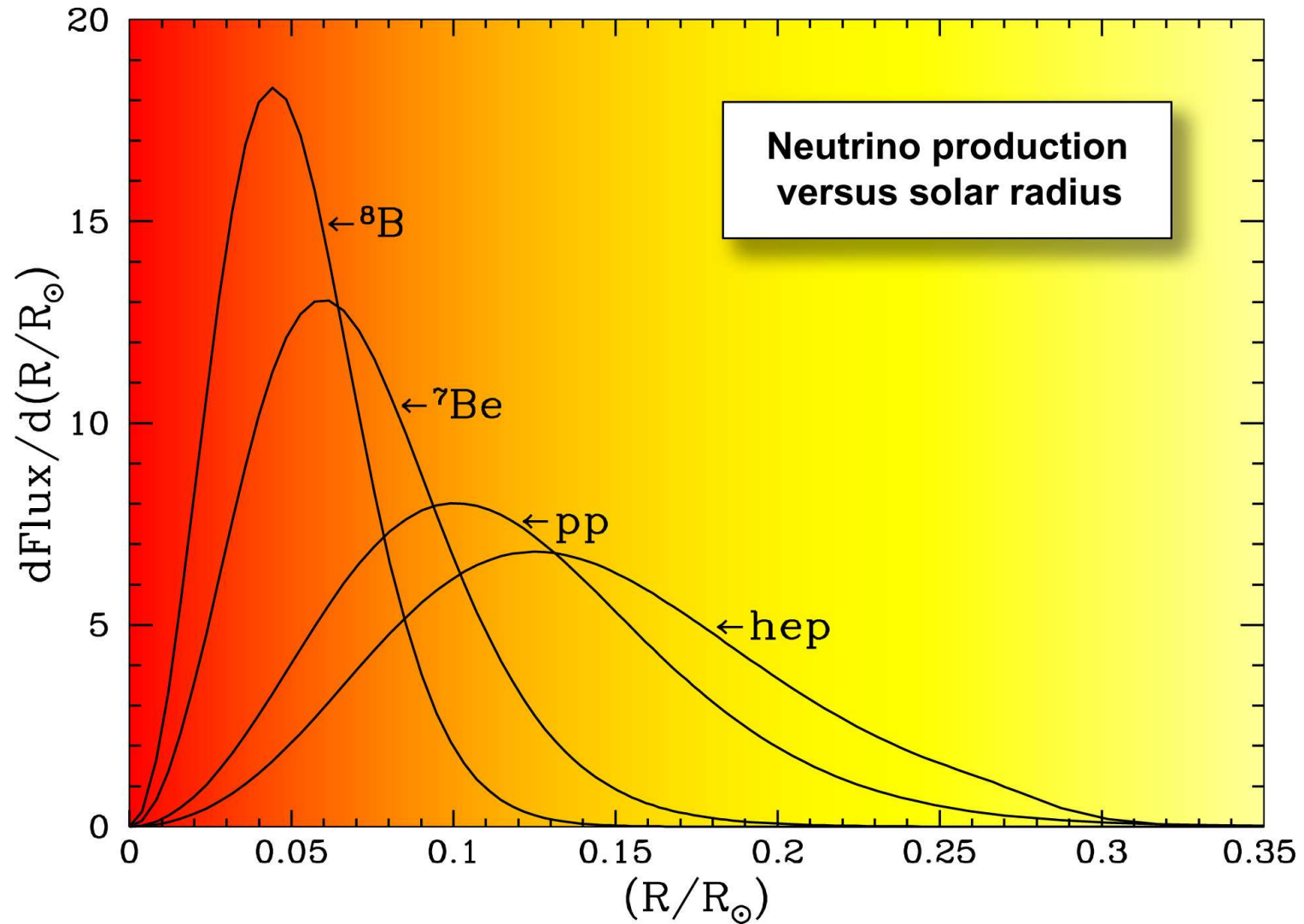


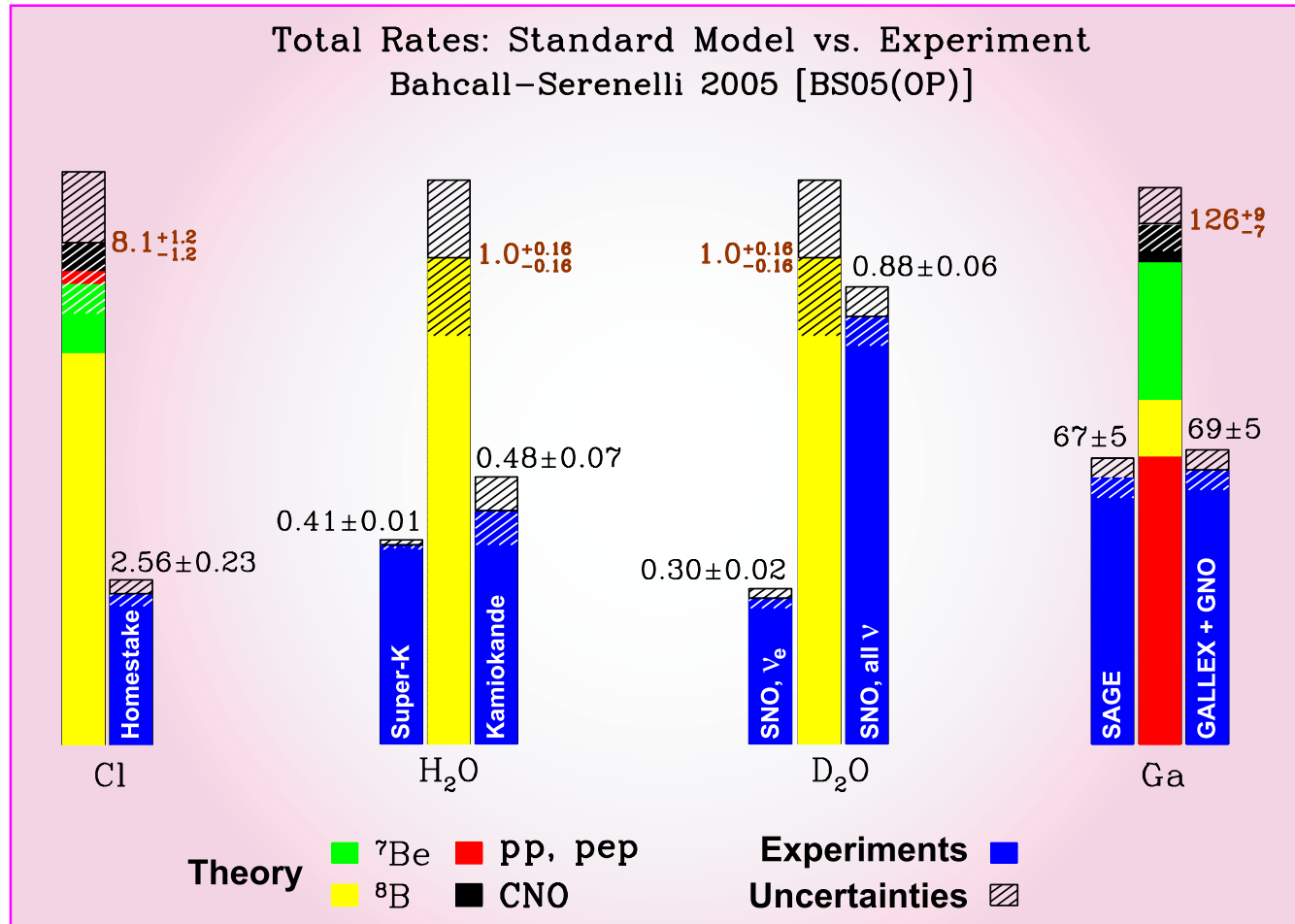
Figure shows where the different neutrino fluxes originate in the Sun according to SSM.

[From John Bahcall's homepage, URL: <<http://www.sns.ias.edu/~jnb/>>.]

Part III

SOLAR NEUTRINO EXPERIMENTS

9 Current status



Current (Oct. 2005) status of the standard solar model and solar neutrino problem.

[Borrowed from John Bahcall's Home Page, URL: <http://www.sns.ias.edu/~jnb/> (slightly modified).]

Table 4: Current status of the solar neutrino data (2005).

Experiment	Measured flux (SNU / 10^{10} count/m ² s)	Ratio experiment/theory	Threshold energy	Years of running
Homestake	$2.56 \pm 0.16 \pm 0.16$	$0.33 \pm 0.03 \pm 0.05$	814 keV	1970-1995
Kamiokande	$2.80 \pm 0.19 \pm 0.33$	$0.54 \pm 0.08^{+0.10}_{-0.07}$	7.5 MeV	1986-1995
SAGE	$75 \pm 7 \pm 3$	$0.58 \pm 0.06 \pm 0.03$	233 keV	1990-2006
GALLEX	$78 \pm 6 \pm 5$	$0.60 \pm 0.06 \pm 0.04$	233 keV	1991-1996
Super-K	$2.35 \pm 0.02 \pm 0.08$	$0.465 \pm 0.005^{+0.016}_{-0.015}$	5.5 (6.5) MeV	from 1996
GNO	$66 \pm 10 \pm 3$	$0.51 \pm 0.08 \pm 0.03$	233 keV	from 1998
SNO (CC)	$1.68 \pm 0.06^{+0.08}_{-0.09}$		6.75 MeV	from 1999
SNO (ES)	$2.35 \pm 0.22 \pm 0.15$			
SNO (NC)	$4.94 \pm 0.21^{+0.38}_{-0.34}$			

- The values are given in SNU (defined as 10^{-36} capture per second per target atom) for the radiochemical experiments and in units of 10^{10} counts/m²s for the water-Cherenkov experiments.
- The first and errors for the relative values correspond to experimental and theoretical errors, respectively, with the statistical and systematic errors added quadratically. The models by Bahcall and Pinsonneault BP98 and BP00 were used in the calculations.

[The data are borrowed from the *Ultimate Neutrino Page* maintained by Juha Peltoniemi and Juho Sarkamo, of Oulu University, URL: <<http://cupp oulu.fi/neutrino/>> (last modified 10.4.2005).]

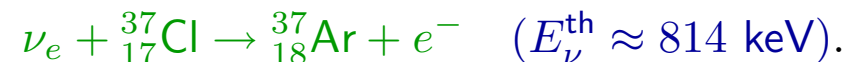
10 Cl-Ar detector at Homestake



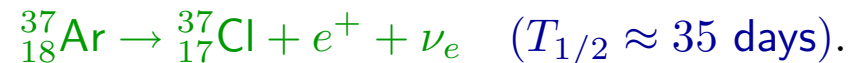
[From URL: <http://www.bnl.gov/bnlweb/raydavis/research.htm>.]

The argon-37 is allowed to build up for several months, then is removed by purging the tank with helium gas. The argon is adsorbed in a cold trap and assayed for radioactivity.

The Homestake Neutrino Trap is a tank 20 feet (6.1 m) in diameter and 48 feet (14.6 m) long filled with 100,000 gallons (378,520 liters) of a common cleaning fluid, tetrachloroethylene (C_2Cl_4). On the average each molecule of C_2Cl_4 contains one atom of the desired isotope, $^{37}_{17}Cl$. The other three chlorine atoms $^{35}_{17}Cl$ contain two less neutrons. When a neutrino of the right energy reacts with an atom of $^{37}_{17}Cl$, it produces an atom of $^{37}_{18}Ar$ and an electron (B. Pontecorvo, 1946, L. V. Alvarez, 1949):



Then the radioactive argon decays back to chlorine:

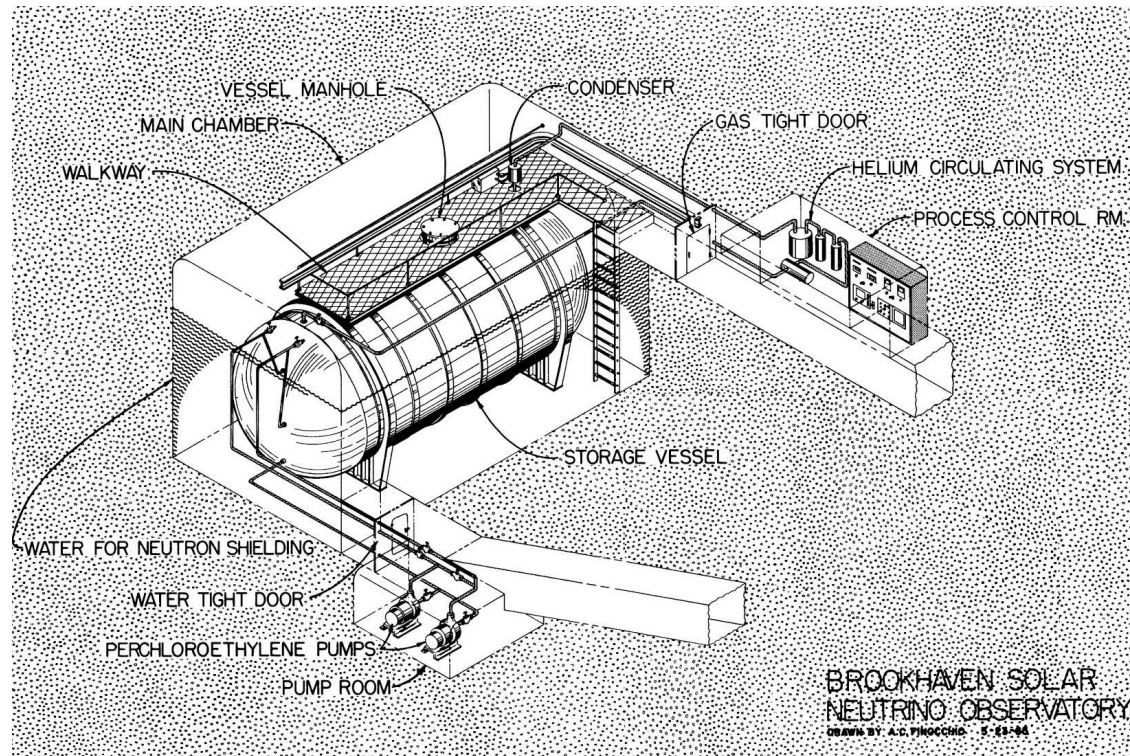


The idea is to tell that the reaction happened by seeing the positron.

The chlorine-argon experiment has been run by Raymond Davis, Jr., Kenneth C. Hoffman and Don S. Harmer of Brookhaven National Laboratory. The detector is located nearly a mile underground, in a rock cavity at the **4,850 foot level (1.48 km)** below the surface in the Homestake Gold Mine in the town of Lead, South Dakota.

Suggested in 1964 by John Bahcall and Raymond Davis, the experiment was begun on **1967** and continued to measure the solar neutrino flux until the **late 1990s**, when the Homestake Mine ceased operating.

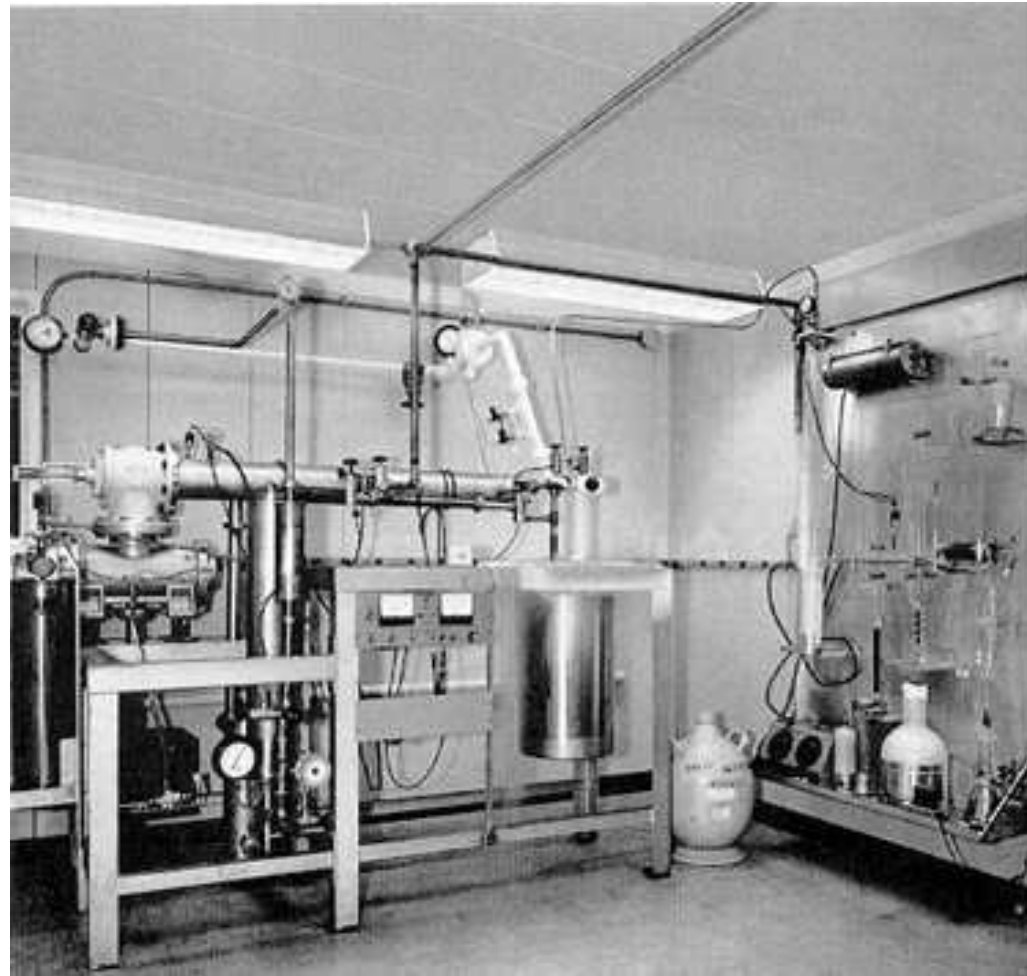
The first results of the experiment showed that **the Sun's output of neutrinos from the isotope boron-8 was less than expected.**



[From J. N. Bahcall, "Neutrinos from the Sun," *Sci. Am.* **221**, No. 1 (1969) 28-37.]

Figure on the right shows the argon extraction system which is deep underground next to the 100,000-gallon neutrino trap. Helium is circulated through the tank to sweep up any atoms of ^{37}Ar that have been formed from ^{37}Cl .

The efficiency of the extraction is determined by previously inserting in the tank a small amount of ^{36}Ar , a rare, nonradioactive isotope of argon. The helium and argon pass through the apparatus at left, where the argon condenses in a charcoal trap cooled by liquid nitrogen.



This argon fraction is purified in the apparatus at the right. The purified sample is then shipped to Brookhaven, where the content of ^{37}Ar is determined in shielded counters.

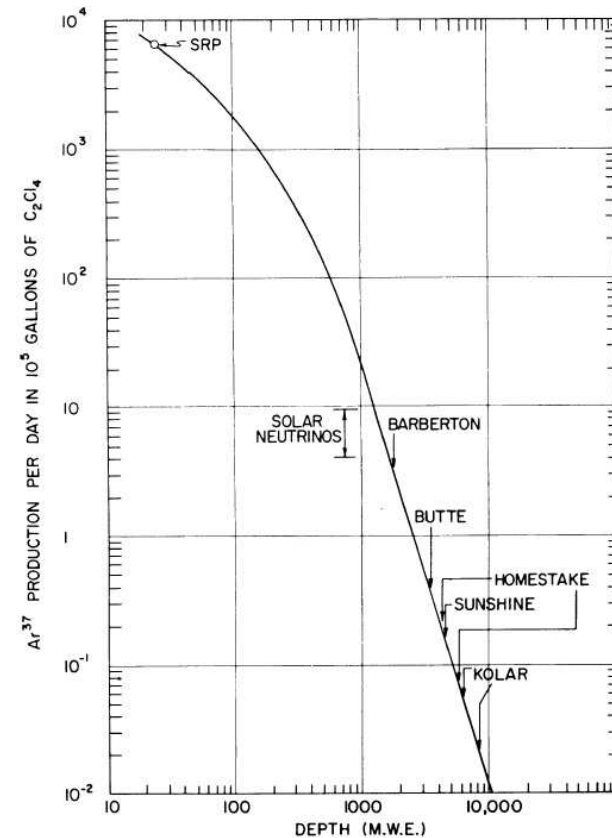
[From J. N. Bahcall, "Neutrinos from the Sun," *Sci. Am.* 221, No. 1 (1969) 28-37.]

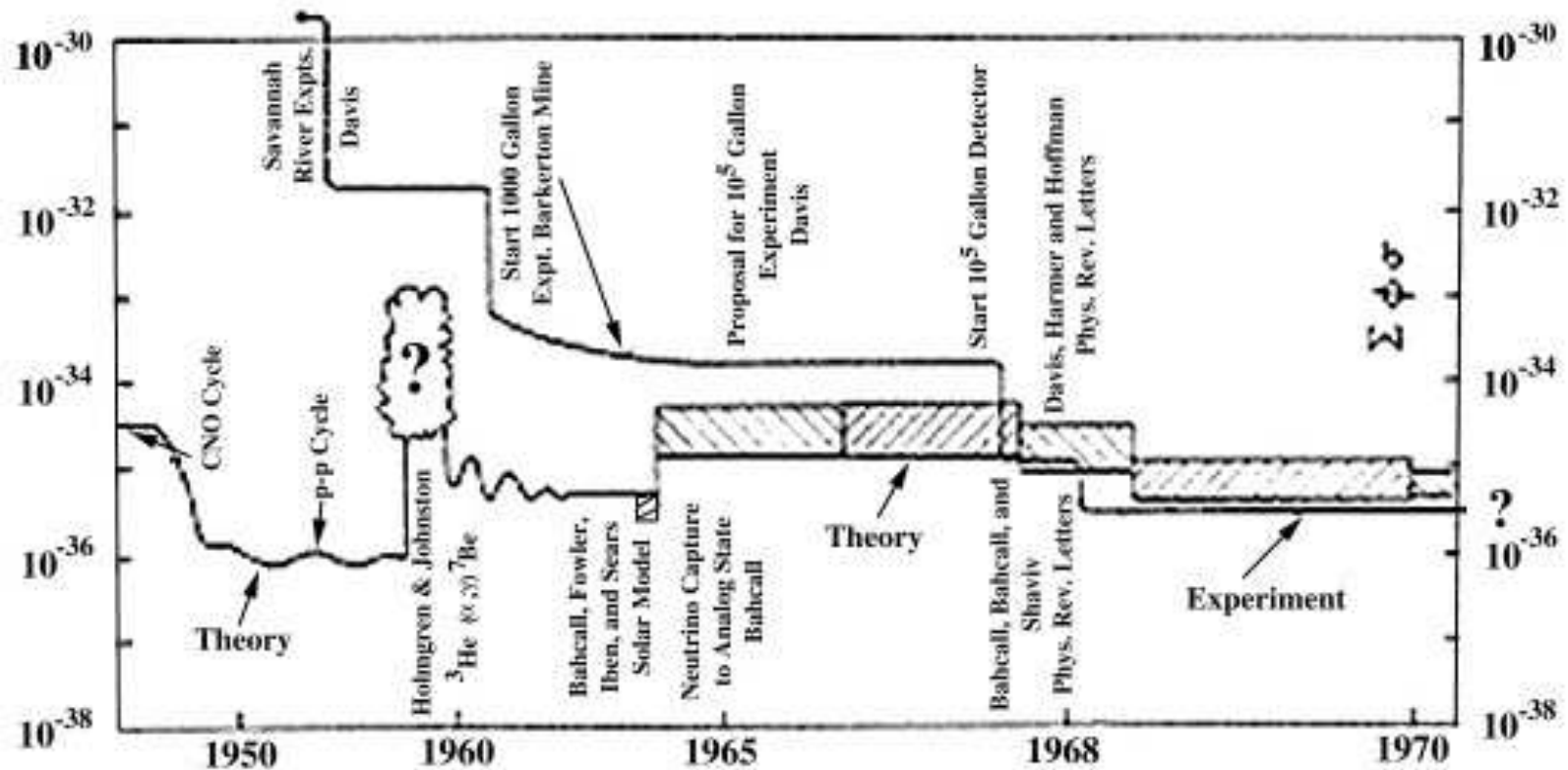
Deep-mine location shields the solar-neutrino detector from the intense flux of cosmic-ray (atmospheric) muons. Being very penetrating, the muons can knock protons out of atomic nuclei well below the earth's surface. If a muon-induced proton entered the neutrino detector, it could mimic the entry of a solar neutrino by converting an atom of ^{37}Cl into an atom of radioactive ^{37}Ar .

Figure on the right shows the ^{37}Ar production rate in 3.8×10^5 liters of perchloroethylene as a function of the depth below the surface. The corresponding background effect is about **0.2 atoms per day in 10^5 gal.** Other sources of the background are estimated to be on the same level or less, in particular,

- fast neutrons from (α, n) reactions and spontaneous fission of U in the rock wall: **0.1–0.3**;
- internal contamination (U, Th, Ca): $\lesssim 0.1$;
- atmospheric neutrino interactions: $\lesssim 0.01$.

[From R. Davis, Jr. and D. S. Harmer, "Solar neutrino detection by the $^{37}\text{Cl} - ^{37}\text{Ar}$ method," in Proc. of the Informal Conference on Experimental Neutrino Physics (CERN, January 20–22, 1965), CERN 65-32, pp. 201–212.]

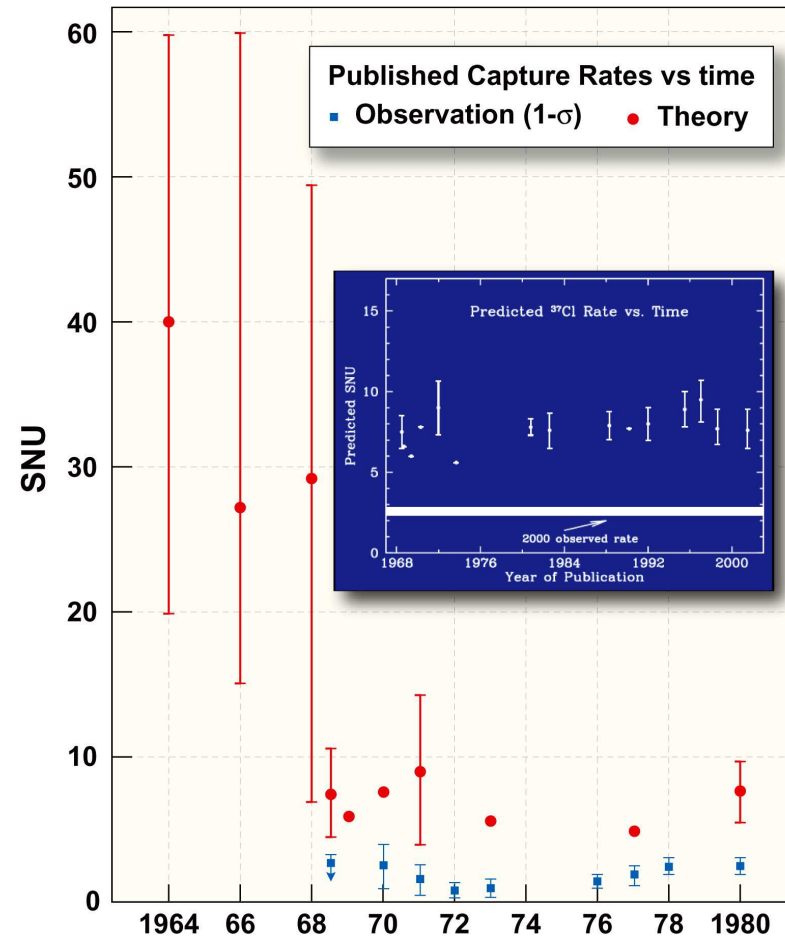




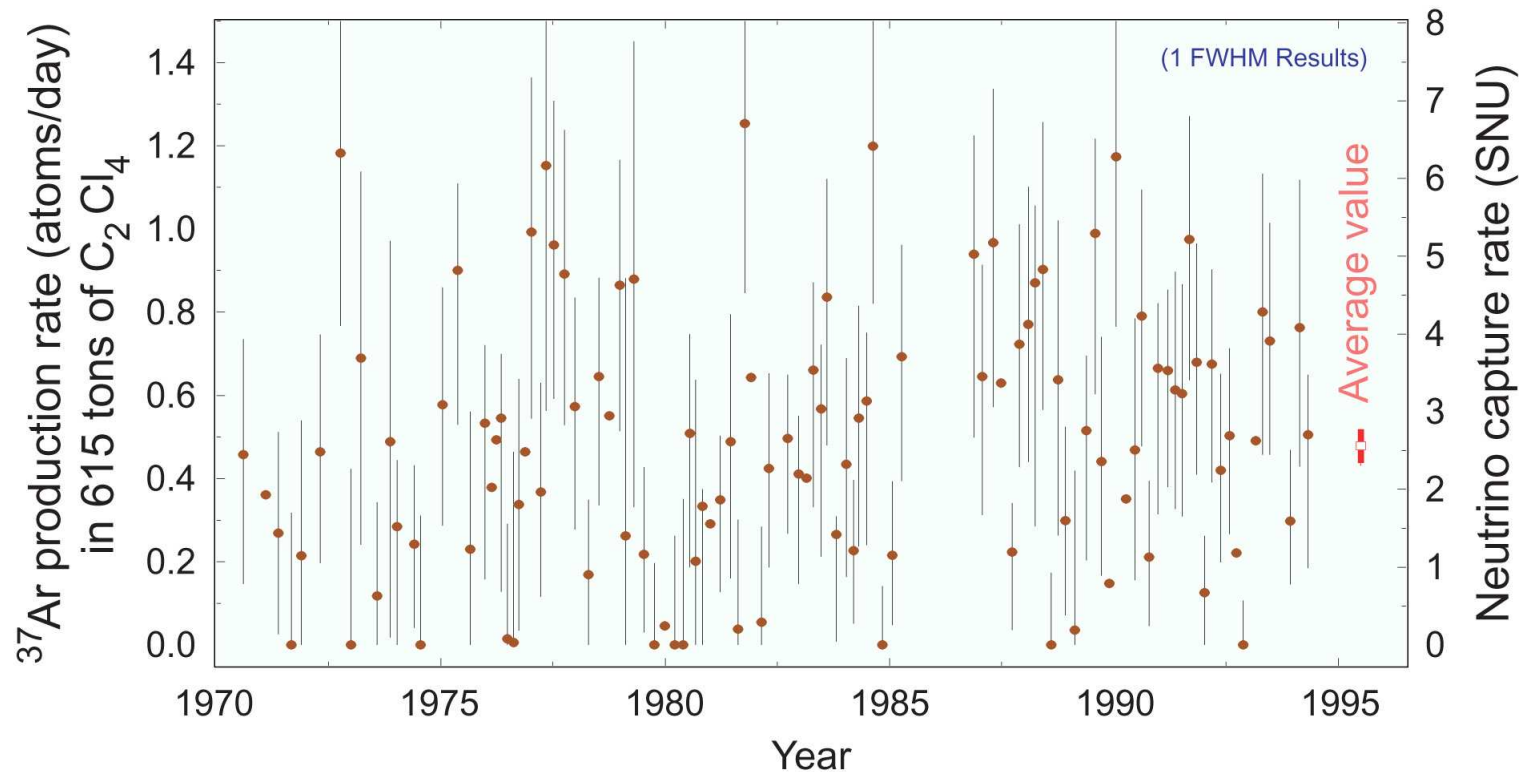
This figure is an overall pictorial history of the subject as it looked in 1970. The experimental upper limit is indicated by the thin curve and the range of theoretical values (after 1964) by the cross-hatched region. The units are captures per target atom per second (10^{-36} captures/atom/s \equiv 1 SNU). A few of the major events are indicated on the figure at the period corresponding to the time they occurred.

[From J. N. Bahcall and R. Davis, Jr., "An account of the development of the solar neutrino problem," in *Essays in Nuclear Astrophysics*, edited by C. A. Barnes *et al.* (Cambridge University Press, 1982), pp. 243–285.]

Figure on the right shows the observed (Davis & coauthors) and predicted (Bahcall & co-authors) neutrino capture rates published within the period from 1964 to 1980. The earliest observational upper limits of 4000 and 160 SNU (obtained in 1955 and 1964, respectively) are not shown since these would not fit conveniently in the plot [see previous slide]. The theoretical uncertainties are more “experimental” than “theoretical” since the basic theory has not changed since 1964. What have changed are the best estimates for many different input parameters. The error bars shown for the theoretical points represent the range of capture rates that were obtained from standard solar models when the various nuclear and atomic parameters were allowed to vary over the range conventionally regarded as acceptable at the time the calculations were made.



[From J. N. Bahcall and R. Davis, Jr., “An account of the development of the solar neutrino problem,” in *Essays in Nuclear Astrophysics*, edited by C. A. Barnes *et al.* (Cambridge University Press, 1982), pp. 243–285.]



The final Homestake chlorine experiment one-FWHM (full width at half maximum) results for 108 individual solar neutrino observations (no. 18 to 133). All known sources of nonsolar ^{37}Ar production are subtracted. The errors of individual measurements are statistical errors only and are significantly non-Gaussian for near zero rates. The error of the cumulative result is the combination of the statistical and systematic errors in quadrature. [From B. T. Cleveland *et al.*, "Measurement of the solar electron neutrino flux with the Homestake chlorine detector," *Astrophys. J.* **496** (1998) 505–526. (1119 citations in SPIRES!)]

10.1 Solar Neutrino Puzzle, Number I'

The average solar neutrino induced ^{37}Ar production rate in the Homestake detector is

$$0.478 \pm 0.030_{\text{stat}} \pm 0.029_{\text{syst}} \text{ day}^{-1}.$$

Since the detector contains 2.16×10^{30} ^{37}Cl atoms, this gives a neutrino capture rate of

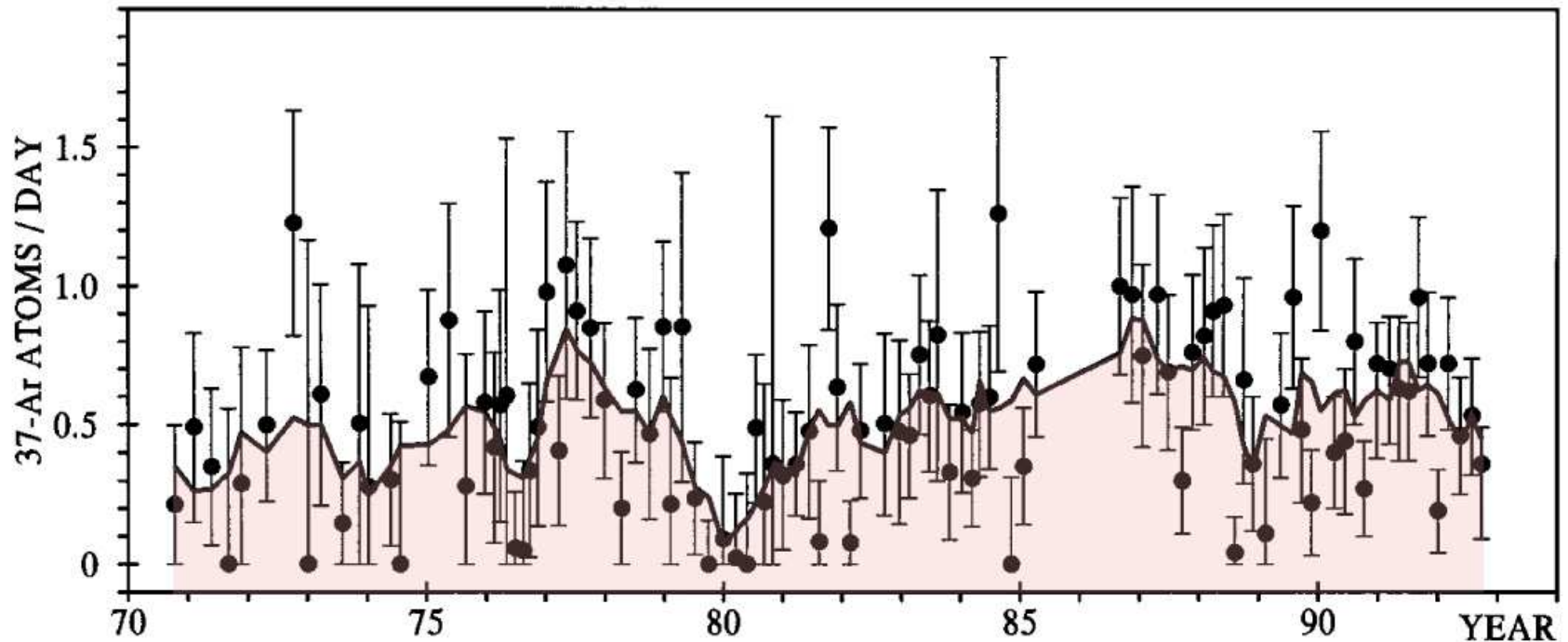
$$\langle \sigma \Phi_{\nu_e} \rangle = 2.56 \pm 0.16_{\text{stat}} \pm 0.16_{\text{syst}} \text{ SNU}.$$

This measurement is to be compared with the SM predictions for the chlorine detector:

$$\langle \sigma \Phi_{\nu_e} \rangle_{\text{theor}} = \left\{ \begin{array}{ll} 7.63 \text{ SNU} & \text{(Sackman, Boothroyd \& Fowler, 1990)} \\ 6.36 \text{ SNU} & \text{(Turck-Chi\`eze \& Lopes, 1993)} \\ (4.2 \pm 1.2) \text{ SNU} & \text{(Dar \& Shaviv, 1994)} \\ (9.3 \pm 1.3) \text{ SNU} & \text{(Bahcall \& Pinsonneault, 1995)} \\ (4.1 \pm 1.2) \text{ SNU} & \text{(Dar \& Shaviv, 1996)} \\ (7.7 \pm 1.2) \text{ SNU} & \text{(Bahcall, Basu \& Pinsonneault, 1998)} \\ (8.1 \pm 1.2) \text{ SNU} & \text{(Bahcall \& Serenelli, 2005).} \end{array} \right.$$

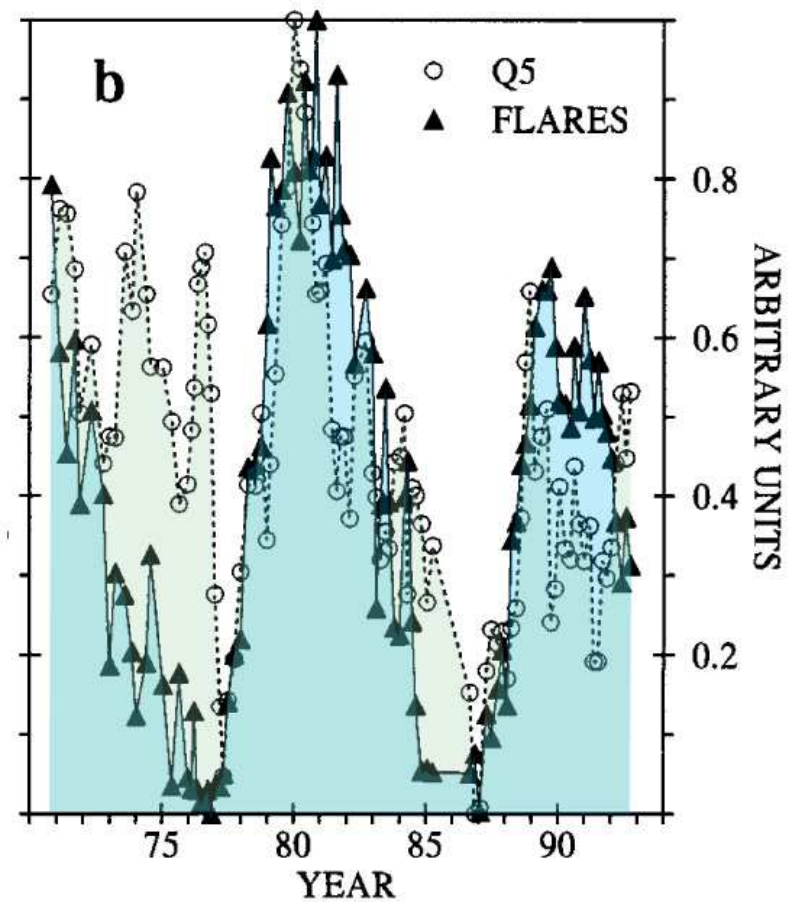
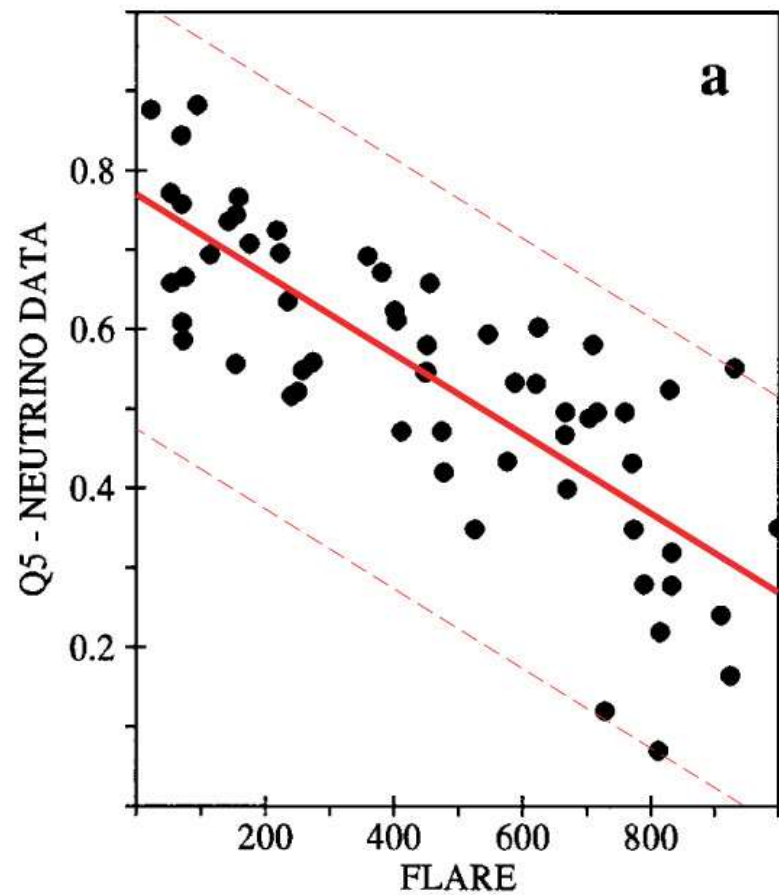
The observed flux is much lower than that predicted (except for the Dar and Shaviv result). This discrepancy between observation and prediction has existed since the early 1970s when the observations of the Homestake detector were first reported.

10.2 Solar Neutrino Puzzle, Number II'

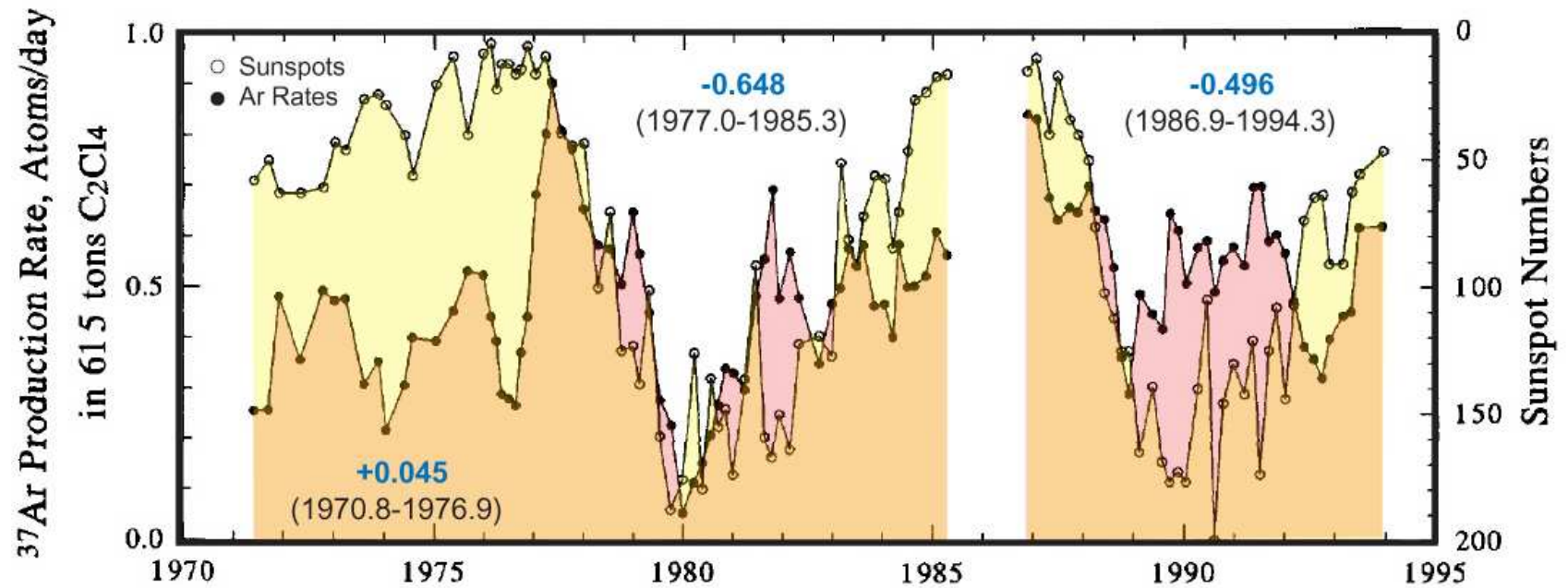


Homestake neutrino data with error bars and 5-point running-averaged values (solid line) from runs No. 18 to No. 126. The 5-point running-average values (Q5) are used to illustrate better the long-term behaviour considering that the original neutrino data are very scattered. Other choices for the smoothing, for instance 3- or 7-point running averages, do not alter qualitatively the results.

[This and next figures are borrowed from S. Massetti, M. Storini, and N. Iucci, "Correlative analyses for Homestake neutrino data," *Nuovo Cim.* **20 C** (1997) 1021–1026.]



Scatter plot of solar flares counts vs. 5-point running averages of Homestake neutrino values in the period 1977 to 1989 (a) and the above data sets plotted as a function of time in the period 1970 to 1992 (b); the neutrino data in (b) are reported with an inverted scale and both data sets are normalized in a way that minimum = 0 and maximum = 1.



The plot shows the 5-point running averages of the Homestake data compared to sunspot numbers; the sunspots are plotted on an inverted scale.

[R. Davis Jr., "A review of measurements of the solar neutrino flux and their variation," Nucl. Phys. B (Proc. Suppl.) 48 (1996) 284–298.]

Some of the conclusions of the authors are:

The Homestake data:

- i) Exhibit a clear modulation of the neutrino signal, almost on the long term.
- ii) Are badly correlated with geomagnetic indices, supporting the hypothesis that the source of the modulation is on the Sun.
- iii) Are correlated with cosmic-rays intensity only in the period 1970-1982, whereas over the total period the correlation is near zero.
- iv) Are better correlated with flare counts than with sunspot numbers. Note that flare phenomena are intimately related to the toroidal component of the heliomagnetic field. The best correlated period (1977-1989) corresponds to that characterized by a reinforcement of the interplanetary magnetic-field intensity, suggesting again an enhancement of the global heliomagnetic field.

More or less similar conclusions were found in the regression analyses reported by many authors. These results suggest a pulsating character of the Homestake data and their anticorrelation with the solar magnetic activity (sunspot or flare numbers).

A veritable host of new ideas was brought forth to resolve the solar neutrino puzzles. Let's consider a (very incomplete) list of these solutions.

10.3 Solutions

10.3.1 Astrophysics and/or Nuclear Physics

- Models with convective mixing of the solar core [*Ezer & Cameron, 1968; Shaviv & Salpeter, 1968; Bahcall, Bahcall & Ulrich, 1968*]
- Models with turbulent diffusion of ${}^3\text{He}$ [*Schatzman 1969*]
- An overabundance of ${}^3\text{He}$ in the present Sun [*Kocharov & Starbunov 1970*]
- Models with the strong central magnetic field (the energy density of the Sun's central magnetic field $|\mathbf{B}|^2/8\pi$ is a few percent of the gas pressure) [*Abraham & Iben 1971; Bahcall & Ulrich 1971; Bartenwerfer 1973; Parker 1974; Ulrich 1974*]
- A secular instability such that the presently observed solar luminosity does not equal the current energy-generation rate [*Fowler 1968, 1972; Sheldon 1969*]
- Models with low heavy elements ("low Z ") abundances in the solar interior [*Bahcall & Ulrich 1971; Schatzman 1981; Maeder 1990*].
- An instability of the Sun that makes now a special time [*Fowler 1972; Dilke & Gough 1972*]
- A low-energy resonance in the ${}^3\text{He} + {}^3\text{He} \rightarrow {}^4\text{He} + 2{}^1\text{H}$ reaction [*Fowler 1972; Fetisov & Kopysov 1972*]
- Helium core (the Sun is assumed to be in a later stage of stellar evolution, such that hydrogen is burned-out and the core is made of helium) [*Prentice 1973*]

- Models with a rapidly rotating solar interior (the rotation is lowering the central pressure and temperature) [*Demarque, Mengel & Sweigert 1973; Roxburgh 1974; Rood & Ulrich 1974*]
- Rotation plus magnetic fields [*Snell, Wheeler & Wilson 1976*]
- A half-solar mass core of large heavy element abundance that survived the big bang and subsequently accreted another half solar mass at the time of the formation of the solar system [*Hoyle 1975*]
- A departure from the Maxwellian distribution [*Clayton et al. 1975*]
- A fractionation of the primordial hydrogen and helium [*Wheeler & Cameron 1975*]
- Models with hydrogen mixing into the core by turbulent diffusion [*Schatzman 1981; Maeder 1990*]
- Mixing of ^3He due to rapid filamental flow downward [*Cummings & Haxton, 1996*]
- Temporal and spatial variations in temperature [*Dar & Shaviv, 1998*]
- Collective plasma processes [*Salpeter & Van Horne, 1969; ...; Tsytovich et al. 1995, Dar & Shaviv, 1998*]
- A new solar model in which the Sun is formed by accretion of fresh SN debris on the collapsed core of a supernova; neutron emission from the SN remnant at the solar core; neutron decay major elements are Iron, nickel, oxygen, silicon [*Manuel, Miller & Katragada, 2003*]

10.3.2 Nonstandard Neutrino Properties

- Vacuum neutrino oscillations [*Gribov & Pontecorvo 1969*]
- An appreciable (anomalous) magnetic moment for the neutrino [*Cisneros 1971; Okun, Voloshin & Vysotsky, 1986*]
- Neutrino instability [*Bahcall, Cabibbo & Yahil 1972*]
- Goldstone neutrinos resulting from a spontaneous breakdown of supersymmetry [*Das 1984*].
- Matter enhanced neutrino oscillations [*Wolfenstein 1978; ...; Mikheev & Smirnov, 1985*] $\implies \gtrsim 10,000$ papers, 100s of alterations, 10s of innovations;
- Matter-induced neutrino decay $\nu \rightarrow \bar{\nu} + \text{Majoron}$ [*Bereziani & Vysotsky 1987*]
- Resonant neutrino spin–flavor precession in the solar magnetic field [*Akhmedov 1987; Lim & Marciano 1988*]
- Nonstandard (in particular, flavor-changing) neutrino interactions with matter [*Roulet, 1991; Guzzo, Masiero & Petcov 1991, Barger, Phillips & Whisnant 1991*]
- A nonstandard (strong enough) $\nu_e \gamma$ interaction that would cause the neutrinos to disappear before they leave the Sun or make them lose energy towards detection thresholds [*Dixmier, 1994*]

10.3.3 Exotics and Science Fiction

- Quark catalysis [*Libby & Thomas 1969; Salpeter 1970*]
- Accretion onto a central black hole (the model assumes that the Sun's energy did not come from fusion, rather from release of energy from accretion onto a black hole at the center of the Sun) [*Clayton, Newman & Talbot 1975*]
- Multiplicative mass creation [*Maeder 1977*]
- WIMPs as a source of solar energy [*Faulkner & Gilliland 1985; Spergel & Press 1985; Press & Spergel 1985; Faulkner, Gough & Vahia 1986; Gilliland et al. 1986*]
- Violation of equivalence principle [*Gasperini, 1988, 1989; Halprin & Leung 1991*]
- Daemon^a catalysis (it is assumed that daemons are capable of catalyzing proton-fusion reactions, which may account for the observed solar neutrino deficiency) [*Drobyshevski 1996, 2002*]

^a**Daemon** = **Dark Electric Matter Object**, a hypothetical Planckian particle carrying a negative electric charge of up to $Z = 10$.

11 Ga-Ge detectors (SAGE, GALLEX, GNO)

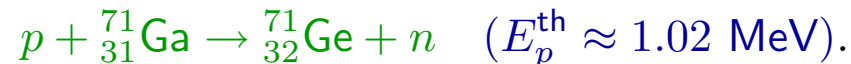
These solar neutrino experiments are based on the reaction (originally proposed by V. A. Kuzmin in 1965)



Then the radioactive germanium decays back to gallium:



Backgrounds for the gallium experiments are caused by ${}^{71}\text{Ge}$ production through non-neutrino mechanisms

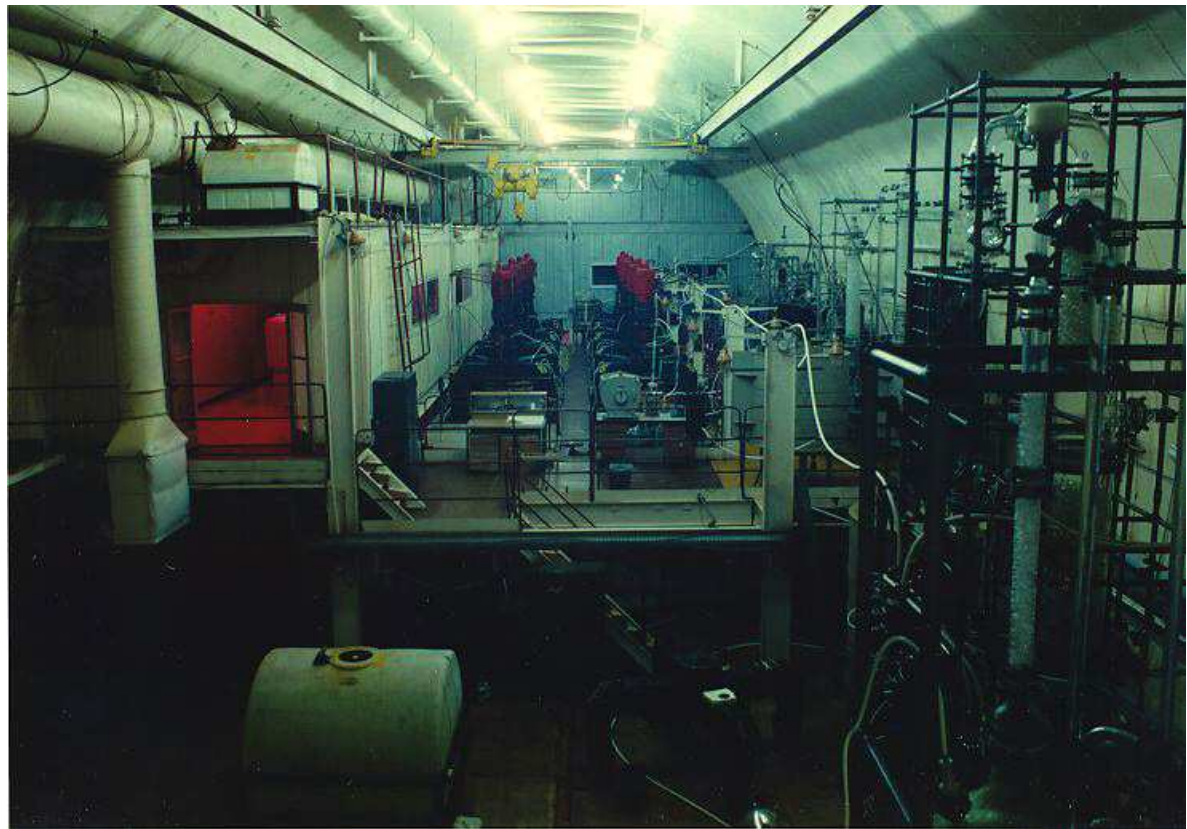


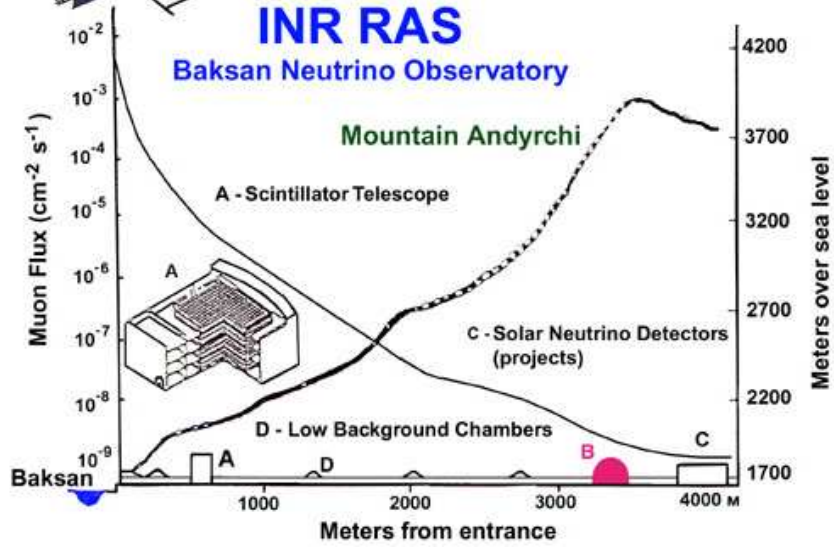
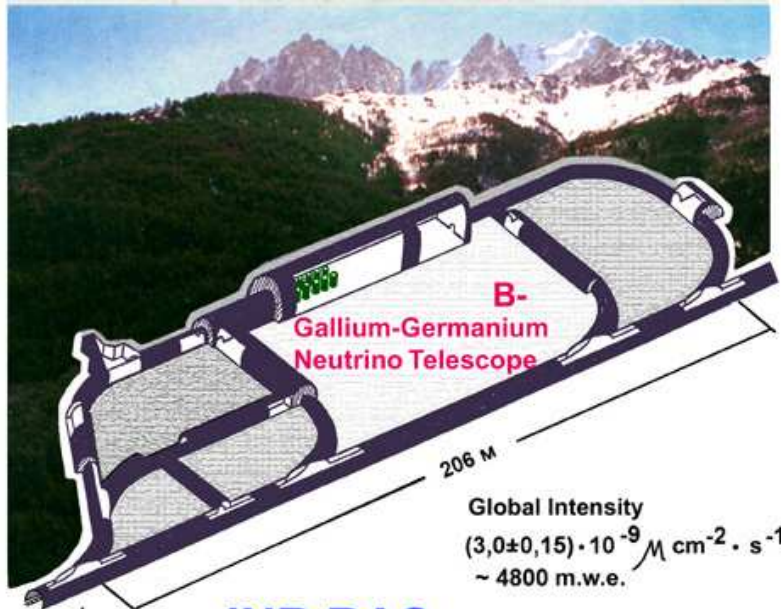
Like in the chlorine experiment, the protons may be produced by cosmic muon interactions, fast neutrons or residual radioactivity. Radon gas and its daughter products are also a large cause of background; the radon half-life is about 3.8 days.

^aThis is the weighted average of all the available measurements for the neutrino energy threshold of this reaction computed (including estimates of systematic errors) by G. Audi and A. H. Wapstra.

In the **SAGE** (**S**oviet–**A**merican **G**allium solar neutrino **E**xperiment), the ^{71}Ge atoms are chemically extracted from a **50-metric ton** target of **gallium metal** and concentrated in a sample of **germane** gas (GeH_4) mixed with **xenon**.

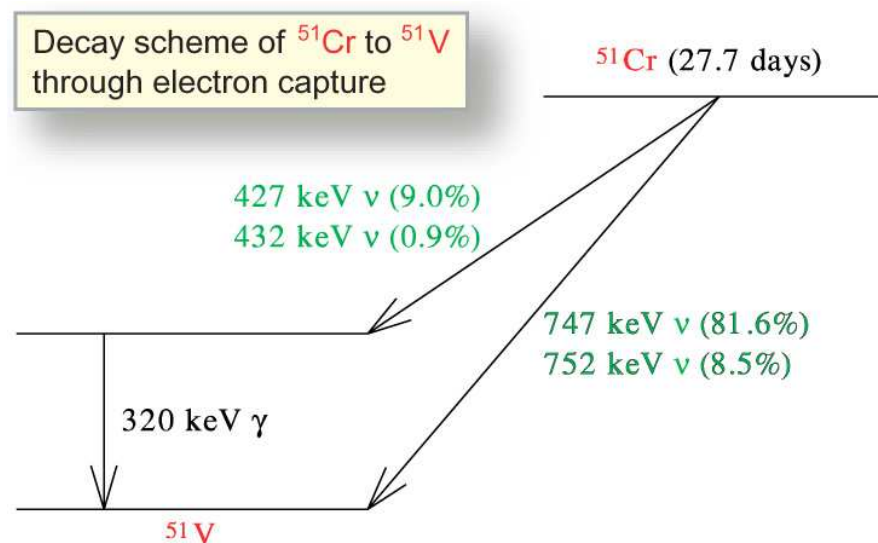
The the ^{71}Ge atoms are then individually counted by observing their decay back to ^{71}Ga in a small proportional counter. The SAGE collaboration regularly performs solar neutrino extractions, every **four weeks**, reducing the statistical error, and explores further possibilities for reducing the systematic uncertainties.





To check the response of the SAGE experiment to low-energy neutrinos, a source of ^{51}Cr was produced by irradiating 512.7 g of 92.4%-enriched ^{50}Cr in a high-flux fast neutron reactor.

This source, which mainly emits monoenergetic 747-keV neutrinos, was placed at the center of a 13.1 ton target of liquid gallium and the cross section for the production of ^{71}Ge by the inverse beta decay reaction $^{71}\text{Ga}(\nu_e, e^-)^{71}\text{Ga}$ was measured to be



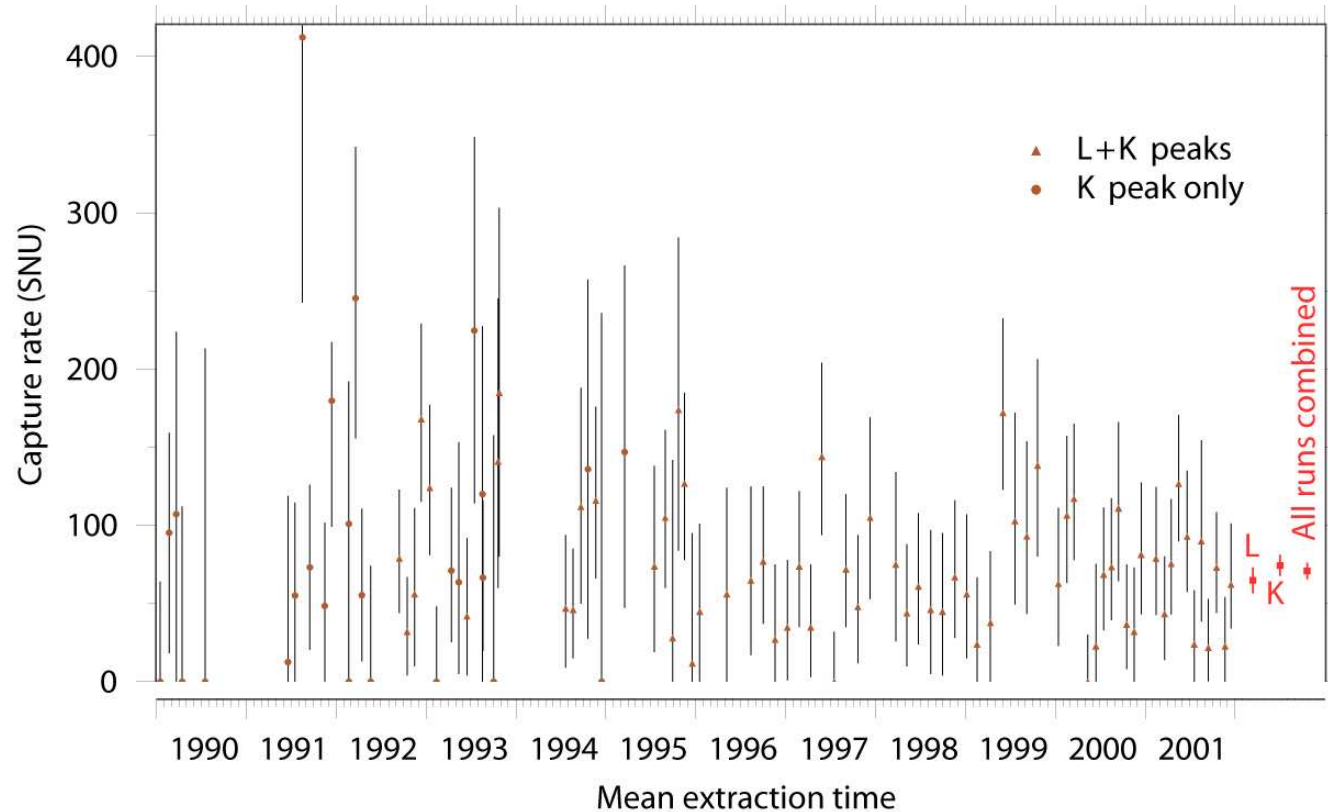
[From J. N. Abdurashitov *et al.*, "Measurement of the response of a gallium metal solar neutrino experiment to neutrinos from a ^{51}Cr source," *Phys. Rev. C* **59** (1999) 2246–2263.]

$$(5.55 \pm 0.60_{\text{stat}} \pm 0.32_{\text{stat}}) \times 10^{45} \text{ cm}^2.$$

The ratio of this result to the theoretical cross section of Bahcall and of Haxton are

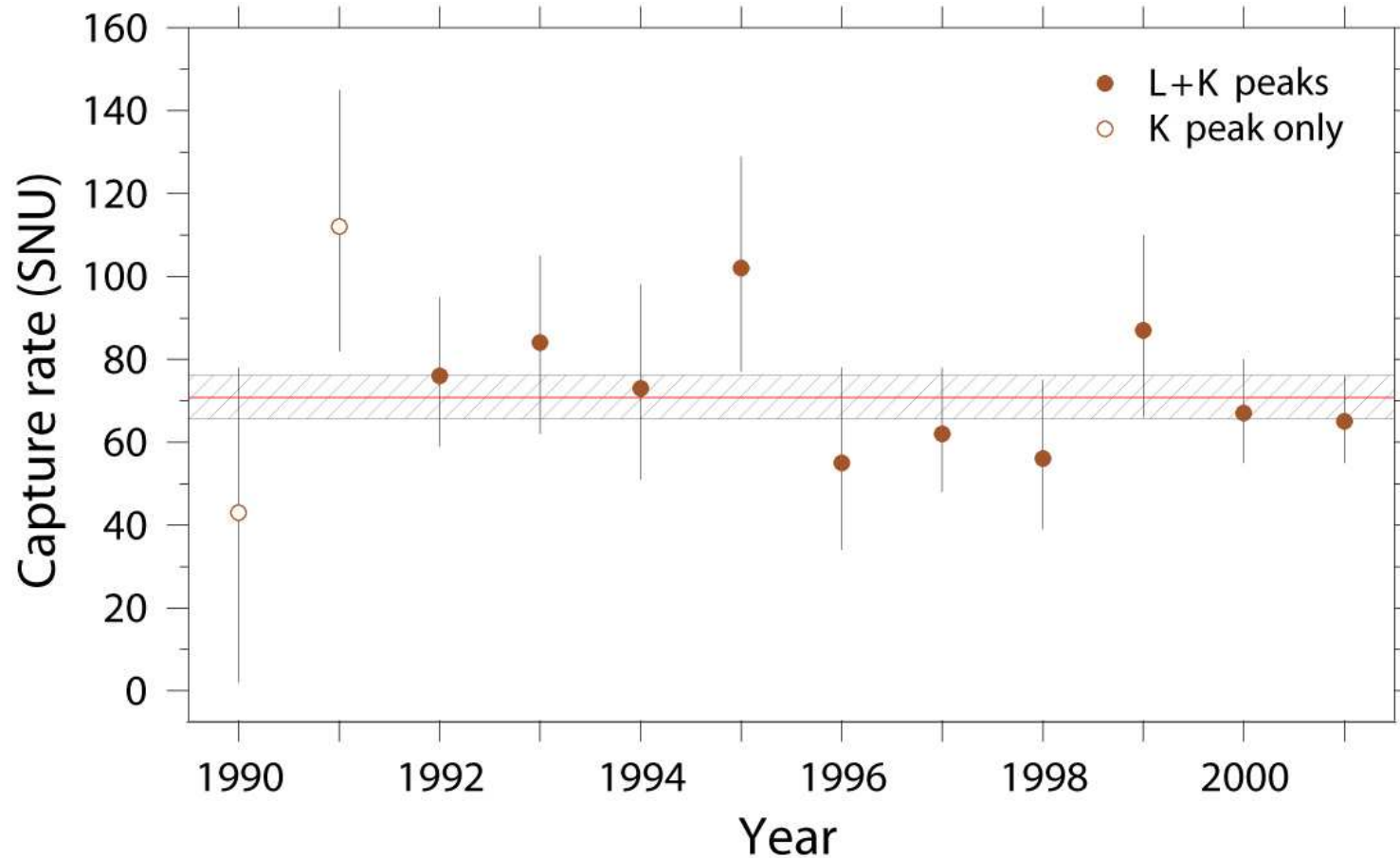
$$0.95 \pm 0.12 (\text{exp}) \begin{matrix} +0.035 \\ -0.027 \end{matrix} (\text{theor}) \quad \text{and} \quad 0.87 \pm 0.11 (\text{exp}) \pm 0.09 (\text{theor}),$$

respectively. This good agreement between prediction and observation implies that the overall experimental efficiency is correctly determined and provides considerable evidence for the reliability of the solar neutrino measurement.



The capture rate from all SAGE extractions versus time: the triangles are for the L and K peaks and the circles are for the K peak alone; the vertical bars near each point correspond to a statistical error of 68%. The average rates for the L , K , and $L + K$ peaks are also shown.

[This and next figures are borrowed from J. N. Abdurashitov *et al.*, “Solar neutrino flux measurements by the Soviet-American Gallium Experiment (SAGE) for half the 22-Year Solar Cycle,” *Zh. Eksp. Teor. Fiz.* **122** (2002) 211–226 [*J. Exp. Theor. Phys.* **95** (2002) 181–193] (astro-ph/0204245).]



Results of the measurements combined by years; open and filled symbols refer to K and $K + L$ peaks, respectively; the hatched region corresponds to the SAGE result of $70.8^{+5.3}_{-5.2}$ (stat) $^{+3.7}_{-3.2}$ (syst) SNU. The data shown have a statistical error of 68%. The neutrino capture rate was constant during the entire data acquisition period with a 83% probability.



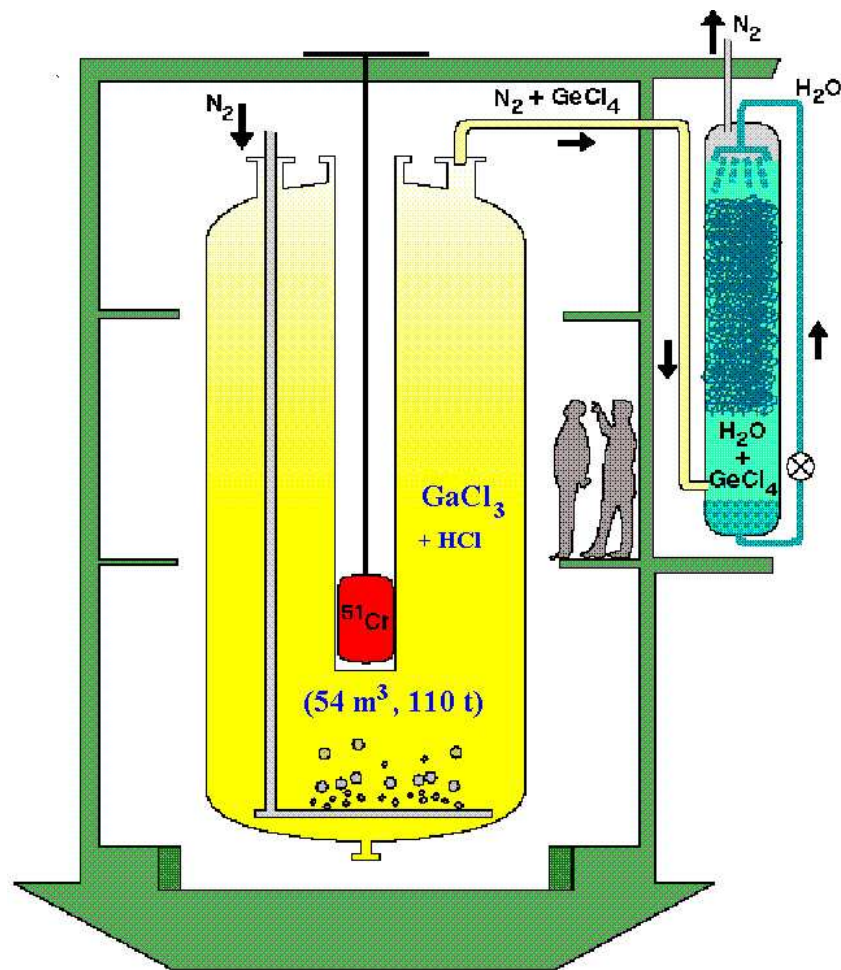
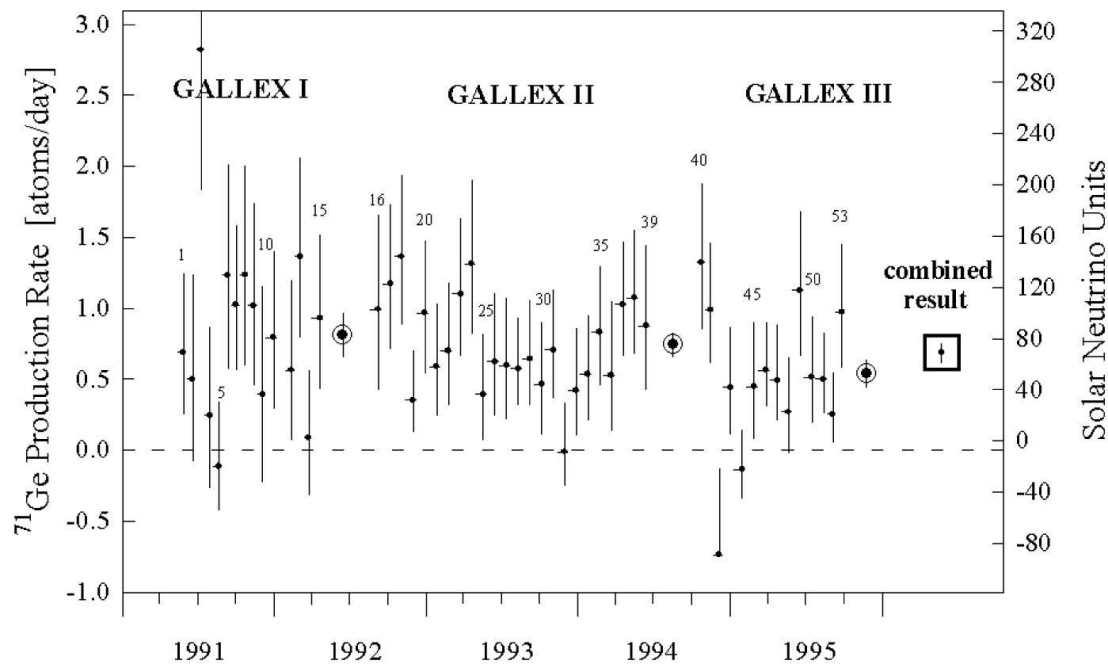


Figure on the left shows a scheme of the GALLEX detector tank with the absorber system and the Chromium source inserted inside the thimble.

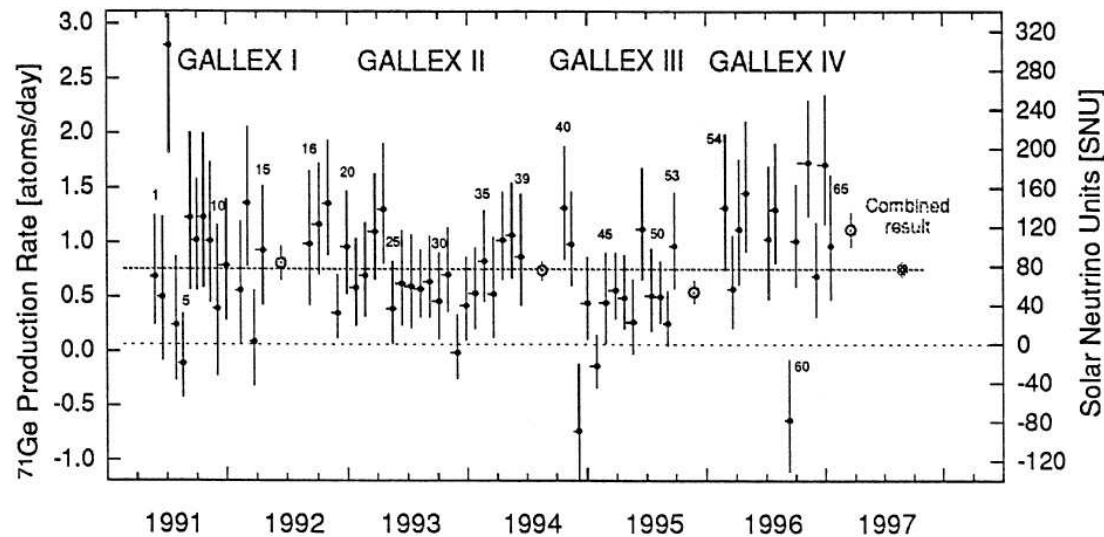
The experimental procedure for GALLEX is as follows: 30.3 tons of gallium in form of a concentrated $\text{GaCl}_3\text{-HCl}$ solution are exposed to solar neutrinos. In $\text{GaCl}_3\text{-HCl}$ solution, the neutrino induced ^{71}Ge atoms (as well as the inactive Ge carrier atoms added to the solution at the beginning of a run) form the volatile compound GeCl_4 , which at the end of an exposure is swept out of the solution by means of a gas stream (nitrogen). The nitrogen is then passed through a gas scrubber where the GeCl_4 is absorbed in water.

The GeCl_4 is finally converted to GeH_4 , which together with xenon is introduced into a proportional counter in order to determine the number of ^{71}Ge atoms by observing their radioactive decay. [From URL: <http://www.mpi-hd.mpg.de/nuastro/gallex/detector.htm>.]



GALLEX I, II, and III single run overview. Results for the 14 solar neutrino runs of GALLEX III (labels 40-53), shown together with the earlier results from GALLEX I (labels 1-15) and from GALLEX II (labels 16-39).

The left hand scale is the measured ^{71}Ge production rate; the right hand scale, the net solar neutrino production rate (SNU) after subtraction of side reaction contributions. Error bars are $\pm 1\sigma$, statistical only. The label “combined” applies to the mean global value for the total of all 53 runs. The visibility is enhanced by a square box, but its error is the small bar inside the box. Horizontal bars represent run duration; their asymmetry reflects the “mean age” of the ^{71}Ge produced.



Summary of the results of GALLEX individual solar runs closed points. The left hand scale is the measured ^{71}Ge production rate; the right hand scale, the net solar neutrino production rate SNU after subtraction of side reaction contributions.

Error bars are $\pm 1\sigma$ statistical only. Open circles are the combined results for each of the measuring periods, GALLEX I, II, III and IV. The label “combined” applies to the mean global value for the total of all 65 runs. Horizontal bars represent run duration; their asymmetry reflects the “mean age” of the ^{71}Ge produced. The combined result which comprises 65 solar runs, is $77.5 \pm 6.2^{+4.3}_{-4.7} (1\sigma)$ SNU. The GALLEX experimental program to register solar neutrinos has now been completed.

In April 1998, GALLEX was succeeded by a new project, the [Gallium Neutrino Observatory \(GNO\)](#), with newly defined motives and goals.

[From W. Hampel *et al.* (GALLEX Collaboration), “GALLEX solar neutrino observations: Results for GALLEX IV,” *Phys. Lett. B* **447** (1999) 127–133.]

12 H₂O detectors (Kamiokande and Super-Kamiokande)

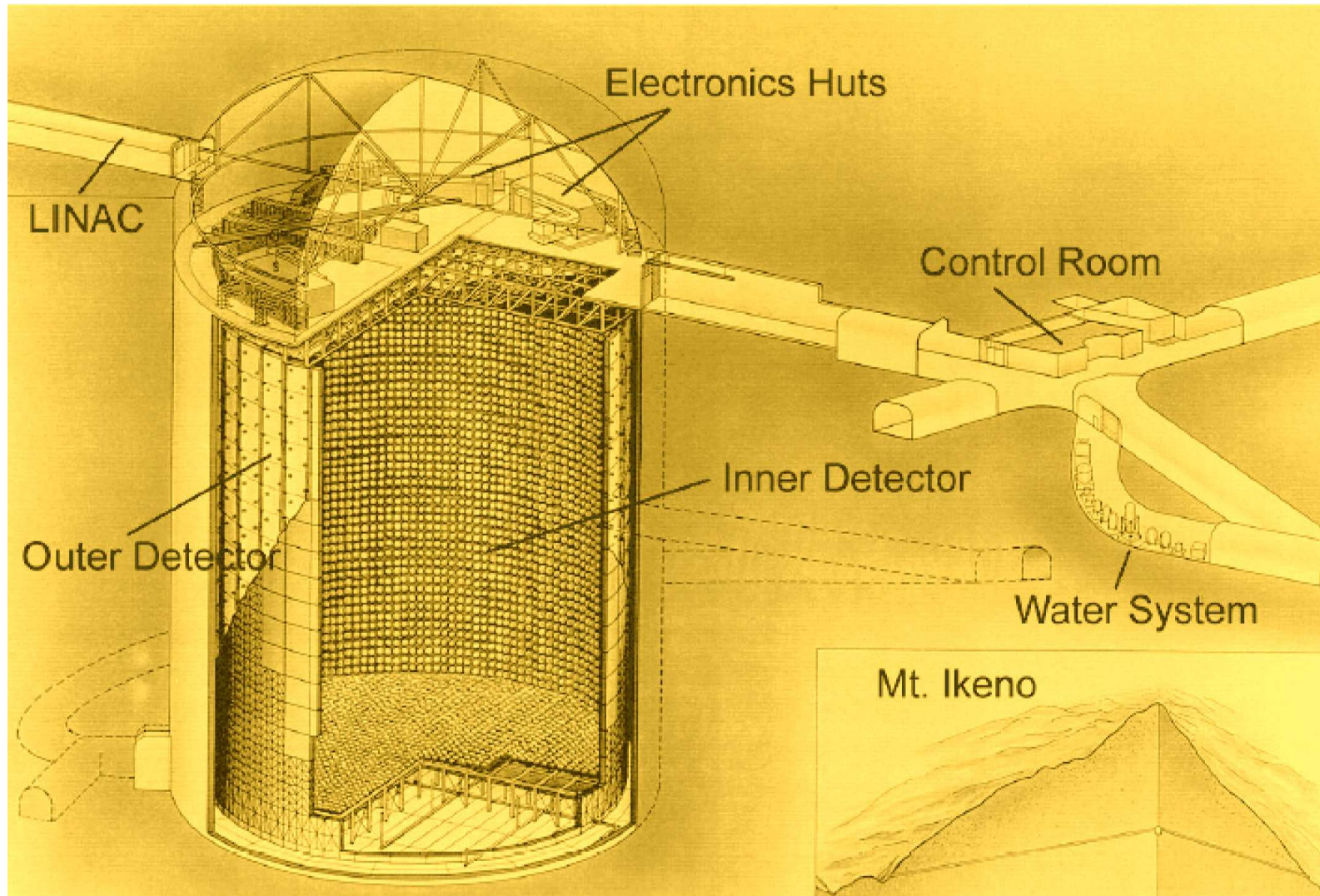
Super-Kamiokande (SK), as well as its precursor Kamiokande (K), is an underground ring-imaging water-Cherenkov neutrino detector located in the Kamioka mine, Japan (137.32° E longitude, 36.43° N latitude).^a

SK is a cylindrical tank (41.4 m in height, 39.3 m in diameter) filled with 50 kton of ultra-pure water, and situated under about 1 km of rock (2700 m.w.e.). The rock provides a shield against the cosmic-ray muons: the muon count rate in the detector is reduced to 2.2 Hz.

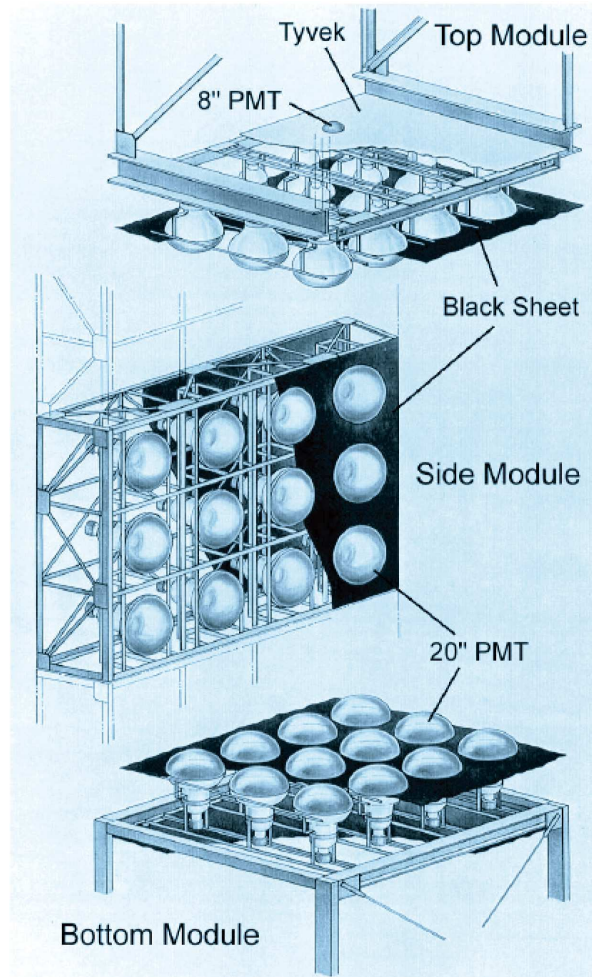
The outer walls of the tank are constructed from 5 cm thick stainless steel sheets, which are attached to the rock cavity and backed by concrete. About 2 m in from the walls is a 1 m wide structure of stainless beams that provide the backbone for the mounting PMTs. The structure divides the whole detector tank into an inner detector (ID) and outer detector (OD).

The 11,146 inward-facing ID PMTs that are used in event detection are mounted on the inside of the steel beam structure and are surrounded with black polyethylene sheets to minimize light reflection within the ID region. They provide a photo-coverage of 40%.

^aSee Part I of these lectures for the details relevant to the atmospheric neutrino studies with K and SK detectors.



[This and next figures are borrowed from D. Turčan, "Solar neutrino at Super-Kamiokande solving the solar neutrino puzzle via neutrino flavor oscillations," Ph. D. Thesis, Faculty of the Graduate School, Maryland University, 2003.]



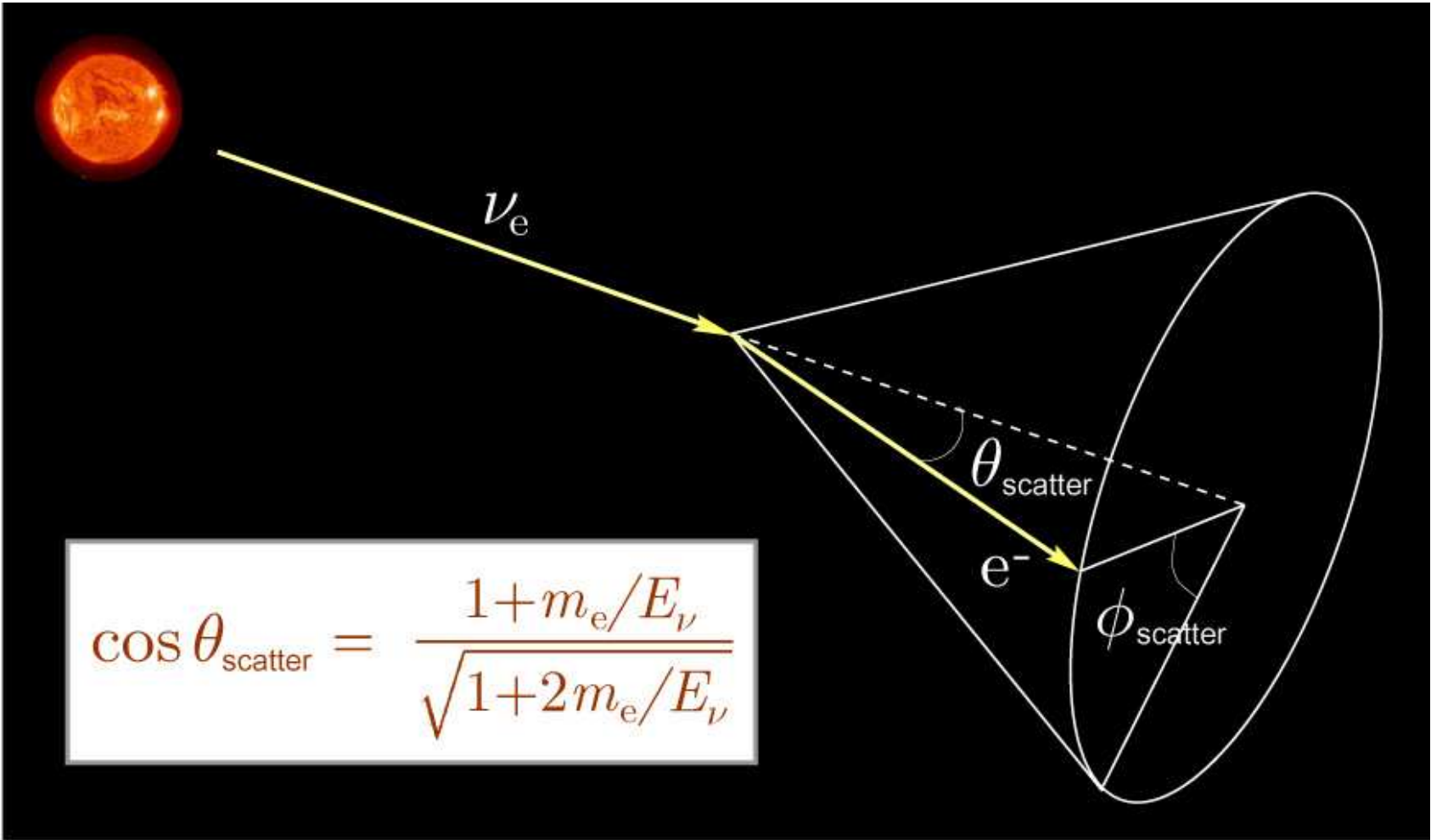
The entire ID region is a volume of 32.5 kt while the region actually used in the analysis is 2 m inside the PMT structure and represents a fiducial volume of 22.5 kt. There are at the least two reasons for excluding the 10 kt volume:

1) It is necessary to reduce the background from radioactive decays of radon which is particularly prominent near the PMTs and beams. The radon is still the main source of background in the fiducial volume, but the 2 m reduction brings the background to a manageable level.

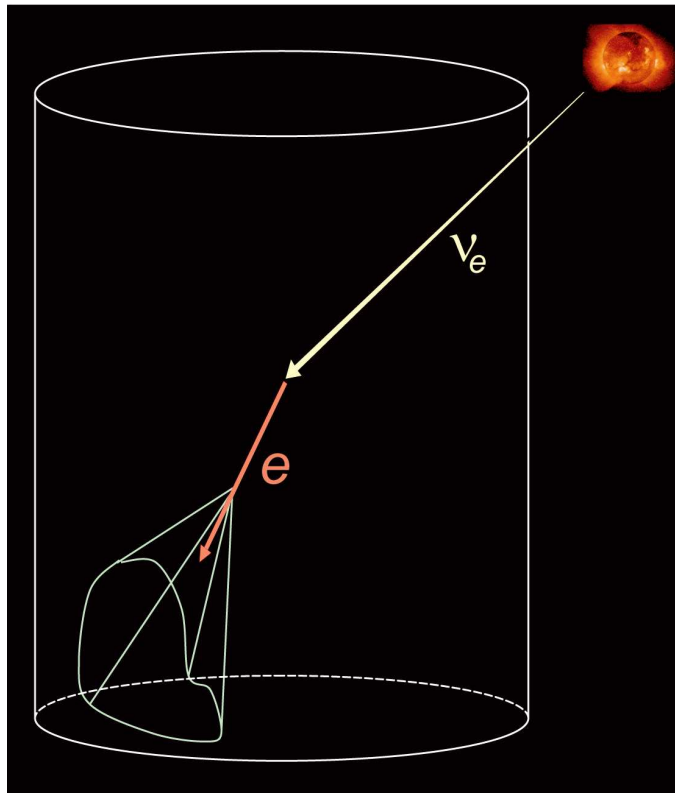
2) There is a need for multiple PMT hits: if an event happens very near a PMT, all the light will be collected by that same PMT, and there will not be sufficient information for reconstructing that event. The PMTs used in SK's ID are 50 cm in diameter; they are largest PMTs in the world, designed and constructed especially for the SK experiment.

The OD, which surrounds the steel structure, has 1885 outward-facing 20 cm PMTs.

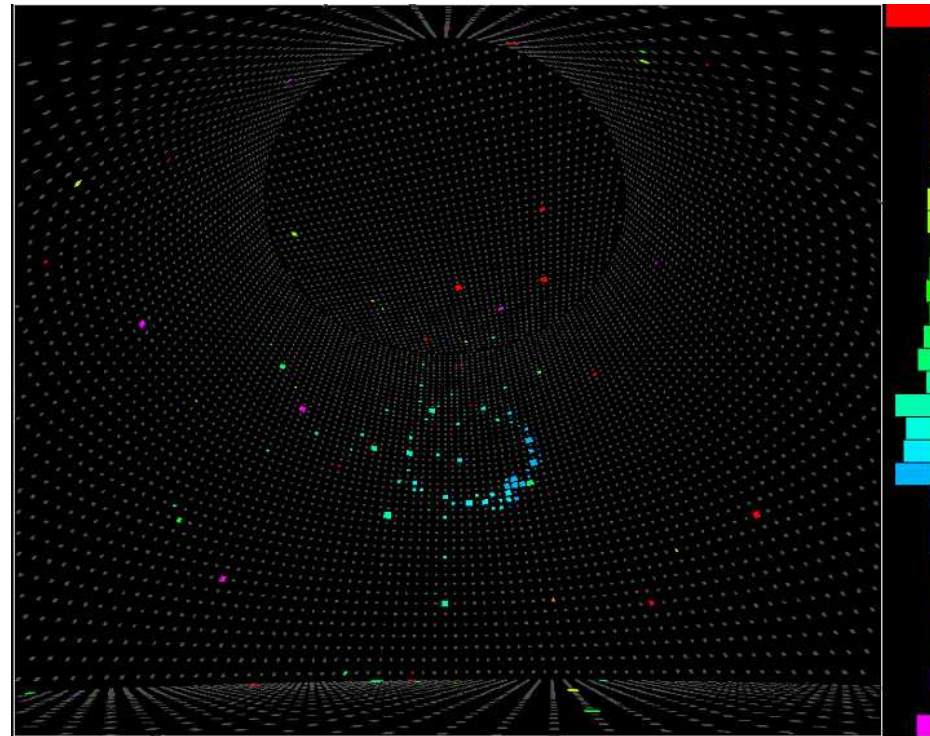
The top of the tank is a flat sheet that covers the entire area of the detector. It is under a dome, which is lined with a polyurethane material ("Mineguard"), to reduce the radon emanation and erosion from the rock walls.



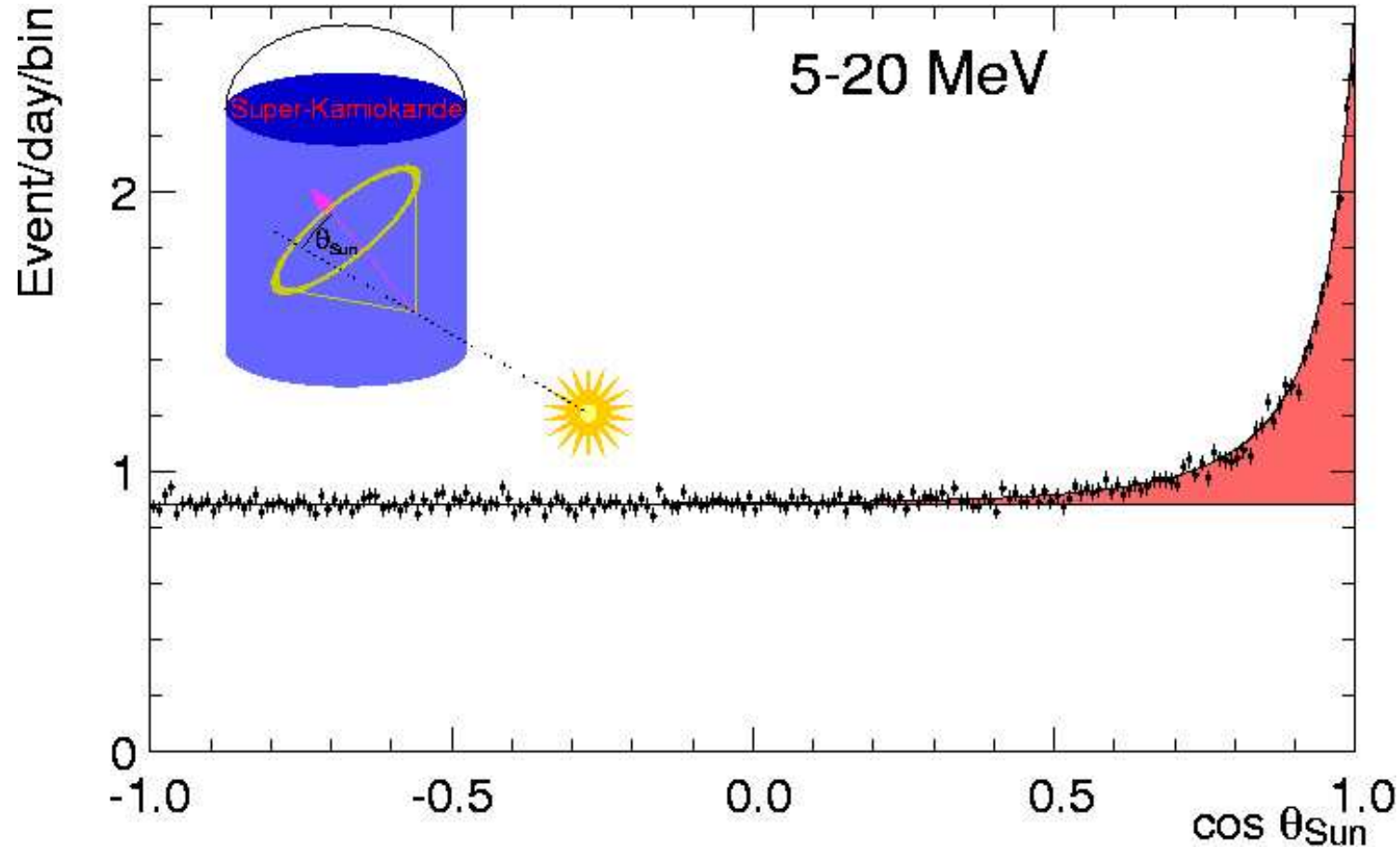
$$\cos \theta_{\text{scatter}} = \frac{1 + m_e/E_\nu}{\sqrt{1 + 2m_e/E_\nu}}$$



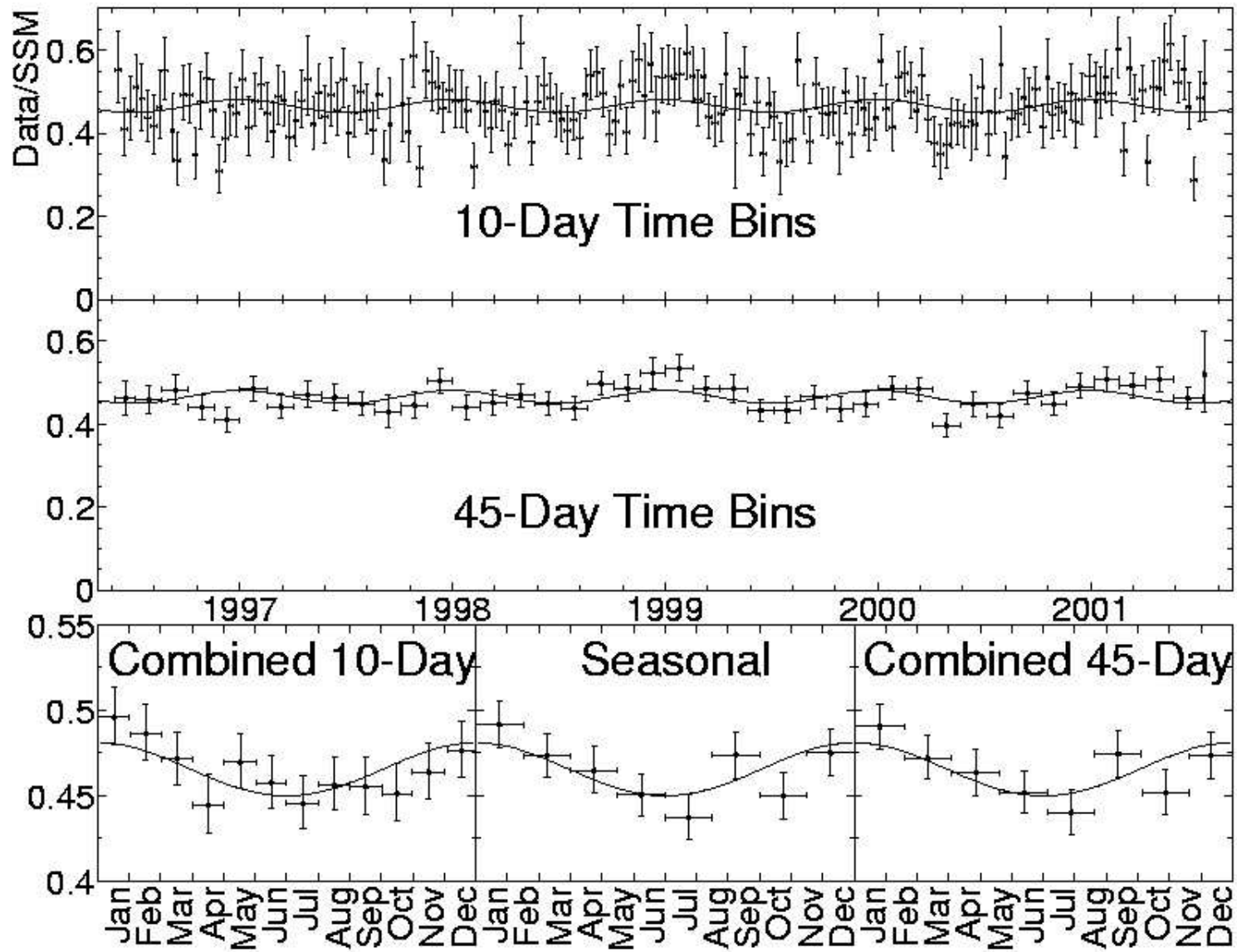
Super-Kamiokande uses elastic scattering of neutrinos from electrons. Cherenkov radiation emitted by the electron is detected by phototubes. The image looks like a diffuse ring on the detector walls.



A real event recorded in the Super-Kamiokande detector on 1998-03-12 14:08:40. It is about 12.5 MeV and has an unusually nice, well-defined ring. The color scale is time. This event was found by Mark Vagins. [From I. Semeniuk, "Feature – Astronomy and the New Neutrino," *Sky & Telescope*, September 2004, pp. 42-48; see also Tomasz Barszczak, URL: <http://www.ps.uci.edu/~tomba/sk/tscan/pictures.html>.]



Angular distribution of solar neutrino event candidates in Super-Kamiokande-I. The angular deviation between the solar and the reconstructed direction of events with total energies ranging between 5 and 20 MeV is shown. From the strong forward peak due to elastic scattering of solar ${}^8\text{B}$ neutrinos with electrons $22,400 \pm 200_{\text{stat}}$ neutrino interactions were observed in 22,500 metric tons of water during 1496 live days.



The observed solar neutrino interaction rate is

$$0.465 \pm 0.005^{+0.016}_{-0.015}$$

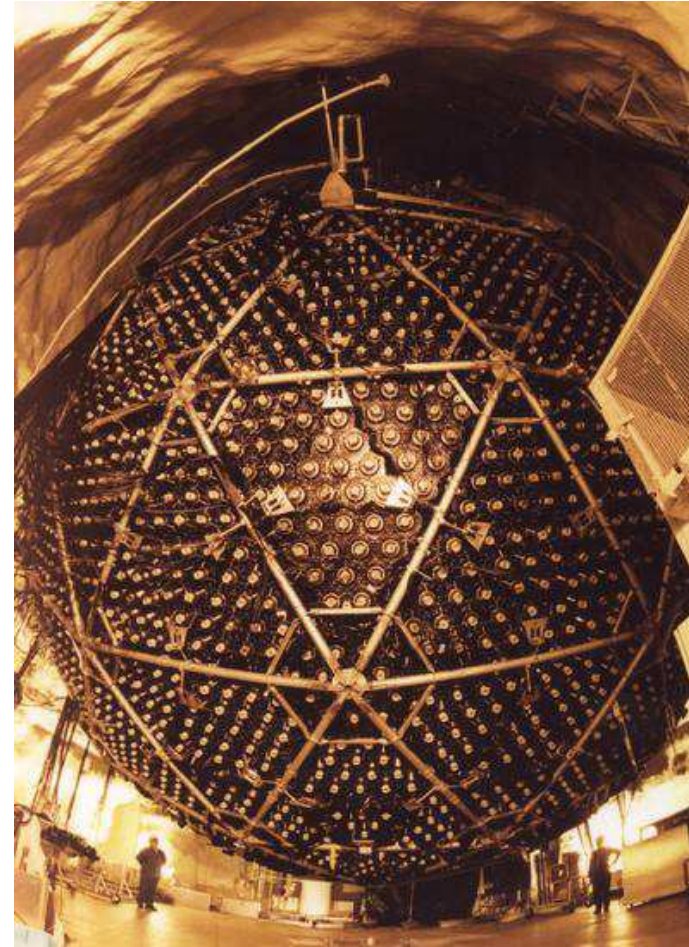
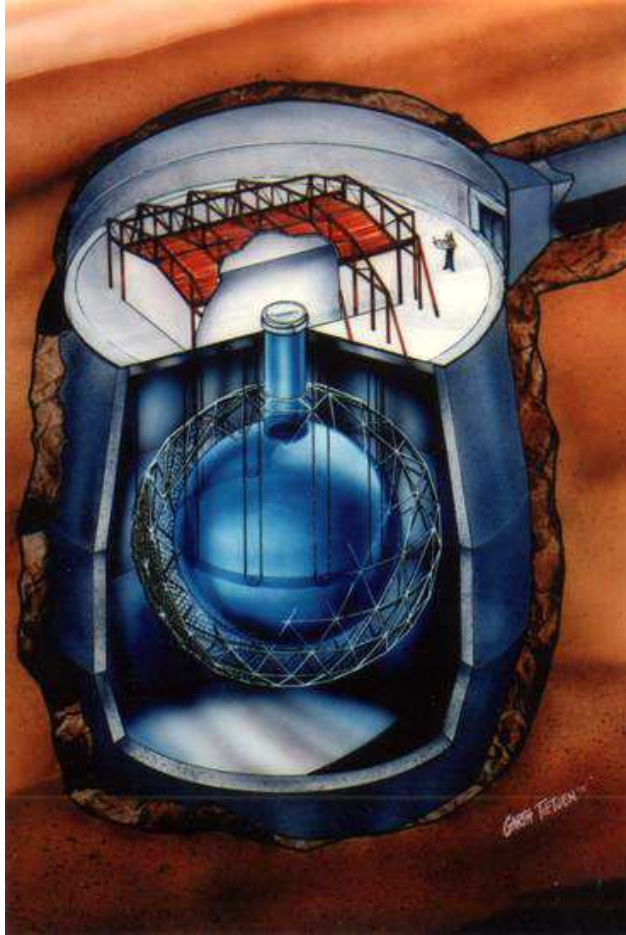
of the rate expected by the standard solar model (SSM). Assuming only solar ν_e the observed rate corresponds to a ${}^8\text{B}$ flux of

$$\Phi ({}^8\text{B}) = (2.35 \pm 0.02_{\text{stat}} \pm 0.08_{\text{syst}}) \times 10^6 \text{ cm}^{-2}\text{s}^{-1}.$$

All uncertainties given for the time variation data are only statistical and based on an asymmetric Gaussian approximation of the underlying likelihood functions obtained by an unbinned maximum likelihood fit to the $\cos(\theta_{\text{Sun}})$ distributions.

The top two panels show the Super-Kamiokande-I rate as a function of time. The topmost panel uses bins of 10 days width, the middle panel displays 45 day bins. The lower left panel combines the 10-day bins into 12 bins to show the yearly cycle assuming asymmetric Gaussians for the probability density functions. The lower right panel shows the yearly variation data in 8 bins obtained from a similar combination of the 45-day data bins. The middle right panel is the yearly variation data in those same 8 bins, but resulting directly from a maximum likelihood fit to the $\cos(\theta_{\text{Sun}})$ distribution.

13 D₂O detector SNO



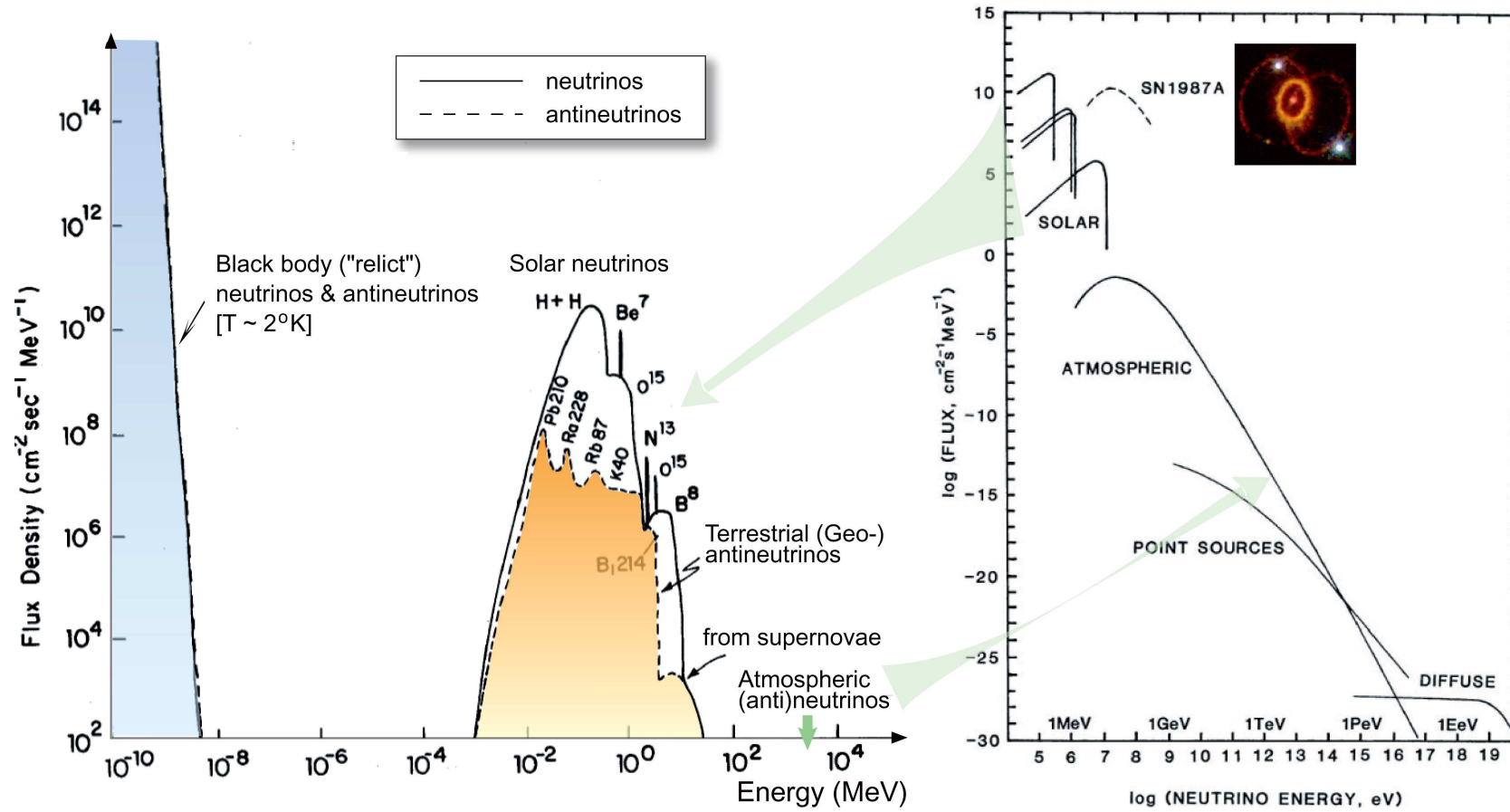
Artist's concept of the SNO detector (left) and a view of the SNO detector after installation of the bottom PMT panels, but before cabling (photo by Ernest Orlando, Lawrence Berkeley National Laboratory).

[From The Sudbury Neutrino Observatory webpage, <<http://www.sno.phy.queensu.ca/sno/>>.]

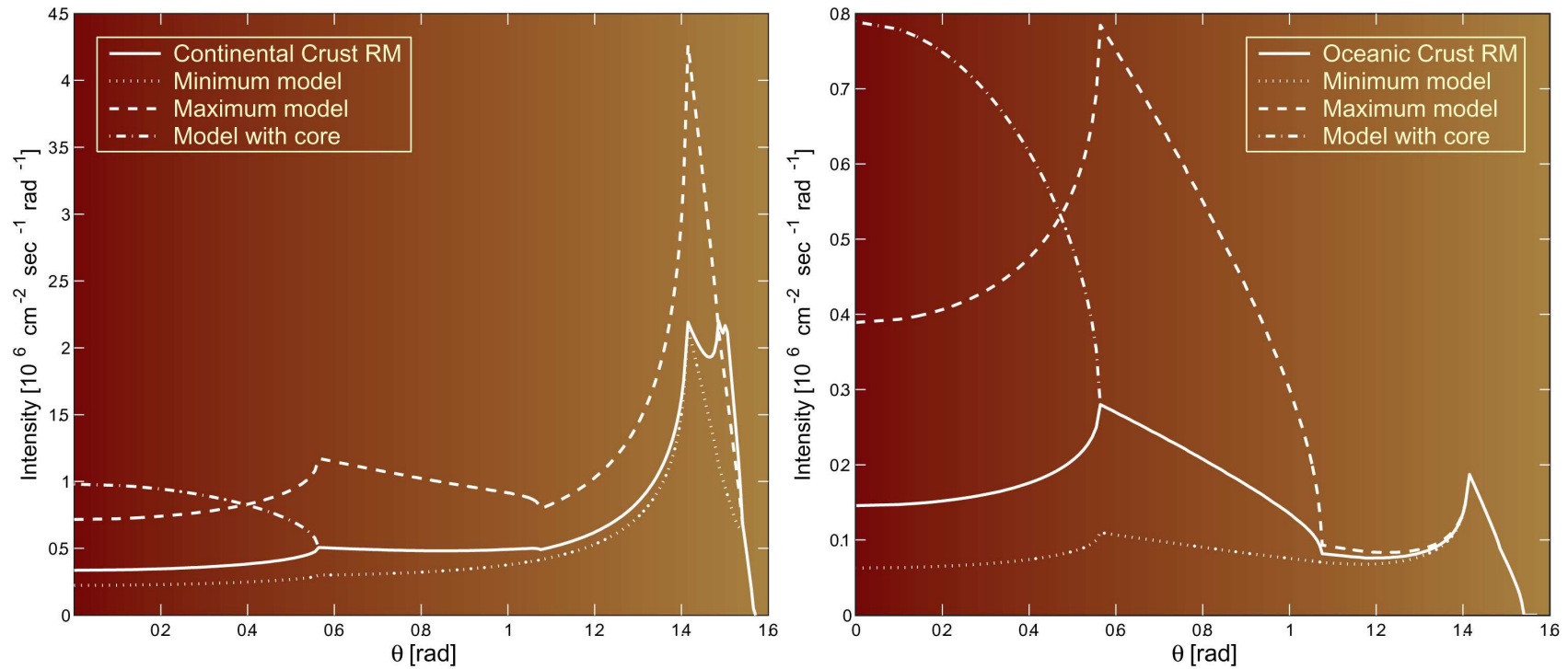
Part IV

REACTOR NEUTRINO EXPERIMENTS

14 Terrestrial neutrinos



[From L. M. Krauss, S. L. Glashow, and D. N. Schramm, "Antineutrino astronomy and geophysics," *Nature* **310** (1984) 191–198 (left) and A. M. Bakich, "Aspects of neutrino astronomy," *Space Sci. Rev.* **49** (1989) 259–310 (right).]



Panel on the left shows the angular dependence of the geo-antineutrino intensity for the continental crust reference model and its variations after taking into account the 1.8 MeV energy threshold of the detection reaction $\bar{\nu}_e + p \rightarrow e^+ + n$ and the neutrino energy spectra (Fermi functions). Panel on the right shows the same but for the oceanic (or “Hawaii”) crust reference model and its variations.

[From K. A. Hochmuth *et al.*, “Probing the Earth’s interior with the low energy neutrino astronomy detector,” [hep-ph/0509136](https://arxiv.org/abs/hep-ph/0509136).]

**15 Past and current (Bugey, Gösgen, Krasnoyarsk,
Palo Verde, Savannah River Site, Braidwood, ...)**

16 CHOOZ, Double-CHOOZ, Triple-CHOOZ

17 KamLAND

**18 What next? (Angra, DaYa-Bay, KASKA,
TEXONO,...)**

Part V

NEUTRINO TELESCOPES

19 Detectors for high-energy neutrino astronomy

In 1960, Markov^a and Reines^b independently suggested to catch high-energy cosmic neutrinos via their charged current interactions using the ocean as a detector medium by observing the Cherenkov light of the produced muons and, simultaneously, as a screen for the cosmic-ray and solar light backgrounds.^c Up-going muons can be identified in a background of down-going, cosmic ray muons which are more than 10^5 times more frequent for a depth of about 12 km. The Earth is therefore also serves as a part of the detector, being the natural filter and “discriminator”. This makes neutrino detection possible over the hemisphere of sky faced by the bottom of the detector.

It was thought that the ocean is a rather inexpensive target, the detector can be build modular and enlarged when necessary. The detector can take the advantage of the rising cross section for neutrino-nucleon interactions with energy. As the range of the

^aM. A. Markov, in Proc. of 1960 Annual International Conf. on High Energy Physics at Rochester, edited by E. C. G. Sudarshan, J. H. Tinlot and A. C. Melissinos (University of Rochester, NY, 1960), p. 578. See also M. A. Markov and I. M. Zheleznykh, Nucl. Phys. **27** (1961) 385–394.

^bF. Reines, Ann. Rev. Nucl. Sci. **10** (1960) 1. Greisen, in the same journal volume [K. Greisen, Ann. Rev. Nucl. Sci. **10** (1960) 63] also mentioned the idea of neutrino astronomy as a “fanciful proposal”.

^cProbably the idea of Reines was a natural consequence of the following note by F. Reines, C. L. Cowan and H. W. Krusenot, “Conservation of the number of nucleons,” Phys. Rev. **109** (1958) 609–610 concerning experimental search for nucleon decay:

Higher sensitivity could be obtained both by using larger counters and by going deep underground or in the ocean to eliminate cosmic rays.

final state muon increases with energy, the effective detector volume is growing as well with energy. Furthermore, it is expected that the energy spectra from many point astrophysical sources fall off less steeply than that from atmospheric neutrinos.

Thus the deep underwater detectors can be used as telescopes for high-energy neutrino astronomy.

The optical requirements on the detector medium are severe. A large absorption length is needed because it determines the required spacing of the optical sensors and, to a significant extent, the cost of the detector. A long scattering length is needed to preserve the geometry of the Cherenkov pattern. Nature has been kind and offered ice and water as the natural Cherenkov media. Their optical properties are, in fact, complementary. Water and ice have comparable attenuation lengths, with the roles of scattering and absorption reversed. Optics seems, at present, to drive the evolution of ice and water detectors in predictable directions: towards very large telescope area in ice exploiting the long absorption length, and towards lower threshold and good muon track reconstruction in water exploiting the long scattering length.

Figure 11^d shows a map of present-day underwater/ice Cherenkov neutrino telescope projects (see also Table 5 for a summary of their status).

^dBy Francis Halzen <<http://icecube.wisc.edu/~halzen/>>.



Figure 11: A map of underwater/ice Cherenkov neutrino telescope projects [by Francis Halzen <<http://icecube.wisc.edu/~halzen/>>].

Table 5: Past, present and future underwater/ice neutrino telescopes.

Lab/Location/Stage	Year(s)	Sensitive area* (10^3 m^2)	Status (fall, 2003)
DUMAND I, II <i>Pacific near Hawaii Big Island; at a depth of ~4.5 km</i>	Historically first underwater project. Closed down... **		
BAIKAL NT <i>Lake Baikal, East Siberia; at a depth of about 1.1. km</i>			
NT-36	1993-95	0.15-0.20	} Stepwise deployment & going into operation Operates
NT-72	1995-96	0.4-3.0	
NT-96	1996-97	0.8-6.0	
NT-144	1997-98	1.0-8.0	
NT-200	1998	2.0-10.0	
AMANDA <i>South Pole; at a depth of 0.8 to 2 km</i>			
AMANDA A	1994	Small	} Stepwise deployment & going into operation Operates Under construction
AMANDA A	1996	1.0	
AMANDA B4	1998	5-6	
AMANDA II	2000	30-50	
AMANDA KM3 or IceCube	2005	1000	
NESTOR <i>Ionian Sea near Pylos, Peloponnesos, Greece; at a depth of about 3.8 km</i>	2004 ?	1 st phase: 20 KM^3 in prospect	Under construction & test
ANTARES <i>Mediterranean near Toulon, France; at a depth from 2.4 to 2.7 km (the most appropriate site is identified)</i>	2004 ?	to 100-200 KM^3 in prospect	R & D
NEMO <i>Capo Passero (Sicily), Italy; at a depth of about 3.4 km</i>	?	to 3500 KM^3 in prospect	R & D

Notes to
Table 5:

- *) The sensitive (effective) area is an increasing function of muon energy. For example, the estimated effective area of the Baikal NT-200 is about 2300 m^2 and 8500 m^2 for 1-TeV and 100-TeV muons, respectively.
- **) Some 1-string prototypes of the DUMAND array were deployed and several useful results were obtained.

20 DUMAND

The DUMAND (Deep Underwater Muon and Neutrino Detector) proposal aimed for a $250 \times 250 \times 500 \text{ m}^3$ array of 756 detector modules to be located at a depth of 4.5 km in the Pacific Ocean near Hawaii Island. The expanded schematic diagram in Fig. 12 shows the underwater location of the detector, the full array of 36 strings with optical sensors and a single PMT module. The enclosed target mass of the detector is 30 Mtons and its effective area is about 10^5 m^2 . The angular resolution was estimated at 15 to 45 mrad, depending on the muon energy.

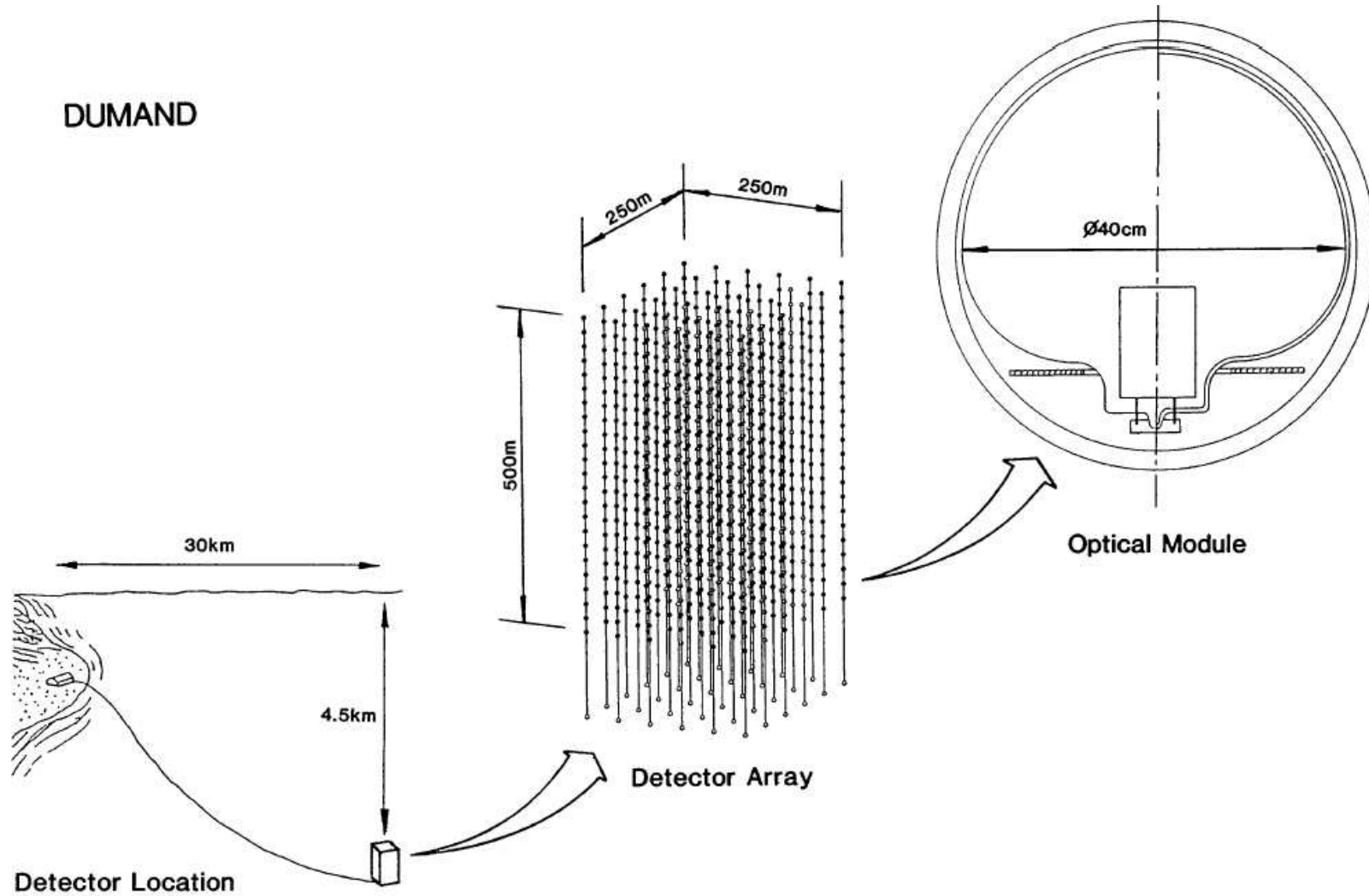


Figure 12: Proposed configuration of the DUMAND detector.

In the middle of 90s, the DUMAND Collaboration intended to deploy a prototype 9-string array (Fig. 13) in two phases: first 3 strings (the triad) as a demonstration, and the remaining 6 strings (complete octagon, plus center string) after about 1 year of testing and operation. The effective detection area of the full 9-string array was estimated as $\sim 2 \times 10^4 \text{ m}^2$.

The Island of Hawaii was selected for the deployment due to exceptional water clarity, proximity of an abyssal plain (4.8 km) with appropriate seabed characteristics to a suitable shore site (30 km away), pre-existing laboratory infrastructure at the shore site (due to an ocean thermal energy research project).

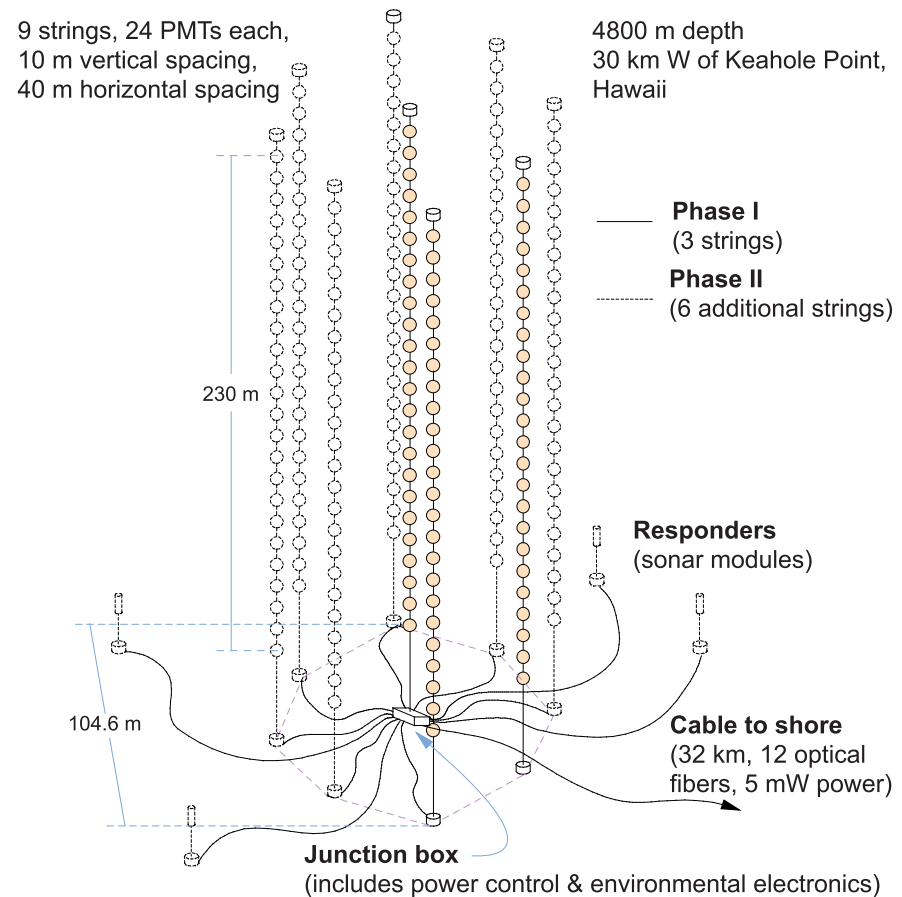


Figure 13: A sketch of the DUMAND-II underwater neutrino detector. [From R. J. Wilkes, [astro-ph/9412019](https://arxiv.org/abs/astro-ph/9412019).]

21 Baikal neutrino telescope

The Lake Baikal neutrino experiment exploits the deep water of the great Siberian lake as a detection medium for high-energy neutrinos via muons and electrons generated in neutrino interactions.



Figure 14: *Left panel:* space image of wintry Baikal. *Right panel:* ice campus of the collaboration with Khamar-Daban mountain at skyline (March, 1987). [From <http://nt200.da.ru/>.]

The neutrino telescope NT-200, put into operation at April, 1998, is located in the

southern part of the lake (51.50° N, 104.20° E) at a distance of 3.6 km from the nearest shore and at a depth of about 1.1 km. The distance to the opposite shore is more than 30 km. This asymmetry allows to study the asymmetry in the azimuth distribution of muons arriving at large zenith angles.

The absorption length of water at the site is about 20 m for wavelengths between 470 and 500 nm, and seasonal variations are less than 20%. Light scattering is subjected strongly to seasonal variations and to variations from year to year.

Figure 15^a shows the layout of the Baikal NT-200 and the preceding array NT-96 (on the right) which took data between April 1996 and March 1997.^b The NT-200 consists of 192 optical modules (OMs) at 8 strings arranged at an umbrella-like frame. Pairs of OMs are switched in coincidence with a 15 ns time window and define a channel. The array is time-calibrated by two nitrogen lasers. Of these, one (fiber laser) is mounted just above the array. Its light is guided via optical fibers to each OM pair. The other (water laser) is arranged 20 m below the array. Its light propagates directly through water. The expansion on the left of the figure shows two pairs of optical modules (“svjaska”) with the electronics module, which houses parts of the readout and control electronics. Three underwater electrical cables connect the detector with the shore station.

^aDescription of the telescope and figures 15 and 17 are borrowed from Ch. Spiering *et al.* (Baikal Collaboration), *Prog. Part. Nucl. Phys.* **40** (1998) 391 [astro-ph/9801044]; V. A. Balkanov *et al.* (Baikal Collaboration), *Yad. Fiz.* **63** (2000) 1027 [*Phys. Atom. Nucl.* **63** (2000) 951] (astro-ph/0001151).

^bVarious stages of the stepwise increasing detector are NT-36 (1993–1995), NT-72 (1995–1996), NT-96 (1996–1997) and NT-144 (1997–1998).

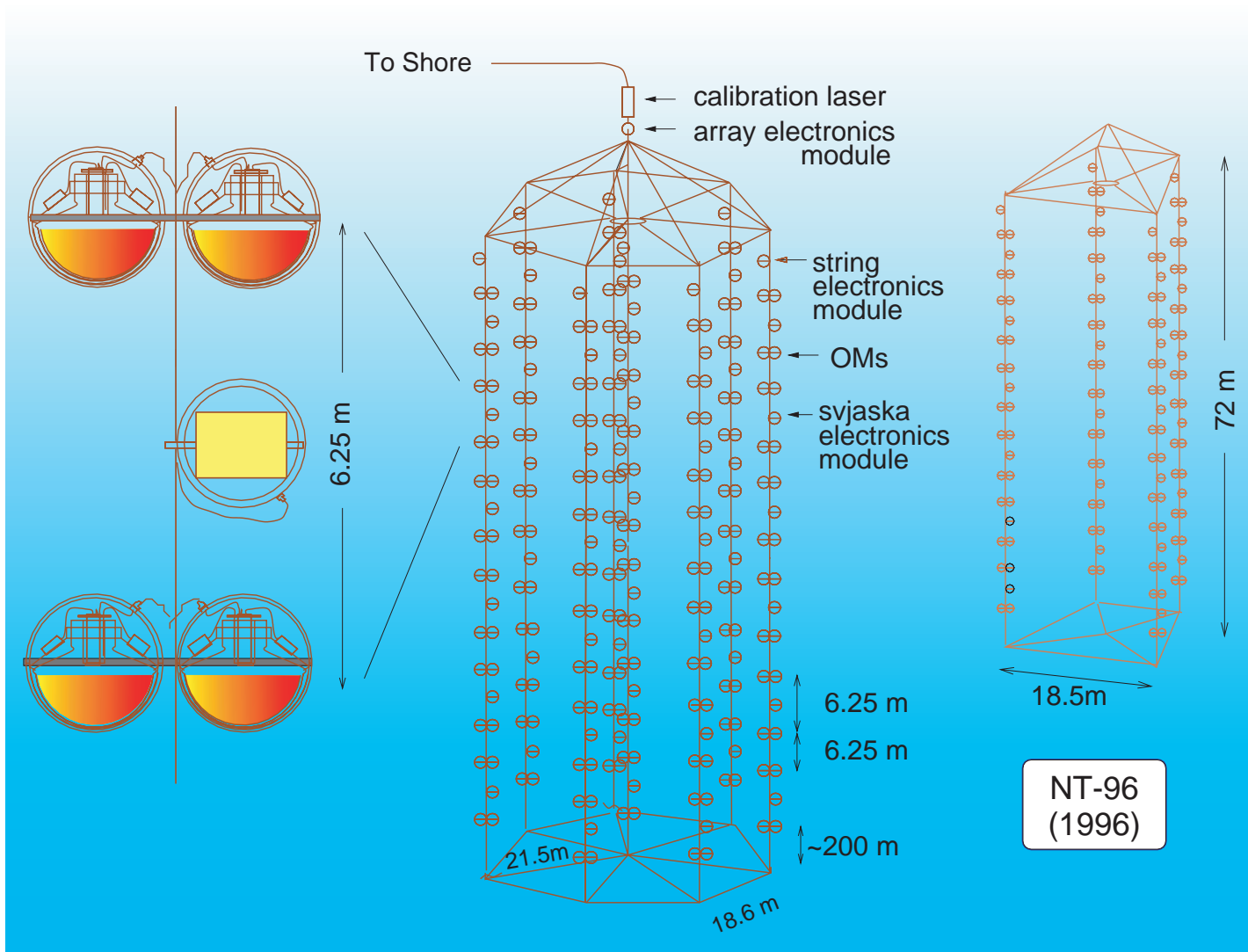


Figure 15: NT-200 and NT-96 schematic view (see text for description and references).

Overall view of the NT-200 telescope is shown in Fig. 16. Here, 1, 2 and 3 are cables to shore; 4, 5 and 6 are the string stations for shore cables; 7 is the string with the telescope; 8 is the hydrometric string; 9–14 are the ultrasonic emitters. The insert at the left bottom of the figure shows two pairs of optical modules (OM) together with the electronic module controlling the OMs. Shown are two pairs of OMs directed face to face.

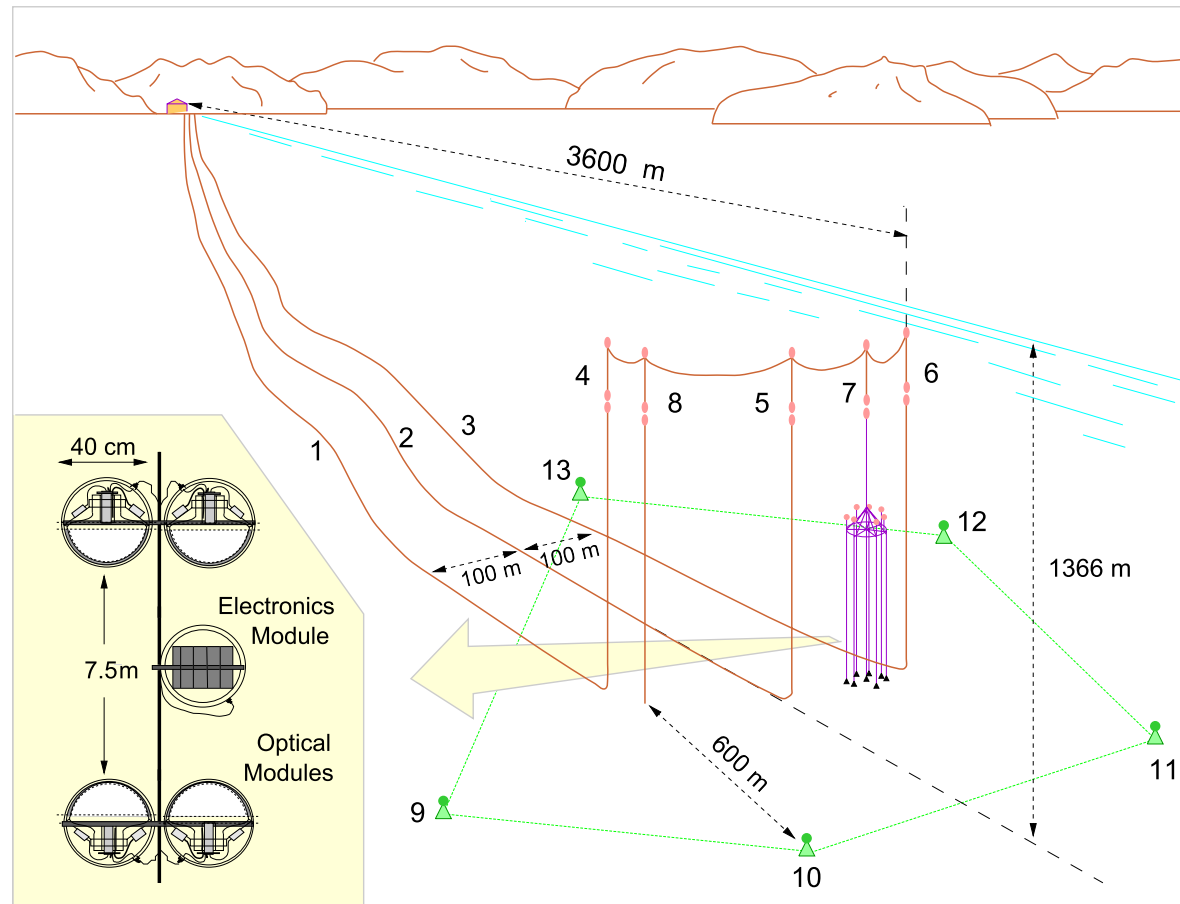


Figure 16: Overall view of the NT-200 complex in Lake Baikal. [From V. A. Balkanov *et al.*, "In-situ measurements of optical parameters in Lake Baikal with the help of a neutrino telescope," *Appl. Opt.* **33** (1999) 6818–6825 (astro-ph/9903342).]

Fig. 17 displays three neutrino candidates separated during 18 days of the NT-96 exposition (the time period between April 16 and May 17, 1996).

- (a) A “gold plated” 19-hit neutrino event. Hit channels are in color. The thick line gives the reconstructed muon path, thin lines pointing to the channels mark the path of the Cherenkov photons as given by the fit to the measured times. The areas of the ellipses are proportional to the measured amplitudes. The fake probability of this event was estimated to be smaller than 1%.
- (b) An unambiguous 14-hit neutrino candidate.
- (c) An ambiguous event reconstructed as a neutrino event (dashed line) but with a second solution above the horizon (solid line). This event is assigned to the sample of downward going muons.

The data set collected with NT-200 during 268 live days (till 1999) yields 84 upward going muons. The MC simulation of upward muon tracks due to atmospheric neutrinos gives 80.5 events. The skyplot of the upward muons is shown in Fig. 18. Fig. 19 shows a comparison between the measured and simulation angular distributions.

Fig. 23 shows NT-200+ – an upgrade of the NT-200 by three sparsely instrumented distant outer strings which will increase the fiducial volume for high-energy cascades to a few dozen Mtons. Correspondingly, the NT-200+ sensitivity will be **4 times better** than that of NT-200, with a moderate 20% increase of optical modules only. A prototype string of 140 m length with 12 optical modules was deployed in March 2003, and electronics, data acquisition and calibration systems for NT-200+ have been tested.

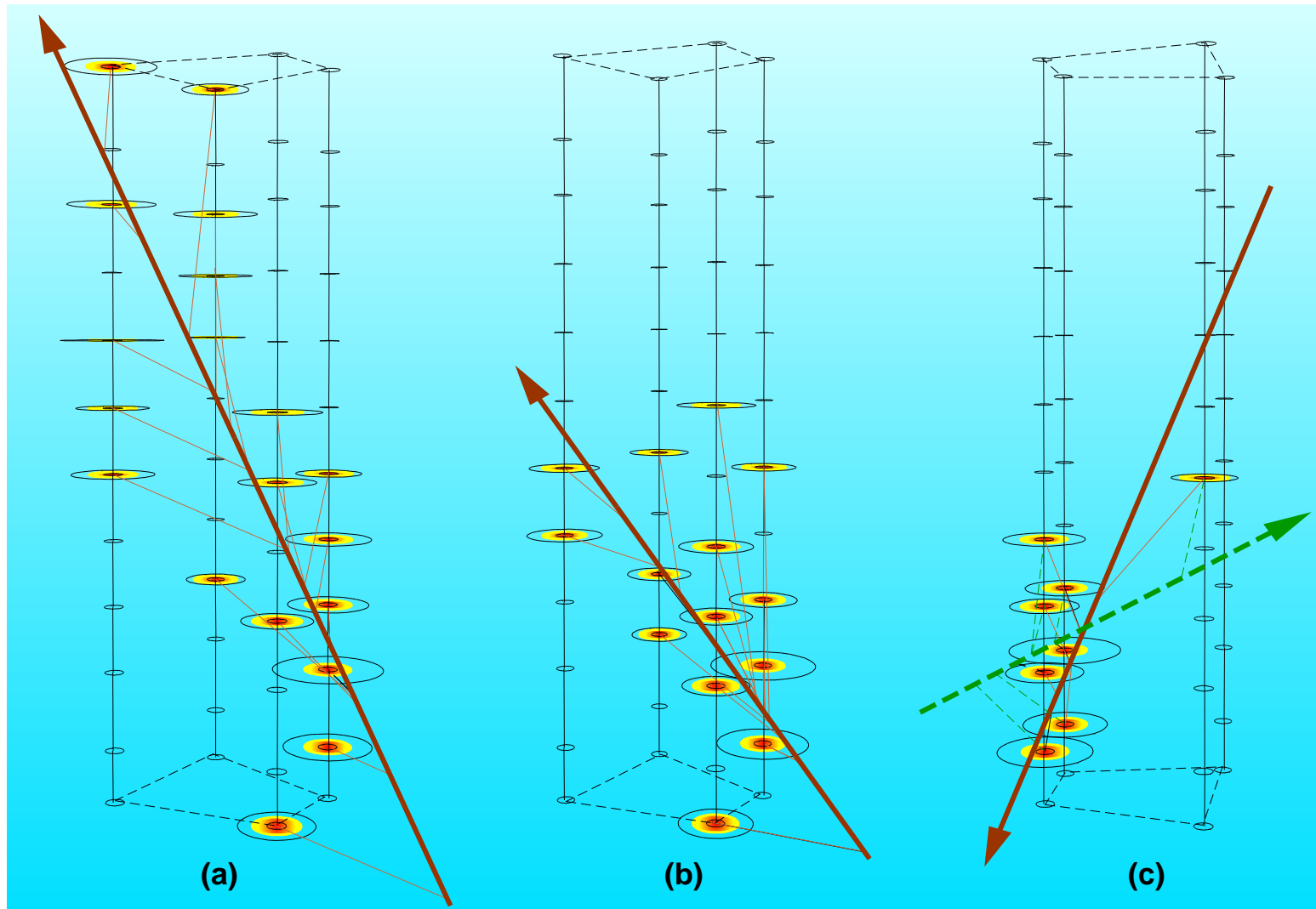


Figure 17: Three neutrino candidates recorded in NT-96 (see text for details).

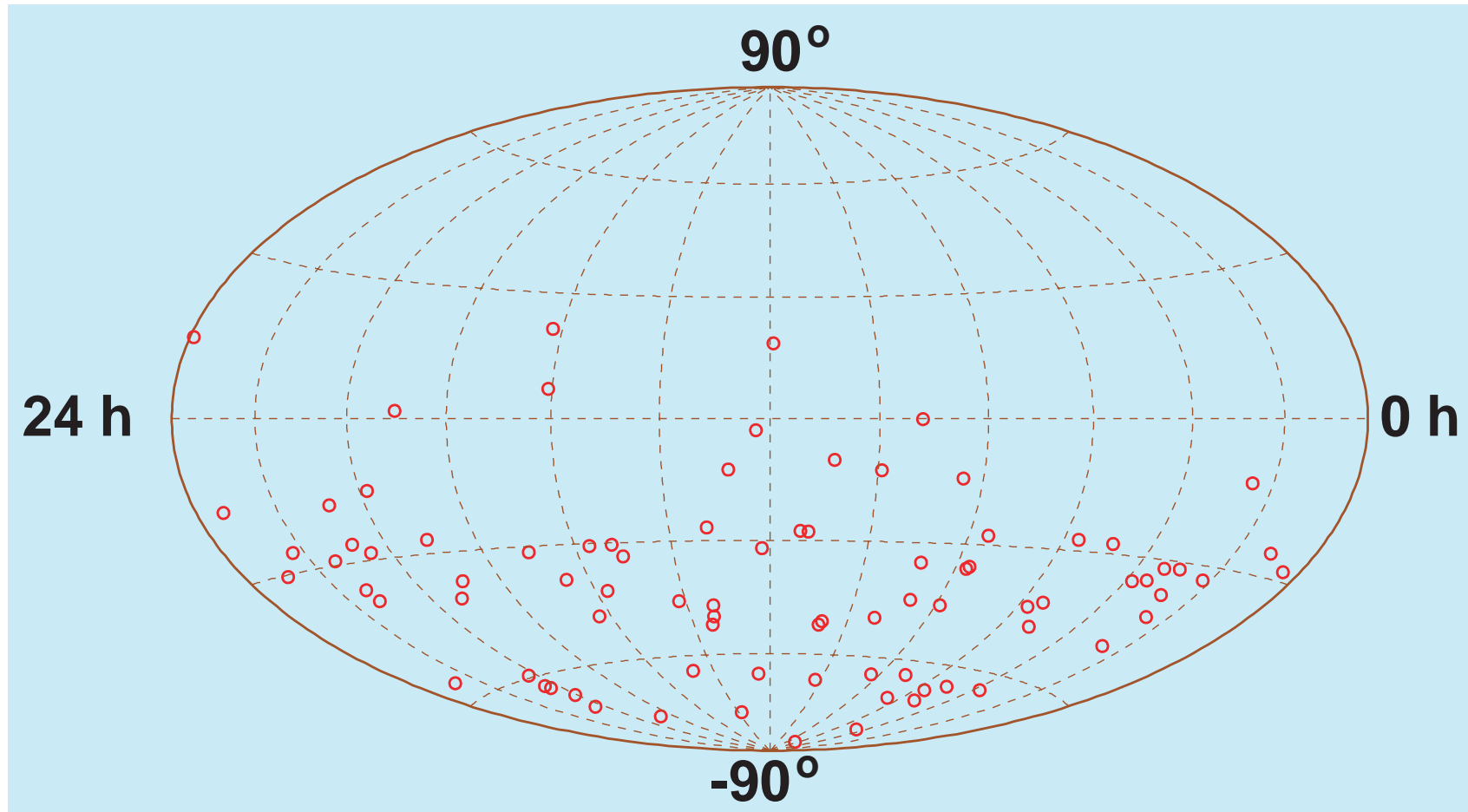


Figure 18: Skyplot (in equatorial coordinates) of 84 upward-going muon events recorded in the Baikal NT-200 experiment. [From R. Wischnewski (for the Baikal Collaboration), contribution to the 28th ICRC, Tsukuda, Japan, July 31 – August 7, 2003 (astro-ph/0305302).]

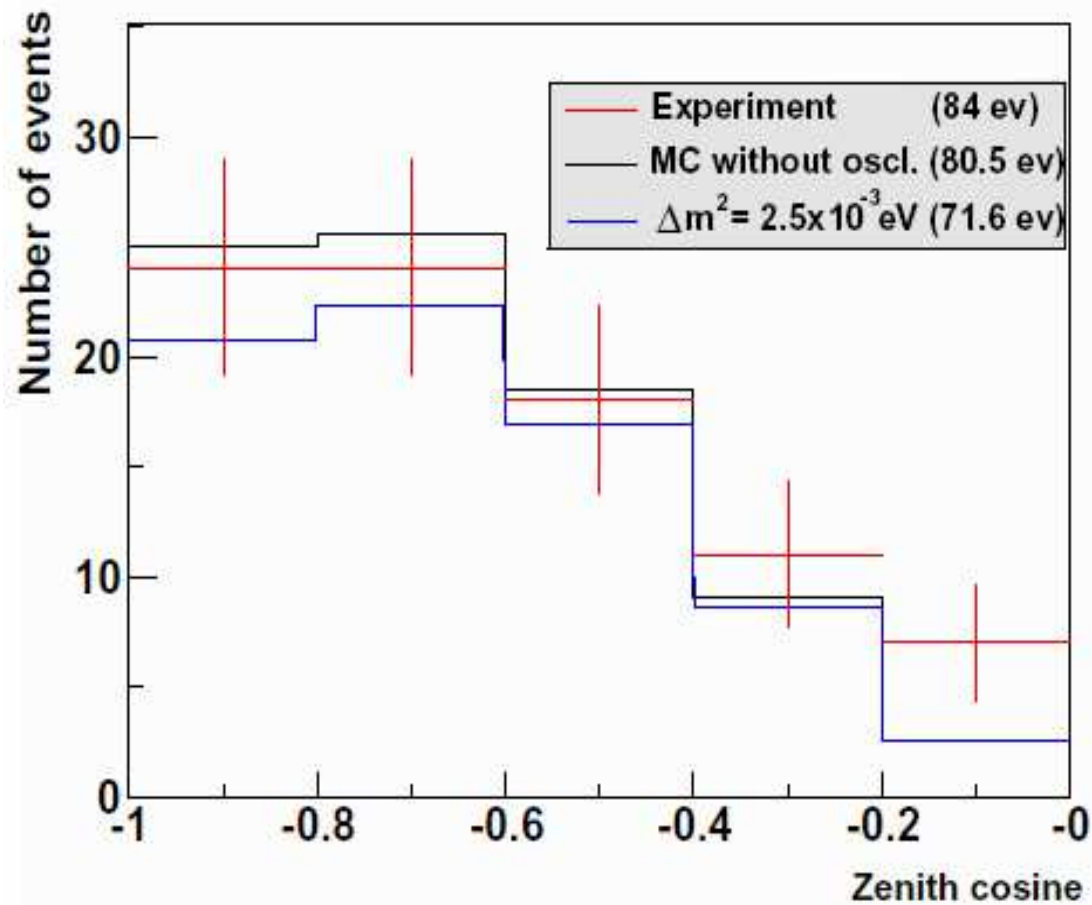


Figure 19: Zenith angle distribution of 84 upward-going reconstructed events in the Baikal NT-200 experiment and MC simulated distribution of upward muon tracks due to atmospheric neutrinos. $E_{\text{th}} = 15 - 20 \text{ GeV}$ in this experiment. [From V. Aynutdinov *et al.*, “The BAIKAL neutrino project: Status, results and perspectives,” Nucl. Phys. B (Proc. Suppl.) 143 (2005) 335–342.]

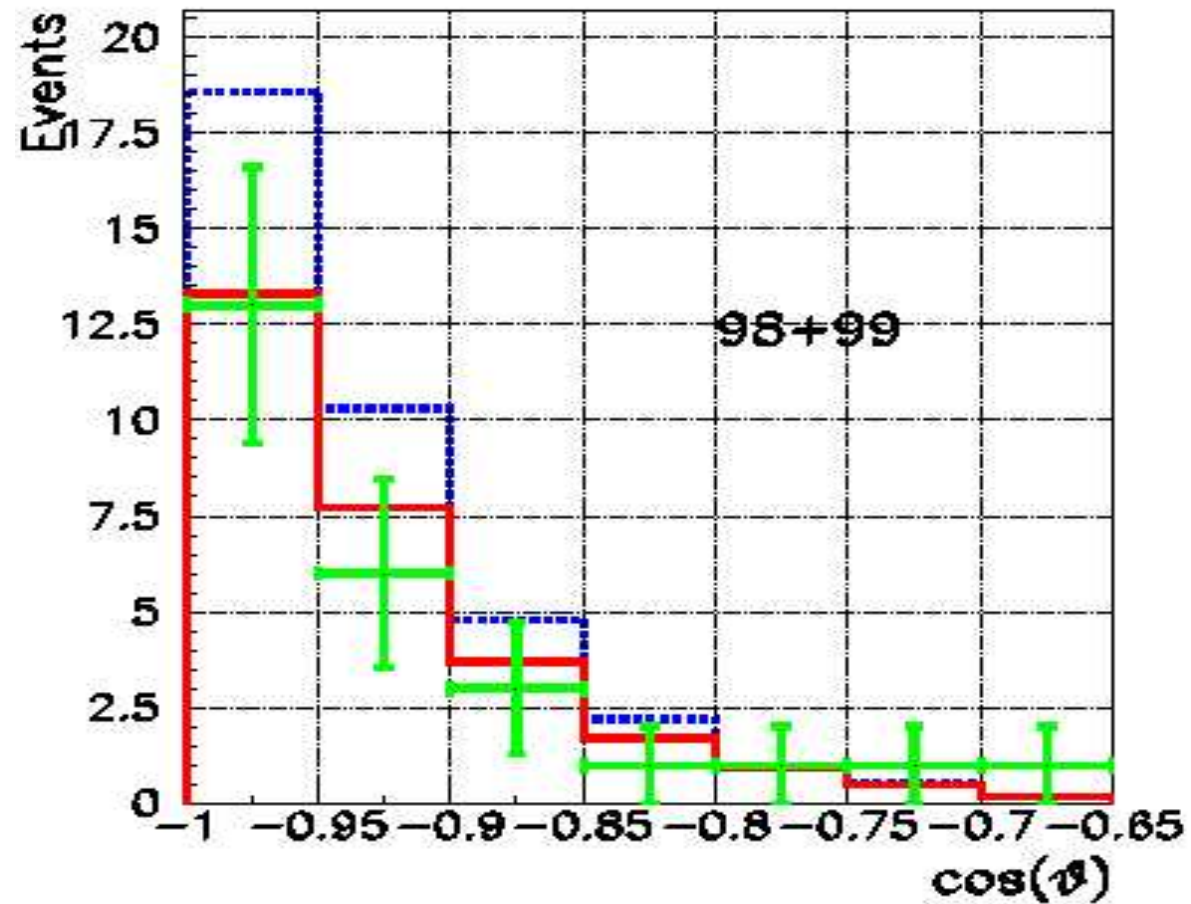


Figure 20: The same as in Fig. 19 but for selected neutrino candidates. $E_{\text{th}} = 10$ GeV.
 [From V. Aynutdinov *et al.*, Nucl. Phys. B (Proc. Suppl.) **143** (2005) 335–342.]

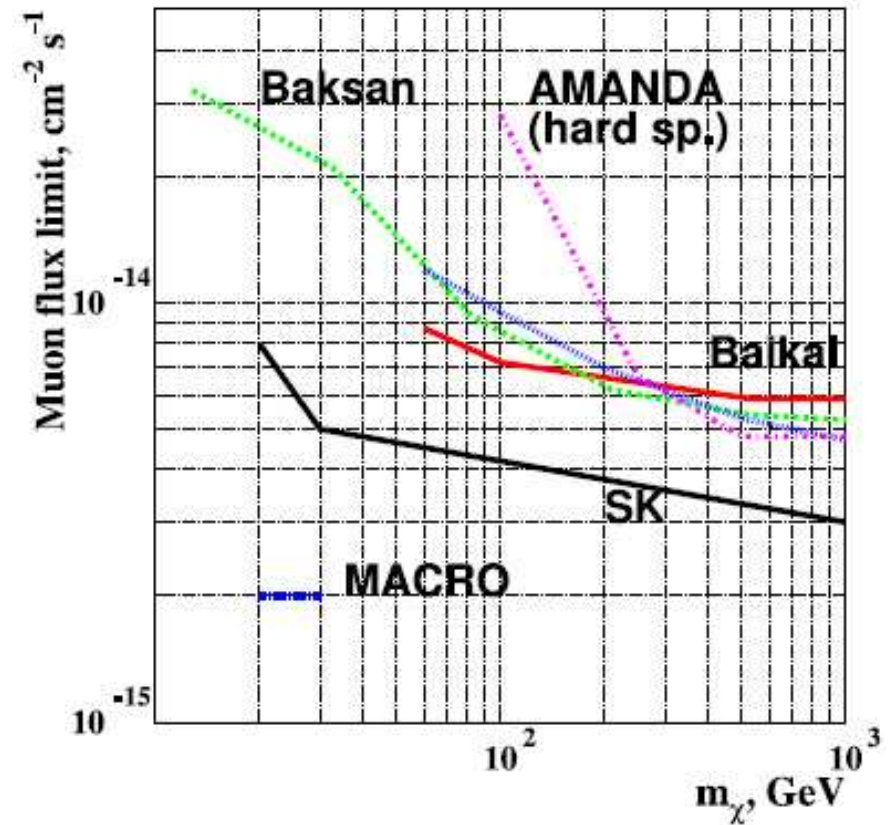
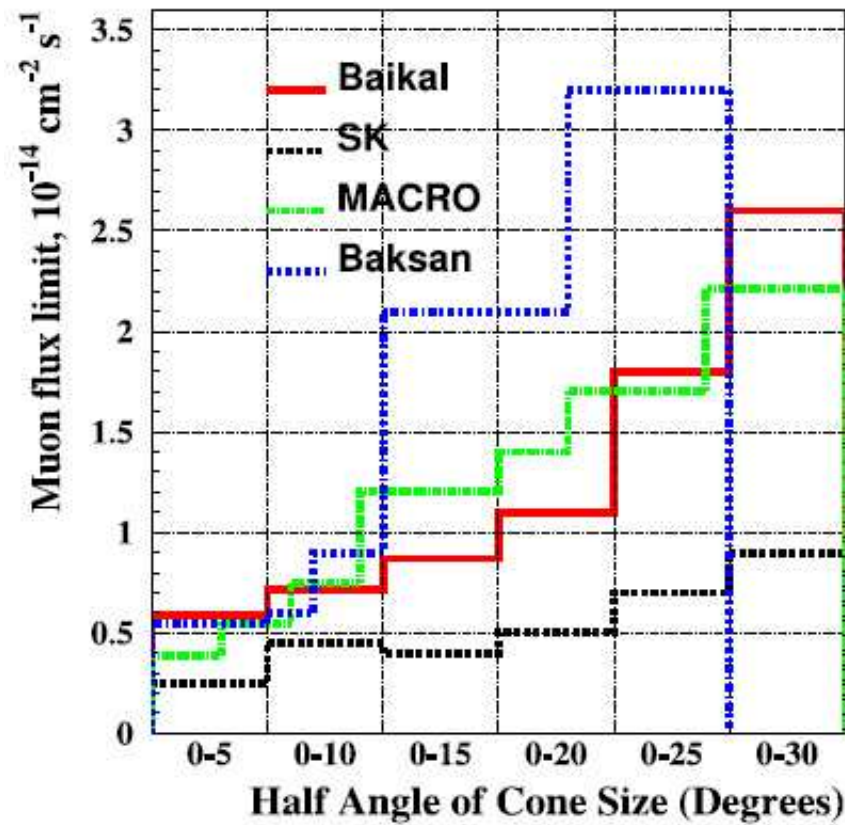


Figure 21: Limits on the excess muon flux from the center of the Earth vs half-cone of the search angle (left) and as a function of WIMP mass (right).

[From V. Aynutdinov *et al.*, Nucl. Phys. B (Proc. Suppl.) 143 (2005) 335–342.]

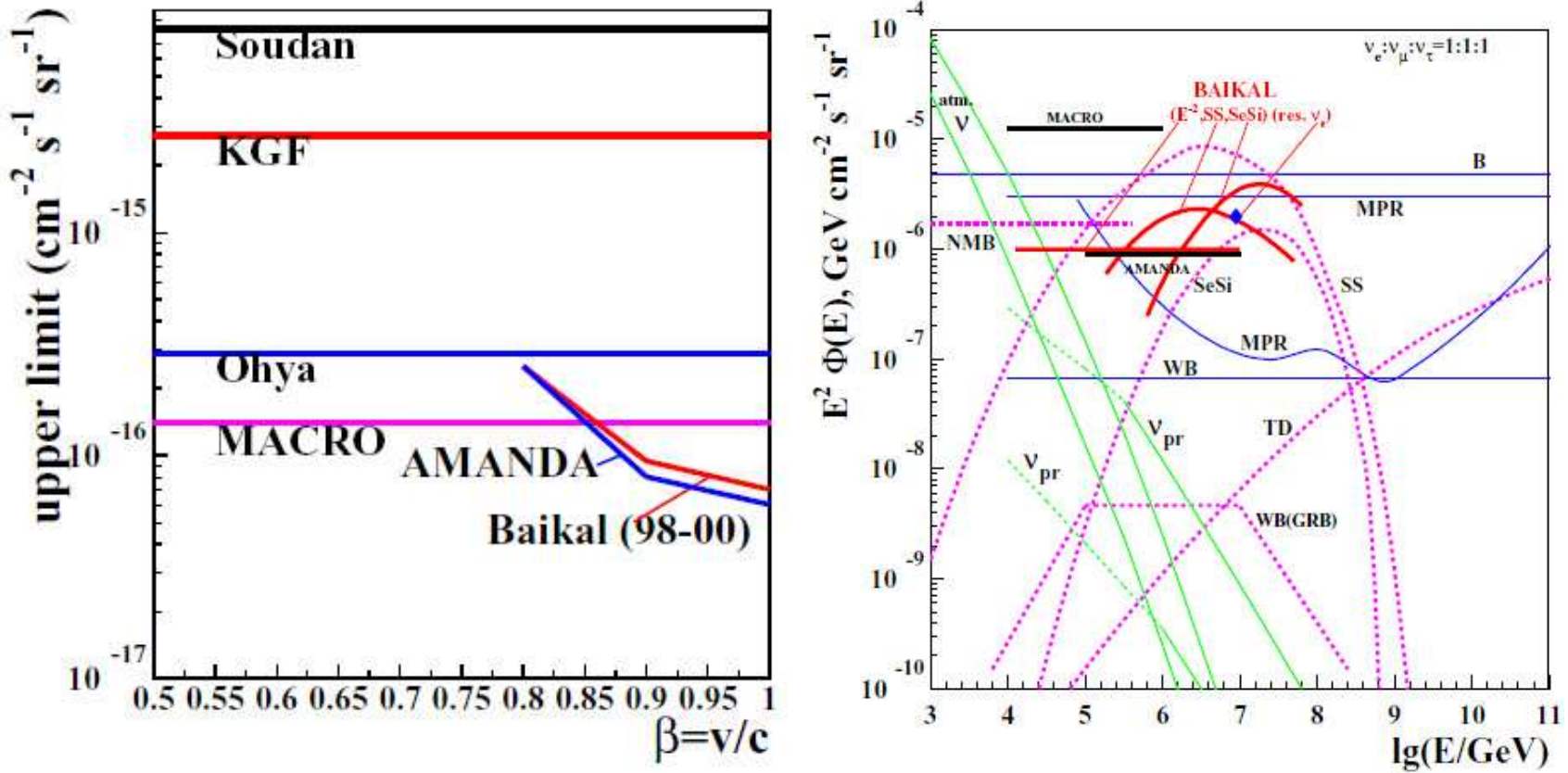


Figure 22: Upper limits on the flux of fast monopoles (left) and neutrino fluxes (right) obtained in different experiments. The neutrino fluxes expected from some astrophysical sources are also shown in the right panel.

[From V. Aynutdinov *et al.*, Nucl. Phys. B (Proc. Suppl.) **143** (2005) 335–342.]

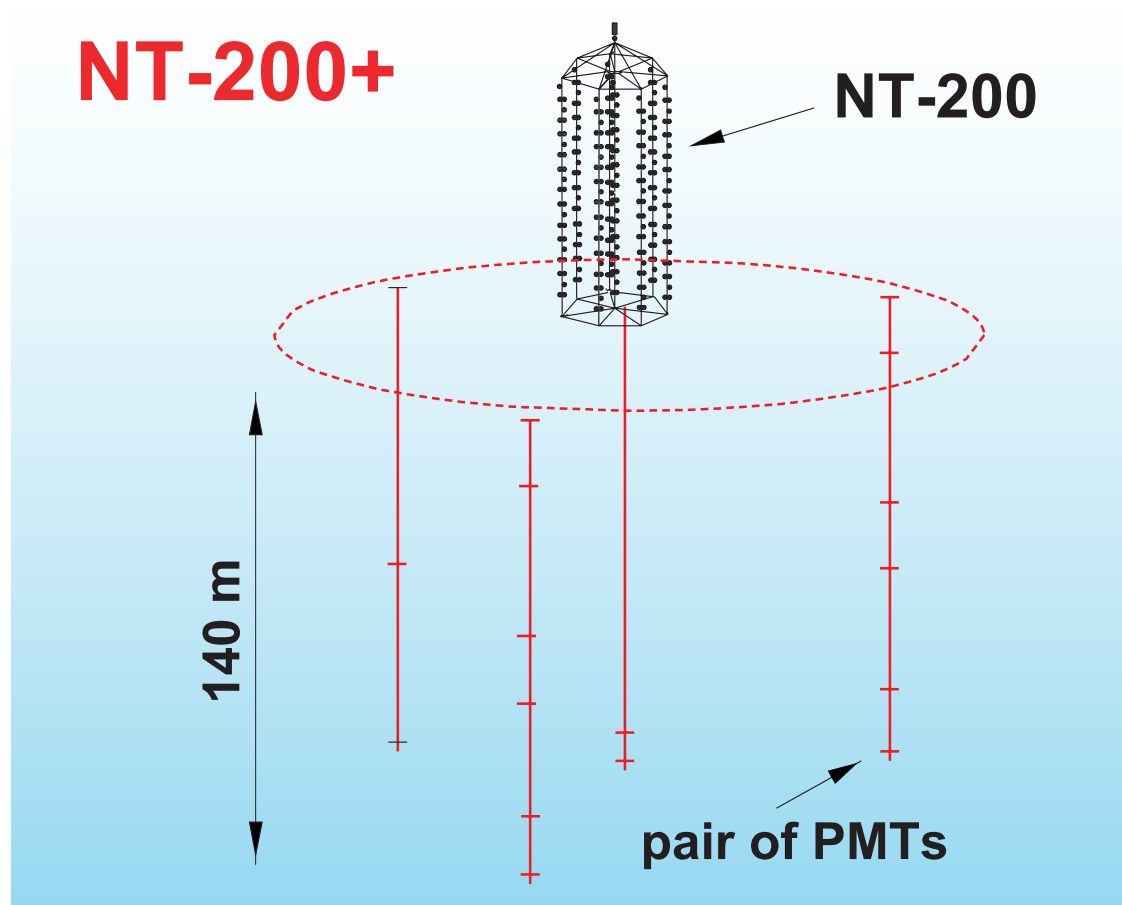


Figure 23: Future NT-200+ configuration. Three additional outer (plus one possible central) strings will allow a much better vertex identification and hence a significantly more precise measurement of cascade energy in a volume around NT-200. [From R. Wischnewski, 2003 (see caption to Fig. 18).]

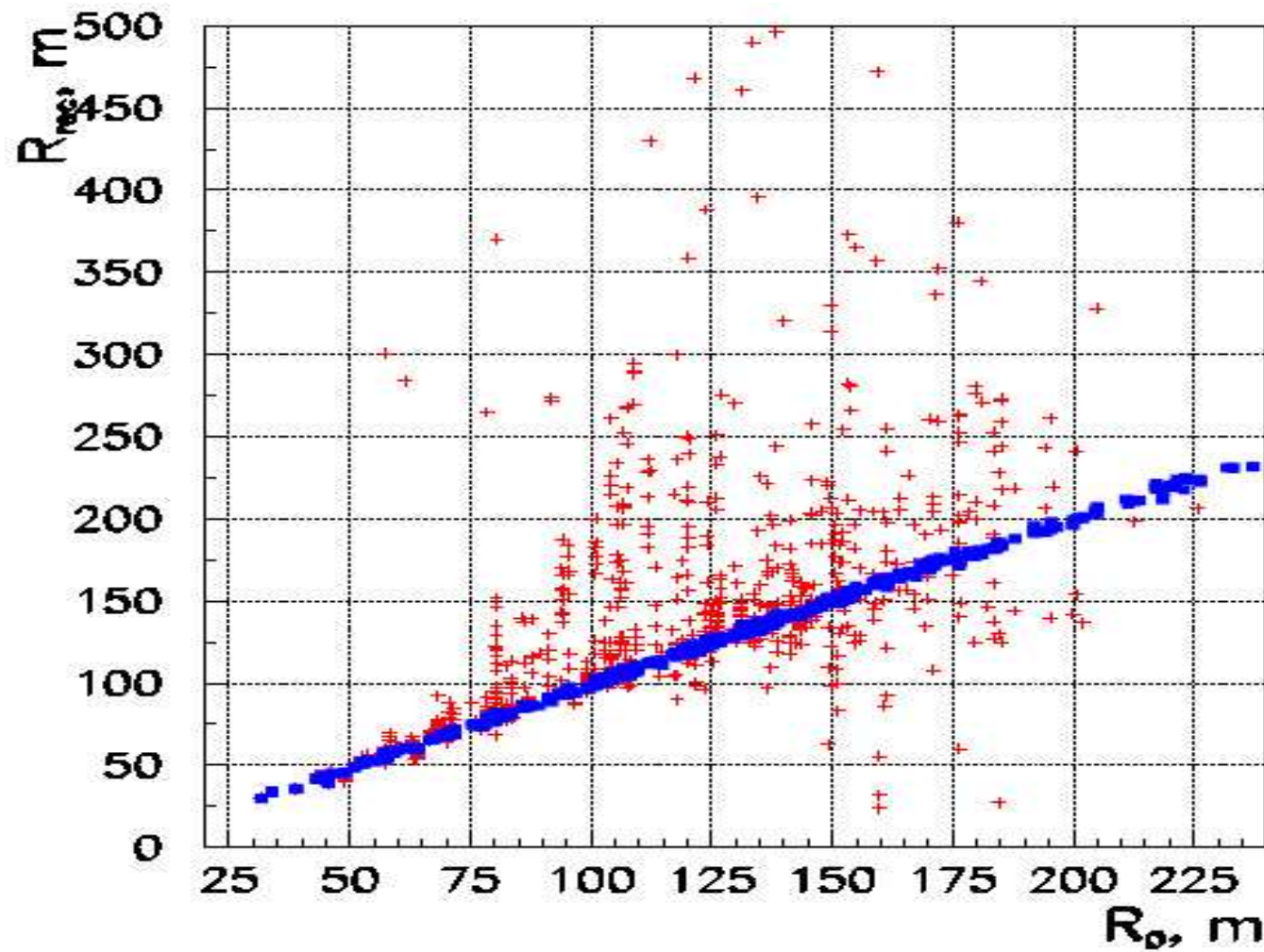


Figure 24: Reconstructed vs simulated coordinates of cascades in NT-200+ (rectangles) and NT-200 (crosses). [From V. Aynutdinov *et al.*, Nucl. Phys. B (Proc. Suppl.) **143** (2005) 335–342.]

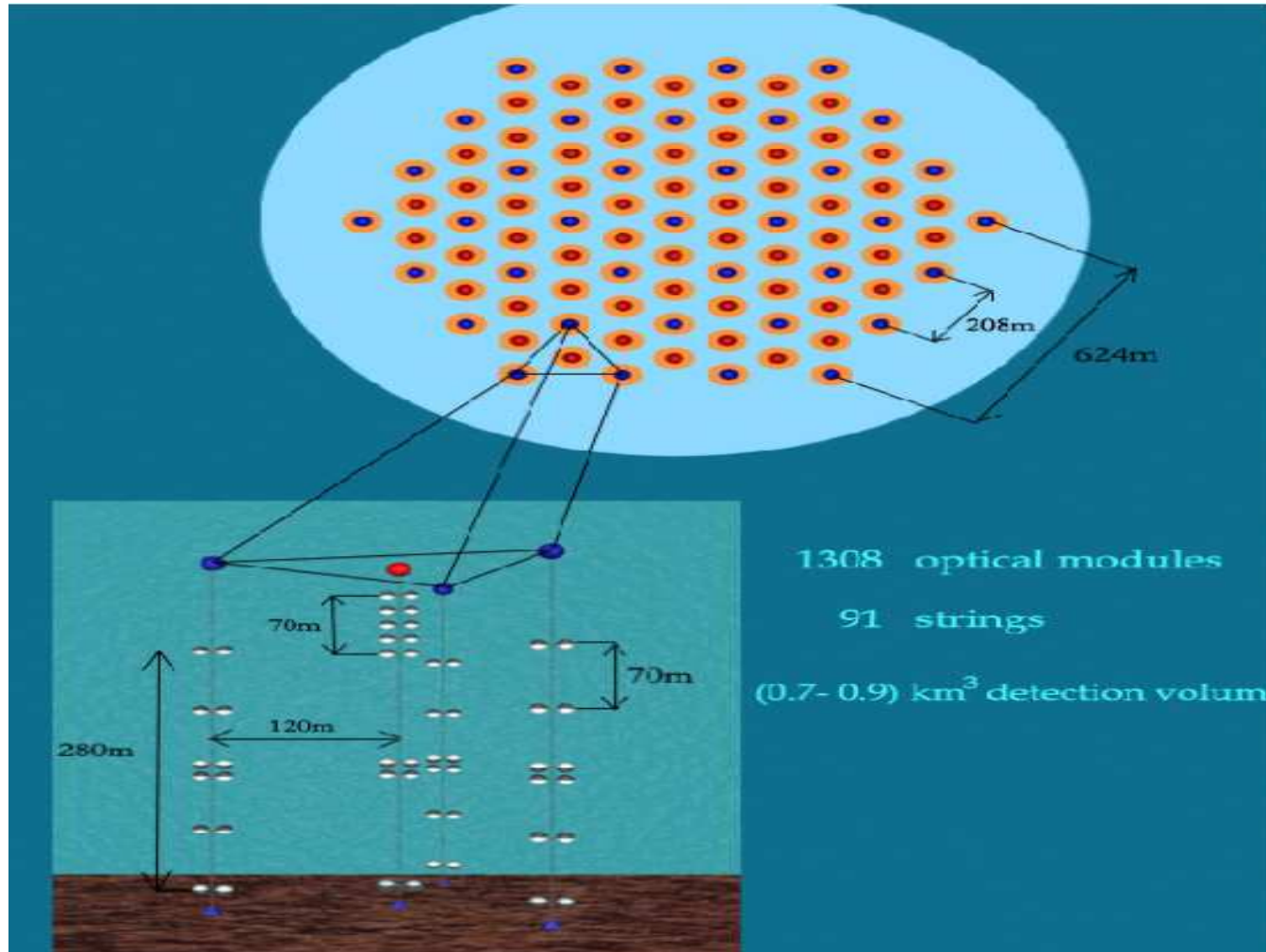


Figure 25: Top view of a Gigaton Volume Detector (GVD) in Lake Baikal with sketch of one of its sub-arrays. [From V. Aynutdinov *et al.*, Nucl. Phys. B (Proc. Suppl.) **143** (2005) 335–342.]

22 AMANDA

The AMANDA (Antarctic Muon And Neutrino Detector Array) detector is located at the South Pole station, Antarctica. Figures 26 and 27 show the South Pole Station.



Figure 26: Construction of the new South Pole Station as of February, 2002. [From [http://www.amanda.uci.edu/.](http://www.amanda.uci.edu/)]

The detector uses the 2.8 km thick ice sheet at the South Pole as a neutrino target, Cherenkov medium and cosmic ray flux attenuator. The detector consists of vertical

strings of optical modules (OMs) – photomultiplier tubes sealed in glass pressure vessels – frozen into the ice at depths of 1500–2000 m below the surface.



Figure 27: The South Pole Station. The AMANDA-II telescope electronics are located on the 2nd floor of MAPO, the blue building shown in this picture. [From <http://www.amanda.uci.edu/>.]

Fine photos of the Amundsen-Scott South Pole Station are given in Figs. 28 and 29.^a

^aBorrowed from the Francis Halzen's homepage <<http://icecube.wisc.edu/~halzen/>>.



Figure 28: Amundsen-Scott South Pole Station.



Figure 29: One another vie of the South Pole Station.

Figure 30 shows the current configuration of the AMANDA detector. The shallow array, AMANDA-A, was deployed at depths of 800 to 1000 m in 1993–1994 in an exploratory phase of the project. Studies of the optical properties of the ice carried out with AMANDA-A showed a high concentration of air bubbles at these depths, leading to strong scattering of light and making accurate track reconstruction impossible. Therefore, a deeper array of 10 strings with 302 OMs was deployed in the austral summers of 1995–1996 and 1996–1997 at depths of 1500–2000 m. This detector is referred to as AMANDA-B10. It was augmented by 3 additional strings in 1997–1998 and 6 in 1999–2000, forming the AMANDA-II array. This detector has been calibrated and in operation since January 2000.

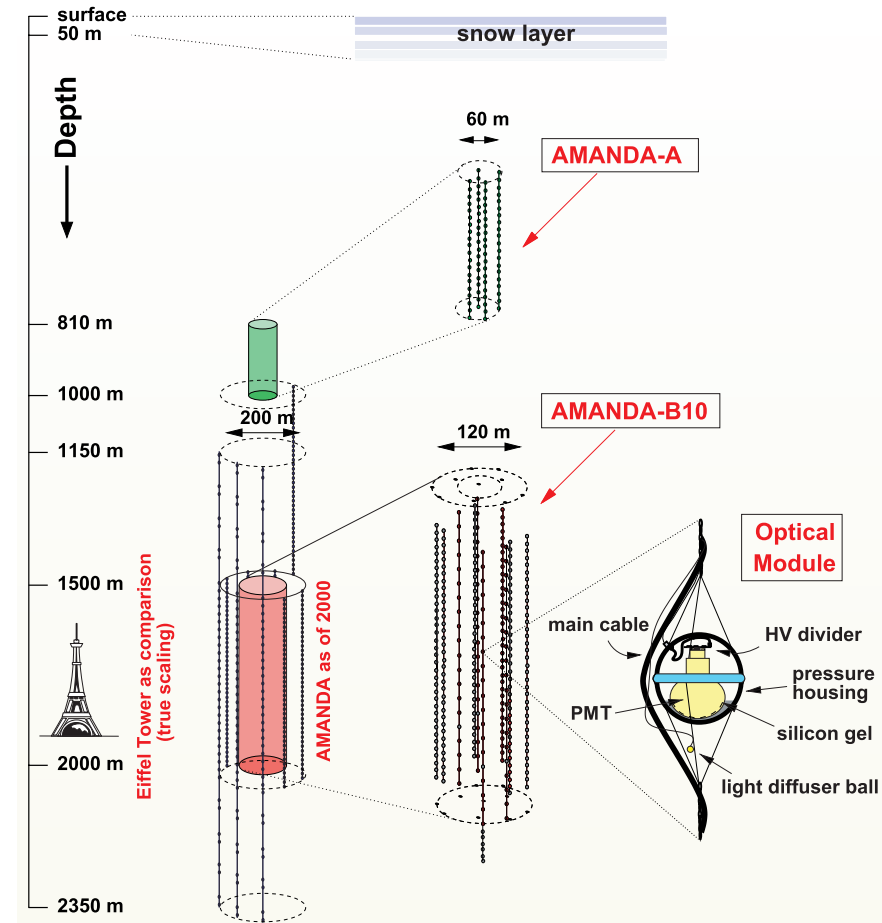


Figure 30: Schematic view of the AMANDA-II array at the South Pole. [From J. Ahrens *et al.*, *Phys. Rev. D* **66** (2002) 012005 [[astro-ph/0205109](https://arxiv.org/abs/astro-ph/0205109)].]

Figure 31 is an artistic view of a neutrino induced event in the AMANDA detector while Fig. 32 displays three real neutrino candidates. Let us describe these with some details.

- (a) Event display of an upgoing muon event. The gray scale indicates the flow of time, with early hits at the bottom and the latest hits at the top of the array. The arrival times match the speed of light. The sizes of the ellipses correspond to the measured amplitudes.
- (b) The upgoing muon event has a smooth distribution of hits along the extended uniform track. The track-like hit topology of this event can be used to distinguish it from background events.
- (c) A background event with a poor smoothness value and a large deviation from a straight line.

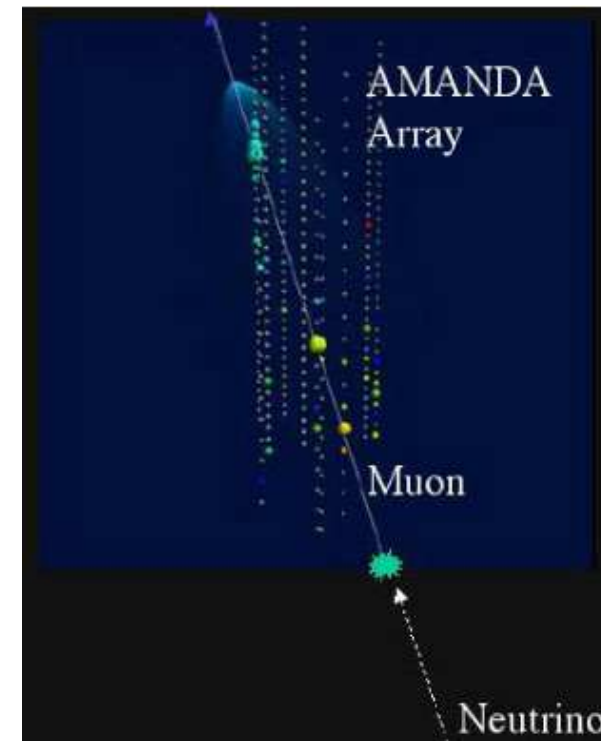


Figure 31: Artistic view of a ν induced event in the AMANDA detector.

Two more neutrino candidates (both were recorded on May 11, 2000) are shown in Fig. 33 borrowed from URL <http://amanda.physics.wisc.edu/>.^a

^aIn this site, there a lot of nice animated images relevant to the subject.

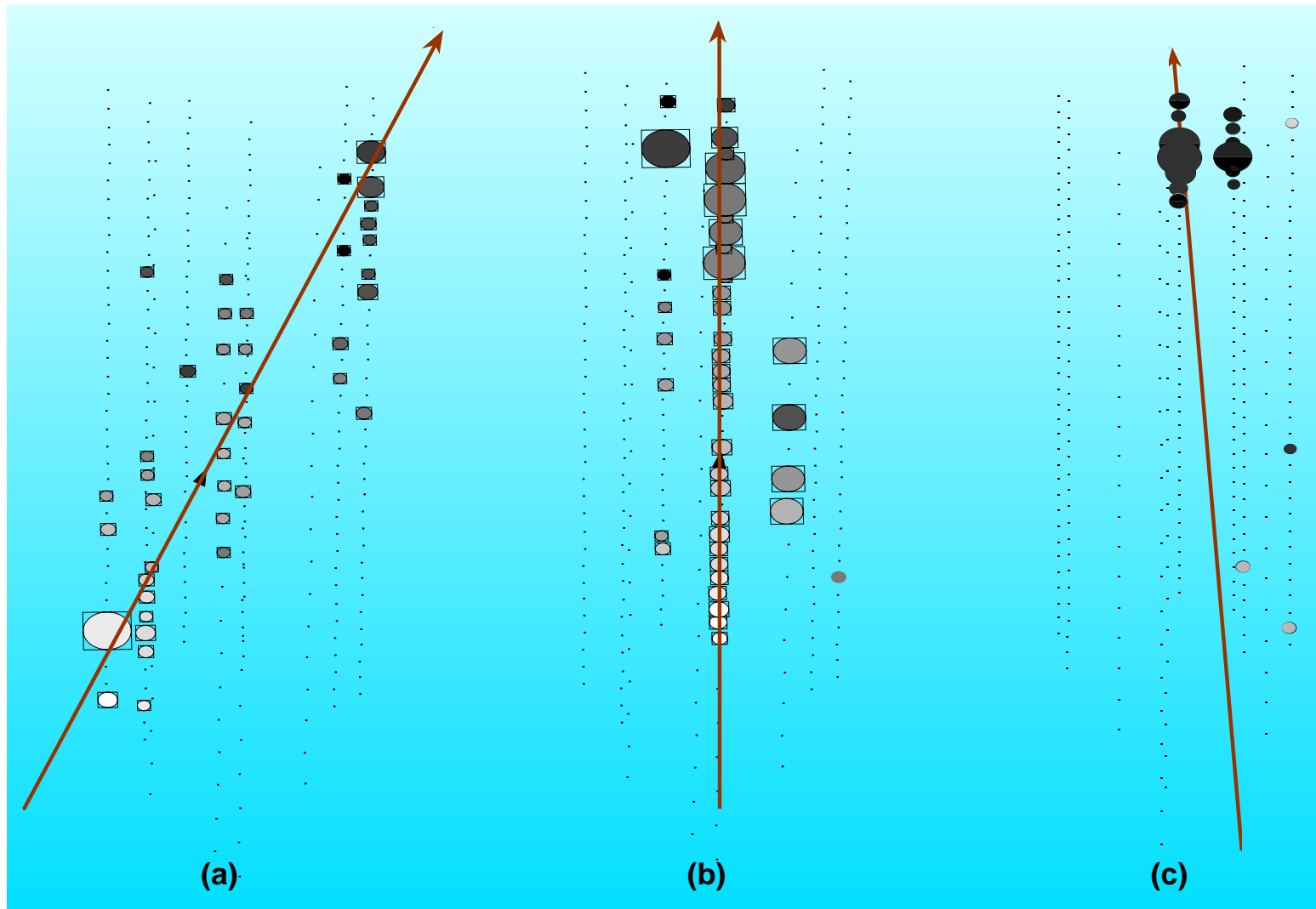


Figure 32: Three neutrino candidates recorded in AMANDA-B10 (see text).

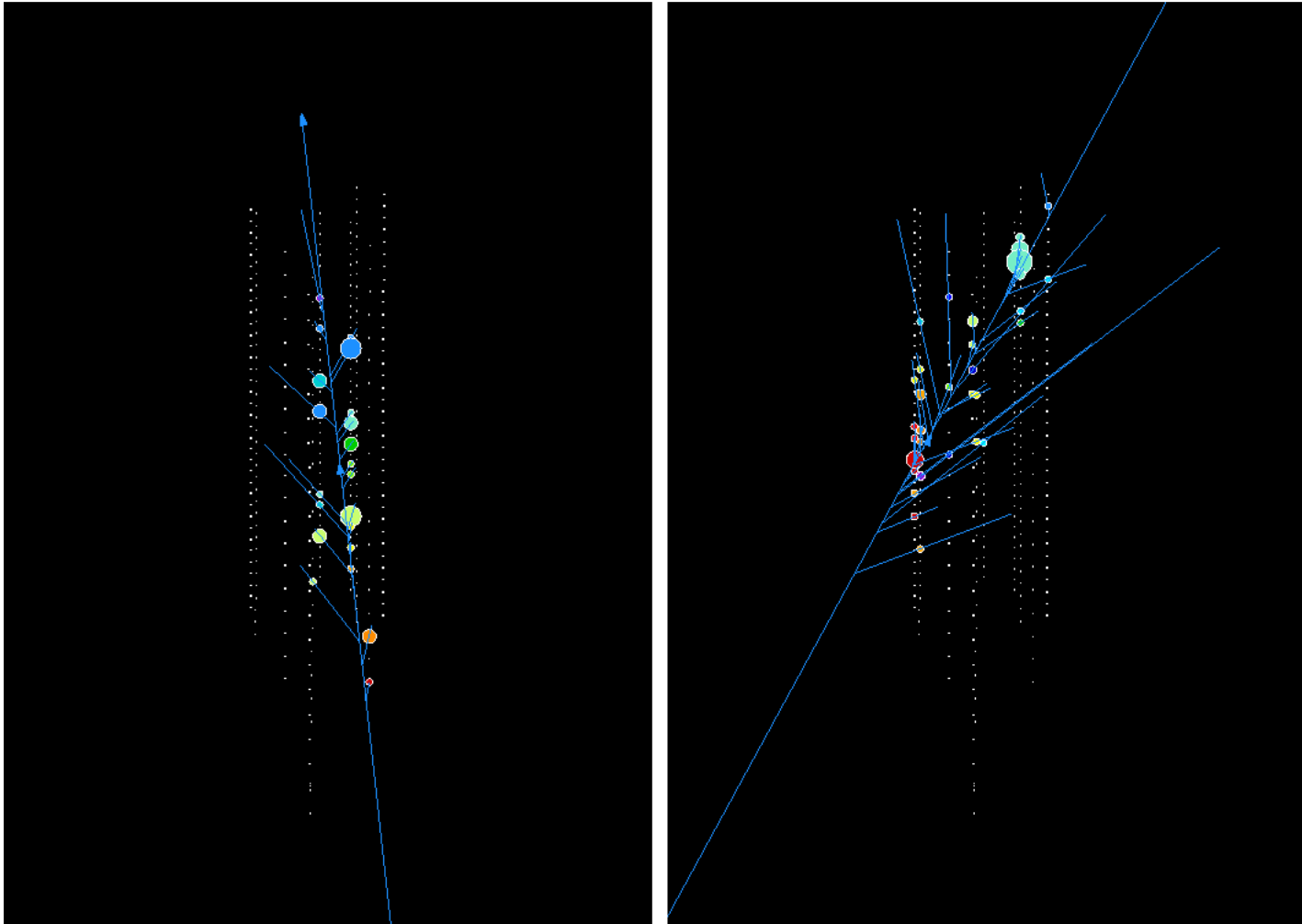


Figure 33: Two more neutrino candidates in AMANDA, #910225 and #10604848 (both were recorded on May 11, 2000). [From <http://amanda.physics.wisc.edu/>.]

Figure 34 shows the skyplot (equatorial coordinates) of all the candidate neutrino events found in AMANDA-B10. The distribution of the events on the skyplot is consistent with a random distribution. The combined skyplot of the AMANDA-B10 and Baikal NT-200 candidate neutrino events is shown in Fig. 35.

The angular distribution for the 204 events is shown in Fig. 36 and compared to that for the simulation of atmospheric neutrinos.^a In the figure the Monte Carlo events are **normalized** to the number of observed events to facilitate comparison of the shapes of the distributions. The agreement in absolute number is consistent with the systematic uncertainties in the absolute sensitivity and the flux of high-energy atmospheric neutrinos. The shape of the distribution of data is statistically consistent with the prediction from atmospheric neutrinos.

Preliminary results on the neutrino energy spectra are shown in Fig. 37. For the first time, the spectrum was measured up to 100 TeV. It is compared to the high-energy data from the Fréjus experiment^b and with the horizontal and vertical AN flux parametrizations according to Volkova.^c The error bars give the statistical error from the unfolding procedure plus an overall systematic uncertainty. The reconstructed data are in agreement with current calculations of the AN flux and shows an overlap with the Fréjus results.

^aFor more recent data see E. Andres *et al.*, Nature **423** (2001) 415.

^bK. Daum *et al.* (Fréjus Collaboration), Z. Phys. C **66** (1995) 417;
W. Rhode *et al.* (Fréjus Collaboration), Astropart. Phys. **4** (1996) 217.

^cL. V. Volkova, Yad. Fiz. **31** (1980) 1510 [Sov. J. Nucl. Phys. **31** (1980) 784].

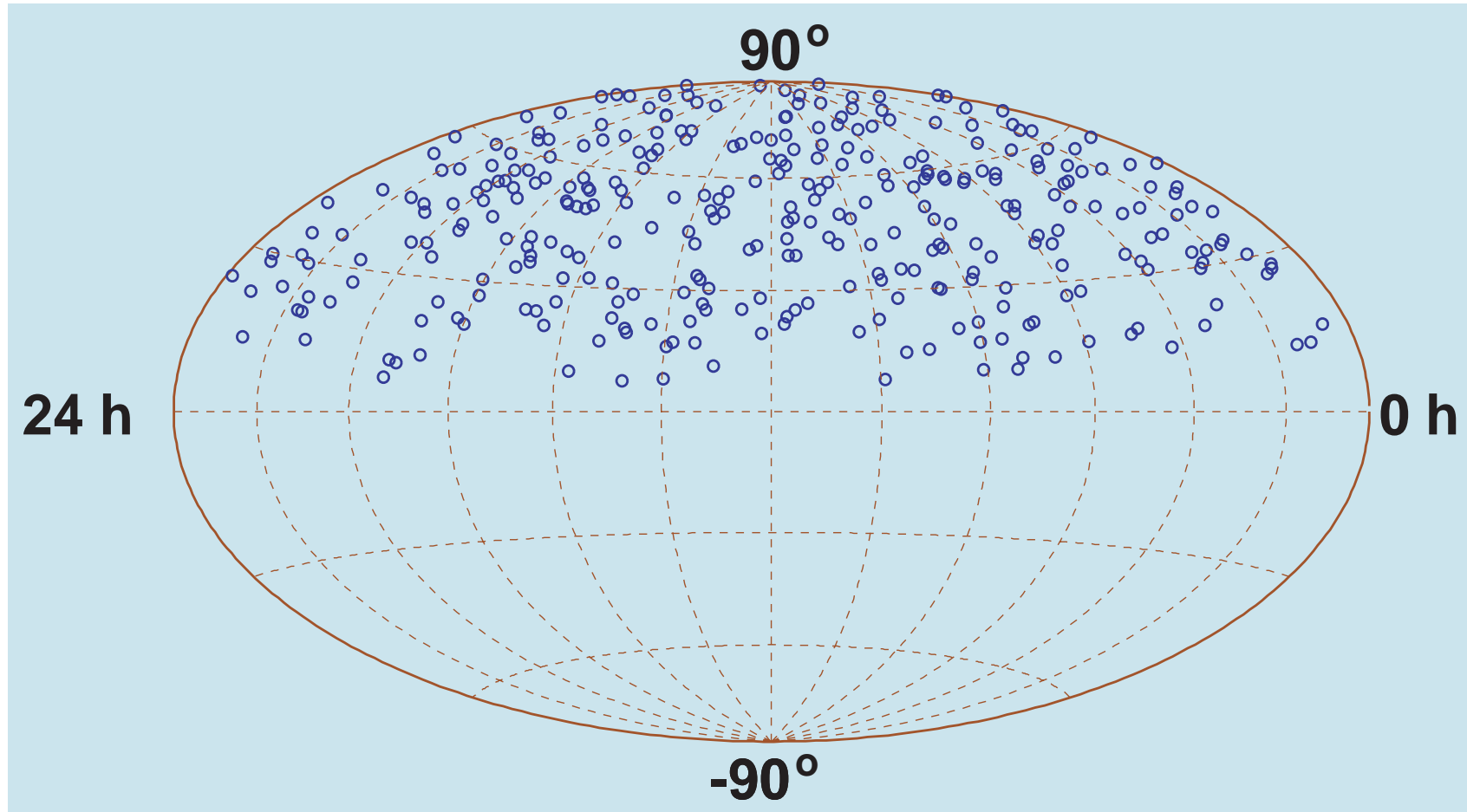


Figure 34: Skyplot of upward-going events as seen with AMANDA-B10 in 1997 in equatorial coordinates. The background of non-neutrino events is estimated to be less than 10%. [From J. Ahrens *et al.* (2002); see caption to Fig. 30.]

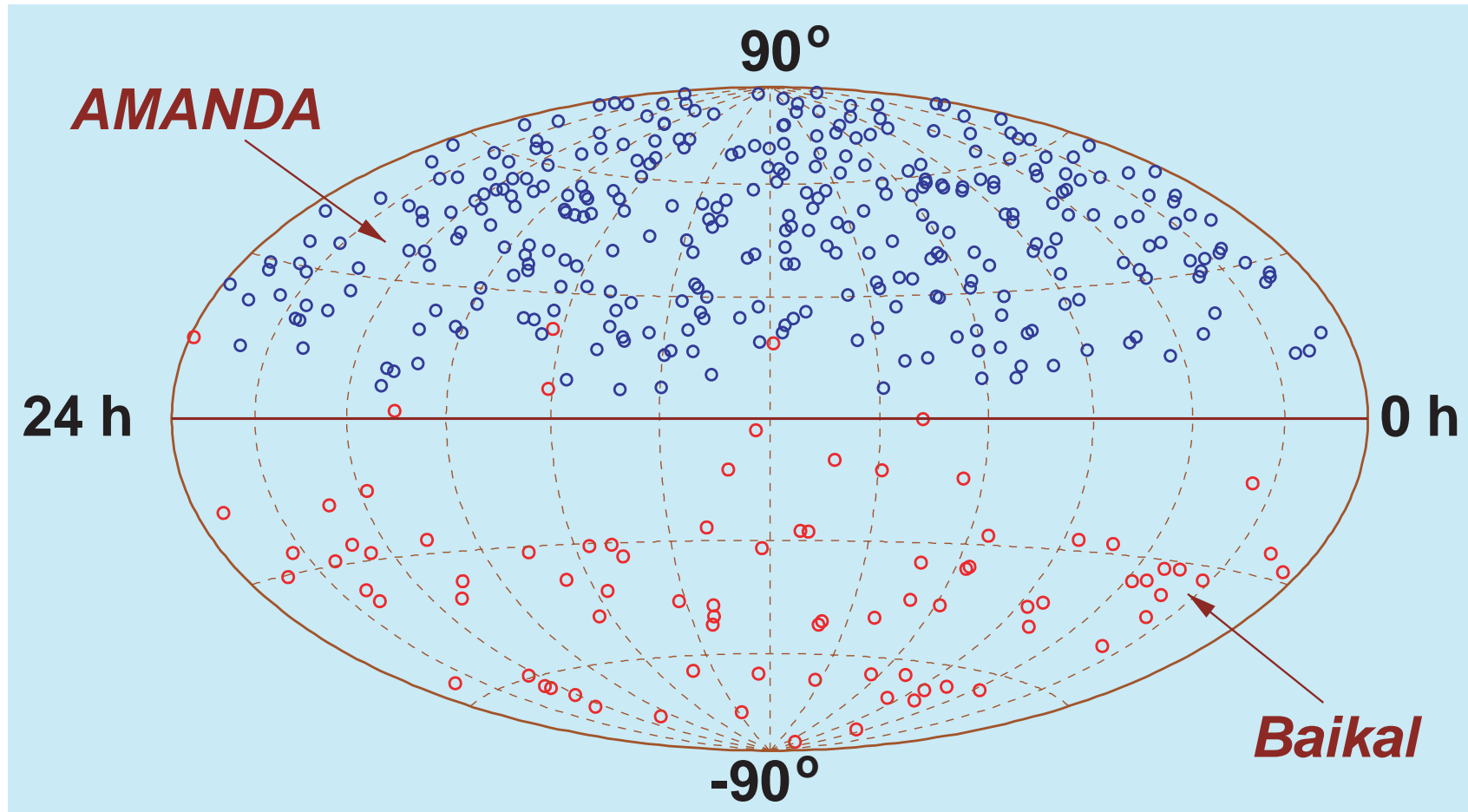


Figure 35: Merged skyplot of upward-going events recorded in both Baikal NT-200 and AMANDA-B10 experiments. The data are the same as in Figs. 18 and 34.

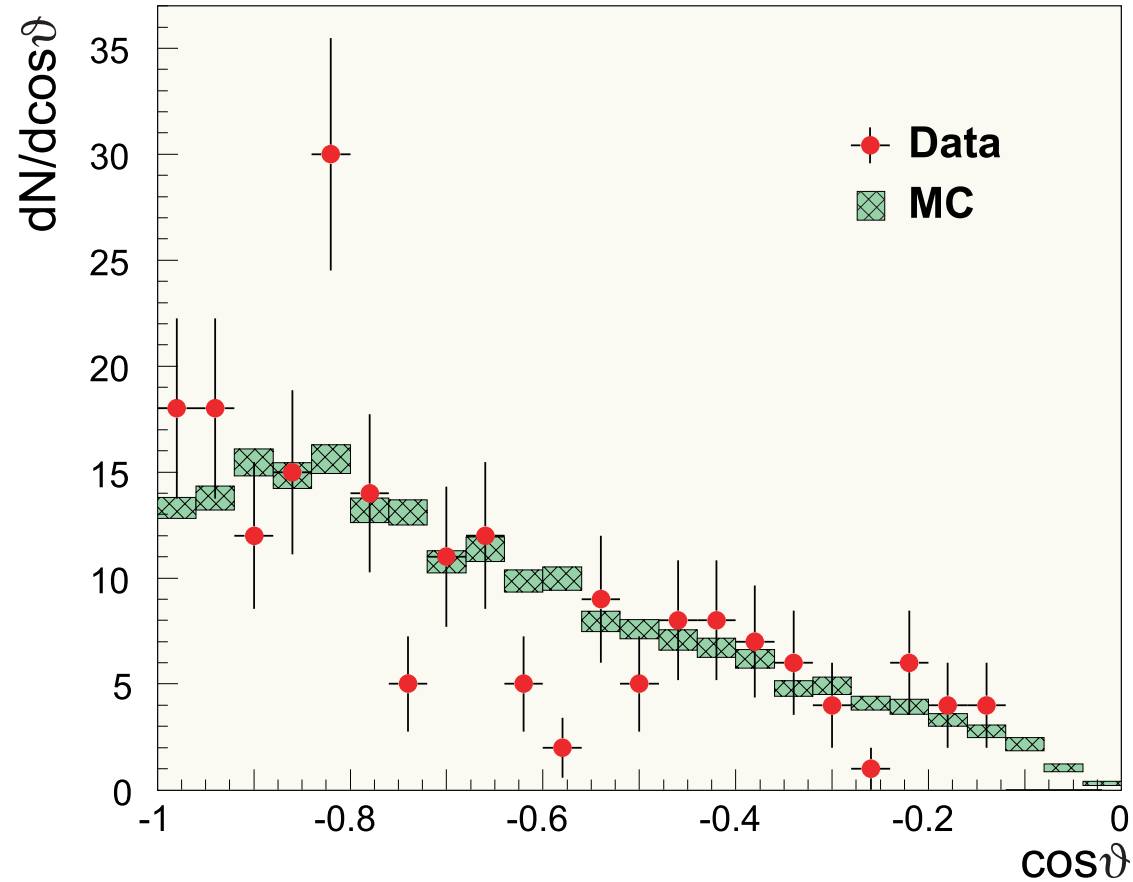


Figure 36: Zenith angle distribution of 204 upward-going reconstructed events in the AMANDA-B10 experiment and MC simulated distribution of upward muon tracks due to atmospheric neutrinos. The size of the hatched boxes indicates the statistical precision of the atmospheric neutrino simulation. The Monte Carlo prediction is normalized to the data. [From J. Ahrens *et al.* (2002); see caption to Fig. 30.]

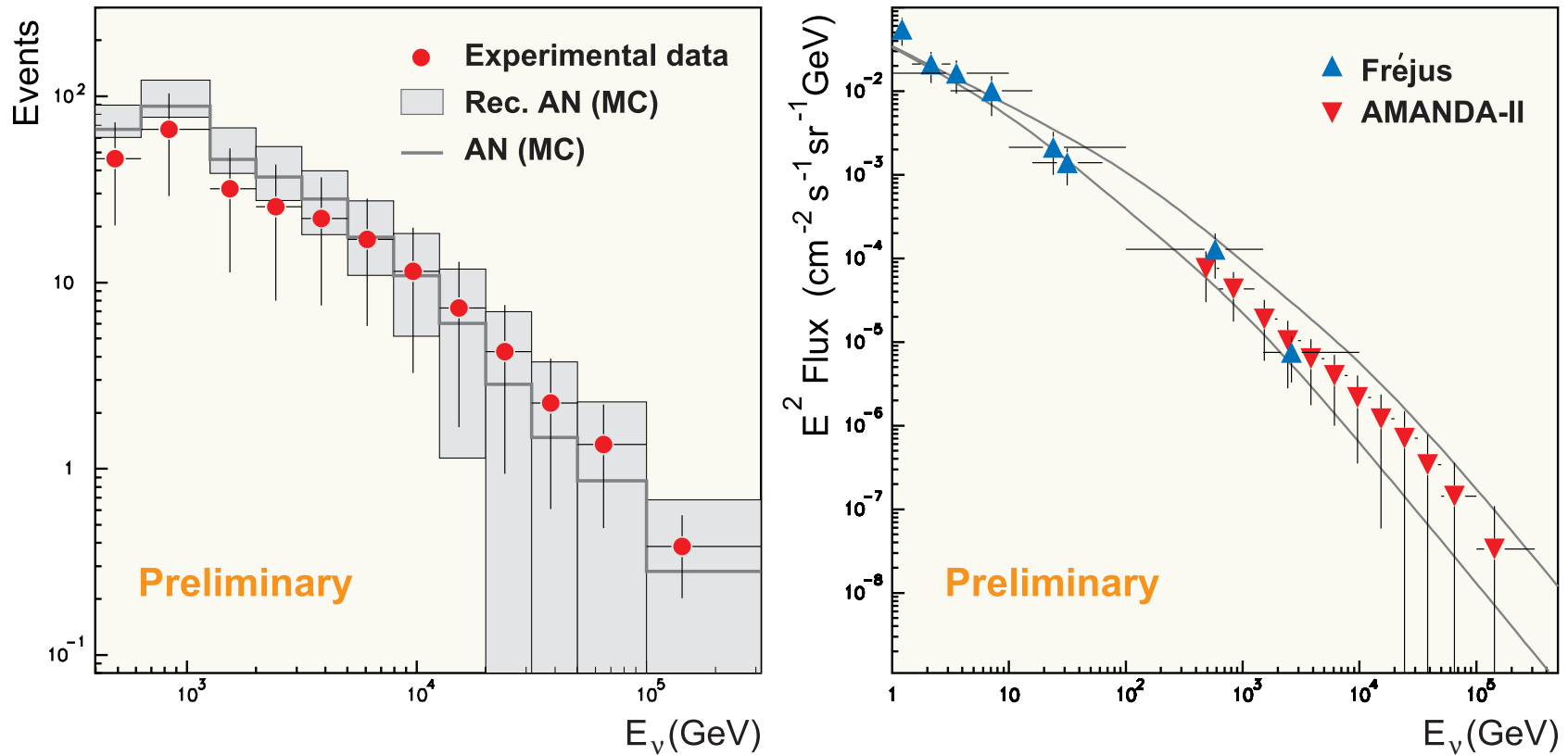


Figure 37: Reconstructed neutrino spectra in AMANDA-II. *Left panel:* on filter level (solid: energy distribution of atmospheric neutrino expectation, boxes: unfolded energy distribution of AN (MC), points: reconstructed data). *Right panel:* reconstructed fluxes compared to Fréjus data. [From H. Geenen (for the AMANDA Collaboration), contribution to the 28th ICRC, Tsukuda, Japan, July 31 – August 7, 2003 (see the AMANDA Berkeley Group homepage <<http://area51.berkeley.edu/>>).]

23 KM3 projects (IceCube, NEMO, NESTOR,...)

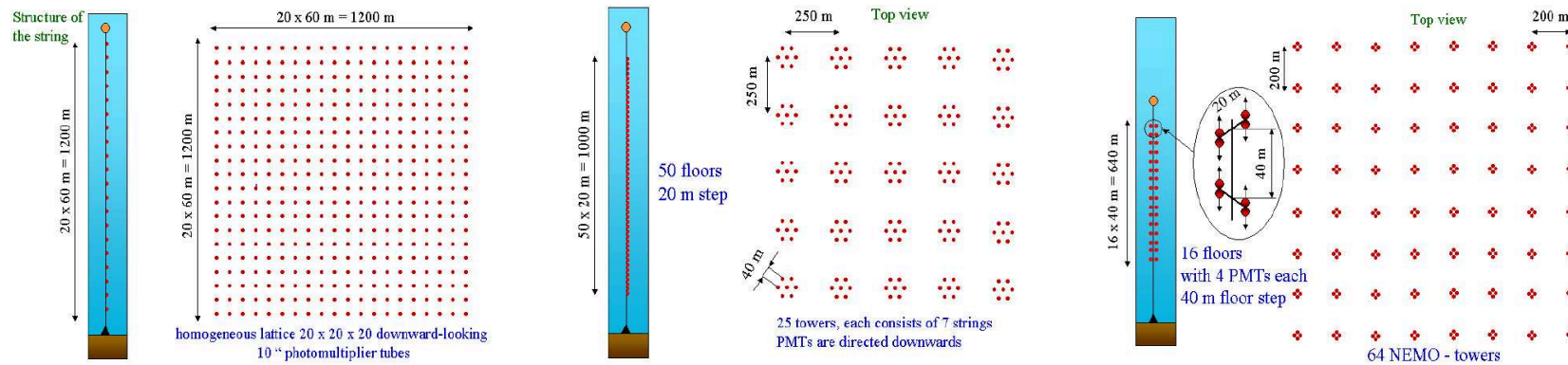


Figure 38: Future KM3 neutrino telescope geometries. *Left panel:* schematic view of a homogeneous detector with 8000 PMTs (not quite optimal to be built); *middle panel:* the layout of a NESTOR-like detector with 8750 PMTs; *right panel:* the layout of a NEMO-like detector with 4096 PMTs. These three designs have very different degrees of homogeneity. One more difference may be due to various numbers of downward-looking and upward-looking PMTs (down-down, up-down, etc.).

[From D. Zaborov, "Comparison of different KM3 designs using Antares tools," in Proc. of the Workshop on Technical Aspects of a Very Large Volume Neutrino Telescope in the Mediterranean Sea "VLV ν T", Amsterdam, October 5-8, 2003, ed. by E. de Wolf (NIKHEF, Amsterdam, The Netherlands), pp. 104–108.]

Part VI

FUTURE

UNDERGROUND

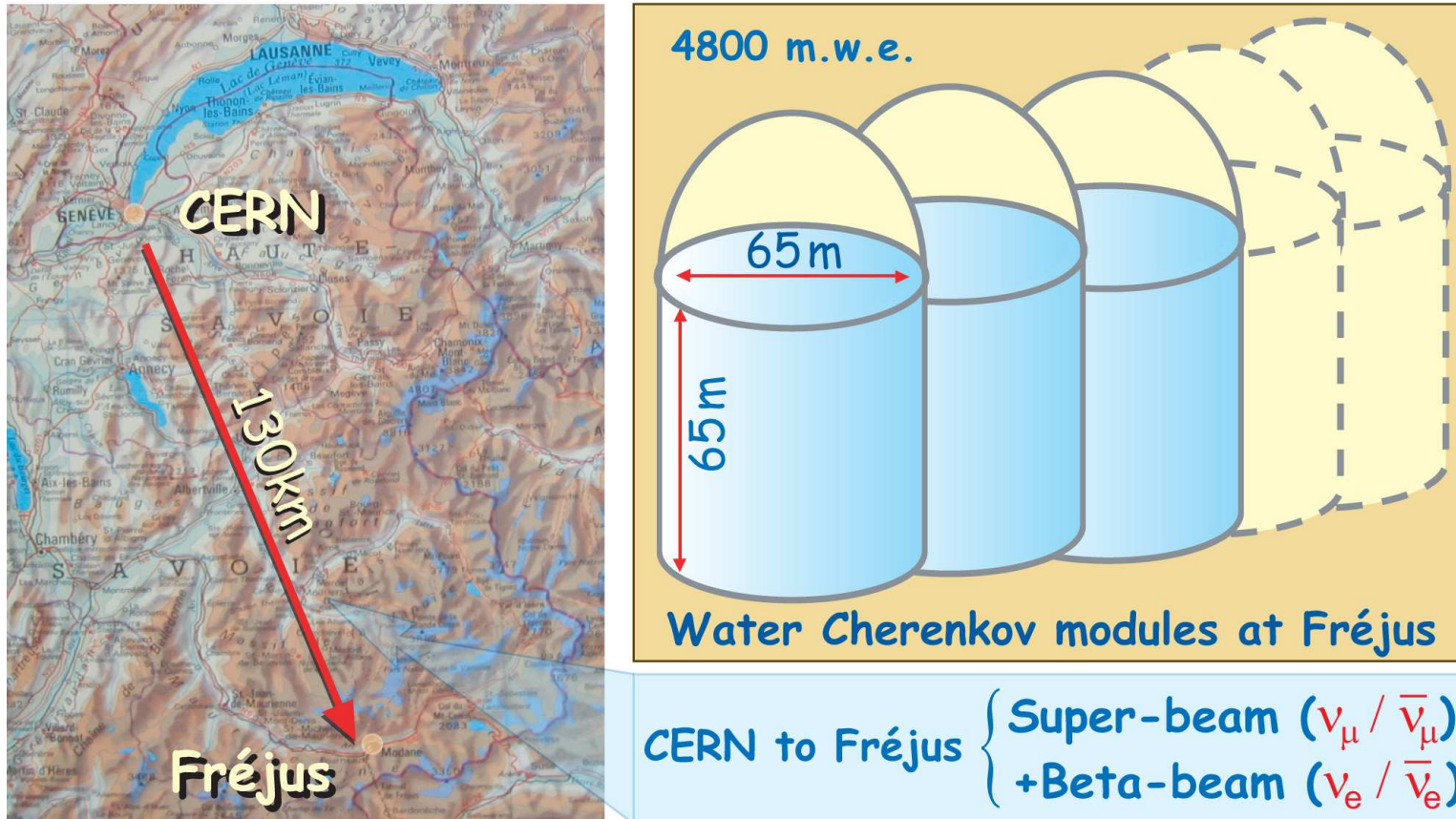
24 List of relevant experimental projects

- Experiments at **LNGS** [+ **CERN** ν beam(s)]:
 - ★ 0.2 kton iron/emulsion detector **OPERA** (**O**scillation **P**roject with **E**mulsion-**t**Racking **A**pparatus),
 - ★ **ICAN^{OE}** = 5 kton solid target **ICARUS** (**I**maging **C**osmic **A**nd **R**are **U**nderground **S**ignals) + 8 kton solid target **N^{OE}** (**N**eutrino **O**scillation **E**xperiment),
 - ★ 34 kton magnetized tracking calorimeter **MONOLITH** (**M**assive **O**bservatory for **N**eutrino **O**scillations or **L**imits on **T**Heir existence);
- experiments with **NuMI** (**N**eutrinos at the **M**ain **I**njector) beam line facility at **FNAL**:
 - ★ **MINOS** (**M**ain **I**njector **N**eutrino **O**scillation **S**earch) with two magnetized iron detectors [near (~ 1 kton) + far (5.4 kton)], **atmospheric ν analysis underway (!)**,
 - ★ **MINER ν A** (**M**ain **I**Njector **E**xpe**R**iment: ν -**A**),
 - ★ **NO ν A** (**N**uMI **O**ff-Axis ν_e **A**ppearance experiment);
- 650 kton underground water Cherenkov detector **UNO** (**U**ltra underground **N**ucleon detector and neutrino **O**bservatory);
- Multi-megaton water Cherenkov detector **TITAND** (**T**otally **I**mmersible **T**ank **A**ssaying **N**ucleon **D**ecay) [former name **TITANIC**];
- and many others [(**Mini**)**BooNE**, **FLARE** and **MiniLANNDD** at **FNAL**, **LANNDD** at **WIPP**, **3M** at **NUSEL**, **Super-ICARUS** and **Aqua-RICH** at **LNGS**, **T2K** at **J-PARC**, **Hyper-Kamiokande**, **MEMPHYS** at **Fréjus**, **INO**, **SCIPIO**,...

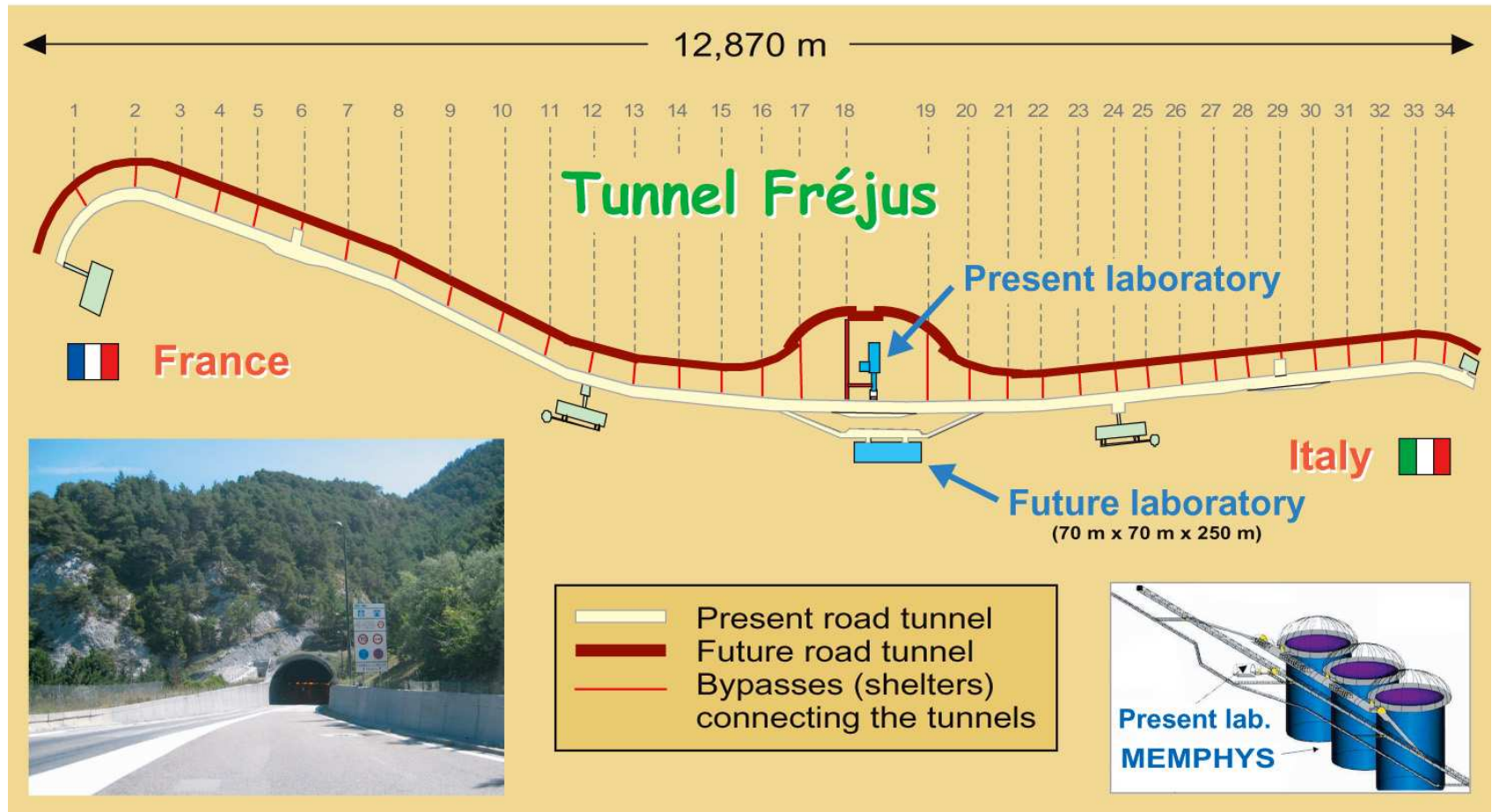
25 Hyper-Kamiokande

26 MEMPHYS

The MEMPHYS (MEgaton Mass PHYSics) is a project for a Megaton scale water Cherenkov detector in a large international underground laboratory in the Fréjus tunnel.^a



^aFor more details see J. E. Campagne, M. Maltoni, M. Mezzetto, and T. Schwetz, "Physics potential of the CERN-MEMPHYS neutrino oscillation project," hep-ph/0603172 and references therein.



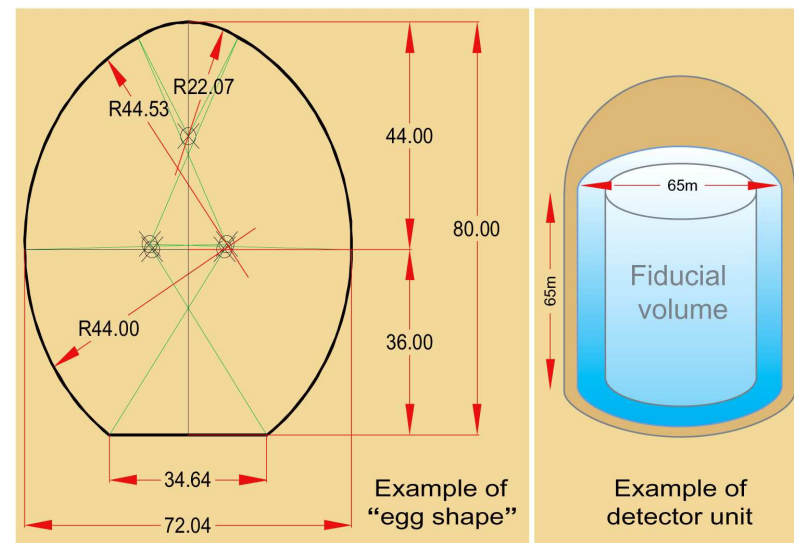
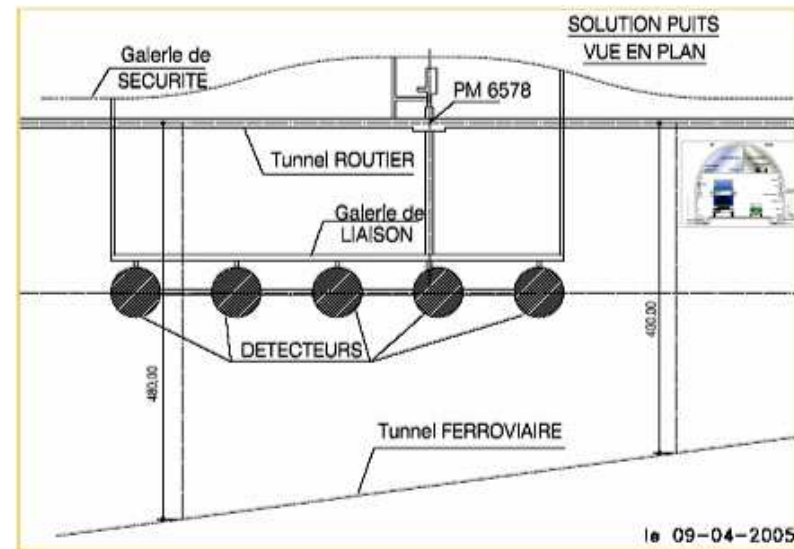
A preliminary investigation shows the feasibility to excavate in the middle of the Fréjus tunnel at a depth of 4800 m.w.e. up to five shafts of about 250,000 m³ each to place 3 to 4 water Cherenkov modules and a liquid argon detector (of about 100 kt total mass).

Main results of the preliminary study are

1. the best site (rock quality) is found in the middle of the mountain, at a depth of 4800 m.w.e.;
2. of the two considered shapes : “tunnel” and “shaft”, the “shaft (= well) shape” is strongly preferred;
3. Cylindrical shafts are feasible up to a diameter $\varnothing = 65$ m and a full height $h = 80$ m (volume $\approx 250,000$ m³);
4. with “egg shap” or an “intermediate shape” the volume of the shafts could be still increased (to $\varnothing = 70$ m);
5. the estimated cost is
 $\sim 80 \times 10^6$ Euros \times Number of shafts.

Detector basic unit:

a cylinder (*a la* SK) 65 m diameter and 65 m height \Rightarrow 215 kt of water ($\sim 4 \times$ SK) taking out 4 m from outside for veto and fiducial cut \Rightarrow 146 kt fiducial target.



Mechanics and photoelectronics is under R&D to minimize the **cost to quality** ratio.

The image is a composite of four parts illustrating detector technology:

- Top Left:** A schematic diagram of a detector array. It shows a grid of yellow spheres (representing PMT/HPD units) within a grey frame. A central purple component is labeled "Electronic water-tight box" with an arrow pointing to it.
- Top Right:** A 3D schematic of the detector array. The top section is labeled "PMT/HPD" with an arrow pointing to a row of yellow spheres. The bottom section is labeled "Basic unit" with an arrow pointing to a single unit.
- Bottom Left:** A photograph of various photomultiplier tubes (PMTs) of different sizes and shapes, some with blue and silver finishes.
- Bottom Right:** A photograph of a PMT assembly. The main spherical unit is mounted on a white base. A dimension line below it indicates a width of "33cm". To its right, a smaller component is shown with a dimension line indicating a width of "13cm".

Physics goals and potential

- ★ proton decay (for 5 Megaton × years):
 - $\tau(p \rightarrow e^+ p^0) \approx 10^{35}$ years,
 - $\tau(p \rightarrow n K p^+) \approx 2 \times 10^{34}$ years,
 - complementarity with liquid argon detector.
- ★ Neutrino bursts from supernovae explosion (collapse studies and explosion alerts):
 - $\sim 200,000$ events from a SN at 10 kpc,
 - ~ 30 events from Andromeda,
 - ~ 2 events at 3 Mpc.
- ★ Relic Neutrinos from past supernovae explosions (for 5 Megaton × years):
 - ~ 100 events with pure water,
 - 2000/4000 events with gadolinium loaded water.
- ★ Solar and atmospheric neutrinos.
- ★ Neutrino SPL super-beam (SB) and beta-beam (β B) from CERN.

27 MONOLITH



29



30

